Study of High Energy Steeply Up-going Air Showers with the Fluorescence Detector of the Pierre Auger Observatory

-

Constraining BSM Scenarios Producing Up-going τ Leptons

Dissertation

zur Erlangung des akademischen Grades eines

Doktors der Naturwissenschaften (Dr. rer. nat.)

der Fakultät Mathematik und Naturwissenschaften

Fachgruppe Physik

der Bergischen Universität Wuppertal

vorgelegt von

M. Sc. Ioana-Alexandra Caracas

(geboren in Bukarest)

July 2022

1. Gutachter:
Prof. Dr. Karl-Heinz Kampert
Bergische Universität Wuppertal

2. Gutachter
Prof. Dr. Jaime Alvarez Muñiz
Universidade de Santiago de Compostela

Abstract

Recent observations of two coherent events with steeply upward going cosmic ray signatures and energies of a few tenths of an EeV by the ANITA detector remain unexplained. The Fluorescence Detector (FD) of the Pierre Auger Observatory is also sensitive to such phenomena, given its substantial operation time and wide field of view (FoV). Using the more than 14 years of FD available data, a generic search for similar events with elevation angles greater than 20° and maximum shower energies of $10^{18.5}$ eV has been performed. Dedicated Monte Carlo simulations of both signal and background have been implemented and used within the analysis procedure. Together with these dedicated simulations, a 10% burn data sample was used for the final quality selection criteria. The obtained FD exposure has been calculated and is provided in a double differential form, in terms of shower energy and height of first interaction. With one event observed above an expected background of 0.45 ± 0.18, upper flux limits on up-going cosmic ray-like air showers have been set.

Events with signatures similar to the ANITA observations can not be explained by Standard Model (SM) physics and require the postulation of Beyond Standard Model (BSM) scenarios. Many such models result in the productions of τ-leptons, which would in turn decay in the atmosphere and induce the steeply up-going air showers. Such a hypothesis has been investigated in detail within this thesis, by translating the generic search in terms of up-going τ-induced air showers. For maximal flexibility, the results are independent of the τ-production mechanism. τ-leptons are directly generated both inside and above Earth, with an injection rate proportional to the media density, and their propagation, decay and interactions are treated in the presented analysis. The goal of the study is achieved by using the zenith angle, decay location and shower energy of any resulting τ-lepton decaying in the field of view of the Fluorescence Detector. The exposure of the FD of the Pierre Auger Observatory to steeply up-going τ-induced air showers is then obtained by folding the exposure results from the generic search with the double differential distribution of τ-leptons decaying and interacting in the FD-FoV. Differential upper limits as low as $10^{-9}\,\mathrm{GeV\,cm^{-2}\,s^{-1}\,sr^{-1}}$ on the flux of τ-leptons produced within less than 50 km distance below Earth are reported for several zenith angle sub-ranges and different primary energy spectra. This treatment insures the applicability of the presented results to a wide range of theoretical models producing τ-leptons and aiming to explain the "anomalous" ANITA events. In any such cases a significantly reduced cross section of the hypothetical particles with matter is needed, in order to insure an increased survival probability during their propagation through Earth. Interactions of such particles within the last few km distance below surface could result in the production of τ-leptons. Several such BSM scenarios have been investigated as part of this thesis, by artificially reducing the SM charged current neutrino-nucleon cross section by several orders of magnitude. Using the obtained upper bounds on high energy steeply up-going τ fluxes, such theories have been correspondingly constrained over a large range of BSM cross sections. The optimum cross section which is maximizing the τ-production and results in the most stringent upper bounds is found to be $\sigma_{BSM} = 10^{-2} \cdot \sigma_{SM}$.

The wide capability of the Pierre Auger Observatory to constrain several SM and BSM scenarios resulting in the production of up-going τ-leptons has been demonstrated by combining the FD results with the Surface Detector sensitivity to the Earth-Skimming channel.

Contents

List of Figures

List of Tables

1
Introduction

Understanding and exploring the mysteries of the universe represents one of the oldest concerns in the history of humanity. The sky itself has amazed people more than thousands of years ago, with the first attempts towards astronomical observations and documentation of several celestial body locations in time, dating back to the Mesopotamian civilisation. Since then, a lot of progress and knowledge has been gained in this regard, which in turn has raised many more questions to be answered. The branch of physics dedicated to such searches of any particle phenomena with a cosmic origin is astroparticle physics and has been actively studied for more than a hundred years. Dark matter, cosmic rays, neutrino and gamma-ray astronomy, as well as gravitational waves represent only few of the main topics of the field [1]. Many of these subjects have been thoroughly studied and benefited of exciting new results within the last years. With the constant development of the detection techniques, the observation of ultra-high energy particles has been improved, the highest recorded energy being beyond 10^{20} eV. This exceeds by far the maximum achievable energy in the biggest man-made accelerator, the Large Hadron Collider (LHC). These ultra high energies were discovered as a result of improved *cosmic ray* (CR) studies, leading to a corresponding enhancement in the CR detectors' capabilities. As at those energies the CR flux is on the order of 1 particle per square kilometer per century, large detectors covering a substantial area at ground are needed in order to obtain significant statistics.

The Pierre Auger Observatory is the biggest observatory dedicated to the detection of ultra-high energy cosmic rays (UHECRs), covering a surface area of 3000 km^2. Combining several detection techniques, both the observation of the secondary particles at ground, resulted from the UHECRs interaction with atmospheric nuclei, using the Surface Detector, as well as the recording of the shower development in the atmosphere, by taking advantage of the Fluorescence Detector, are possible. As a result of its enhanced detection capabilities, the Observatory is providing an unmatched sensitivity and largest statistics for CRs at the highest energies. Being operational since January 2004, the Pierre Auger Observatory has contributed tremendously in the CRs study, answering long standing questions regarding the features in the CR spectrum at the highest energies [2], the existence of an anisotropy in the arrival directions of CRs with energies above 8 EeV [3], mass composition studies of UHECRs [4, 5] etc. Furthermore, dedicated searches towards UHE photons [6] and neutrinos [7, 8, 9, 10] are also possible and have provided the most competitive results worldwide at the investigated energies. However, as shown in this thesis, the Observatory is, for the first time, also be shown to be sensitive to non-standard signatures, e.g. in terms of steeply up-going extensive air showers.

A dedicated search for upward propagating cosmic-ray like showers has been performed using the Fluorescence Detector (FD) of the Pierre Auger Observatory and represents the main subject of this thesis. The study has been triggered by the observation of two unusual events

by the ANITA detector [11, 12], with signatures that can be interpreted as steeply up-going cosmic-ray like showers, with few tenths of an EeV energies [13] and elevation angles greater than 20° from the horizon [14, 15]. As such events are in strong disagreement with the Standard Model (SM) physics, the corresponding neutrino fluxes exceeding the already existent upper bounds by several orders of magnitude [16, 7, 8], a follow-up search is of great interest. The FD of the Pierre Auger Observatory is also sensitive to this phenomena, and has a wide field of view, as well as a substantial operation time. Having more than 14 years of available FD data, the obtained results can be further used to either confirm or refute such observations. As these events have been later reanalyzed with dedicated MC simulations, it was shown that their energy is dependent on their first interaction point, where the shower starts to develop in the atmosphere [13]. Consequently, the dedicated follow-up study has investigated such events starting to develop at different altitudes and the final results in terms of FD exposure are provided accordingly and presented in a double differential form, in terms of shower energy, E_{sh}, and first interaction height H_1. This way of presenting the results is extremely useful and can be further adopted in order to test any primary model. Such an example application has been studied, in terms of τ-lepton induced air showers, and represents another personal contribution presented in this thesis. As no candidate event above the expected background has been found, corresponding stringent upper bounds have been set on the fluxes of steeply up-going showers, using the FD of the Pierre Auger Observatory. The obtained results regarding the upper flux limits on τ-induced air showers have been further translated in terms of BSM particle fluxes. In this scenario hypothetical particles with reduced cross sections are propagated through Earth, having a sufficiently high survival probability. Interactions close to the surface can then result in the production of τ-leptons that escape into the atmosphere and initiate extensive air showers. This study results in upper bounds on various BSM scenarios and serves as a proof of concept of the wide applicability of the investigated τ-lepton induced air showers scenario. To emphasize the capability of the Observatory to constrain a large range of models resulting in the creation of τ-leptons, the BSM study has been extended to the Earth-Skimming channel. Consequently, combined upper limits on particles producing upwards going τ-leptons are provided for a large range of cross sections, both for the SM and BSM scenarios, using the Pierre Auger Observatory.

This thesis is divided in eight chapters. After the current introduction, a short overview of cosmic rays physics, from their discovery up to nowadays knowledge and open questions, is addressed in Chapter 2. A brief summary regarding the spectrum of CRs and its main features, the still elusive nature of the CR fluxes' suppression at highest energies, together with its possible interpretations, is given. The main acceleration mechanisms which are believed to be able to accelerate CRs up to the highest energies are also shortly presented. In the second section of the chapter Extensive Air Showers (EAS) are introduced, as they represent the main phenomena studied and detected within the Pierre Auger Observatory. This comprises of a short overview of the main characteristics of an EAS. Since the study presented in this thesis is using the Fluorescence Detector, this section is focused on the longitudinal development of the shower profile in the atmosphere.

In Chapter 3 the Pierre Auger Observatory is introduced. A short synopsis over the different detection techniques and instrumentation within the Observatory is given. As men-

tioned above, the results presented in this thesis are obtained using the Fluorescence Detector. Therefore, a dedicated section within this thesis is focusing on the FD, with information regarding both the instrumentation and the main background that has to be properly monitored and accounted for in order to achieve precise measurements. As most of the obtained results are heavily dependent on simulations, a separate section provides information about the reconstruction of an EAS using the FD observations. Lastly, the collaboration analysis software, which has been heavily used in order to obtain the presented results, is introduced in the final section of this chapter.

A short overview on up-going air showers is given in Chapter 4, with the main differences between such events and the down-going case being emphasized. Further on the ANITA experiment, with a main focus on the anomalous events and their disagreement with SM predictions is presented. In the remaining sections the pioneering steps towards simulating up-going air showers, as well as the main updates implemented to the existent framework are presented. In the end of the chapter the first exposure results obtained from this preliminary step are discussed.

Chapter 5 focuses on the dedicated search of up-going cosmic ray-like air showers with the Fluorescence Detector of the Pierre Auger Observatory. The adopted signal simulation procedure, with a main focus on the adopted events geometry, is explained. Additional steps in the study are represented by background simulations, as well as data cleaning, which has been achieved using a burn data sample, containing 10% of the total available data. Using the results in terms of signal, background and burn data, a final cut regarding the candidate selection is determined and the FD exposure to steeply up-going cosmic ray-like air showers is obtained. In order to widen the applicability of the current study, the obtained results are presented in a double differential form, with respect to shower energy E_{sh} and first interaction height H_1. With 1 event observed after unblinding the whole data set, which is consistent with the expected background of 0.45 ± 0.18, corresponding upper flux limits on up-going cosmic ray air showers are set.

The generic results regarding cosmic ray-like showers are further translated in chapter 6, in terms of steeply up-going τ-lepton induced air showers. Given the surprising nature of the ANITA observations, several theoretical interpretations involving Beyond Standard Model physics have been proposed, attempting to interpret them. Many of these scenarios, such as heavy dark matter [17], sterile neutrino mixing [18], stau decays [19] etc. result in the production of τ-leptons. To widen the applicability of the obtained results, τ-leptons are directly generated inside Earth and in the atmosphere, with an injection rate proportional to the media density, without considering any specific production mechanism. The leptons are propagated inside Earth, taking into account their energy losses, until they decay, using a heavily modified version of NuTauSim [20]. The τ-decays are modeled by TAUOLA [21] and the resulted decay daughters are further evaluated in terms of their potential to contribute to the shower energy deposit in the atmosphere. The resulted distribution of τ-decay induced air showers is then presented in a double differential form, in terms of height of first interaction H_1 and shower energy E_{sh}. This 2D distribution is further folded together with the double differential exposure results to up-going cosmic ray-like air showers. As a result, the exposure of the FD of the Pierre Auger

Observatory to steeply up-going air showers induced by τ-decays due to τs produced inside Earth or within the first few kilometers in the atmosphere, by an unspecified mechanism is obtained. Given the non-observation of any candidate events, corresponding upper flux limits are set on steeply up-going τ-induced air showers with primary energies $E_0 \in [10^{16.5}, 10^{20}\,\text{eV}]$ and zenith angles $\theta \in [110^\circ, 180^\circ]$. The current study in terms of τ-induced air showers is not only extremely important for the scientific community, but it also represents a proof of concept, emphasizing the importance of providing the exposure to cosmic ray-like air showers in a double differential form: H_1 vs E_{sh}. By following the presented approach, any primary can be correspondingly tested, as long as the decay mechanism is well known.

Chapter 7 is dedicated to the study of hypothetical BSM particles which are surviving Earth propagation up to very small distances below ground, and further interact within the last few kilometers distance below the surface, resulting in the creation of τ-leptons. Given the steeply up-going context in any such scenario, the BSM cross section needs to be significantly lower than the SM neutrino one at the energies of interest: $E \geq 10^{17}\,\text{eV}$. Starting from the obtained upper flux limits in terms of τ-induced air showers presented in chapter 6, several such BSM scenarios can be correspondingly constrained using the FD of the Pierre Auger Observatory. Two different cases are investigated in detail: a fixed cross section scenario and an energy dependent one, and the corresponding BSM upper bounds are presented. The study is further extended to the Earth Skimming (ES) channel, where the Surface Detector has an unmatched sensitivity to ν_τ-induced air showers. By combining the obtained results in terms of steeply up-going and ES channel, the capability of the Pierre Auger Observatory to constrain a wide range of both SM and BSM scenarios resulting in the production of τ-leptons with energies $E > 10^{17}\,\text{eV}$ is emphasized.

The obtained results are summarized in Chapter 8. The importance of the dedicated follow-up study of up-going cosmic ray-like showers with the fluorescence detector of the Pierre Auger Observatory is highlighted, representing the first attempt to constrain such anomalous events. Presenting the exposure results in a double differential form represents a pioneer in such searches and is of a particular interest for the scientific community. As shown in the presented τ-leptons study, starting from these results any primary scenario can be correspondingly constrained. The stringent upper flux limits obtained for steeply up-going τ-induced air showers are discussed within this chapter and the importance of this study is emphasized. The investigated BSM scenarios are also reviewed and several further improvements to the presented procedure are proposed.

2

Cosmic Rays and Extensive Air Showers

Cosmic rays represent the pioneering field of elementary particle physics. The first strong evidence of the existence of cosmic rays dates back to 1909, when Theodor Wulf used an electrometer to measure the ionization of the air at different altitudes. Contrary to the expectations at that time, the measured radiation level at increasing heights on the Eiffel Tower decreases at a much slower rate than expected for a terrestrial-only origin, pointing to a secondary radiation source [22]. However, since Wulf's efforts were largely dismissed by the community, the hot air balloon experiment of Victor Hess is commonly taken to represent the first concrete proof, as well as the starting point of cosmic rays physics.

In order to test the hypothesis of the existence of a celestial source for the air ionization measured by Wulf, Victor Hess performed a series of measurements at different altitudes, up to 5.3 km a.s.l. Having first improved the accuracy of the existing instruments, he performed air balloon flight measurements over more than three years, both during day and night. He observed there was a slight decrease of radiation for altitudes up to 1.4 km [23], followed by a strong increase with the increase in altitude. Having measured no reduction of the radiation level during the night or during the solar eclipse, he correctly concluded there must be a cosmic radiation source that originated from regions much further than the Sun. For these outstanding findings he was awarded with the Nobel Prize in 1936 [24].

In the first years following Hess's observations, it was strongly believed this cosmic radiation had an electromagnetic origin and it was therefore referred to as *Cosmic Rays* (CR). However, in 1927, using an ionization chamber, Jacob Clay showed the existence of a significant difference in the cosmic ray intensity measured at different latitudes. This variation was shown to be correlated with the strength of the Earth's magnetic field, disproving the very popular gamma ray hypothesis. He has thus correctly concluded that most of the cosmic rays consist mainly of charged particles [25].

The Geiger-Müller (GM) counter, developed in 1928 [26], represented a major improvement in the cosmic rays research. In 1930, Bruno Rossi suggested the Earth's magnetic field should strongly influence the different charged particles [27]. Assuming that CRs likely have the same charge, he expected to see a difference in the flux of particles coming from the east than from the west, due to the Earth's magnetic field orientation. Using the GM detector he was able to verify his theory, which is now-called the *East-West effect*. Notably, he observed an excess in the intensity of CRs coming from the West, showing that most of the cosmic rays are positively charged. Several different studies have further confirmed Rossi's discovery.

In 1940 Marcel Schein performed a balloon flight in a first attempt towards discovering the nature of the positive charged particles. Using lead absorbers and GM tubes for detection, Schein observed that the high energy particles pass through the lead material without creating any low energy secondaries, from which he concluded that the observed positively charged cosmic

rays were mainly composed of protons [28]. Between 1932 and 1953 several studies towards the cosmic rays composition were performed, which further confirmed the predominance of protons [29, 30]. Nowadays it is well known that CRs are ionized nuclei, composed of $\approx 90\%$ protons, $\approx 9\%$ Helium nuclei and $\approx 1\%$ heavier nuclei [31].

After more than one hundred years since Hess's discovery, the knowledge towards cosmic rays has increased significantly. Nowadays cosmic rays are defined as high energy charged particles, travelling at speeds close to the speed of light. CRs detection has also improved significantly over time, their observed energy extending over more than 12 orders of magnitude, providing thus valuable information about the nature of galactic and extra-galactic processes in the Universe. Being electrically charged, it is difficult to extract information regarding the position of their sources from CRs alone, since they are deflected by the galactic and extra-galactic magnetic fields during their propagation. However, by measuring the corresponding CRs fluxes and composition, important information regarding their origin can be obtained. Additional information on the source locations can be achieved by detecting neutral particles with similar energies. In this sense, neutrinos and gamma-rays constitute the main candidates. The study of high energy gamma-rays and neutrinos, combined with gravitational waves (GW) detection, constitutes the relatively new field of research of multi-messenger physics, which attempts to give a complete picture of the Universe.

2.1 Cosmic Ray Fluxes

Covering a wide energy range, the study and detection of CRs requires a complex combination of technological equipment and analysis techniques. Energies of detected cosmic rays are spanning over more than 12 orders of magnitude (from $10^8\,\text{eV}$ to beyond $10^{20}\,\text{eV}$). The highest energies in this range, $E \geq 10^{18}\,\text{eV}$, are exceeding by far the maximum obtained energies from any man-made accelerator. As these Ultra High Energy Cosmic Rays (UHECR) interact with atomic nuclei in the atmosphere, the center of mass energy in the nucleon-nucleon system exceeds the LHC one by more than 2 orders of magnitude [31].

The energy spectrum of cosmic rays (flux of particles as a function of energy) has a distinct pattern which can be well described through a broken power law:

$$\frac{dN}{dE} \propto E^{-\gamma} \tag{2.1}$$

where γ represents the so-called spectral index. Depending on the energy range of interest, γ has different values, which can provide information on the CR's origin and propagation.

As the CRs energy increases, the number of particles reaching Earth decreases significantly, from $\approx 1\text{m}^{-2}\,\text{s}^{-1}$ at $E \approx 10^{10}\,\text{eV}$ to $\approx 1\text{km}^{-2}\,\text{yr}^{-1}$ at $E \approx 10^{19}\,\text{eV}$, as expected from Eq. 2.1. Consequently, two main detection methods are used, depending on the investigated energy range. For low energy CRs, $E \leq 10^{13}\,\text{eV}$, direct measurements using detectors at the top of the atmosphere are performed [31]. At higher energies, this technique is ineffective, given the much lower CR fluxes. For $E \geq 10^{13}\,\text{eV}$, an indirect detection using the air shower measurements is used. More details on air showers are given in section 2.2.

The cosmic rays spectrum, obtained from the indirect detection and measured by sev-

eral air shower experiments, is shown in Fig. 2.1. In order to underline the various features of the spectrum, the provided value of the flux is scaled with energy.

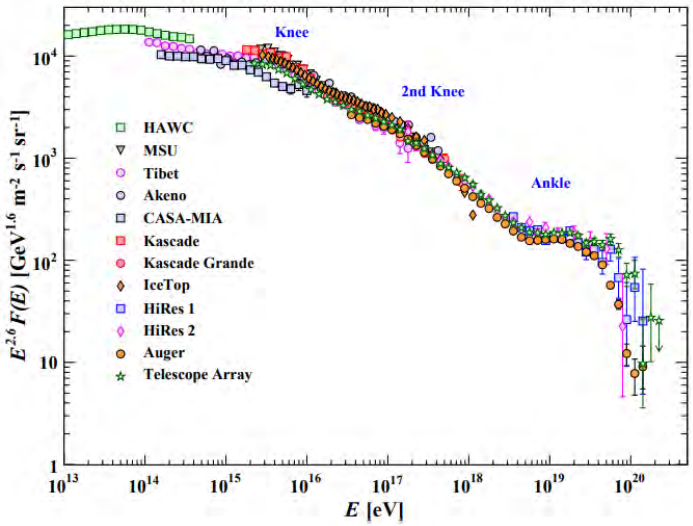

Figure 2.1: The CR energy spectrum, taken from [32].

2.1.1 Features in the Cosmic Ray spectrum

As expected from the broken power law in Eq. 2.1, the flux of cosmic rays rapidly decreases with increasing energy. For energies below $\approx 10^{13}\,\text{eV}$ the flux of cosmic rays is very high and can therefore be directly measured at high altitudes by balloon experiments or in space-born instruments [33].

The only exactly known source of CRs is the Sun, which is responsible for the emission of CRs with energies up to the GeV range. At those low energies, the galactic cosmic rays can not enter the solar system due to the termination shock produced when the solar wind intersects the interstellar medium. As the energy increases past few GeV, the Sun reaches its maximum acceleration and becomes less and less predominant as the main source in the CRs spectrum. For higher energies, as revealed by the direct measurements, the galactic sources represent the predominant component in the CR fluxes. For such observations, the CRs composition can be directly detected. By comparing the relative abundance of several nuclei from these observations to the corresponding elements abundances in the solar system, a similar composition is found. A slight increase towards lighter elements is observed in the cosmic radiation, notably for the Li, Be, B elements [34]. As these elements are absent as final products in stellar nucleosynthesis, they appear as a result of CRs collisions with the interstellar medium (ISM), via the spallation of heavier and more abundant C, N and O nuclei. A very strong source candidate for such CRs is represented by supernova remnants (SNRs). At these energies, $E \in [10^9, 3 \times 10^{15}\,\text{eV}]$, the corresponding CR spectrum is described by a spectral index of $\gamma \approx 2.7$. For higher energies the direct detection method is no longer possible, and indirect measurements are performed by air shower detectors.

At an energy of $E \approx 3 \times 10^{15}\,\text{eV}$ the spectrum steepens, exhibiting a feature called the *knee*. This is likely indicating the maximum acceleration of the galactic sources for protons.

Measurements in [35] are consistent with this interpretation, exhibiting a predominant light CR composition at these energies. The spectrum shape within this region is not very stable, but can be well described by a spectral index of $\gamma \approx 3.1$. Since the maximum source rigidity is dependent on the primary's atomic number, a shift towards heavier nuclei is expected with the increase of energy, as the galactic sources are expected to reach their maximum acceleration for heavier and heavier primaries. A second steepening in the spectrum appears at an energy of $E \approx 10^{17}$ eV, referred to as the *second knee*. This is thought to mark the maximum energy that Fe-nuclei may reach in galactic sources. The corresponding spectral index describing the CR fluxes at this energy is $\gamma \approx 3.3$. Two main acceleration mechanisms are known to be able to accelerate particles up to these energies and result in a power law spectrum: first and second order Fermi acceleration [36]. The most powerful shock acceleration appears in supernova remnants (SNR), considered one of the main source candidates for the CRs produced up to the second knee [37].

At higher energies the composition, acceleration and production mechanisms are even less understood. This is on one hand due to the fact that direct observation is not possible at those energies, and on the other hand due to the fact that the investigated energies exceed the maximum energies produced via shock acceleration. Energies higher than $E > 10^{17}\,\text{eV}$ mark the transition region between galactic and extra-galactic sources. As mentioned above, the spectrum in this region is described by a spectral index of $\gamma \approx 3.3$, extending up to energies of $E \approx 5 \times 10^{18}\,\text{eV}$. Here, another feature, referred to as *the ankle*, is observed in the CR spectrum and is well described by a spectral index of $\gamma \approx 2.5$. The ankle is believed to indicate the region where the extra galactic sources become dominant in the cosmic ray fluxes. This is consistent with the very light CR composition at energies slightly below the ankle, with a remarkable proton fraction which is shifting towards heavier elements as the energy increases [38], [39], [40].

The nature of cosmic rays beyond the ankle is still unknown and represents one of the most challenging subjects in CR physics. This is mainly due to the low rate of events at the given energy: $< 1\text{km}^{-2}\text{yr}^{-1}$, as well as due to the very high energies, where theoretical interaction models need to be extrapolated by several orders of magnitude. As seen in Fig. 2.1, a strong *cutoff* in the CR spectrum is observed at energies $E \approx 10^{20}\,\text{eV}$. This has several interpretations which will be discussed in detail in subsection 2.1.2.

2.1.2 The Cutoff in the Cosmic Ray Spectrum

Indirect detection methods, using air shower detectors at ground, are required for the observation of very high energy cosmic rays with $E \geq 10^{15}\,\text{eV}$. In order to be able to detect ultra high energy cosmic rays (UHECRs), with $E \geq 10^{18}\,\text{eV}$, giant air shower arrays are needed. The two largest CRs observatories, the Pierre Auger Observatory and Telescope Array(TA), with exposures of thousands of $\text{km}^2\,\text{sr}\,\text{yr}$, allow spectrum measurements below the ankle, up to the cutoff region. The cutoff in the CR spectrum is a subject of great interest and debate in the scientific community. As CRs statistics at these energies is very limited, definite conclusions are difficult to achieve. Mass composition studies represent one of the key elements regarding the phenomenology of the cutoff. Different results are obtained by the two collaborations regarding the UHECR composition below the ankle. While the Pierre Auger Observatory's data indicates a transition towards heavier elements at the highest energies [41], TA's data are in agreement

with a constant light composition at the energies of interest [42]. This is a matter of continuous debate and will not be further covered here. It is however worth mentioning the discrepancy between the two different results can be related to differences in statistics, data analysis, detector calibration or different sources' spectrum in the two hemispheres [43]. However, this is a subject which is constantly investigated and future updates of the two detectors are believed to lead to a definite answer.

There are several possible phenomena which could result in the observed cutoff at the highest energies in the CR spectrum. These scenarios are listed below.

The GZK cutoff: The GZK (Greisen-Zatsepin-Kuzmin) cutoff [44, 45] represents a theoretical upper limit on the maximum energy of a high energy proton propagating through the intergalactic space, which is filled with relic photons from the big bang. These photons are often referred to as cosmic microwave background (CMB). In the reference frame of an ultra high energy (UHE) proton, the CMB photons appear as highly blue shifted, with correspondingly high energies. These high energy photons can create a Δ^+ resonance as a result of their interaction with the protons. Being a highly unstable state, Δ^+ will further decay via two different channels:

$$p + \gamma_{CMB} \rightarrow \Delta^+ \rightarrow p + \pi^0 \tag{2.2}$$

$$p + \gamma_{CMB} \rightarrow \Delta^+ \rightarrow n + \pi^+ \tag{2.3}$$

The resulting pions will correspondingly decay via the pion decay channels: the neutral pions decay into two photons and the charged ones into muons and neutrinos.

The protons in Eq. 2.2 will propagate further and can either be detected or interact with the CMB as long as their energy allows it. The neutron produced in Eq. 2.3 is propagating for a long distance and is eventually decaying into electrons, anti-electron neutrinos and protons. These protons can in turn further interact with the relic photons. For each interaction with the CMB described in Eq. 2.2 and 2.3, the protons are loosing $\approx$ 20% of their energy [44]. Consequently, the high energy protons will have a significant energy loss during their propagation from the sources to the detector. This process occurs until the proton energy is too low to produce a Δ^+ resonance at their scattering on CMB photons. This happens at a proton energy of $\approx 5 \times 10^{19}$ eV and represents the *GZK threshold*.

A concrete evidence supporting the GZK limit would be the observation of a definite cutoff at this energy, with a primary CR composition dominated by protons. Moreover, photons and neutrinos resulting from pion decays in Eq. 2.3 and 2.2 should be observed at similar rates as the corresponding protons. Many searches for UHE neutrinos and photons have been performed by various experiments [46, 47], but up to date no candidate has been observed. Additionally, data from the Pierre Auger Observatory indicate an increasingly heavy composition towards the GZK threshold, disfavoring the GZK effect [41]. As mentioned above, since the TA and Pierre Auger data show some tension in the inferred mass composition of UHECRs above the ankle, this is still a subject of debate.

Photo-disintegration: The photo-disintegration process is very similar to the GZK effect, but is concerning heavier primaries. An UHE nuclei travelling through intergalactic space will

interact with the blue shifted CMB photons. Once the energy of the photon exceeds the binding energy per nucleon of the nuclei, it is able to remove individual nucleons. When the process takes place, the mass and energy of the nucleus are reduced. The process is shown in Eq. 2.4 below, where the nucleus X with N neutrons and Z protons absorbs a photon and releases a neutron as a result of the photo-disintegration.

$$ {}^{N}_{Z}X + \gamma \rightarrow {}^{N-1}_{Z}X + n \tag{2.4} $$

As in the GZK case, this results in an upper energy limit for heavier nuclei. However, in this case the cutoff would not be so hard, since it highly depends on the mass of the primary particles, but it is expected to take place at similar energies.

The GZK limit together with the photo-disintegration process could in principle explain the observed cutoff in the CRs spectrum. As mentioned above, this has to be further investigated.

Maximum Rigidity: The maximum rigidity effect on the CR spectrum cutoff is very similar to the explanation for the knee and the second knee. While the knees are assumed to be an effect of the maximum rigidity of the galactic sources (protons for the first knee and iron for the second one) [48], the cutoff at the highest energies can be correlated to the maximum rigidity of the extra-galactic sources.

In this case the primary composition would be mainly dominated by protons in the ankle region of the CR spectrum, leading towards heavier primaries at higher energies. The high energy end of the spectrum would be dominated by heavy elements in this scenario. The cutoff can thus be explained as the point where the extra-galactic sources have reached their maximum rigidity, after which point they are not able to accelerate the heavier primaries any further [49].

The data of Pierre Auger Obervatory indicate a heavier mass composition towards the highest energies [4], [5], favoring thus this scenario.

Given the limited statistics at these ultra-high energies, and having only indirect measurements which can provide insights regarding the CR composition, no definite answer can be given regarding the spectrum cutoff. Consequently, none of the three above mentioned scenarios can be either refuted or confirmed at the present moment, given the tension between the two biggest CR observatories [43]. It is however possible that all the three effects contribute to the cutoff of the energy spectrum. This is a subject which is strongly investigated, as the understanding of the cutoff origin is of crucial importance regarding CR sources and acceleration mechanisms. Future upgrades of the existing detectors will increase the statistics and provide more insights on this matter.

2.1.3 Cosmic ray acceleration scenarios

The origin of cosmic rays represents a major interest ever since their discovery. Outstanding discoveries were made in the CR physics field within the last ≈ 100 years, as a result of considerable developments in the detection technology. With improved detection techniques and extended knowledge, new inquiries regarding CRs have arisen. The observations of ultra-high

energy cosmic rays with energies up to $\approx 10^{20}$ eV suggest the existence of extremely powerful accelerators in the Universe. The origin of such energetic cosmic rays is most likely extra-galactic, since the galactic magnetic field is too weak to confine particles at these ultra-high energies[1].

There are two main acceleration mechanisms concerning a *bottom-up*[2] production of CRs:

1. The **one shot acceleration scenario** is an inductive acceleration mechanism. It describes the particles being continuously accelerated by a large scale electric field before leaving the accelerator. Such electric fields can be associated to the fast rotation of magnetized objects such as neutron stars, black holes, active galactic nuclei (AGN) [50]. This mechanism is mostly disfavored due to the fact that it can not explain the observed power law energy spectrum.

2. **The stochastic acceleration mechanisms** regard the particles' acceleration in a gradual way, as a result of several encounters with massive objects in the interstellar space. These scenarios date back to 1949, when Fermi proposed the acceleration of particles via several collisions with a moving magnetized plasma [36]. The stochastic acceleration mechanisms result in a power law energy spectrum, as is the case for observed CRs (see Eq. 2.1). There are two such scenarios, *the second order Fermi acceleration* and *the first order Fermi acceleration*.

   The second order Fermi acceleration explains the energy gained by a CR particle as a result of its collision with the interstellar clouds. As the clouds are constantly moving, they behave as *magnetic mirrors* upon the particles, which are reflected off them. During this process particles can both gain and loose energy. However since the probability of a head-on collision is higher than the probability of a tail-on collision, the mean energy of the particles is increasing. After several such head-on collisions, particles can be significantly accelerated. The average energy gained per one encounter from such a process is proportional to β^2, where $\beta = v/c$ and v is the cloud's velocity. The value of the exponent is what gives the name of *second order* acceleration mechanism. Although this scenario results in a power-law spectrum, its main caveat is the very slow acceleration process, given the much lower clouds velocities compared to the speed of light.

   A more effective stochastic acceleration mechanism is ***the first order Fermi acceleration***, often referred to as *diffusive shock acceleration*. In this scenario the cosmic rays gain energy as a result of their collisions nearby relativistic shock waves. A plane shock front is propagating with a given velocity. In the reference system of the shock, two regions are created: the downstream region comprised of the shocked gas behind, which is receding from the shock front, and the upstream region referring to the gas in front of the shock front, approaching it. CRs crossing the shock front are scattered back and forth, being able to traverse it several times and gaining energy at each "crossing". The magnetic irregularities on either side of the shock wave can be identified as clouds of magnetized plasma,

[1] As discussed in section 2.1.1, the maximum galactic sources acceleration is rigidity dependent. However it is strongly believed that extra-galactic sources are dominant for energies below the ankle

[2] The *bottom-up* scenario is describing a low energy CR that is accelerated up to the observed energy. The *top-down* models are describing high energetic particles which decay to the observed energy in the CR energy spectrum. The latter scenario is generally used to describe exotic particles.

as in the case of second order Fermi acceleration. A particle travelling through the shock wave (upstream to downstream) will be accelerated in the shocked gas within the downstream region. A similar process repeats for the particle crossing the shock downstream to upstream. Given its ability to diffuse on both sides of the shock, the particle can have several collisions with the downstream/upstream region. This is due to the fact that in the reference frame of the particle located on either side of the shock front, the plasma on the opposite side is always approaching it. Consequently, the particles are accelerated as they are recoiled back and forth between the downstream and upstream regions of the shock wave. Within this mechanism the energy gain is proportional to $\beta = v/c$. This makes the acceleration mechanism much more efficient. In the case of strong shocks, the first order Fermi acceleration results in an E^{-2} spectrum. Moreover, shock waves are expected to be created in different astrophysical media, making the diffusive acceleration mechanism one of the most promising scenarios.

The acceleration mechanisms are only one of the puzzling elements regarding CR sources. The corresponding location of the sources remain a mystery, since at all but the very highest energies, the trajectory of the CRs is strongly affected by the galactic and extra-galactic magnetic fields. As a consequence, CRs are strongly deflected and loose all the information regarding the position of their emission. There are however several studies towards anisotropies in the CR arrival directions which are focusing on this subject. The Pierre Auger Observatory has the largest statistics of high energy events and has performed several studies in this regard [51],[52],[53]. Together with the new field of multimessenger physics, via the detection of ultra-high energy neutrinos and gamma rays, more light will be shed on this subject in the near future.

As at the very high energies the only possible detection method is represented by the shower array detectors, the primary cosmic ray can not be directly observed. As the CR is entering the atmosphere, it interacts with the atmospheric nuclei, producing a cascade of secondary particles, often referred to as an extensive air shower. Only the particles reaching the ground can be directly detected. Therefore a good knowledge of the extensive air showers, their development in the atmosphere together with their main parameters, as well as detector systematics and interaction models are required in order to obtain the necessary information about the primary CR particle.

2.2 Extensive Air Showers

As mentioned above, in order to study high energy cosmic rays with energies $E \geq 10^{15}\,\mathrm{eV}$, indirect detection methods are required. Sparse ground based detectors are used in this regard. As the UHECR fluxes are extremely low, very large detection areas are needed in order to achieve exposures of thousands of $\mathrm{km}^2\,\mathrm{sr}\,\mathrm{yr}$ [31].

When a high energy particle enters the atmosphere, it interacts with the atmospheric nuclei and a cascade of secondaries, which is often referred to as an *Extensive Air Shower (EAS)*, is produced. An EAS comprises all the secondary particles produced from the first interaction point down to the ground, where the surface detector arrays are located. A good understanding

of the air shower development is of crucial importance for inferring the main parameters of the primary cosmic ray. A sketch of an EAS is shown in Fig. 2.2.

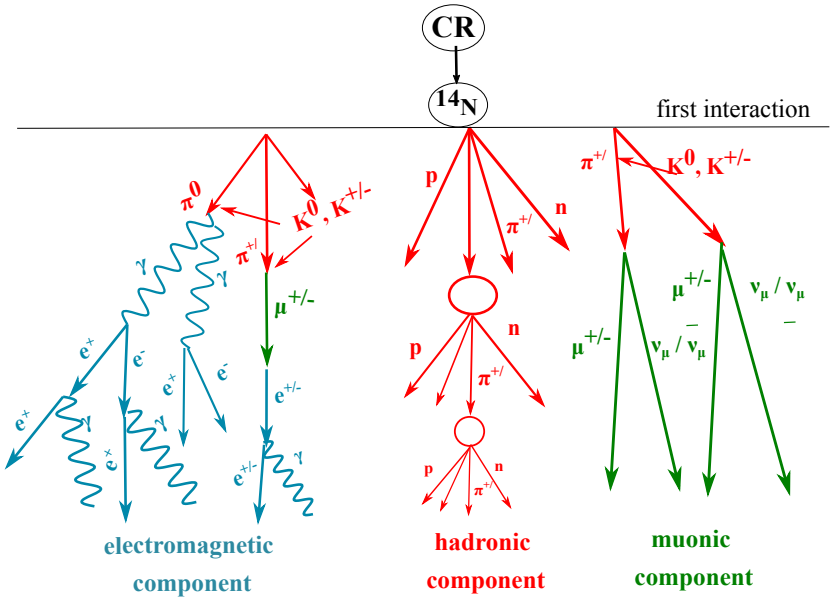

Figure 2.2: Sketched development of an extensive air shower. After the first interaction of the CR with the atmospheric nuclei, depending on the produced secondaries, the EAS is divided in three main components: electromagentic (blue), hadronic (red) and muonic (green)

The collision of a primary CR with an atmospheric nucleus marks the first interaction point after which the EAS starts to develop. Depending on the primary's energy and mass, the first interaction point can vary significantly. As seen in Fig. 2.2, the majority of secondary particles produced after the first interaction are pions and Kaons. Depending on their charge, the pions interact differently. Most of the charged pions can further interact with atmospheric nuclei, given their relatively large decay times, and produce additional pions. Furthermore, protons and neutrons produced in this interaction, as well as fragments of the primary particle, can interact further with the atmospheric nuclei, creating even more hadrons. This chain constitutes the so called *hadronic component* of the shower, sketched with red in Fig. 2.2. Any charged pions and kaons which decay before interacting with atmospheric nuclei produce muons. All secondaries in the hadronic component are eventually contributing to one of the other two components [31], as explained below.

As a result of the charged $\pi^{\pm}$ and $K^{\pm}$ decays, muons and muon neutrinos are produced. Given their long lifetimes, muons are very likely to travel all the way to the ground with no interaction. This creates the *muonic component*, sketched with green in Fig. 2.2. Having very low cross sections, the resulting neutrinos are not expected to interact or to be detected.

The neutral pions π^0 decay into a pair of photons, which create an electron-positron pair via pair-production. The resulting electrons / positrons are loosing energy via bremsstrahlung, producing thus additional photons. This process is creating the *electromagnetic component* of the particle's cascade. The charged pions can also contribute to the electromagnetic component by decaying into a charged muon which can in turn decay into an electron and two neutrinos. Kaons $K^0, K^{\pm}$, may also feed the electromagnetic component via their decay into neutral and charged pions. However the main contribution to the electromagnetic component is the one

resulting from the π^0 decays, given the longer decay time of the charged pions and muons.

2.2.1 EAS Development

While traversing the atmosphere, the air shower extends by producing more and more secondaries. One of the most important parameters in the study of the EAS development is represented by the *slant depth* or travelled depth, usually noted with X. It represents the amount of the atmosphere the particle has passed through and is measured in g/cm^2. The minimum slant depth is defined at the top of the atmosphere in the case of down-going air showers [3]. The slant depth is strongly dependent on the zenith angle of the primary CR, θ, and on the vertical travelled depth, X_v.

$$X = \frac{X_v}{\cos\theta} \tag{2.5}$$

The vertical depth represents the amount of vertical atmosphere a particle has passed through, and is defined as the depth corresponding to a given height at a given atmospheric density $\rho_{\text{atm}}(h)$.

$$X_v(h) = \int_{\infty}^{h} \rho_{\text{atm}}(h')\, dh' \tag{2.6}$$

The propagation of particles in the atmosphere can be analytically described using *cascade equations*. The equations strongly depend on the type of particles and their interactions within the atmosphere [31]. They describe the variation in the number of particles of type i and energy E_i while traversing an amount of atmosphere defined by the slant depth X. The equation contains two main terms:

$$\frac{dN_i(E_i, X)}{dX} = -\left(\frac{1}{\lambda_i} + \frac{1}{d_i}\right) N_i(E_i, X) + \sum_j \int \frac{F_{ji}(E_i, E_j)}{E_i} \frac{N_j(E_j)}{\lambda_j} dE_j \tag{2.7}$$

where $N_i(E_i, X)$ represents the flux of type i particles at a slant depth X with a corresponding energy E_i.

The first term of the equation is a *loss term*. It describes the disappearance of a particle i into other particle types, either via decay after a decay distance d_i or via interaction with other particles after an interaction length λ_i. The second term is referred to as a *creation term* and contains the probability of a particle of type i to be created from the decay or interaction of a particle of type j. The function $F_{ji}(E_i, E_j)$ describes the probability of a particle of type j and energy E_j to create a particle of type i and energy $E_i < E_j$.

Since in practice one would need a separate cascade equation for each particle type, solving Eq. 2.7 analytically is not possible. Numerical solutions exist and are implemented in MC cascade simulation frameworks like CONEX [54].

2.2.1.1 Heitler Toy Model

A very simplified way of understanding the development of a cascade has been given by Heitler[55] in the so called *Heitler Toy Model* and is sketched in Fig. 2.3. In this model there is only one

[3] This changes in the case of upward going air showers, which start interacting at the bottom of the atmosphere and the minimum slant depth has to be correspondingly re-defined, as is explained in chapter 4

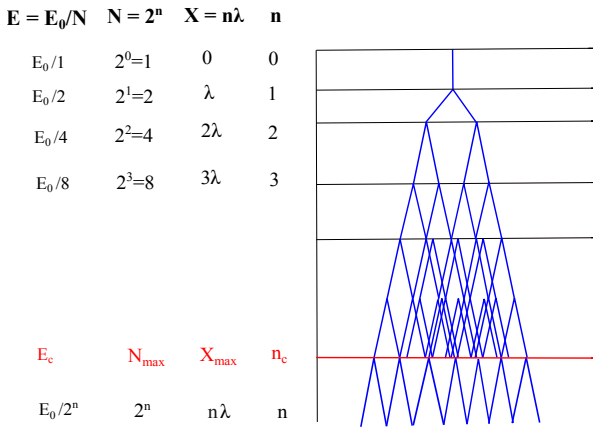

Figure 2.3: Sketch of Heitler's Toy Model. The energy of the secondary, the number of secondaries N and the corresponding depth X are shown. The step corresponding to the critical energy E_c is shown in red.

type of particle interacting, with a primary energy E_0 and a fixed interaction length λ. After each interaction length, two particles are created, equally sharing the energy of the primary particle: $E = E_0/2$. After each individual interaction the number of particles is doubled and the energy is shared between the resulting particles. The splitting process continues until the particle reaches a *critical energy*, E_c. Below this energy the particles can only lose energy, decay or get absorbed. Consequently, the maximum number of particles produced is defined as:

$$N_{max} = \frac{E_0}{E_c} \tag{2.8}$$

with a corresponding depth of

$$X_{max} = \lambda \frac{\ln(E_0/E_c)}{\ln 2} \tag{2.9}$$

Even if the Heitler Toy Model is a very simplified one, it introduces the concepts of *shower development*, the maximum number of particles in the shower, N_{max}, and the corresponding *shower maximum*, X_{max}. Moreover it describes qualitatively the shower development up to the shower maximum and is applicable to pure electromagnetic showers.

2.2.2 Characteristics of EAS

In reality, the study of the air shower development is more complicated. A schematic representation of an EAS travelling through the atmosphere and reaching the ground level is shown in Fig. 2.4. Once the primary particle enters the atmosphere and collides with the atmospheric nuclei the *first interaction* is defined, with the corresponding first interaction depth X_1. After this point the particle cascade is created and starts to evolve. The energy of the primary particle is shared among the resulting secondaries. The number of secondaries reaches a maximum once their energy is not enough to maintain the splitting process. After this point the production rate of particles starts to decrease again. The atmospheric depth corresponding to the highest particle number is called *the shower maximum*, X_{max}. The evolution of the EAS while traversing the atmosphere, in terms of number of secondary particles per travelled depth is called *longitudinal development profile* and is sketched in Fig. 2.4 in red. As the number of secondaries produced

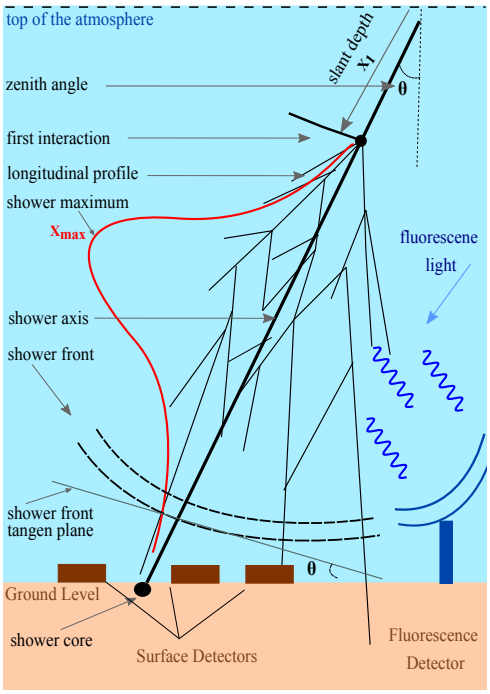

Figure 2.4: Development of an EAS, from the top of the atmosphere to the ground level. Illustrated are the main shower characteristics: the shower axis, the first interaction point, corresponding to the first interaction depth X_1, the shower maximum, X_{max} together with the shower longitudinal profile sketched in red. As the shower is approaching the ground level, the shower front and shower core are determined. The particles arriving at ground are detected using the surface detectors, while the longitudinal profile can be measured using the fluoresce detection technique.

is strongly related to their energy, and since, as mentioned above, the hadronic component is eventually feeding into the electromagnetic or muonic component, the shower maximum is also the point where the shower deposits the maximum energy in the atmosphere, $(dE/dX)_{max}$. The deposited energy in the atmosphere is often referred to as *calorimetric energy* and can be very accurately measured with fluorescence telescopes (see 3.2). This is of a crucial importance for the reconstruction of the primary CR energy, as it is discussed within the next sections.

As seen in Fig. 2.4, the *shower axis* is a very important geometric quantity in describing the EAS development. It is determined by the direction of the primary CR, being the vector along which the shower is developing. It is defined by the zenith angle θ, the azimuth angle Φ and the *shower core* position. The shower core represents the point where the shower axis intersects the ground.

As the shower is approaching the ground level, the *shower front* can be defined. It can be viewed as the leading edge of the shower, having the shape of a disk comprising of high energy secondary particles. The particles are not equally distributed in the shower front, but heavily present next to the shower axis, determining the curved shape of the shower front. The tangential plane on the shower front is referred to as the *shower front tangent plane.*

When the shower front intersects the ground, *the shower footprint* can be detected. It is characterized by the shape, density and timing of particles arriving at ground. By detecting the shower footprint, the energy of the primary CR can be inferred. This is the quantity used by the surface arrays to analyze and reconstruct the CR induced air showers.

As mentioned above, the longitudinal development of the shower is of great importance

in the study of EAS. It shows the evolution of the number of particles within the shower, N, as a function of the traversed atmospheric depth X, and is usually noted as $N(X)$.

The longitudinal development profile is illustrated in Fig. 2.4 with red, and can be parameterized using the Gaisser-Hillas function [33]

$$N(X) = N_{max}\left(\frac{X - X_0}{X_{max} - X_0}\right)^{\frac{X_{max}-X_0}{\lambda}} \exp\left(\frac{X_{max} - X_0}{\lambda}\right) \tag{2.10}$$

where N_{max} represents the maximum number of particles produced at the maximum shower depth X_{max}, and λ and X_0 are two fit parameters related to the primary composition and energy. An example of this fit is shown in Fig. 2.5.

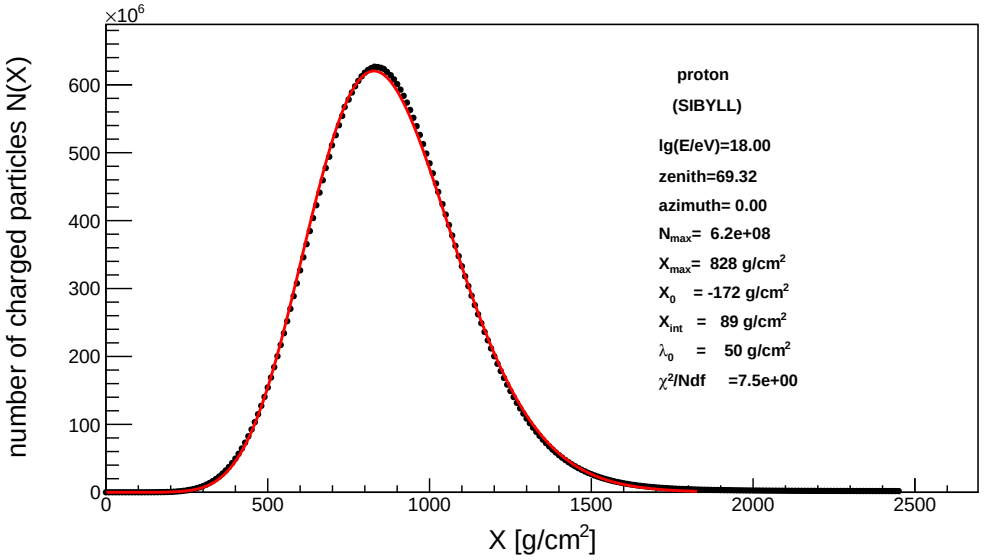

Figure 2.5: Exemplary plot of a Gaisser-Hillas fit (red line) on the MC data (black bullets) resulted from the simulation of a proton induced EAS using CONEX[54]. A proton with a primary energy of 10^{18} eV and zenith angle of 69.32° has been simulated using Sibyll [56] for the high-energy interaction model. The shower parameters as well as the Gaisser-Hillas fit parameters are shown.

A high energy proton induced air shower has been simulated using CONEX [54]. The shower parameters are shown in the graph. The red line represents a fit to the Gaisser Hillas function defined in Eq. 2.10. It can be seen it accurately describes the MC data, plotted with black bullets in the figure. The corresponding Gaisser-Hillas parameters are also shown.

Depending on the detection method, as well as on the studied quantity of interest, several of the above mentioned parameters of the EAS are used in order to reconstruct and obtain information about the primary CRs. There are considerably different detection techniques concerning EAS, but within this thesis only the Pierre Auger Observatory with its various detectors will be discussed in detail.

3

The Pierre Auger Observatory

The Pierre Auger Observatory is the biggest cosmic rays detector in the world. Designed for the study of ultra-high energy CRs (UHECR), focusing on energies $E > 10^{16}$ eV, the detection technique is aiming towards the observation of extensive air showers. The observatory is situated in Malargue, Argentina and is covering a surface area of ≈ 3000 km^2 [57]. It has been operated successfully since its completion in 2008 and has contributed to many scientific discoveries concerning CRs physics ever since.

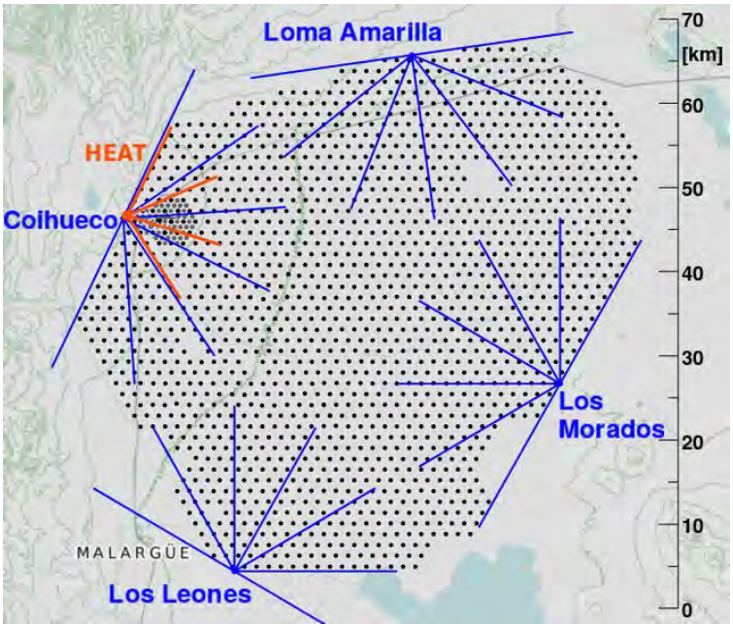

Figure 3.1: Sketch of the Pierre Auger Observatory layout. The black dots represent the water Cherenkov stations. The blue lines represent the 24 fluorescence telescopes, while the HEAT telescope is shown with orange lines.

The observatory consists of several detection techniques, meant to study different components of the EAS and therefore infer various information regarding the primary particle. The *Surface Detector* (SD) together with the *Fluorescence Detector* (FD) represent the pioneer detectors within the observatory. Two additional detector types have been deployed during the time: the *Radio Detector* (RD) and the *Underground Muon Detector* (UMD). This thesis will be focused mainly on the FD, with a short review over the SD. Additional information regarding the other detectors enumerated above can be found somewhere else: [58], [59], [60], [61], [57], [62], [63]. These different detectors are operated simultaneously, taking advantage of, and combining, the individual detection methods in an attempt to maximize the accuracy and efficiency regarding of the information inferred about the primary CRs. This makes the Pierre Auger Observatory a hybrid observatory.

The largest exposure of the observatory comes from the surface detector, which consists of 1660 *water Cherenkov detectors* (WCD). The SD is detecting the charged particles reaching the ground. Additionally, 27 telescopes, forming the FD, are monitoring the atmosphere above the ground detectors. The telescopes are located in 4 different building locations around the ground array, as it can be seen in Fig. 3.1. Each of the sites comprises of 6 fluorescence telescopes, with additional three telescopes designed as a low energy extension, the *high elevation fluorescence telescopes* (HEAT), placed in the north-western part of the array. Using these two detector types, a complete study regarding the EAS development within the atmosphere, as well as the shower footprint at ground, can be conducted via the hybrid detection.

An upgrade of the observatory, *The AugerPrime Upgrade*, has been planned and is currently being deployed. It consists of an extension of the current detectors, as well as an improvement of the existing ones. More details about this upgrade can be found in [64]. The Muon Detector is part of the *Auger Muon and Infilled Ground Array* (AMIGA) enhancement [57]. It is designed to measure the muon content of EAS and is located at a shallower depth compared to the SD. The Radio Detector part of the upgrade is using the Auger Engineering Radio Array (AERA) in order to improve the statistics at very high energies and inclined zenith angles.

3.1 The Surface Detector

As mentioned above, the SD comprises of $\approx$ 1660 water Cherenkov stations. The WCDs are located at a distance of 1.5 km away from each other, covering a total area of $\approx$ 3000km^2. Additionally, as part of the extension towards lower energies, a more densely instrumented area, called *the in-fill area* has been deployed. This area covers $\approx$ 23.5 km^2 and contains WCDs with an inter-spacing of 750 m.

An SD station is composed of a cylindrical tank with a diameter of 3.6 m and a height of $\approx$ 1.5 m [57]. The tanks are filled with 12 000 liters of ultra pure water, encapsulated in a highly reflective liner. Each tank is monitored by 3 photomultiplier tubes (PMTs), symmetrically distributed within the liner. Due to the properties of the tank materials, the water can be considered very well optically isolated, and therefore very accurate measurements can be obtained.

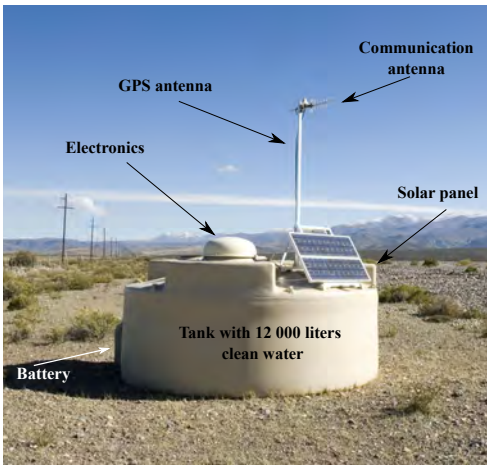

Figure 3.2: Sketch of the Pierre Auger Observatory Surface Detector. Original picture from [65].

The detection principle behind the WCDs is based on the Cherenkov radiation. This is emitted when a charged particle is travelling through any given medium with a velocity greater than the speed of light within the specific medium. As a result, Cherenkov photons are created and a flash of light can be detected. Recording the intensity and timing of these photons, each station is able to provide information regarding the flux of high energy charged particles passing through it at any given point in time.

The electronics inside the tanks ensures a self-sufficient operation of each of the stations. As it can be seen in Fig. 3.2, each station has its own electronics, solar power system, GPS receiver and communication antenna. However, the measurement of UHECRs requires information from more than one single station. In order to have an accurate measurement of the shower energy and direction, several stations need to have signals within a given time window, ensuring thus the EAS has hit the corresponding sequence of ground detectors [57]. Additionally, each of the stations is prone to background, produced by a large number of high energy particles randomly passing through the air. Therefore, with the aim of ensuring that the registered signal comes from a CR induced air shower, each tank has its own internal triggering system, together with an additional triggering system which relies on information provided from the rest of the array.

The SD has 5 main triggers, noted with T1 - T5. The first two triggering levels are concerning each station individually. The first trigger, T1, is concerning the simultaneous recording of a signal by 2 or 3 PMTs inside the tank. It has two modes: the simple threshold trigger (TH), which is operated when all 3 PMTs simultaneously register a signal above a certain value, and is very useful for the detection of inclined air showers. The second mode of the T1 trigger is a time-over-threshold (ToT) which requires recording a signal above a certain value in a given time window from at least 2 of the PMTs within the tank. It is very useful for the detection of vertical air showers, as it aims towards the selection of small signals with a significant spread in time. The second trigger, T2, is applying several selection criteria to events that have already passed the T1 trigger. Once an event is passing the T2 trigger, it is further sent to the Central Data Acquisition System (CDAS) and a global trigger T3 is determined.

The triggers T3-T5 are created in the CDAS and are strongly related to the signal from multiple detectors within the Observatory. The T3 trigger is looking for coincidence signals from SD and/or FD, being referred to as a central trigger. The *main trigger* condition of T3 regards the SD stations in the vicinity of the station of interest. A concentric hexagonal shape is defined, having the station of interest in the center. This can be seen in Fig. 3.3. The groups of clustered stations, both in space and time, are further identified. One of the requirement is the existence of a coincident T2-ToT trigger of at least 3 detectors that are also placed nearby. At least one of the 3 detectors must have a neighbouring detector that passed the T2-ToT criteria in the first hexagon, while the other one can not be located further than the second hexagon. More information about the SD triggering system can be found in [66]. As mentioned above, the T3 trigger is also checking for signal from the FD. Once a coincident signal from a SD station and the FD is detected, the signal is sent to the FD T3 trigger, which is evaluating whether the signal is corresponding to a hybrid measurement.

Once the event is passing the T3 - SD related trigger, it is further sent to the fourth

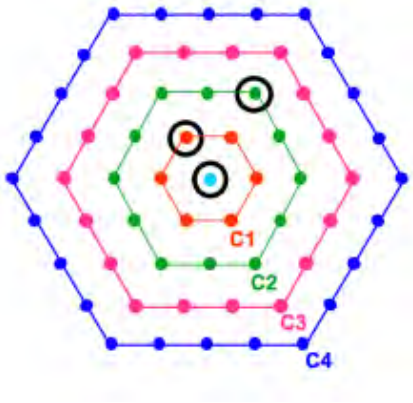

Figure 3.3: Example of the T3 trigger configuration. The station in the center, represented with the blue dot, represents the triggered station. The first, second, third and forth neighbours are represented by the C1, C2, C3 and C4 hexagons. Figure from [66]

T4 trigger. This is a physics related trigger, requiring for a geometry and timing corresponding to a real EAS. By doing so, events passing the T4 trigger are related to true feasible cosmic ray showers. The last trigger, T5, is not mandatory to be passed in order for an event to be classified as an EAS. It is mainly related to events landing on the edge of the array and it is assuring that all the tanks around the triggered station are fully functional.

The functionality and performance of the surface detectors is independent on the weather conditions, having thus a duty cycle of 100%. This makes it the most powerful source of statistics of the Pierre Auger Observatory. However, since the SD is detecting only particles at ground, the measurement accuracy is reduced. As the shower development profile can not be measured by the SD, it is not directly sensitive to the primary composition. Furthermore this is also affecting the primary energy studies, since the secondary particles at ground are only empirically related to the energy of the primary particle. However, an energy calibration of the SD is possible by using the FD described in the next section.

3.2 The Fluorescence Detector

The Fluorescence Detector (FD) of the Pierre Auger Observatory contains 27 fluorescence telescopes located at four different sites around the array. These different telescope locations are often referred to as *Eyes*. Each of the eyes contains 6 fluorescence UV telescopes. Each telescope has a field of view (FoV) of 30° elevation $\times$ 30° azimuth. This gives a total viewing angle of 180° in azimuth for each of the eyes. The FoV of the telescopes, together with their location within the observatory is shown in Fig. 3.1. The building location is marked with a blue dot and the FoV is represented with the blue lines around the eyes. A fifth Eye, the *high elevation fluorescence telescope* - HEAT, is located in the western part of the array, in the very proximity of one of the four eyes. It is designed as an additional extension for low energies, in the region between the second knee up to the ankle [57]. It contains three telescopes able to monitor the atmosphere at an elevation between 30° - 60° when tilted upwards. The data obtained from the telescopes within the five buildings, Los Leones (LL), Los Morados (LM), Loma Amarilla (LA) Coihueco (CO) and HEAT is of crucial importance for the purpose of this thesis.

The FD is not directly detecting the cosmic rays, but only their effect on the atmosphere while they are traversing it. It can be regarded as a calorimetric detector, where the energy is deposited in the atmosphere. In section 2.2.2 the characteristics and development of an EAS have been discussed. The main components of an EAS have also been described in the previous chapter, where it has been emphasized that most of the primary energy is eventually transferred to the electromagnetic component of the shower. The propagation of the electromagnetic component of the shower within the atmosphere is producing fluorescence light, as a result of the interaction of charged particles with the nitrogen nuclei of the atmosphere. When a charged particle is passing through the atmosphere, it is exciting nitrogen molecules. As a result of this excitation, fluorescence light is being emitted isotropically. The fluorescence telescopes are designed to register the intensity, timing and spatial-temporal evolution of this emission. Since this fluorescence light is in the UV band, it can not be distinguished by the instruments from the other atmospheric background light. As a result, the FD can only take meaningful data on very dark, moonless and cloudless nights, reducing its duty cycle to $\approx 14\%$ [57]. This is limiting the FD statistical power compared to the SD which has a 100% duty cycle.

A schematic view of a fluorescence telescope is shown in Fig. 3.4, where its main components are highlighted. The *shutter* of the telescope is open during the data taking period, and is used as a safety measure, which is automatically closing when strong wind or rain is detected. Additionally, a safety curtain is installed with the purpose of preventing a malfunction of the shutter. The fluorescence light enters through the 1.1 m *aperture* and is further filtered using a UV light filter. The UV filter helps with reducing the background light and improves the signal detection accuracy. The fluorescence light is further reflected by a *spherical mirror* with a curvature radius of ≈ 3.4 m and focused onto the camera [67].

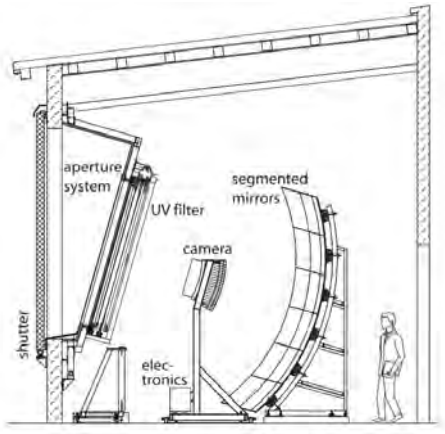

Figure 3.4: Sketch of the fluorescence telescope of the Pierre Auger Observatory. Picture from [57]

Each camera has a total number of 440 PMTs, which are arranged in a hexagonal grid and distributed on 20 rows, containing 22 PMTs each. Each PMT is equipped with an electronic unit which gathers information about the electric signal. This makes the counting of individual photons possible with a 100 ns resolution. The detection of the number of photons as a function of time makes the ADC trace accessible [68].

With the processing of the PMT data, a FD triggering system is implemented and activated. Similarly to the surface detector, the first two triggers are also internally processed

by each individual detector. The first level trigger (FLT) is a threshold trigger designed to exclude short noise signals and keep the triggering rate of each telescope at a value of $\approx 100\,\mathrm{Hz}$. Data that passed the FLT is further sent to the Second Level Trigger (SLT). The SLT is selecting the events based on their geometry within the camera. It requires for at least 5 pixels in a row to be triggered within the camera. By doing so, the SLT ensures the rejection of events that could not be initiated by cosmic rays. Once an event is passing the SLT trigger it is further sent to the EyePC. Two additional triggers are implemented in the EyePC. The third level trigger (TLT) is designed to clean the data of potential background or noise events like lightning, which might have passed the previous two triggers. It does so by verifying the camera's response in terms of geometry and time-ordering of the triggered pixels and is assuring that the two characteristics correspond to a shower event signature. As a result of this process, the *pixel trace* within the camera is obtained. This is done by looking at the largest group of triggered pixels in the camera and defining it as the center of the shower in the camera. Further on the time information of the pixels is being evaluated and a trace of the event within the camera is created. An example of such a trace is shown in Fig. 3.8(b).

The last trigger concerns the hybrid detection. It is strongly related to the T3 SD trigger mentioned in section 3.1. Here the FD is looking for measurements in correlation with the SD events. The EyePC is performing an elementary reconstruction of the event in order to evaluate the position of the core, as well as the timing of the event in the surface detector. These kind of events that are detected both by the SD and the FD are called *hybrid events* and are of a great importance regarding the energy calibration of the SD. Events which are simultaneously detected in at least two FD sites are called *stereo events* and provide a more accurate geometry and energy reconstruction than in the case of an event observed by only one eye, referred to as *monocular event*.

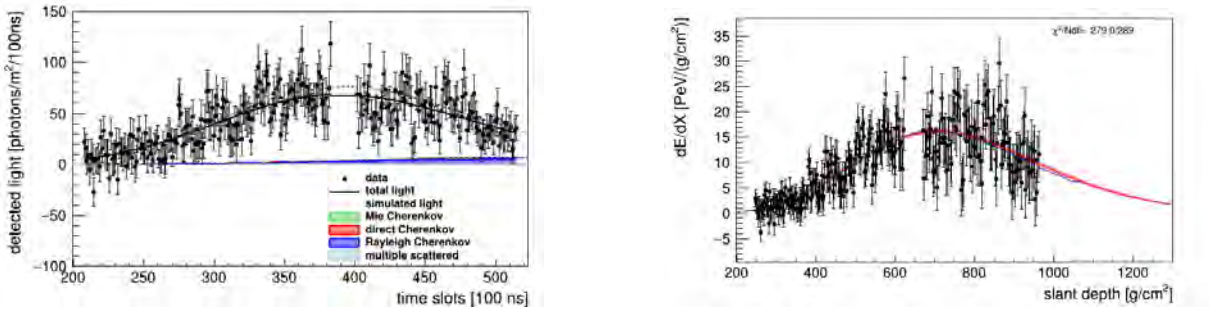

(a) Detected light profile of a typical cosmic ray induced air shower

(b) Energy deposit profile of the same cosmic ray induced air showers .

Figure 3.5: Example of a typical cosmic ray event as measured by the FD. The plots have been obtained by using the Auger collaboration framework, Offline [69]

The trace of triggered pixels inside the camera, together with the recorded light profile and the resulting shower energy deposit in the atmosphere, represent the key points in obtaining the signature of an EAS. Crucial information about the primary cosmic rays inducing the corresponding air showers, like primary energy and mass composition, can be further obtained with high accuracy.

In Fig. 3.5(a) the light profile of a down-going shower, as recorded by the FD is shown,

together with the corresponding energy deposit profile (Fig. 3.5(b)). Additional light sources are present in the recorded profile and need to be further subtracted for a proper reconstruction. In order to differentiate them from the true signal of a cosmic ray induced air shower, additional atmospheric conditions have to be properly monitored.

3.3 Atmospheric Monitoring

As it was mentioned above, the atmosphere acts as a calorimeter for the FD. Therefore very accurate measurements of the atmospheric conditions above the Observatory are required in order to obtain precise information about cosmic rays induced air shower with the FD. The main factors that need to be monitored are the density and temperature atmospheric profiles, as well as the cloud coverage and the aerosol content in the atmosphere. Several devices are installed in this regard within the observatory. A schematic overview of the monitoring devices existent in the Pierre Auger Observatory is shown in Fig. 3.6.

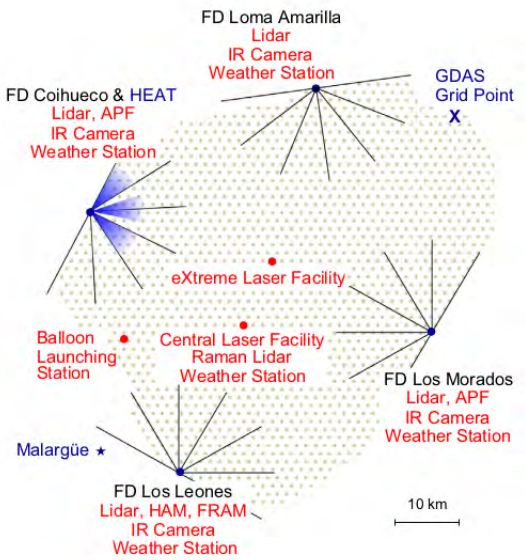

Figure 3.6: Sketch of the atmospheric monitoring system of the Pierre Auger Observatory. At each FD site a Lidar, an IR camera and a weather station are mounted, with the main goal of recording the clouds coverage. Additionally, in the center of the array two laser facilities (CLF and XLF) can be found. Their main purpose is a precise measurement of the aerosol content within the atmosphere. Figure taken from [57]

Information regarding the atmospheric profiles is taken from the Global Data Assimilation System (GDAS). The existence of clouds is influencing tremendously the taken data, by creating additional scatterings of the light within the atmosphere, as well as modifying the shower timing information or by obscuring the UV emission itself. As a result, the cloud coverage studies are crucial for a good functioning of the fluorescence detector. Due to the important role it is playing, several systems regarding the cloud coverage data are used within the Observatory. The Geostationary Operational Environmental Satellite (GOES) is one of the systems used, providing valuable cloud coverage data, which is constantly updated, in a 15 minutes interval. Additionally, GOES is also providing information regarding the atmospheric density profile, moisture and temperature. Since the data provided by GOES only refers to the cloud

coverage probability [70], additional on-site devices are used for a more accurate measurement. The Lidars and IR cameras situated at each Eye provide precise measurements regarding the cloud conditions in the FoV of the telescope site. The IR camera scans and monitors the FoV of each Eye, every 15 minutes, while the Lidar provides information regarding the clouds heights at the site at regular time intervals [57]. Valuable information regarding the existence of the clouds in each individual pixel, together with the distance to the specific cloud, can be obtained by combining the IR and Lidar readings.

Furthermore, two laser facilities are used to provide additional information about the cloud height: The Central Laser Facility (CLF) and the eXtreme Laser Facility (XLF). However, the main role of the two lasers is the aerosol measurement of the atmosphere above the Observatory.

3.3.1 Laser Facilities

The presence of the aerosols in the atmosphere causes an additional scattering of the fluorescence UV photons. Since the FD relies on an exact evaluation of the light profile resulting from EAS development in the atmosphere, any additional factors which might influence the fluorescence photons and therefore contribute to the final measured results, need to be precisely known in order to infer the correct information about the shower parameters. The Mie scattering theory describes the scattering of photons due to the aerosol content in the atmosphere. However, since the real conditions can vary significantly due to different amounts and shapes of the aerosols, measurements on site are needed [57]. In order to calculate the aerosol transmission factors, the vertical aerosol optical depth (VAOD) needs to be known. A regular measurement of the VAOD is therefore performed. This is achieved with the help of the two laser facilities.

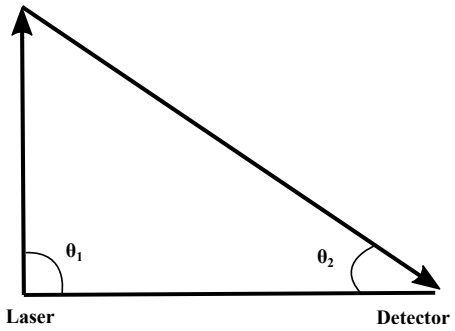

Figure 3.7: Sketch of the main setup behind the VAOD measurement. The laser is shooting upwards at a known angle with the horizontal, θ_1. The light arrives at the telescope and is detected at the zenith angle θ_2. The two zenith angles together with the observed light intensity are used for calculating the VAOD value.

The CLF and XLF are placed near the center of the array and can be seen in Fig. 3.6. The lasers represent controlled light sources. Therefore, a laser shot can be recorded by any of the FD Eyes, via the detection of the laser light intensity at each telescope at a given angle. A schematic view is shown in Fig. 3.7. The VAOD value can be calculated by comparing the observed light N_{obs} from the laser shot, resulting from the aerosols scattering, with the corresponding light intensity obtained when no aerosols are expected in the atmosphere. In this case, only the molecular scattering, N_{Mol}, is expected. The molecular scattering intensity

can be either taken from measurements under clear atmospheric conditions, with no measurable aerosols, or from dedicated simulations. The VAOD value is also dependent on two main angles, mainly the angle between the laser shooting direction and the horizontal, θ_1, and the detection angle of the incoming light, θ_2, which are also shown in Fig. 3.7.

It is important to emphasize that the laser shots are shooting in an up-going direction, from the ground level towards the atmosphere. This is in general very easy to distinguish from any down-going EAS, by using a zenith angle discrimination. However, for the current study in this thesis, the laser shots represent the main background and have to be properly identified and extracted in order to obtain a pure data signal. This has been achieved and is explained in more detail in section 5.2.2.

Once the atmosphere is properly monitored and the atmospheric background is well known, the corresponding contributions can be extracted and the cosmic ray air shower profile can be accurately reconstructed.

3.4 FD Reconstruction

In order to correctly describe the shower parameters and get the necessary information regarding the primary particle, the recorded event within the FD has to be properly reconstructed. For a full and detailed description of the event's timing and geometry, several variables have to be defined:

- $\boldsymbol{\theta}$, $\boldsymbol{\phi}$ **:** the zenith and azimuth angle of the shower, which are defining the *shower axis* $\hat{\mathbf{S}}$
- ***(x, y)*** coordinates: describe the position of the event's axis at ground, also referred to as the *shower core*
- $\mathbf{T_0}$: the time the shower is passing through the closest point from the showers axis to the Eye.

Consequently, a total number of five parameters is needed. In order to properly calculate the parameters listed above, the reconstruction of an event seen by FD is divided into two different main steps:

1. Determining the *Shower Detector Plane (SDP)*. The SDP is the plane which contains the shower axis and the center of the eye. In this step only the geometry of the triggered FD pixels is used.
2. Determining the *shower axis*. This is achieved by using the timing and angular data obtained from the triggered pixels.

By dividing the reconstruction in the two steps, the geometric issue is simplified. Focusing first on the shower detector plane, the 5 parameters are reduced to only 3. Once the SDP is found, the shower axis is further constrained. Depending on the type of event, three different methods can be used. The simplest method is called *monocular reconstruction* and regards events which have only triggered one Eye. A better quality is obtained when using the *hybrid reconstruction*, in the case of events that are triggering both the FD and the SD. The highest

reconstruction quality is obtained for the case of a stereo event and is correspondingly called *stereo reconstruction*. The latter reconstruction method uses data from two or more different Eyes which have measured the same event. Since in this work only the FD is used, the hybrid reconstruction will not be explained in detail. Information regarding this method can be found elsewhere [57].

3.4.1 Reconstruction of the Shower Detector Plane

As mentioned above, the SDP is defined as the plane containing the shower axis and the center of the Eye, as it can be seen from the illustrative sketch in Fig. 3.8(a).

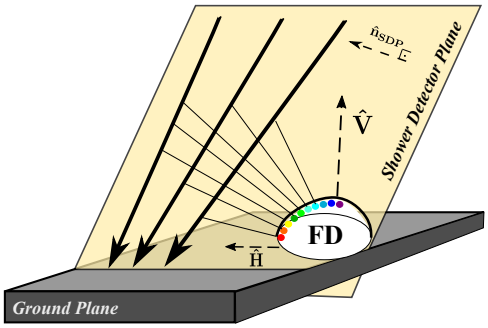

(a) Schematic view of the shower detector plane. The SDP defines the plane where the event is occurring, using the geometry of the triggered pixels. It can be seen that even if the SDP is fixed, there may be various event geometries, as indicated by the numerous arrows pointing to the ground plane

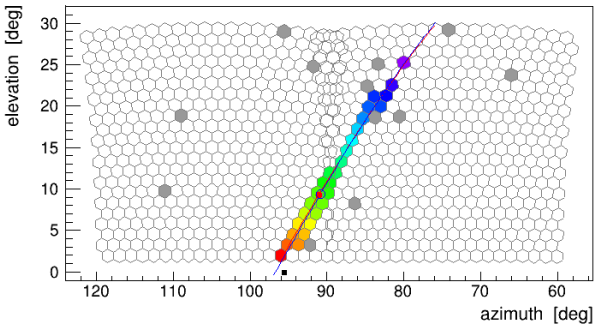

(b) Light track of a simulated event in the cameras of two adjacent telescopes of one Eye:Los Morados. The timing is indicated by the different colors, where purple represents the earliest point and red indicates the latest arrival time. The plot has been obtained by using the Offline Framework [69].

Figure 3.8: SDP Reconstruction

The geometry of the triggered pixels within the camera enables the reconstruction of the shower detector plane. However, not all of the triggered pixels are used. The criteria defining the SDP pixels are:

1. The pixels should not be isolated spatially and temporarily. This is done by ensuring each valid pixel is not further than 4 pixels away from another SDP pixel and the geometric center of reconstructed ADC traces must be within 6 μs of another SDP pixel's center

2. The time ordering of the pixels has to be correlated with a physical event, similar to a cosmic ray induced air shower

The emitted fluorescence light of the SDP pixels creates a hit pattern in the camera, often referred to as a light track or pixels trace, as it can be seen in Fig. 3.8(b). The SDP pixels are further used for fitting the SDP plane, by choosing the plane that fits the pointing directions of the pixels $\overrightarrow{r_i}$. The normal vector of the plane, $\overrightarrow{n}_{SDP}$, is chosen so that its cross product with the vertical vector pointing from the Eye $\overrightarrow{V}$ results in a horizontal vector $\overrightarrow{H}$ which points from the Eye towards the shower core. The core is defined as the intersection of the shower axis with the ground. As a result of this choice, the SDP is independent of the shower direction,

meaning that a shower travelling upwards (more details about upward going showers are given in chapter 4) will have the same SDP as a shower travelling downwards.

Using a χ^2 minimization method, the SDP is found, as the plane which describes best the triggered pixels:

$$\chi^2_{SDP} = \sum_i |\overrightarrow{n}_{SDP} \cdot \overrightarrow{r_i}|\ w_i \tag{3.1}$$

where i iterates over the SDP triggered pixels and w_i is related to the sum of the signal within pixel i. The χ^2 fit is found to be very accurate, resulting in an uncertainty of 0.08° in the SDP position, respectively a 0.5° angular uncertainty [71].

3.4.2 Monocular Shower Axis Reconstruction

Once the shower detector plane is fixed, the geometry is reduced to a 2D problem. As mentioned above, by doing so the number of parameters is reduced to three, out of the five parameters enumerated in the beginning of this section. As illustrated in Fig. 3.9, the three parameters needed for describing the event's geometry are:

1. $\mathbf{T_0}$: the time at which the event is closest to the telescope; it is used a reference time
2. $\mathbf{R_P}$: the shortest distance between the eye and the shower axis; it is always perpendicular to the shower axis
3. $\boldsymbol{\chi}_0$: the angle between the horizontal vector pointing from the Eye towards the shower core and the shower axis

Finding the three parameters of interest is defining the *axis reconstruction*. The *monocular reconstruction* is applied to events observed by at least one FD, which are passing the TLT trigger. The monocular reconstruction is performed by using data provided by cameras within one single Eye.

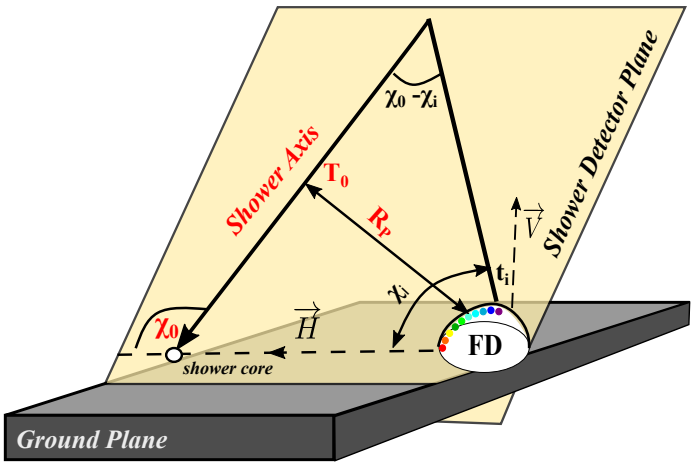

Figure 3.9: Geometry of an event seen with only one Eye and used for the monocular reconstruction

Using the geometry illustrated in Fig. 3.9, the expected arrival time of the signal in

the i^{th} pixel of the telescope can be calculated:

$$t_i^{exp} = T_0 + \frac{R_p}{c} \tan\left(\frac{\chi_0 - \chi_i}{2}\right) \tag{3.2}$$

where χ_i is the viewing angle of the i^{th} pixel, between the horizontal and the shower axis.

First a best guess of the three parameters T_0, R_p, χ_0 is used and inserted into Eq. 3.2, together with the corresponding χ_i, in order to obtain the value of t_i^{exp}. Further on the expected time of arrival t_i^{exp} is compared with the measured time of arrival t_i and a χ^2 minimization is performed

$$\chi^2_{FD} = \sum_i \frac{\left(t_i - t_i^{exp}\right)^2}{(t_i^{err})^2} \tag{3.3}$$

where the sum is performed over all triggering pixels with the centroid time uncertainty t_i^{err}. The value of the three parameters T_0, R_P, χ_0, which minimizes the χ^2_{FD} and defines the shower axis is obtained.

Even if the χ^2 minimization method is very accurate, given the small amount of available input data, taken from only one Eye, the monocular reconstruction method is prone to high uncertainties. However, depending on the physics involved, if the primary energy is high enough and the landing point of the shower allows it, the event can be seen by more than one eye as well as by the SD, making the stereo and hybrid reconstructions possible. By observing the event with more than one detector the reconstruction accuracy is significantly increased.

3.4.3 Stereo Reconstruction

The stereo reconstruction uses information from two Eyes which are simultaneously observing the same event. In this way, both the SDP and the shower axis are obtained using the geometry provided by the two eyes, resulting in a significant improvement of the geometric reconstruction. By using the pixels geometry and timing from each of the triggered eyes, the χ^2 fit for the stereo reconstruction becomes:

$$\chi^2_{Stereo} = \chi^2_t + 4\chi^2_{geo} \tag{3.4}$$

where χ^2_t is related to the pixels timing profile and χ^2_{geo} is minimizing the pixels geometry. It can be seen from Eq. 3.4 that the geometry information is more reliable compared to the timing one. The timing minimization χ^2_t follows the same approach as in the monocular case, with the additional sum over all the triggered Eyes:

$$\chi^2_t = \sum_{Eyes} \sum_i \left(\frac{(t_i^{Eye} - t_i^{exp,Eye})^2}{(t_i^{err,Eye})^2} \right) \tag{3.5}$$

where t_i^{Eye}, $t_i^{exp,Eye}$ and $t_i^{err,Eye}$ represent the same terms as in Eq. 3.3, corresponding to each individual eye triggered by the event.

The second term of Eq. 3.4 is very similar to χ^2_{SDP}, with the exception that the pixel's signal w_i is no longer used. This is mainly due to the fact that not all triggered pixels will be equally reliable. The uncertainty in the pointing direction of the pixels is used instead: $\overrightarrow{r_i}err$.

The corresponding χ^2_{geo} takes the form:

$$\chi^2_{geo} = \sum_{Eyes} \sum_{i} \left(\frac{\pi/2 - \arccos(\overrightarrow{r_i}^{Eye} \cdot \overrightarrow{n}^{Eye}_{SDP})^2}{(\overrightarrow{r_i}^{Eye} err)^2} \right) \tag{3.6}$$

with $\overrightarrow{r_i}^{Eye}$ and $\overrightarrow{n}^{Eye}_{SDP}$ the equivalent terms from Eq. 3.1, corresponding to each triggered Eye.

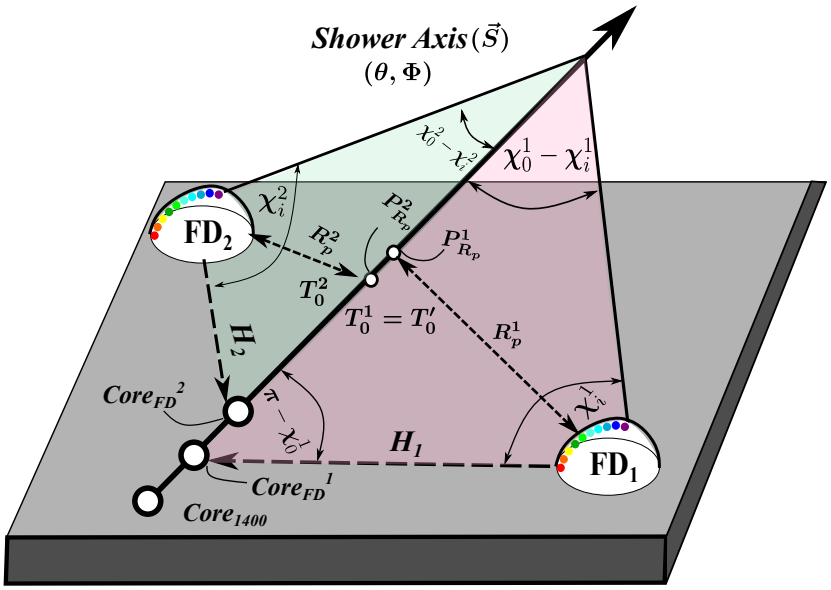

Figure 3.10: Geometry of an event seen by two Eyes and used for the stereo reconstruction. FD_1 is the triggered eye with the lowest index, and therefore used as *Eye'*. In the figure there are also represented the positions of the shower core in the UTM coordinate system $Core_{1400}(N_{1400}, E_{1400})$, as well as the shower core determined by each of the eyes together with the parameters of interest. The SDP for each of the Eyes is sketched with the colored area: red for FD_1 and green for FD_2.

The stereo reconstruction differs from the monocular one mainly due to the minimization procedure. In this case the minimization is done directly on the shower parameters $\theta, \phi, x_{core}, y_{core}$ and T_0. A schematic overview of the stereo reconstruction procedure is illustrated in Fig. 3.10. The location of the shower core (x_{core}, y_{core}) is replaced with the UTM coordinates in terms of Northing and Easting (N_{1400}, E_{1400}), which define the core location at an altitude of 1400 m. By doing so, a universal coordinate system is used and therefore the different Eye locations can be easily related to each other. The 1400 m altitude corresponds to the average altitude of the Observatory above sea level. Furthermore, due to the fact that more Eyes are observing the same event, each of the eyes will provide different values of T_0. Therefore, the time corresponding to the closest point from the shower axis of the lowest index triggering Eye (LL = 1, LM = 2, LA = 3, CO = 4, HEAT = 5) will replace T_0 and will be further referred to as T_0'. Since the same event is observed simultaneously by more Eyes, only one value for each of the shower parameters is expected.

Following the geometry illustrated in Fig. 3.10, the expected triggering time of each pixel can be calculated as:

$$t_i^{exp,Eye} = T_0^{Eye} + \frac{R_p^{Eye}}{c} \tan\left(\frac{\chi_0^{Eye} - \chi_i^{Eye}}{2} \right) \tag{3.7}$$

Equation 3.7 is very similar to Eq. 3.2, with the exception that it is performed individually for each of the triggering Eyes. Unlike the monocular reconstruction, the values of R_P^{Eye}, χ_0^{Eye} and T_0^{Eye} are calculated using the shower parameters $\theta, \phi, N_{1400}, E_{1400}$ and T_0. The angle between the shower axis $\overrightarrow{S}$ and the horizontal $\overrightarrow{H}$, χ_0, is then calculated as:

$$\chi_0^{Eye} = \arccos\left(\frac{\overrightarrow{H}^{Eye} \cdot \overrightarrow{S}}{|\overrightarrow{H}^{Eye}|}\right) \tag{3.8}$$

where $\overrightarrow{H}^{Eye}$ is the horizontal vector pointing from the Eye to the shower core and is defined as:

$$\overrightarrow{H}^{Eye} = FD_{Core}^{Eye} - P_{FD}^{Eye} \tag{3.9}$$

where P_{FD}^{Eye} represents the location of the Eye in UTM coordinates: $(N_{FD}^{Eye}, E_{FD}^{Eye}, Z_{FD}^{Eye})$. FD_{Core}^{Eye} is the position of the shower core at the same altitude as the Eye and is defined by the three coordinates $(X_{core}, Y_{core}, Z_{core})$:

$$\begin{aligned} X_{core}^{Eye} &= E_{1400} - \left((1400 - Z_{FD}^{Eye}) \cdot \tan\phi \sin\theta\right) \ , \\ Y_{core}^{Eye} &= N_{1400} - \left((1400 - Z_{FD}^{Eye}) \cdot \tan\phi \cos\theta\right) \\ Z_{core} &= Z_{FD}^{Eye} \end{aligned} \tag{3.10}$$

Further on R_P^{Eye} is calculated:

$$R_P^{Eye} = |\overrightarrow{H}^{Eye}| \sin(\pi - \chi_0^{Eye}) \tag{3.11}$$

and correspondingly T_0^{Eye} is calculated as:

$$T_0^{Eye} = T_0' + \frac{P_{R_p}^{Eye} - P_{R_p}'}{c} \tag{3.12}$$

where P_{R_p}' is the closest point to the shower axis for the lowest index observing Eye, corresponding to T_0'. Analogously $P_{R_p}^{Eye}$ represents the point of the closest approach for the current investigated Eye. Both of them can be calculated as:

$$P_{R_p}^{Eye} = P_{FD}^{Eye} + R_P^{Eye}\,(\overrightarrow{n}_{SDP}^{Eye} \times \overrightarrow{S}) \tag{3.13}$$

replacing the *Eye* with the observing Eye of interest, $\overrightarrow{n}_{SDP}^{Eye}$ is obtained from:

$$\overrightarrow{n}_{SDP}^{Eye} = \overrightarrow{S} \times \left(\frac{\overrightarrow{H}^{Eye}}{|\overrightarrow{H}^{Eye}|}\right) \tag{3.14}$$

The parameters values $\theta, \phi, N_{1400}, E_{1400}$ and T_0' are further adjusted in order to minimize the value of χ^2_{Stereo}. The corresponding values of the parameters represent the most probable timing and geometry of the investigated event. Due to the fact that both the pixels geometry and timing profiles are used within the stereo reconstruction, it has the highest accuracy of any

reconstruction types used in the collaboration. However, as mentioned above, the stereo reconstruction suffers from the lack of statistics. Not all of the physical events are able to trigger more than one telescope simultaneously, the process being highly dependent on the physics nature of the primary cosmic ray.

3.5 The Offline Framework

As mentioned in the beginning of the chapter, the Pierre Auger Observatory is not only the biggest cosmic ray detector, but it is also a very complex one. Combining different detection techniques, it is able to simultaneously observe several stages within the air shower development, being thus sensitive to a large variety of shower parameters. This results in an unmatched precision in the detection of UHECR induced air showers. Due to its complexity, the coordination of the responses of different detector types within the Observatory, the tracking of all the recorded data, as well as accounting for several time dependent variables, is rather challenging and needs to be properly handled. In order to be able to accurately monitor the different analysis techniques, translate the detector parameters into useful information towards the physics phenomena and optimize the productivity, the Pierre Auger collaboration invested in building a precise, powerful and fully adaptable cosmic ray analysis software, Offline [69].

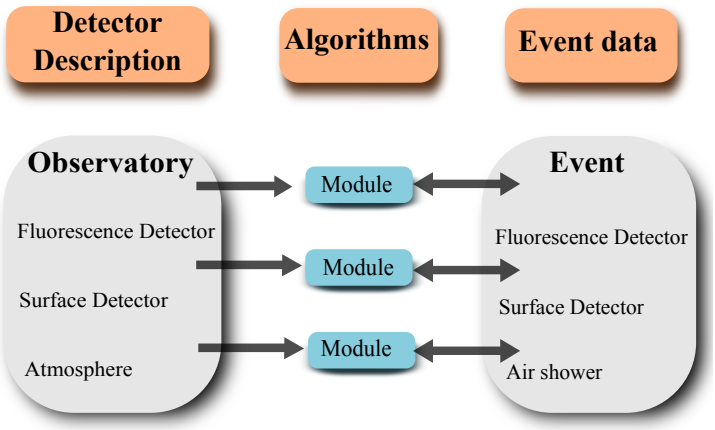

Figure 3.11: The structure of the Offline Framework. The main part of the analysis is handled by implemented algorithms called modules. The modules can be combined and updated as needed. Each module can read data from both the detector description and the event data structure, carries out the analysis and writes the updated information back into the Event data structure [69].

The Offline framework is implemented in C++, taking advantage of the object-oriented design and of various open-source common tools. Its main purpose is to facilitate the simulation and reconstruction of cosmic ray induced air showers by using the available detectors within the observatory. The software is constantly improved and updated according to the growing detectors and the constant development of the analysis techniques. The framework is composed of three principal parts, as shown in Fig. 3.11.

1. **Processing Modules**

   The processing modules are the main blocks of the framework, representing sequences of self contained steps, often called *modules*. Each individual module handles a specific analysis task and is constantly updated by the collaborators. The modules are imported into the framework using a dedicated macro. The main advantage of this modularization is the complexity and interchangeability of the code within the collaboration. The exchange of algorithms and analysis methods, as well as building of various applications is facilitated by combining the modules in different sequences. Each module interacts with the *detector description* and *event data* only. By doing so, the compatibility within the different modules is ensured. Furthermore, the update or exchange in a specific module does not influence the behavior of another one. In order to perform a specific analysis, the user has to choose which modules are needed and order them accordingly. This is done via an *XML* - based run controller, called *Module Sequence*. The settings of each module can be modified via the *XML* files associated with the respective module. These individual *XML* files also contain specific parameters and configurations, which can be changed at any point according to the user's needs. The *bootstrap* file contains all the information needed for the analysis. It is a central *XML* - file pointing the modules to their configuration files and contains the desired modules sequence, as well as additional changes regarding the parameters of interest. The Offline software can further be compiled via a *makefile* and can start the data analysis accordingly.

   This user friendly and flexible design ensures the analysis is accessible by any collaborator and can be easily tweaked according to the specific needs. Standard modules and module sequences are built within the framework and deal with simulation, reconstruction and analysis of various events.

2. **Event Data Structure**

   The event data structure stores all the variables related to an event. It has dedicated fields related to raw detector response, simulations parameters, calibration, reconstruction, Monte Carlo data etc. This data is further used by the analysis modules described at point 1. The structure is organized in classes, which are divided into categories corresponding to the different detector types within the observatory. These classes are then subdivided, depending on the data type they are storing: Monte Carlo truth, calibration information, reconstructed parameters etc. The event data structure acts as a pillar for communication between different modules, which can access the structure at any point and use the updated values of its constituents. In the case of simulated air showers, the event itself needs to be given to the framework. This is done by creating an event builder, which is accessing the event data structure. The detector response is then simulated and sent to the structure. Eventually the event data structure will contain all the information about the simulated event. In the case of real showers, the first step is skipped and the event data structure is giving the detector response and is further providing information regarding the reconstruction results according to the chosen reconstruction modules.

3. **Detector Description**

   The detector description is a structure which can be accessed by the modules in a *read-only* form, in contrast to the event data structure where modules can also write into. It provides non-event related parameters, including the configuration and performance of the detector at a particular point in time, as well as information related to the atmospheric conditions. Similarly to the event data structure, the detector description also contains classes divided into categories related to the different types of detectors. The requested data is passed by the Detector Description to a registry of *managers*, which are able to extract specific information from a particular data source. Data sources are divided into two main types: detector static information, stored in XML files, and time-varying data regarding atmospheric monitoring and calibration, usually stored in MySQL databases. By handling the detector information in this way, one can simulate different conditions and performances of the observatory, allowing for a wide range of possible investigations.

3.5.1 Advanced Data Summary Trees

Since the stored data occupies a tremendously large volume and in order to facilitate the interpretation of the results, the Offline framework also provides access to the tools available through Cern's ROOT [72] analysis software.

Furthermore, the Pierre Auger Collaboration has developed its own data structure, *Advanced Data Summary Trees (ADSTs)*, for storing the numerous variables resulting from the analysis. All the information provided by the Offline framework and discussed above, including both detector and event related variables is stored inside the ADST, in the ROOT format. This can be further on accessed and used for browsing through the events of interest, but more importantly, it represents the starting point of any dedicated physics analysis, containing all of the parameters of interest.

Example applications of the Offline framework will be discussed in the next chapters, as the Offline software has been heavily used for obtaining a significant part of the presented results within this thesis.

4

Up-going Air Showers

In general, when discussing cosmic ray induced air showers, the direction of shower propagation is *down-going*. This means the primary particle is coming from above, hitting an atmospheric nuclei and producing the shower cascade described in section 2.2.2. The shower development thus starts from the top of the atmosphere and moves to the bottom, with secondary particles eventually being detected at ground. It is most natural to think about air showers in this way, since the detectors either monitor the particles count at ground or look for showers developing within the atmosphere. However, up-going extensive air showers are also a physical possibility if non-traditional CR primaries are considered, for example tau neutrinos [73].

4.1 Up-going EAS

In order for a primary particle to be able to induce an up-going EAS, with a brightness high enough to be detectable by ground-based observatories, it needs to survive the propagation through the Earth. Once the particle exits the Earth it can interact with the atmospheric nuclei, and thus create a particle cascade similar in form to a typical down-going shower. The main difference affecting the resulting shower evolution is that the first encountered atmospheric layer in the up-going case will correspond to the bottom atmospheric layer. This reversed atmospheric profile is extremely important to the study of up-going extensive air showers and will be discussed in more detail in section 4.3. A schematic overview of the differing geometries for up-going and down going induced air showers is illustrated in Fig. 4.1(a). These two types of showers are mainly differentiated by their zenith angles. By convention, down-going air showers have zenith angles up to $90° : \theta_{down} \in [0°, 90°]$, while the corresponding up-going zenith angles are greater than $90° : \theta_{up} \in (90°, 180°]$. The development of an up-going EAS is also schematically illustrated in Fig. 4.1(b). It can be seen here that the shower starts to develop at the bottom of the atmosphere.

If the up-going zenith angle is steep, the surface detectors become very inefficient at detecting these kind of showers, as the amount of particles at ground is tremendously reduced and spatially localised at ground. However, the detection of steeply up-going air showers is possible by using the fluorescence detectors (FDs), which are able to monitor the shower's energy deposition directly in the atmosphere (see Section 3.2). Leveraging this fact, a search for steeply up-going induced air showers has been carried out using the FD of the Pierre Auger Observatory and constitutes one of the main subjects of this thesis.

As seen in Fig.4.1(a), the primary particle initiating an up-going EAS needs to be able to traverse the Earth without decaying or loosing all of its energy inside. Because charged particles have a large cross section, and the density of the Earth is orders of magnitude larger than that of the atmosphere, up-going induced air showers are generally discussed in terms of

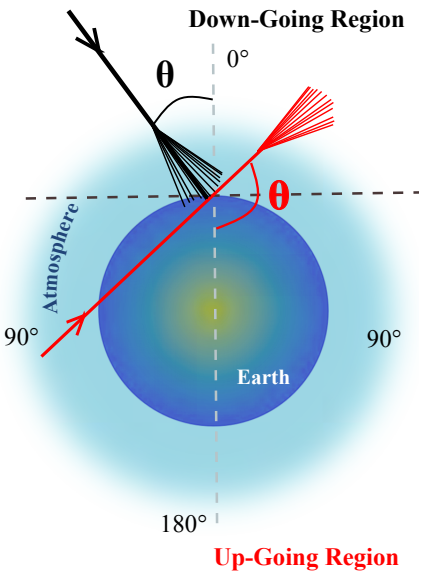

(a) Schematic representation of a down-going (black) and up-going (red) air shower geometry. By convention, the down-going region is defined by $\theta \in [0°, 90°]$, while the up-going region is defined by $\theta \in (90°, 180°]$

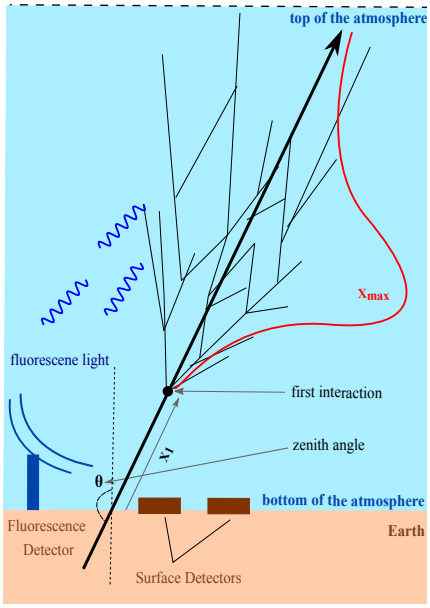

(b) Longitudinal development of an up-going air shower. The first interaction point is in the proximity of the lower part of the atmosphere and the shower continues its development towards the top of the atmosphere, in a reversed manner compared to the down-going profiles sketched in Fig.2.4

Figure 4.1: An illustrated view of up-going induced air showers geometry

neutrino initiated showers. This is because neutrinos can survive propagation inside Earth up to very large distances, and can interact at any point via the charged current (CC) channel to produce charged leptons. The charged leptons can further initiate the EAS, in exactly the same manner as explained within Chapter 2. A schematic overview of neutrino induced up-going showers is illustrated in Fig. 4.2.

The up-going induced EAS is further divided into two main categories, based again on their zenith angles: Earth-Skimming (ES) and steeply up-going showers. This division is mainly motivated by the neutrino cross sections, and correspondingly their probability to escape the Earth, as well as by the different amount of traversed matter for a given zenith angle of interest. As mentioned above, neutrino primaries are the main candidates in up-going studies since they are the only particles within the Standard Model (SM) able to survive propagation through the Earth. However, various Beyond Standard Model (BSM) particles that are able to induce such showers can also be considered. A specific study in this direction has been performed within this thesis and is explained in detail in Chapter 7.

4.1.1 Earth Skimming Showers

The ES channel has been widely studied and used in literature in the context of tau neutrino ν_τ induced air showers. This is because, as mentioned above, in order for an up-going EAS to be produced, a particle with a sufficiently high cross section and energy has to be created and interact within the atmosphere. For a tau-neutrino, this charged particle is created as a result

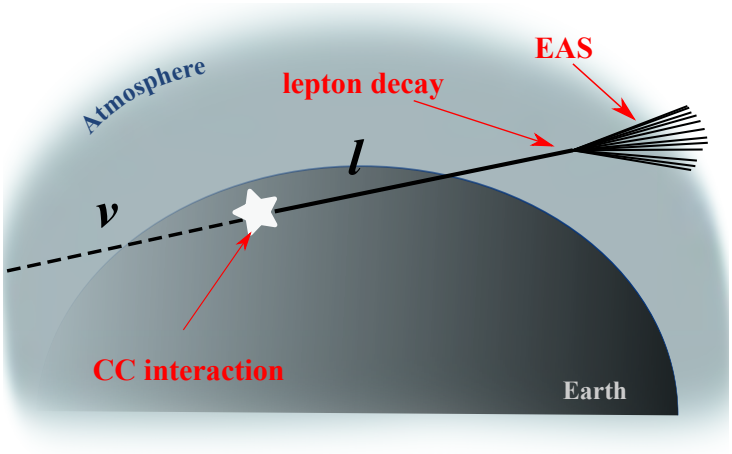

Figure 4.2: Sketch of neutrino induced air showers. The neutrino has to survive Earth propagation up to small distances below the Earth's surface and further on interact via the CC channel in order to produce a charged lepton. If the lepton in turn escapes the Earth with sufficient energy, it can decay or interact in the atmosphere, producing an EAS.

of a CC interaction of the neutrino with the Earth's matter. In order for the charged lepton to be able to produce a detectable air shower it also needs to escape into the atmosphere. Due to a high rate of energy loss in dense media (i.e. the crust of the Earth), electrons would quickly loose all their energy and therefore not escape. Muons are also subject to high energy losses inside Earth. However it is possible for muons to escape Earth, but they will not decay in the atmosphere, as their decay length is much larger ($\approx 10^8$) than the tau leptons one. As a result, tau leptons represent the main candidates able to escape Earth and decay in the atmosphere, thus producing an EAS.

Furthermore, in order for this process to be detectable, the geometry of the primary neutrinos is very much restricted in terms of their zenith angles. Neutrinos must be almost horizontally in order to survive Earth propagation and interact close to the surface. The interaction point has to be very close to the Earth's surface in order for the tau leptons to be able to escape the Earth, and decay in the atmosphere. These criteria are defining the *Earth Skimming showers*. The zenith angles of interest are ranging between $\theta \in [90, 95°]$.

The ES channel is a very powerful one in terms of detection of neutrino induced air showers with the Pierre Auger Observatory. Being highly horizontal, these showers can be detected by the surface detector (SD), taking advantage of its 100% duty-cycle. Several studies regarding tau neutrinos induced air showers have already been performed by the Pierre Auger Collaboration [7], [8]. In all of these studies the dominance in terms of exposure of the ES neutrinos is undeniable. Given the high exposure to these very horizontal showers using the SD, FD studies towards the same type of showers are redundant: mainly because of the much reduced duty cycle of the FD.

4.1.2 Steeply Up-going Showers

Steeply up-going air showers have the same characteristics as the ES ones, in terms of Earth propagation of the primary particle and the corresponding interaction of the resulted second-

ary. In this context however the primaries are interacting at much steeper zenith angles: $\theta \in [110°, 180°]$. The differentiation between the two types of up-going showers is mainly motivated by their detection methods, as well as the probability of interaction of the primary particle[1]. As mentioned above, in order for a primary particle to be able to initiate an EAS, it has to survive Earth propagation up to smaller distances below Earth's crust. Since the neutrinos represent the only SM particles able to propagate very long distances without interaction, they could also be considered the main candidates in this case. The resulted leptons able to produce the EAS are also the τ-leptons, as explained above.

However, in the case of steeply up-going AS, several challenges emerge. The first one is regarding their detection. The surface detector is not able to properly detect such showers since the shower front with the resulted secondaries will not reach the ground anymore. However, since the shower is developing in the atmosphere, the fluorescence detectors (FD) are able to record and provide valuable information about the shower profile of the investigated EAS. As the only detector able to observe such events is the FD, this results in a reduced exposure to steeply up-going EAS, given the reduced FD duty cycle of $\approx 14\%$. Secondly, the survival probability of the neutrinos inside the Earth is tremendously reduced with steeper zenith angles. Therefore, in this scenario, under the SM assumptions, neutrinos are highly disfavored as the main candidates initiating the showers. A concrete observation of these kind of events would indicate the existence of BSM physics and would need additional studies towards the matter.

4.2 The ANITA experiment

The ANtartict Impulsive Transient Antenna (ANITA) is a balloon experiment directed towards the observation of ultra-high energy (UHE) neutrinos via the detection of radio Cherenkov pulses emitted as a result of neutrinos interaction in the Antarctic ice [11]. At their interaction with ice, neutrinos are initiating particle showers. During their development within the ice, the showers will be subject to the Askaryan effect: they will present a negative charge excess and will emit coherent radio Cherenkov radiation.

The balloon has an array of radio antennas attached to it and is overlooking the Antartic ice, flying at heights of $\approx 37\,\text{km}$ [11]. Several flights of the balloon have already taken place, and most of the collected data has been analysed. Depending on the weather conditions, the time of each flight is slowly varying, ranging between 22 and 35 days [74].

Besides detecting neutrinos, ANITA is also able to detected cosmic-ray induced air showers via the radio emission. The radio signals are produced as a result of the geosynchrotron emission, which arises when the positron and electron-secondaries of the shower interact with the geomagnetic field. As a result the electrons and positrons are deflected and will spiral in opposite directions around the magnetic field lines. As the geomagentic field in Antarctica is almost vertical, this results in a horizontal polarization of the radio pulses of comisc ray induced AS. ANITA can detect both direct and reflected cosmic ray events, as it can be seen in Fig. 4.3. The *direct events* do not touch the ground, originating from above the horizon [12] and resulting in a signal with a non-inverted polarity. The *reflected events* are down-going induced air showers,

[1] As no dedicated searches using the Pierre Auger Observatory have been performed in the zenith ranges $\theta \in (95°, 110°)$ this interval is not further discussed

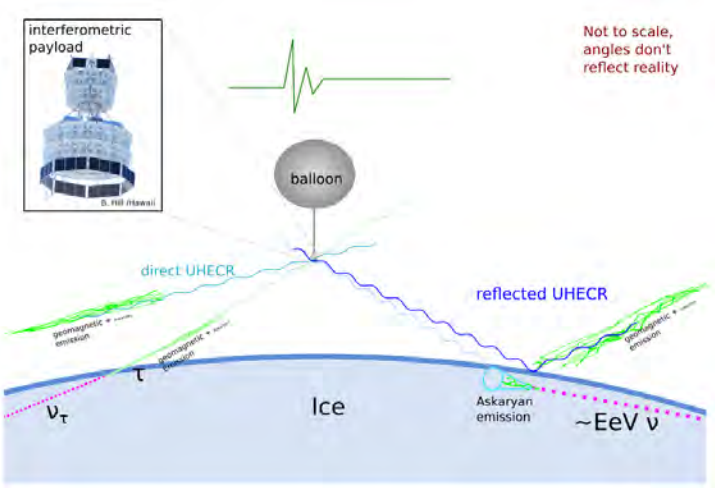

Figure 4.3: Schematic overview of the ANITA balloon experiment and the main detection mechanisms. Picture from [75]

detected via the reflected radio pulses on the ice surface and resulting in an inverted polarity of the field strength wave-forms [12], [74], [15]. Additionally, the experiment can also detect tau neutrinos emerging from ice [75].

The distinction between cosmic-ray and neutrino induced air showers is straightforward. The Askaryan signal produced as a result of neutrino interactions will have a vertical polarization, due to its passage through the ice-air interface [74].

As mentioned in the beginning of the chapter, up-going cosmic-ray induced air showers allowed within the SM are discussed in terms of the Earth-skimming channel. The ANITA experiment is also sensitive to such showers. However, the ANITA collaboration has published in 2018 the observation of two steeply up-going *anomalous events* with a cosmic-ray like origin [15]. The observation of such events has triggered a wide scientific interest, including the research performed within this thesis.

4.2.1 Anomalous events observed by the ANITA experiment

The ANITA collaboration has reported the observation of two steeply up-going cosmic ray - like induced air showers during two of their fourth flights [14], [15]. The two events have a horizontal polarity, characteristic to CR induced air shower and a non-inverted polarity, excluding a reflection in the ice of the CR event. Moreover, the estimated zenith angles are rather steep, of more than 110° for both events, with estimated primary energies of few tenths of an EeV [13]. For the detected arrival angles the scenario of a τ-neutrino induced air shower is in tension with both the SM values for the neutrinos cross sections, as well as with the current upper flux limits on diffuse isotropic neutrinos fluxes [13, 16, 16, 8] .

The corresponding field strength wave-forms of four cosmic ray events detected in the third flight of ANITA, containing the anomalous events, has been plotted by the ANITA collaboration and is shown here in Fig. 4.4. The anomalous event is plotted in panel *(a)*. Two non-inverted cosmic ray events with elevations of few degrees above horizon, as signatures of the direct CR events, are shown in panels *(b)* and *(c)*. In panel *(d)* a CR event with similar elevation but with inverted polarity, indicating its reflection at the ice surface, is also shown.

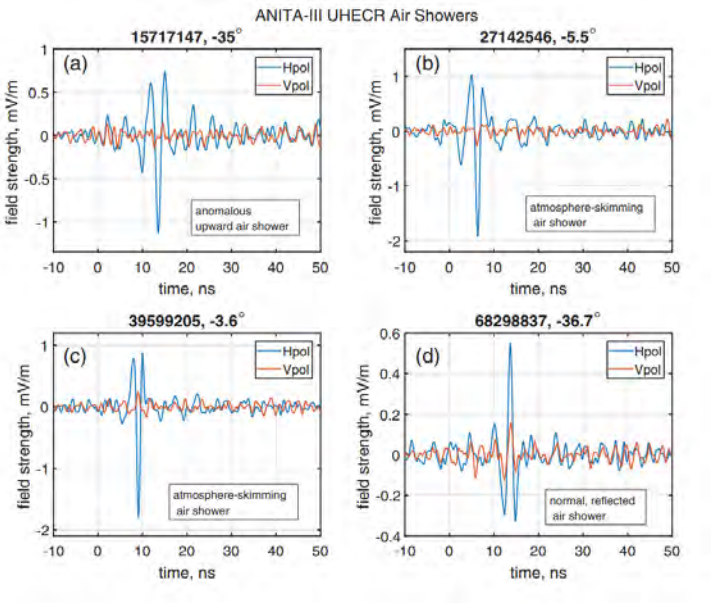

Figure 4.4: Field strength waveforms of four CR events detected within the third flight of ANITA. Above each plot the event ID together with the elevation angles are indicated. The anomalous event (panel *(a)*) has an elevation of $\approx 35°$ above the horizon. Figure from [15]

The other anomalous event observed in the first flight of ANITA has a similar wave-form as event 15717147 and is discussed in more details in [14].

The characteristics of the two anomalous events, from flight I (event 3985367) and flight III (event 1517147) respectively, are described in [14] and [15] and enumerated below, in terms of the main variables of interest:

1. elevation angles: $-27.4 \pm 0.3°$, respectively $-35.0 \pm 0.3°$
2. zenith angles (corresponding to the given elevations): 117.4° respectively 125°
3. shower energy: $0.6 \pm 0.4\,\mathrm{EeV}$ respectively $0.56^{+0.3}_{-0.2}\,\mathrm{EeV}$

As mentioned above, the observation of these anomalous events is in strong disagreement with the SM predictions of neutrinos cross sections, requiring ≈ 18 SM interaction lengths of a ν_τ at 1 EeV [15]. For such an event to be initiated by neutrinos, their cross sections should be significantly reduced and can't be explained with the current SM knowledge. However BSM physics can be involved and various scenarios have been already proposed in literature [76], [77], [18], [17], [19], [78]. A study towards a BSM scenario of a primary particle with artificially decreased cross section has been investigated within this thesis. The studied method and obtained results are presented in detail in Chapter 7.

4.3 First simulations of steeply up-going EAS with the FD of the Pierre Auger Observatory

As the two discussed ANITA events [15] are in strong disagreement with the SM physics, a follow-up towards such events is crucial. The Fluorescence Detector (FD) of the Pierre Auger Observatory is able to detect events with signatures similar to these anomalous events. Therefore

a dedicated study has been performed in this direction, using the 14 years of available FD data. This study is described in detail in Chapter 5. The first phase of such a study is represented by the simulations of the events of interest, which constitute a major part of this thesis. In this section the first steps regarding the up-going showers simulations and their signatures in the FD are discussed.

The simulation procedure is divided into two main steps: simulations of the EAS and simulations of the detector response to such showers. Both steps have been successfully completed, after several updates to the simulation framework have been implemented.

4.3.1 Simulation of steeply up-going induced air showers using CORSIKA

The extensive air showers have initially been simulated using CORSIKA [79]. It is a widely used and complex code which is simulating in detail the extensive air showers initiated by high energy particles. The initiating particles can be chosen from a large variety of primaries, as well as their parameters in terms of energy, zenith angle, azimuth angle etc. The shower development in the atmosphere is tracked at each step, together with the resulted secondaries. In order to describe the hadronic interactions within CORSIKA, different high energy and low energy models can be chosen by the user. The electromagnetic processes can be described both analytically, using the NKG [80], [81] treatment, or by using the Monte Carlo technique, within the EGS4 package [82]. More details about the CORSIKA simulation code and user guide can be found in [79].

Neutrinos were chosen in a first step as primary particles to be studied, with zenith angles $\theta \in [110^\circ, 180^\circ]$. The zenith range has been chosen in accordance with the detected angles of the ANITA events. Lower zenith angles have not been investigated, as the choice of a flat atmosphere does not hold for $\theta < 110^\circ$. However in order to study the observed anomalous events the chosen zenith range is well motivated.

In order to perform the desired simulations, the CORSIKA program had to be set accordingly. As a first approach, the SIBYLL [56] model was chosen for the high energy hadronic interactions and GHEISHA [83] was describing the low energy region. The choice of the interaction models was arbitrary at the time, as the first trials were only concerning the possibility of performing such simulations and the resulted events geometry. The non-curved version of the atmosphere was chosen.[2] The UPWARD option, available within the compilation stage, is crucial for the current study. This option is allowing one to treat up-going EAS. As it can be seen in Fig. 4.5, additional parameters have to be set. One of the parameters of interest is the height of the first interaction above sea level, which can be set using the keyword *FIXHEI* as an input. Once the first interaction is set, the shower development is followed up to the observation level, which can also be set as an input parameter, by using the keyword *OBSLEV*. The first natural requirement is that in such a case the observation level has to be situated above the altitude of the shower's first interaction. The value of the observation level was set to $OBSLEV = 40$ km above sea level. Since the Pierre Auger Observatory is situated at an altitude of ≈ 1.4 km a.s.l, the minimum value of the height of the first interaction will be $FIXHEI = H_1 = 1.4$ km. As the FD is the only instrument used within the current study, the longitudinal profiles represent the

[2] For the zenith angles of interest, $\theta \geq 110^\circ$ the CURVED option is not required. As mentioned in the CORSIKA user guide, this option becomes necessary for elevations lower than 20° [84]

starting point towards simulating the detector's response.

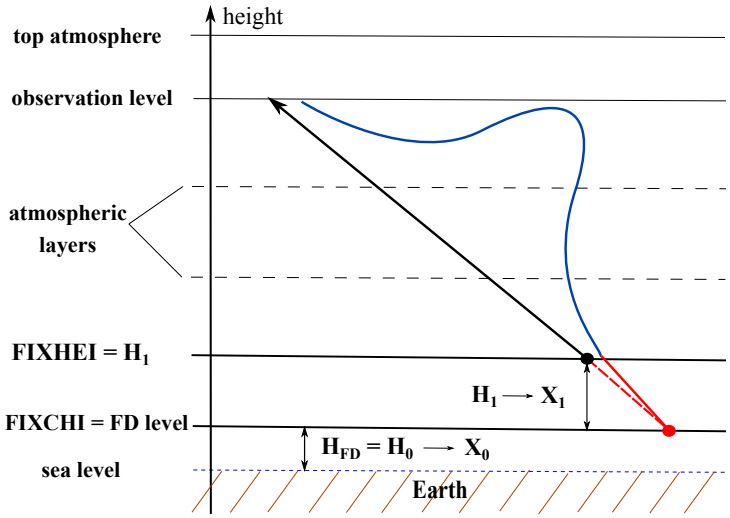

Figure 4.5: Skematic view of the geometry of an up-going air shower as defined in CORSIKA with the UPWARD version. The height of the first interaction H_1 is set by using the keyword *FIXHEI*. The observation level has to be set above this height, with a maximum value corresponding to the top of the atmosphere. The shower development is followed through the different atmospheric layers up to the observation level. The standard longitudinal profile written in the output file is sketched in blue. By setting a fixed value of the injection height H_0 via the *FIXCHI* keyword, the profile is written starting from the respective altitude, including the red region, as it is seen by the FD. If the first interaction height is higher than the injection height, the red region will be filled out with the corresponding depth and a null energy deposit.

Electron neutrinos, ν_e, have been initially used as the main primary particles. Simulations of ν_μ and ν_τ were also considered but it was soon discovered that the leptons decay could not be forced within CORSIKA at a specific height. Therefore, many times the longitudinal profiles would be almost empty, given the high altitude of the decay. Additional simulations of proton induced air showers have been simultaneously studied, given the cosmic-ray like features of the ANITA events and the better known behavior of such showers. The energy range was initially rather high, with $E_{prim} \in [10^{18.5}, 10^{20}\,\mathrm{eV}]$, in order to insure a proper energy profile reconstruction[3]. As the exact altitude of the primary particle initiating the shower is not well known within the ANITA context, different heights of first interaction have been studied. Since the Fluorescence Detector is situated at the ground level, the longitudinal profiles need to be recorded from the very lowest values of the slant depth, even when the particle starts interacting at higher altitudes. In those cases, the lowest values of the traversed depth will have a null energy deposit (red line of the longitudinal profile in Fig. 4.5). The shower will only start to deposit its energy in the atmosphere at an atmospheric depth, X_1, corresponding to the chosen height of first interaction H_1. By doing so the FD response to the up-going induced AS can be properly simulated.

This can be achieved within CORSIKA by using both the *FIXHEI* and *FIXCHI* keywords. As explained within the user guide [84], the height of the first interaction, H_1, can be set by changing the value of *FIXHEI*. By fixing the value of the injection depth, *FIXCHI* $= X_0 \approx 875.6\,\mathrm{g/cm^2}$, corresponding to the vertical atmospheric depth at the FD altitude,

[3]It is well known that for low energies the FD exposure will be much lower

$H_{FD} \approx 1.4\,\text{km}$ a.s.l, the profiles are written out accordingly. This is sketched in Fig. 4.5. Moreover, the *VERTICAL* option regarding the longitudinal profile output file has to be used: the results are further provided in terms of vertical depth X_v. The slant depth X defined in Eq. 2.5 is further calculated within the Offline [69] software of the collaboration, which is used for the simulation of the FD response. By using the option *SLANT* within CORSIKA the profiles are correctly calculated but the profile can only be followed starting with the slant depth corresponding to the first interaction and not from the altitude of the FD, as desired.

$$X = \frac{X_v}{|\cos\theta|} \tag{4.1}$$

4.3.2 Simulation of the FD response to up-going EAS

Having set the showers simulations approach, the second part in the preliminary study regards the FD response and reconstruction. The first modification implemented in to the Offline software was regarding the definition of the slant depth defined in Eq. 2.5. An absolute value of the cosine term has been added, as shown in Eq. 4.1. Without this change, the slant depth resulted negative values for the case of up-going showers and therefore the simulations were failing. Using the Offline framework, the first results of the reconstructed energy profile of such showers have been produced and are plotted in Fig. 4.6. It can be seen that the dE/dX profiles are having a rather reversed shape as a function of the slant depth: showers starting at higher altitudes (larger H_1) only have the very end region of the profile (corresponding to high values of X) reconstructed and seen by the telescope. This is a clear signature of a wrong interpretation of the profile in the case of up-going showers. Since the slant depth represents the amount of atmosphere traversed by the particles, a particle starting at the detector level should be observable from the very few g/cm^2 up to the end point of the profile. On the contrary, the profile of a particle starting at higher altitudes would not be seen entirely by the detector, except for the starting region of its Gaisser Hillas profile, corresponding to larger values of the slant depths than in the case of particles interacting at ground. In contrast, by looking at Fig. 4.6(d), the only recorded part of the profile is the very end one, indicating a problem within the simulation procedure.

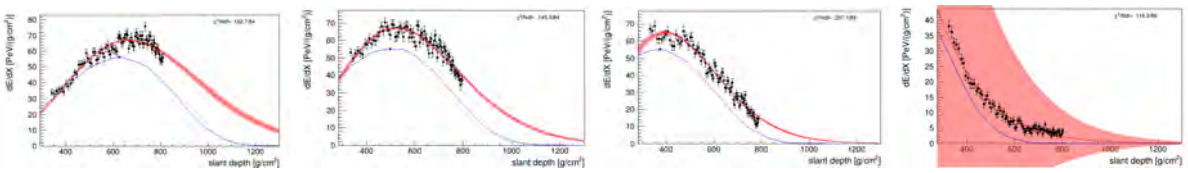

(a) $H_1 = 1.4\,\text{km}$ a.s.l (b) $H_1 = 2\,\text{km}$ a.s.l (c) $H_1 = 3\,\text{km}$ a.s.l (d) $H_1 = 5\,\text{km}$ a.s.l

Figure 4.6: First energy deposit profiles (wrong profiles - see text for details) as obtained from the Offline framework in terms of dE/dX versus the slant depth X, defined in Eq. 2.5. The profiles correspond to simulated up-going protons with $\theta = 129.5°$ and primary energy $E_p = 3.65 \cdot 10^{19}\,\text{eV}$. The protons are interacting at different values of H_1

By checking the longitudinal profiles resulted from the CORSIKA simulations, the issue has been detected. The energy deposit is produced in terms of vertical atmospheric depth, and further on the slant depth is calculated according to Eq. 4.1 within Offline. The difference

between up-going and down-going induced air showers is strongly related to the atmospheric borders. A maximum value of the vertical depth coincides to a minimum altitude of the shower, corresponding to the sea level. A down-going shower reaching the minimum altitude has already travelled through the atmosphere, and therefore the slant depth will be maximum. An up-going shower, however, will only start its development at the corresponding minimum altitude, therefore its slant depth has to increase with the increase of height above sea level. In order to be able to use Eq. 4.1 and correctly describe the travelled depth of an up-going shower, the energy deposit profile has to be reversed with respect to the vertical depth. This has been solved by keeping the resulted values provided by CORSIKA in terms of deposited energy and secondaries, and reversing the vertical depth correspondingly, as sketched in Fig. 4.7. In this

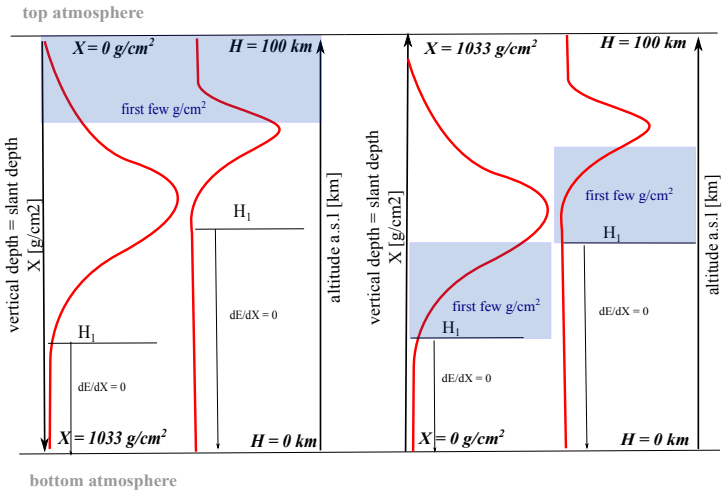

Figure 4.7: Illustrated view of the atmospheric profile as resulted from CORSIKA (left plot) and the corrected profile for up-going induced air showers (right plot). As in the case of down-going EAS the shower development starts from the top of the atmosphere (minimum X) towards the bottom (maximum X), the slant depth is defined accordingly and represents the depth a particle has traversed. To keep the same definition of the slant depth, the atmospheric depth has to be reversed: the shower starts its development at the bottom of the atmosphere (minimum H_1) towards the top (maximum H_1). To reflect the same behavior in terms of travelled atmospheric depth, the minimum vertical depth will correspond to the bottom of the atmosphere and will continue to increase up to the top. This will be reflected in the slant depth as well. The sketch shows two vertical $\theta = 180°$ up-going shower profiles with different heights of first interaction H_1. The *first few* g/cm^2 mark the region where the shower starts depositing its energy in the atmosphere.

way the particle starts depositing its energy at the lowest depth values. For simplicity, in the figure a vertical shower ($\theta = 180°$) is illustrated. In the first case (left side of the figure) the energy deposit profile, as taken from CORSIKA is shown. The first few g/cm^2 with a non-zero energy deposit correspond to the very top of the atmosphere, for any height of first interaction H_1 of the up-going shower. This corresponds to the region of the profile which would be reconstructed using the FD and is plotted in Fig. 4.6. Thus, in the case of showers starting at a high altitude (Fig.4.6(d)), the only visible part of the profile corresponds to the very end region of the shower profile, while for a shower starting at low altitudes a larger part of the profile is reconstructed, as the shower is immediately depositing energy in the atmosphere and developing up to the top of it. However this is wrong, as explained above, since in this representation the resulted slant depth does not mirror the shower's traversed depth. In the second sketch from

Fig. 4.7 the adopted correction is sketched. The same two showers are considered, while the atmospheric depth is being reversed. In this case the minimum atmospheric depth corresponds to the minimum altitude, which represents the starting point of the shower development. It can be seen that in this scenario the first g/cm^2 corresponding to a non-zero energy deposit are different for different values of H_1, which is desired. A shower starting at a higher altitude will start developing later (at a higher value of the slant depth) in the atmosphere. In this case the reconstructed energy profiles should correctly reproduce the shower development.

After implementing the above explained changes within Offline, the first test results have been obtained. For a fast check a study has been performed for vertical $\theta = 180°$, high energy $\lg E\,/\,\mathrm{eV} = 19.5$, proton induced air showers. The resulted energy deposit profiles, together with the pixel traces within one of the telescopes camera are shown in Fig. 4.8. The black dots in the profiles correspond to the data provided by CORSIKA. The red line gives the Gaisser Hillas curve as plotted within Offline, while the blue line represents the Gaisser Hillas fit calculated within CORSIKA. The updated profiles start at different slant depths, corresponding to their height of first interaction: for a $H_1 = 1.4\,\mathrm{km}$ a.s.l the shower starts to deposit its energy at a depth of $X_1 \approx 200\,\mathrm{g/cm^2}$, while for an altitude of $H_1 = 5\,\mathrm{km}$ the corresponding depth is $X_1 \approx 500\mathrm{g/cm^2}$. As sketched in Fig. 4.7, this is the physical result expected for such showers, as particles interacting higher in the atmosphere, and propagating upwards, will start their development closer to the top of the atmosphere and therefore at higher values of the slant depth. Moreover, it can be seen that the energy deposit recorded by the FD is minimum for the maximum investigated height (Fig. 4.8(d)). The validity of the obtained results is also mirrored in the corresponding pixel traces. The pixels color code in Fig. 4.8 is related to the arrival time, purple representing the earlier recorded signal. A shower starting at the detector level, $H_1 = 1.4\,\mathrm{km}$ a.s.l, triggers the very first row of the camera pixels, while for a shower starting higher in the atmosphere only the last pixel rows are triggered.

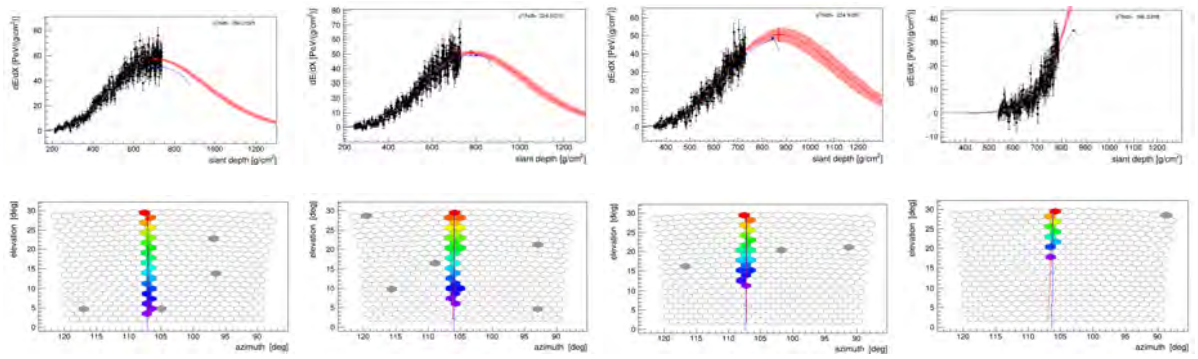

(a) $H_1 = 1.4\,\mathrm{km}$ a.s.l (b) $H_1 = 2\,\mathrm{km}$ a.s.l (c) $H_1 = 3\,\mathrm{km}$ a.s.l (d) $H_1 = 5\,\mathrm{km}$ a.s.l

Figure 4.8: Correct energy deposit profiles in terms of dE/dX versus the slant depth X, defined in Eq. 4.1, with the atmospheric correction for the up-going showers applied. The profiles correspond to up-going vertical protons, $\theta = 180°$ with primary energies $E_p = 10^{19.5}\,\mathrm{eV}$ induced air showers, with different heights of first interaction H_1. The corresponding pixel traces as seen within Los Leones(LL) - FD site are also plotted.

Within the same study the angle of the first triggered pixel, χ_1, has been investigated for different heights of first interaction H_1 and different positions of the shower core with respect

to the FD, R_{FD}. The two variables can be interpreted by looking at Fig. 3.9, where the geometry of the monocular reconstruction is sketched. The angle χ_1 is the angle between the first triggered pixel and the shower axis. For a vertical event, $\theta = 180°$, the distance between the shower core and the FD location is equal to the R_p parameter: $R_{FD} = R_p$. By varying this distance, the FD-FoV can be correspondingly reduced or increased, resulting in a different number of triggered showers at different heights of first interaction. By simulating a number of 100 proton induced air showers, with $\theta = 180°$ and primary energy $E = 10^{19.5}$ eV, the corresponding values of the first triggered pixel angle, χ_1, have been studied for different values of R_{FD}. In Fig. 4.9 representative plots are shown, as obtained from simulations with R_{FD} calculated with respect to the Los Leones (LL) eye. The choice of the telescope building is completely arbitrary within this testing stage.

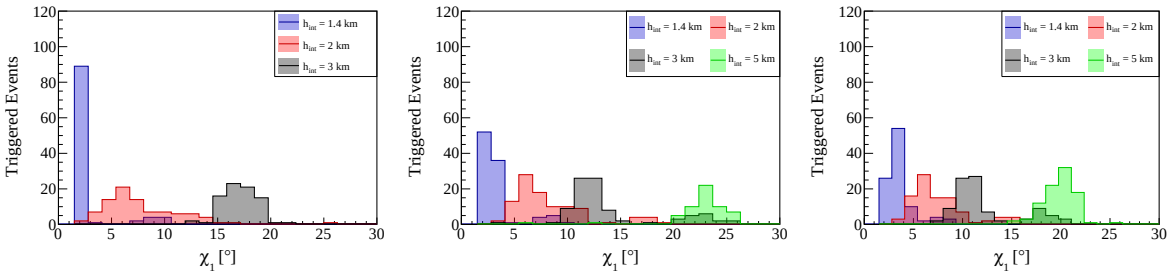

(a) $R_{FD} = 5$ km (b) $R_{FD} = 10$ km (c) $R_{FD} = 14$ km

Figure 4.9: Events triggering the LL Eye, resulted from the simulations of 100 up-going proton ($\theta = 180°, E = 10^{19.5}$ eV) air showers, with respect to the angle of the first triggered pixel, χ_1, within the camera, at different values of the core-eye distance R_{FD}. Showers starting at the highest altitudes (green area) are found to peak towards the highest values of χ_1.

Most of the triggering events corresponding to up-going showers starting at the detector level, $H_1 = 1.4$ km a.s.l, are found to peak around the lowest values of the the first triggered pixel: within the first 5°. With the increase of the height of the first interaction, the peak of triggered events is shifted towards higher elevation pixels. This confirms the correctness of the up-going shower simulation setup. Furthermore, with the increase of the shower core distance, R_{FD}, the sensitivity of the FD is increased towards showers starting higher in the atmosphere.

The position of the shower core, (i.e the value of R_{FD}) also influences the number of FD sites able to observe the same shower, resulting in the possibility of observing stereo (two different FD sites triggered) or even triple (three different FD sites triggered) events. The FD triggering efficiency has been calculated as a function of the R_{FD} distance for the different event types and is plotted in Fig. 4.10. Showers starting at the detector level always provide the highest efficiency, since the telescope is able to follow their profiles in a most consistent way. The higher the shower starts in the atmosphere, the less pixels will be triggering within the FD camera, as the shower development is starting at higher altitudes [4]. The increase in the trigger efficiency with the increase of the distance R_{FD} is also visible. For very small values of R_{FD} there are no stereo (Fig. 4.10(b)) or triple (Fig.4.10(c)) events, regardless of their height of first

[4] Note that this is a discussion regarding vertical up-going showers: $\theta = 180°$. For up-going inclined air showers the situation is slightly different, but the principle stays the same: the FD sensitivity is decreasing at higher values of H_1 (See Chapter 5)

interaction. Moreover, for very small values of R_{FD}, there are no monocular events triggered by the showers starting high in the atmosphere (black bullets in Fig. 4.10(a)).

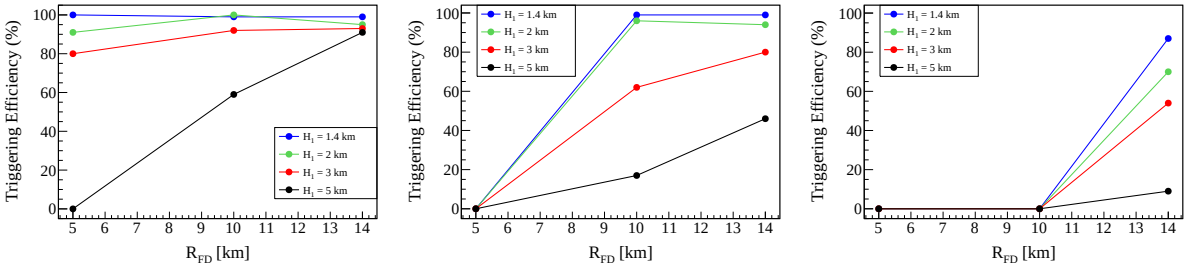

(a) Monocular Events (b) Stereo Events (c) Triple Events

Figure 4.10: Trigger efficiency of the FD for monocular, stereo and triple events, as resulting from the simulation of 100 up-going proton ($\theta = 180°, E = 10^{19.5}$ eV) induced air showers starting at different altitudes as a function of their eye-core distance R_{FD}, calculated with respect to LL eye position

Once the presented modifications have been implemented and after all the above mentioned cross checks have been performed, the simulation of up-going induced air showers and their correct reconstruction using the FD has been possible. As a result, the next logical step towards a follow up of the anomalous events observed by the ANITA collaboration was to simulate up-going showers with the observed parameters and check the FD response.

4.3.3 First simulation sets towards a follow-up of the ANITA events

In a first attempt towards checking the FD response and sensitivity to steeply up-going EAS, showers initiated by both protons and electrons with similar parameters as the anomalous events discussed in subsection 4.2.1 have been simulated. CORSIKA simulations have been performed using UrQMD 1.3.1 [85] model for describing low energy hadronic interactions and QGSJET-II model [86] for the high energy interactions. The parameters used in the configuration of CORSIKA, as well as an example of the input file can be found in Appendix A. The main shower parameters are listed below. For a detailed study, the simulations were done for different sub-ranges of the parameters of interest, therefore each parameter is also listed together with the corresponding bin widths. A full azimuthal range has been simulated: $\phi \in [-180°, 180°]$.

1. *primary particles:* proton, electron
2. *zenith angle:* $\theta \in [115°, 130°]$ - 5° bin
3. *primary energy:* $E_0 \in [10^{17}, 10^{18.5}\,\text{eV}]$ - $10^{0.5}$ eV bin
4. *height of first interaction:* $H_1 \in [1.4, 5.4\,\text{km a.s.l}]$ - 0.5 km bin

The showers have been simulated having a flat in logarithm of energy spectrum. This decision is motivated by the possibility of re-weighting the events to any desired energy spectrum afterwards, as well as having enough statistics for all energies of interest. A number of 500 showers has been simulated for each energy, zenith and height bin.

As it can be seen in Fig. 4.10 the FD sensitivity to up-going showers is strongly related to a proper choice of the distance between the shower core and the FD-site. Therefore a preliminary study of the simulated events has been done in this regard. As the maximum sensitivity is achieved for showers starting at the detector level, showers with $H_1 = 1.4\,\text{km}$ a.s.l and the most inclined zenith sub-range $\theta \in [115°, 120°]$, which are able to trigger the FD from distances much larger than in the case of more vertical zenith ranges, have been chosen for this preliminary study. The three different energy ranges have been investigated separately, simulating a number of 500 proton induced air showers per simulation set. The results regarding the number of triggered events within a given eye are plotted in Fig. 4.11 with respect to the distance R_{FD}. Within the simulations the maximum allowed value was set to 40 km: $R_{FD} \in [0, 40]\,\text{km}$, with showers being uniformly thrown in front of the Eye. A different value for the maximum distance R_{FD}^{max} at which events are still triggering within the FD is reached for different energy ranges. This is to be expected, given the proportionality between the primary particle energy and its energy deposit in the atmosphere and having otherwise the same shower parameters (zenith, azimuth and heights of first interaction). As a result, in order to maximize the simulations efficiency, different maximum distances are set for different energy ranges. For proton induced air showers, the maximum distance is set: $R_{FD}^{max} = 15\,\text{km}$ for $\lg E_0 \,/\, \text{eV} \in [17, 17.5]$, $R_{FD}^{max} = 20\,\text{km}$ for $\lg E_0 \,/\, \text{eV} \in [17.5, 18]$ and $R_{FD}^{max} = 30\,\text{km}$ for $\lg E_0 \,/\, \text{eV} \in [18, 18.5]$.

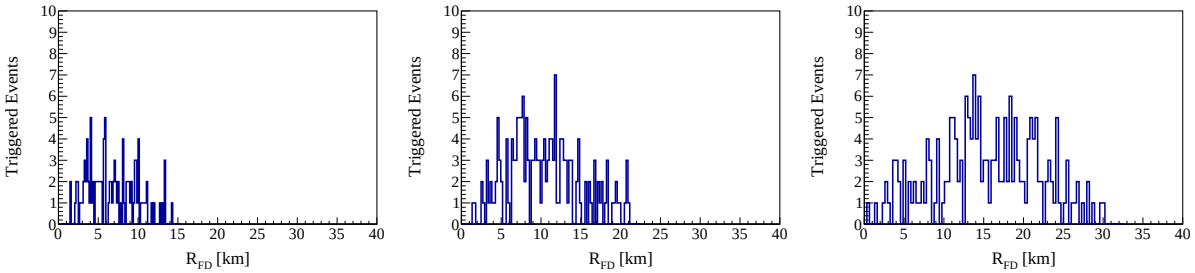

(a) $\lg E_0 \,/\, \text{eV} \in [17, 17.5]$ (b) $\lg E_0 \,/\, \text{eV} \in [17.5, 18]$ (c) $\lg E_0 \,/\, \text{eV} \in [18, 18.5]$

Figure 4.11: Triggering proton events resulting from a simulation set of 500 proton induced air showers per energy range, at a fixed zenith range of $\theta \in [115°, 120°]$ and fixed interaction height of $H_1 = 1.4\,\text{km}$ a.s.l. Simulations are eye centric and R_{FD} represents the distance between the shower core and the site of the investigated Coihueco eye.

A similar study has been performed for electron induced air showers, as the shower profile and correspondingly the maximum R_{FD} will have different values, given the different contribution to the electromagnetic component of the shower initiated by the two primaries. This is mainly due to the fact that an electron induced air shower will mainly feed into the electromagnetic component, while showers induced by proton primaries result in a significant muonic component, reducing thus the primary energy fraction deposited in the atmosphere. The corresponding histograms are shown in Fig. 4.12. The chosen values for the electron induced air showers are: $R_{FD}^{max} = 20\,\text{km}$ for $\lg E_0 \,/\, \text{eV} \in [17, 17.5]$, $R_{FD}^{max} = 30\,\text{km}$ for $\lg E_0 \,/\, \text{eV} \in [17.5, 18]$ and $R_{FD}^{max} = 35\,\text{km}$ for $\lg E_0 \,/\, \text{eV} \in [18, 18.5]$.

Once the maximum value R_{FD}^{max} has been set for different energy ranges, the simulations of proton and electron induced air showers were performed. A number of 100 events for each zenith, height of first interaction and energy bin has been simulated within CORSIKA. Due to

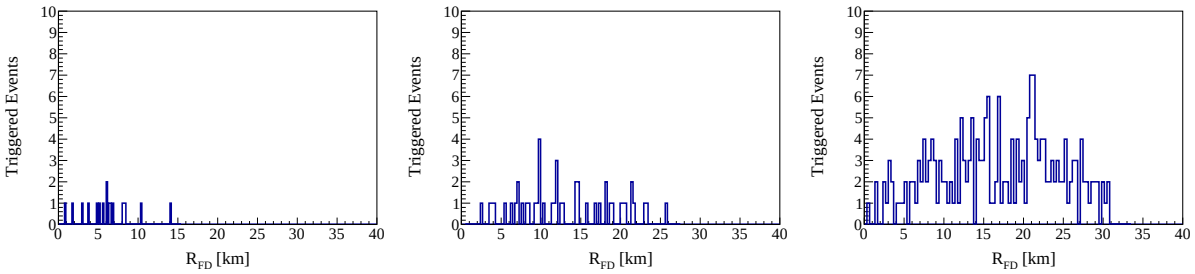

(a) $\lg E_0 \,/\, \mathrm{eV} \in [17, 17.5]$ (b) $\lg E_0 \,/\, \mathrm{eV} \in [17.5, 18]$ (c) $\lg E_0 \,/\, \mathrm{eV} \in [18, 18.5]$

Figure 4.12: Triggering events resulting from a simulation set of 500 electron induced air shower per energy range, at the fixed zenith range of $\theta \in [115°, 120°]$ and fixed interaction height of $H_1 = 1.4\,\mathrm{km}$ a.s.l., as a function of the distance between the shower core and the telescope location

the Offline framework complexity, one CORSIKA shower (with its longitudinal energy profile) can be re-thrown an arbitrary number of times within the array, in order to produce different FD responses[5]. Therefore, the statistics can be easily increased without a very expensive computation time. Consequently, each CORSIKA shower has been additionally thrown 5 times at different positions inside the array, resulting in a full simulations set of 500 events per zenith, height of first interaction and primary energy bin. All simulations are *eye centric*, meaning only one FD site is being studied, while the other telescope buildings are forcefully turned off. This is done in order to ensure a proper study of the detector's response to up-going induced air showers with the parameters of interest. All telescope eyes are considered in the final study, as described in Chapter 5. The Coihueco site has been set as the central eye of interest. The choice of this specific location is motivated by having the HEAT telescope nearby. As HEAT has a higher elevation when tilted upwards, $(30°, 60°)$, as described in Section 3.2, it is of a great interest in the up-going study.

4.3.4 Additional corrections in the up-going showers simulations

Having enough statistics from the above mentioned simulation sets, additional cross checks have been made regarding the correctness of the up-going induced air showers simulations. Several parameters of interest have been chosen and studied in detail. One of the first investigated parameters which turned out not to be properly calculated in the up-going air showers context, within the Offline framework, was the depth of the first interaction, X_1. This is further used in the calculation of light profiles and needs to be corrected for in order to have a proper simulated FD response. Events starting higher in the atmosphere are expected to have a larger X_1, compared to those starting at the detector level (see the right plot in Fig. 4.7). Studying two different sets of showers, simulated with the same energy and zenith range, but with different heights of first interactions, it was discovered that the first interaction depth X_1 was not calculated properly, generating a rather unexpected result.

As can be seen in Fig. 4.13(a) and 4.13(b), showers starting at higher altitudes have a lower value of X_1. The source of the error has been detected and corrected for. The first

[5] By taking the shower characteristics from CORSIKA, the detector response is re-simulated by placing the shower core at different positions within the array. The same shower gives different response in the FD depending on its core localization.

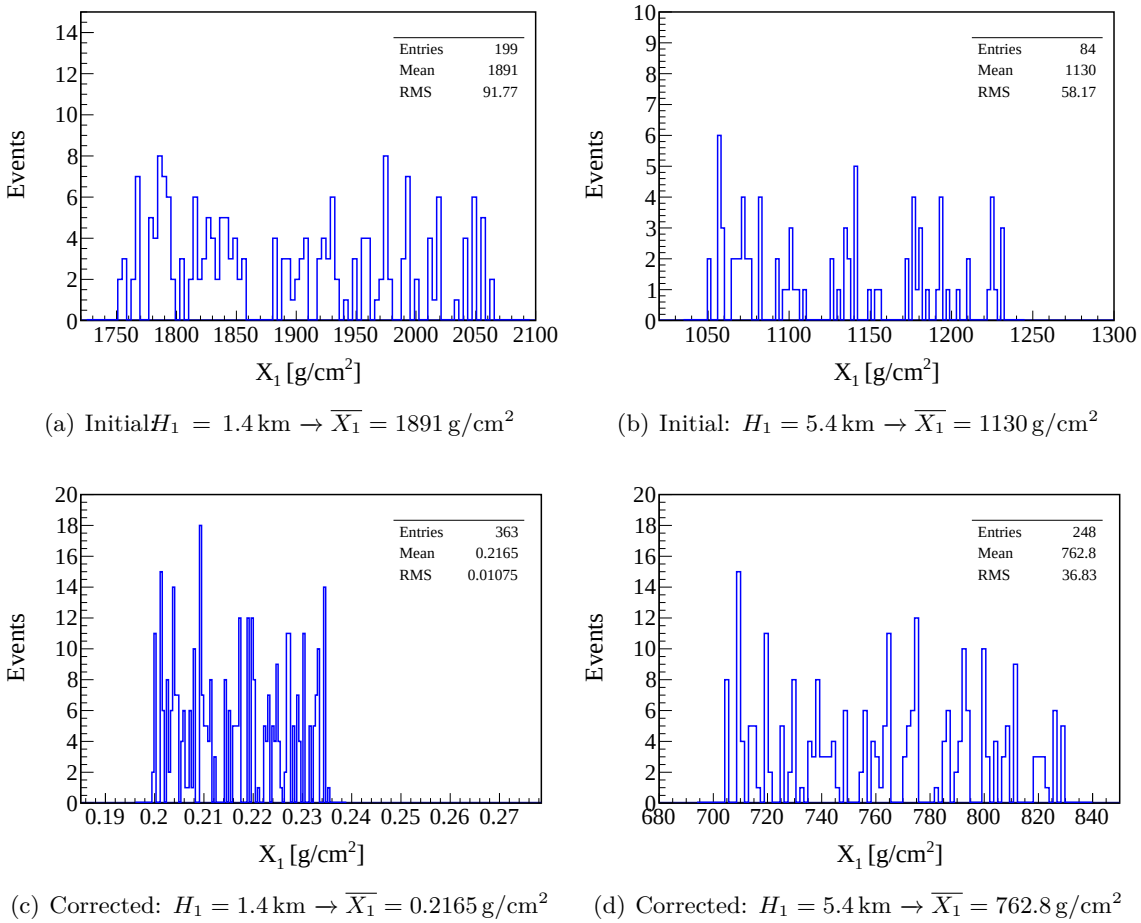

(a) Initial $H_1 = 1.4\,\text{km} \rightarrow \overline{X_1} = 1891\,\text{g/cm}^2$

(b) Initial: $H_1 = 5.4\,\text{km} \rightarrow \overline{X_1} = 1130\,\text{g/cm}^2$

(c) Corrected: $H_1 = 1.4\,\text{km} \rightarrow \overline{X_1} = 0.2165\,\text{g/cm}^2$

(d) Corrected: $H_1 = 5.4\,\text{km} \rightarrow \overline{X_1} = 762.8\,\text{g/cm}^2$

Figure 4.13: Triggering events distribution in terms of first interaction slant depth, X_1, as resulted from a simulation set of 500 proton induced air showers, with zenith angles $\theta \in [115°, 120°]$ and primary energy $\lg E_0/\text{eV} \in [18, 18.5]$. Figures (a) and (b) show the initial distributions for different values of H_1, together with the average value $\overline{X_1}$, while figure (c) and (d) show the correct resulted distribution for the same set of showers.

interaction depth used within Offline was calculated using the height of first interaction, read from the CORSIKA file. Since the vertical option is chosen, the formula used for getting the slant depth X_1 is the one from Eq. 4.1, with the only difference being that the vertical depth, X_1^{vert}, is calculated using the value of H_1. The calculation was done considering an atmosphere profile with a maximum depth at the lowest altitudes, as is the case for down-going showers, sketched in the left plots from Fig. 4.7. However, as explained in section 4.3.2, in the case of up-going induced air showers the atmospheric profile has to be reversed so that the minimum slant depth lays at the bottom of the atmosphere and increases towards the top. Therefore, this has to be accounted for as well within the calculation of X_1. In order to correct for this, the calculated vertical first interaction depth $X_1^{vert}(H_1)$ has been subtracted from the fixed value of the injection depth, $X_0^{vert}(H_0)$, corresponding to the injection height H_0 and set by the keyword *FIXCHI* within CORSIKA[6]. The corresponding formula is shown in Eq.4.2.

$$X_1 = \frac{X_0^{vert}(H_0) - X_1^{vert}(H_1)}{\cos\theta} \tag{4.2}$$

[6]This is equivalent with the reverse of the atmospheric profile for up-going induced air showers

By implementing this change, the atmospheric depth is properly calculated for up-going showers and the value of the first interaction depth is set accordingly, as it can be seen in Fig. 4.13(c) and 4.13(d). A second side effect of this correction, is the increase in the total amount of triggering events for both heights of first interactions. This is to be expected since as a result of this modification the values of X_1 are lower and therefore the shower profiles can be properly followed.

The second parameter that has been checked and needed additional corrections was X_{max}. Comparing the MC value and the one resulted from the Gaisser Hillas (GH) fit, a discrepancy between the two variables has been observed. The initial results are plotted in Fig. 4.14(a) and 4.14(b) together with the corresponding average value $< X_{max} >$. Since the studied showers have the same set of parameters, except their height of first interaction H_1, and looking at the two sets of values, it is clear the value of X_{max}^{GH} is calculated wrong. The reasoning here

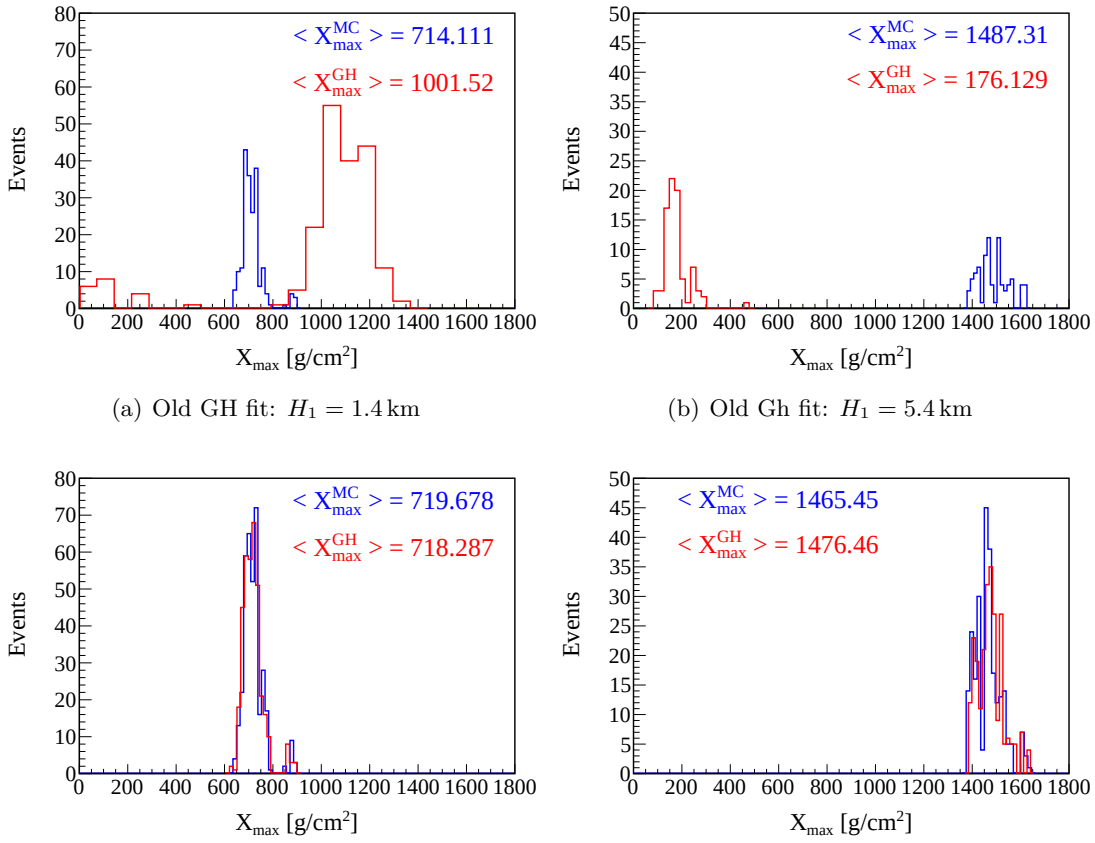

(a) Old GH fit: $H_1 = 1.4\,\text{km}$

(b) Old Gh fit: $H_1 = 5.4\,\text{km}$

(c) New GH fit: $H_1 = 1.4\,\text{km}$

(d) New GH fit: $H_1 = 5.4\,\text{km}$]

Figure 4.14: Distribution of triggered events in terms of maximum depth, X_{max}, as resulting from a simulation set of 500 proton induced air showers, with zenith angles $\theta \in [115°, 120°]$ and primary energy $\lg E_0/\text{eV} \in [18, 18.5]$. The MC (blue line) and the GH values (red line) of X_{max} are plotted and their mean is highlighted. Before the new fit procedure, the GH distributions shown in figures (a) and (b) show contradictory results. After the X_{max} correction from the new fit, the two distributions agree with each other (figures (c) and (d)) and the GH values of X_{max} have the proper values given the different values of H_1

is similar with the one from the X_1 case. Showers travelling upwards and starting at higher altitudes should reach the maximum energy deposit point, X_{max}, higher in the atmosphere.

Therefore, a higher value of X_{max} is expected in the case of showers starting deeper in the atmosphere. Since the MC variable X_{max}^{MC} is calculated based on the energy deposit profile, which has been corrected for the up-going induced AS case, the corresponding distributions provide the correct expected results. The GH parameters used within the Offline framework are directly read in from CORSIKA. However, as it has been discussed, in the case of up-going showers used with the VERTICAL option the atmosphere has to be reversed for a proper interpretation of the energy deposit profile. Since the fit is done automatically in CORSIKA, the solution was to re-calculate the corresponding parameters by re-fitting the profile (with the reversed atmosphere corresponding to up-going showers) with a Gaisser Hillas function and further use the resulted fit parameters.

The fitting procedure has been performed in two different steps. Since the GH parameters provided by CORSIKA and further used within Offline are N_{max}, X_{max}, X_0 and λ, the desired Gaisser Hillas function which needs to be fitted is the one defined in Eq. 2.10. However, working with the longitudinal profile and having direct access to the data in terms of the energy deposit per atmospheric depth, $dE/dX(X)$, an intermediate step had to be done. The fit has been first performed in terms of dE/dX.

$$\frac{dE}{dX}(X) = \left(\frac{dE}{dX}\right)_{max} \cdot \left(\frac{X - X_0}{X_{max} - X_0}\right)^{\frac{X_{max}-X_0}{\lambda}} \cdot \exp\left(\frac{X_{max} - X_0}{\lambda}\right) \tag{4.3}$$

The main parameters obtained from this fit are $\left(\frac{dE}{dX}\right)_{max}$, X_{max}, X_0 and λ. In order to obtain the value of N_{max}, the mean ionization loss rate α_{eff} is used, according to [87]:

$$N_{max} = \left(\frac{dE}{dX}\right)_{max} \cdot \frac{1}{\alpha_{eff}(X_{max})} \tag{4.4}$$

A more detailed description of the new fit procedure together with the parametrization of α_{eff} is given in Appendix B. The distribution of the triggering events resulted after the GH fit is shown in Fig.4.14(c) and 4.14(d).

No other investigated parameters indicated any problems in the context of up-going air showers within the current simulation configuration. Therefore, after the above mentioned corrections were implemented in the Offline framework, the simulation sets described in Section 4.3.3 have been successfully reproduced. Both the CORSIKA and the detector simulations have been uploaded on the local collaboration database.

4.3.5 Simulations of up-going τ-induced air showers: CORSIKA and TAUOLA

Having the proton and electron induced air shower simulations properly working and not knowing the origin of the primary particle in the context of the anomalous events, additional simulations of τ-induced air showers are required for a proper follow-up. As mentioned above, results for different heights of first interaction of the up-going induced AS are crucial, given the uncertainties of the shower starting point within the ANITA observations. Simulations of τ-lepton induced air showers are possible in CORSIKA, but the τ decay point can not be manually set. As a

result, the τ-leptons have their first interaction height H_1 set as discussed above, by using the keyword *FIXHEI*. However, as mentioned in the CORSIKA user guide [79], the first interaction of the unstable particles will not correspond to their decay. Since within the current study one is interested in investigating up-going showers with different first interaction heights, setting the τ-decay point at given altitudes is necessary for a consistent analysis.

In order to do so the τ-lepton decays have been simulated separately using TAUOLA [21] and further on the *STACKIN* option has been used within CORSIKA. This option allows the user to take advantage of an input file, containing the secondary particles that result from any of the previously studied interactions. These secondaries are further used as input parameters and the EAS initiated after their collision with the atmospheric nuclei are simulated accordingly. The first line within the input file contains the total number of secondaries and the energy of the primary particle. The following lines are dedicated to each secondary separately, comprising of information regarding the particles' ID, p_{ID}, their energy, E_0, and the three momenta components: p_x, p_y, p_z. Once this option is used, the secondaries are read from the file accordingly and the simulation of the air shower can be done as explained above. By setting different values of the height of first interaction via *FIXHEI* the decay height of the τ-leptons can be fixed as desired by using the corresponding decay daughters with their parameters.

The τ-decays have been simulated using TAUOLA [21]. Since the TAUOLA program is based on the HepMC event record format, each event comprises several vertices, with the *generation vertex* describing the main reaction to be studied. Each vertex represents a certain interaction within the event and is composed of *input: I* and *output: O* particles. The input particles represent the initiating particles of the reaction, while the output ones represent the resulted secondaries. In the case of decays the input particles represent the mothers and the output particles are the daughters resulted from the specific decay. The first step towards the τ-decay studies was to initiate the *generation vertex*. This has been done by generating a τ-lepton and considering it as both the input and the output part of the vertex, since the interest in the current study is only towards the decay products. All the τ-decay branches have been considered for the current study. Additionally, TAUOLA is giving information about all secondaries resulting from a τ-decay, including the intermediate mesons. However, within CORSIKA only the final secondaries are needed, therefore additional modifications were done in order to have the information regarding only the final state daughters. Finally, a conversion between the PDG id used for the particle identification in TAUOLA and the particle IDs in CORSIKA was implemented.

The simulation is initially done in the tau rest frame τ_{CM}, and the corresponding momenta and energy values of the secondaries are stored. These parameters are further boosted along the z-direction according to the desired tau energy, E_τ, and the corresponding energy and momenta of each secondary are calculated, accounting for the relativistic factors $\gamma = \frac{E_\tau}{m_\tau}$ and $\beta = \sqrt{1 - \frac{1}{\gamma^2}}$ in Eq. 4.5.

$$\begin{aligned} p_x &= p_x(\tau_{CM}) \\ p_y &= p_y(\tau_{CM}) \\ p_z &= \gamma \cdot [p_z(\tau_{CM}) + \beta E(\tau_{CM})] \\ E &= \gamma \cdot [E(\tau_{CM}) + \beta p_z(\tau_{CM})] \end{aligned} \tag{4.5}$$

Focusing on the same energy range as in the case of the proton and electron induced air showers described in Subsection 4.3.3, an energy range of $E_\tau \in [10^{17}, 10^{18.5}]$ eV has been investigated. τ-leptons with fixed energies in this range have been simulated for each 0.1 steps in $\lg \mathrm{E} \,/\, \mathrm{eV}$ and their decay products have been stored with the required information in an external file, which was further passed as an input in CORSIKA. Each event represents a τ-decay and has an individual file.

A number of 10.000 TAUOLA events have been simulated for each energy range of 0.5 $\lg \mathrm{E} \,/\, \mathrm{eV}$ corresponding to the simulation library. Further on 500 showers per energy bin have been randomly sampled and simulated in CORSIKA for each zenith and height of the first interaction, according to the simulation parameters enumerated in Subsection 4.3.3. The sampling procedure is repeated every time a new zenith and/or height range is considered.

As a result of the above described procedure, the simulation of up-going τ-lepton induced air showers with a fixed decay height is possible with CORSIKA. The resulted showers have been simulated together with the FD response. Similar to the procedure described in Subsection 4.3.3, the corresponding maximum distance between the shower core and the FD position, R_{FD} has been investigated. A maximum distance of $R_{FD} = 40$ km has been chosen. The trigger efficiency, considering the *eye centric* detector simulations, resulted from the simulation of 50.000 τ-induced air showers per zenith range per height of first interaction range is shown in Fig. 4.15. The results for the whole zenith range of interest, $\theta \in [115°, 130°]$, and different different heights of first interaction, H_1,[7] are plotted. The highest efficiency is obtained for the largest energy range and lowest decay height H_1. Showers starting higher in the atmosphere and having a high primary energy (red symbols in Fig. 4.15(b) and Fig. 4.15(c)) are able to trigger the FD from larger distances R_{FD}.

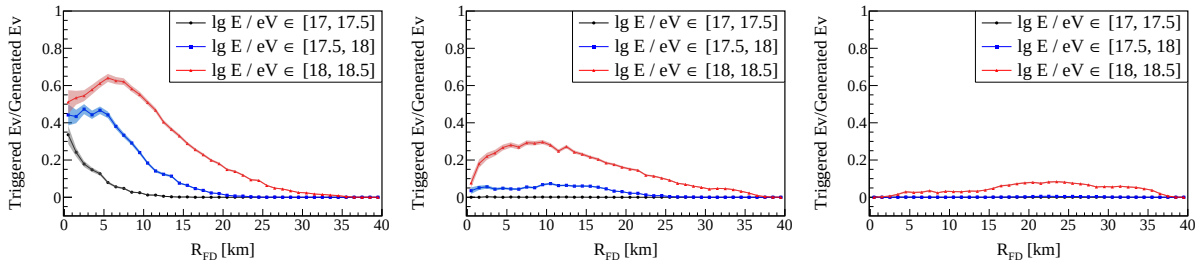

(a) $H_1 = 1.4$ km a.s.l (b) $H_1 = 3.4$ km a.s.l (c) $H_1 = 5.4$ km a.s.l

Figure 4.15: Triggering efficiency of the FD to up-going τ-induced air showers as resulting from 50.000 τ simulated AS per zenith bin, for the entire zenith range, $\theta \in [115°, 130°]$, of interest, for different primary energy ranges and decay heights, H_1, with respect to the distance between the shower core and the FD location, R_{FD}. The symbols represent the data points while the shaded areas represent the corresponding uncertainty bands

[7] From here on the decay height of the τ-leptons is referred to as the height of first interaction H_1

4.4 First FD exposure results to simulated up-going air showers

Having the simulation setup described above properly working, the exposure calculation to simulated up-going air showers has been possible. The results presented in this section are considering only the simulations described above, with no additional cuts being applied. This results in an over estimation of the exposure but it sets the grounds for the in-depth study described in Chapter 5. Furthermore, another approximation that has to be considered when analyzing the results within this section is the fact that the described simulations are *eye centric*. This means only the response of one eye has been simulated and further on the results have been extrapolated to the other 3 telescope buildings. Additionally, as no real MC data[8] has been used at this stage, the up-time fraction of the FD telescopes has been calculated separately using the internal database. A more detailed description regarding the up-time calculation can be found in Appendix C. This procedure itself gives a good approximation of the telescope duty cycle, but the real MC simulations provide the most up to date information regarding the detector configuration. The FD exposure has been calculated using the formula:

$$\mathcal{E}(E) = \mathcal{A}(E) \cdot t \tag{4.6}$$

where $\mathcal{A}(E)$ is the detector aperture and t represent the up-time of the FD.

$$\mathcal{A}(E) = \int_{\Omega} S_{eff}(E) \cos\theta d\Omega \tag{4.7}$$

with Ω the solid angle, θ the zenith angle and $S_{eff}(E)$ the effective area, defined as:

$$S_{eff}(E) = \int_{S_{gen}} \eta(E) dS \tag{4.8}$$

Substituting the value of $S_{eff}(E)$, Eq. 4.7 becomes:

$$\mathcal{A}(E) = \int_{S_{gen}} \eta(E) dS \int_{\theta} \cos\theta \sin\theta d\theta \int_{\phi} d\phi \tag{4.9}$$

where $\eta(E)$ represents the detection efficiency at a given energy and is calculated as the ratio between the triggering events with reconstructed energy[9] and the total number of generated events

$$\eta(E) = \frac{N_{rec}(E)}{N_{gen}(E)} \tag{4.10}$$

Since the simulated events are eye centric, with the shower cores being generated around the telescope location and isotropically thrown only in front of Coihueco (CO) telescope building, the generated area S_{gen} is equal to the area of a semi circle with radius r equal to the maximum chosen distance: $r = R_{FD}^{max}$. With the current configuration the results are missing any showers

[8] Real MC data comprises of information regarding the detector configuration during different time periods and can be directly accessed within the Offline [69] framework

[9] not all the triggering events used in the triggering efficiency plot (Fig. 4.15) have a reconstructed energy within the Offline simulation Framework. In order for an event to have a reconstructed energy it has to fulfill additional conditions besides the triggering one.

landing behind the telescopes. However this is accounted for in the general study.

$$S_{gen} = \frac{\pi r^2}{2} \tag{4.11}$$

The total FD exposure, considering all five telescope buildings, can be calculated as the sum of each telescope's exposure individually

$$\begin{aligned}\mathcal{E}_{FD}(E) &= \mathcal{E}_{CO} + \mathcal{E}_{LA} + \mathcal{E}_{LM}(E) + \mathcal{E}_{LL}(E) + \mathcal{E}_{HEAT}(E) \\ &= \mathcal{A}(E)_{CO} \cdot t_{up}(CO) + \mathcal{A}(E)_{LA} \cdot t_{up}(LA) + \mathcal{A}(E)_{LM} \cdot t_{up}(LM) \\ &+ \mathcal{A}(E)_{LL} \cdot t_{up}(LL) + \mathcal{A}(E)_{HEAT} \cdot t_{up}(HEAT)\end{aligned} \tag{4.12}$$

The individual values t_{up} represent the up-time fraction of the different telescope sites, related to the telescopes duty cycle and performance, and are calculated using the internal collaboration database. More details regarding the calculation of these fractions can be found in Appendix C. The time period of interest for the results presented in this section is spanning from 01.07.2007 up to 01.10.2019.

By extrapolating the results from one eye (CO), to the other three eyes, and using the individual results from HEAT, considering the equal FoV of the 4 telescope sites, the exposure can be calculated accordingly by assuming equal apertures of the 4 different eyes.

$$\begin{aligned}\mathcal{E}_{FD}(E) &= \mathcal{A}(E)_{CO} \cdot t_{up}(CO) + \mathcal{A}(E)_{CO} \cdot t_{up}(LA) + \mathcal{A}(E)_{CO} \cdot t_{up}(LM) \\ &+ \left[\, \mathcal{A}(E)_{CO} \cdot t_{up(FoV=180^\circ)}(LL) + 0.9 \cdot \mathcal{A}(E)_{CO} \cdot t_{up(FoV=162^\circ)}(LL) \,\right] \\ &+ \mathcal{A}(E)_{HEAT} \cdot t_{up}(HEAT)\end{aligned} \tag{4.13}$$

where the two separate terms for LL come from dismantling one of the outer LL telescopes, which reduces its FoV at 162° after 14.07.2009.

The corresponding exposure for τ-lepton induced air showers with zenith angles $\theta \in [115^\circ, 130^\circ]$ and primary energies $\lg E \,/\, \mathrm{eV} \in [17, 18.5]$ are plotted in Fig. 4.16.

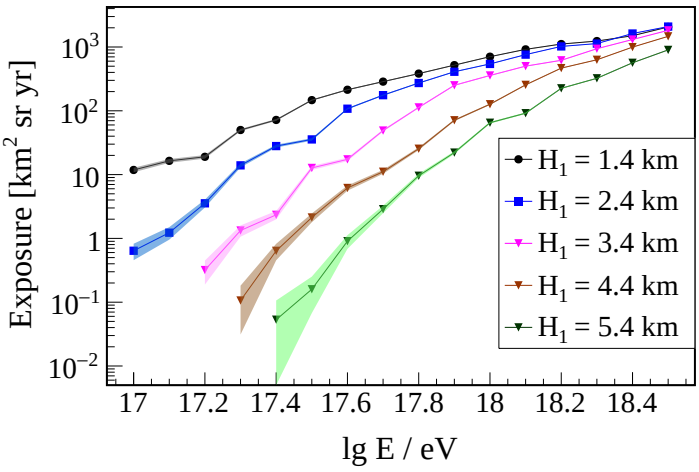

Figure 4.16: FD exposure to up-going τ-induced air showers for different τ-decay heights H_1, with a zenith range $\theta \in [115^\circ, 130^\circ]$ and primary energies $\lg E \,/\, \mathrm{eV} \in [17, 18.5]$. The plotted results are obtained under the assumptions mentioned in this section, with the τ simulations described in Section 4.3.5.

It is important to mention that the given results do not consider the τ propagation inside Earth. As described in section 4.3.5, the simulated τs are forcefully decayed at different heights without considering any previous interactions. A complete study of the up-going τ induced air showers represents one of the main contributions within this thesis and is described in detail in Chapter 6. Furthermore, the presented results do not include any event selection, the only requirement being the simulated events must have their energy reconstructed within the FD simulations.

The preliminary τ-exposure results plotted in Fig. 4.16 confirm the correctness of the simulation procedure of up-going air showers. The exposure values increase with increasing primary energy, as is physically expected. Furthermore, the maximum exposure is obtained for the lowest heights of the shower's first interaction. Leptons decaying high in the atmosphere only contribute to the exposure once the primary energy is high enough: for the maximum value of the investigated decay height, $H_1 = 5.4$ km a.s.l. (green symbols in Fig. 4.16), the events only contribute to the FD exposure once the primary τ-energy is $\lg E / \text{eV} \geq 17.4$. An additional study in terms of exposure has been done in order to cross check the effects of events triggering in the very vicinity of the FD (i.e. small values of R_{FD}). This was mainly triggered by the very

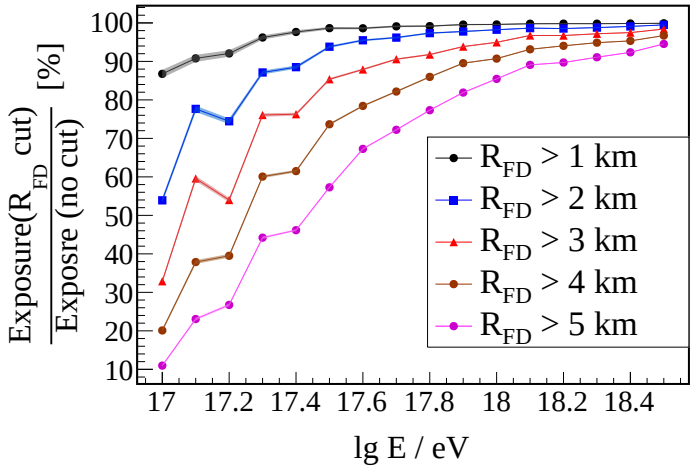

Figure 4.17: Percentage of the total FD exposure after the exclusion of events triggering in the very vicinity of the telescope building as a function of the primary energy, for different cut values of R_{FD}.

first investigation of a *burn data sample*[10], where the only events surviving the implemented cuts at that time were appearing very close to the fluorescence detector. As a result, a cut in terms of R_{FD} has been implemented and the results for up-going τ induced air showers with a decay height of $H_1 = 1.4\,\text{km}$ a.s.l have been plotted in Fig. 4.17 for different cut values. High energy induced air showers are the least affected in terms of exposure. This is physically understood since the very low energetic events need to be in the proximity of the detector in order to be observed and properly reconstructed. This result can also be seen in Fig. 4.15(a), where the lowest energy range exhibits a triggering peak at very low values of R_{FD}.

The preliminary exposure results have been calculated for all simulated primaries:

[10]The definition of the burn data sample as well as the main results regarding the laser rejection and final cuts are detailed in Chapter 5

electrons, protons and taus for a first comparison. Figure 4.18 shows the FD exposure for up-going air showers induced by different primaries at a height of first interaction $H_1 = 1.4\,\mathrm{km}$ a.s.l, a primary energy range of $\lg E\,/\,\mathrm{eV} \in [17.5, 18]$ and a zenith range of $\theta \in [115°, 120°]$.

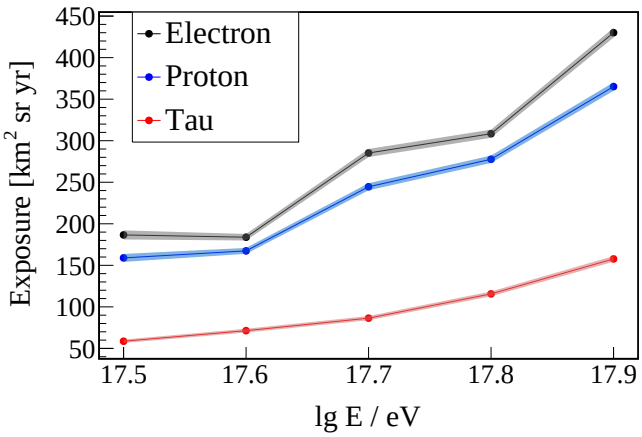

Figure 4.18: Preliminary FD exposure results to up-going induced air showers for a zenith range $\theta \in [115°, 120°]$ and primary energy $\lg E\,/\,\mathrm{eV} \in [17.5, 18]$ as resulting from a small signal simulation set without applying any additional cuts. The exposure is calculated without real MC simulations, as explained within the current chapter.

Starting from these results, it has been decided that, in order to speed up the signal simulations, and taking into account the unknown origin of the primary particles initiating the ANITA anomalous events, the follow up can be performed using only one species as a primary. By presenting the final results in terms of shower deposited energy and height of first interaction of the initiating particles, the FD exposure will be similar at a given value of the calorimetric energy for different primaries. Further on, one can consider the propagation process of a given primary in order to calculate the exposure in terms of the particle energy, starting from the value of the shower energy. This has been done within this thesis for the case of up-going τ-induced air showers and is presented in detail in Chapter 6.

These simplified results represent the very first confirmation of the ability of the FD of the Pierre Auger Observatory to observe steeply up-going induced air showers. Since the above presented studies have been mainly focused on the simulation procedure and implementation of all the necessary updates in the steeply up-going showers context, a dedicated study towards such events is required. This research has been performed within the Pierre Auger collaboration and represents one of the main contribution within this thesis.

5

Search of Steeply Up-going Air Showers with the FD of the Pierre Auger Observatory

The anomalous steeply up-going cosmic ray like events observed by the ANITA collaboration [15] are in strong disagreement with the Standard Model (SM) physics and remain unexplained. Therefore, a dedicated search for such showers which could either confirm or refute the occurrence of the intriguing events represents a major point of interest in the scientific community. The Fluorescence Detector (FD) of the Pierre Auger Observatory is a good candidate for observing such phenomena, having a wide Field of View (FoV) and substantial operation time. A generic search for up-going cosmic ray like induced air showers has been performed within the collaboration and represents one of the main contributions within this thesis. Preliminary calculations suggest the resulted FD exposure exceeds the one of ANITA[1] by a factor of at least 10, emphasizing the importance of the current study. Given its complexity, the search has been done using the common effort of several people in the collaboration. A generic overview of the procedure is given within this chapter, with the accent on the signal simulations, which represent the personal contribution within the working group.

The obtained results are of a major importance to the scientific community. With one event observed, consistent with the expected background of 0.45 ± 0.18, within the ≈ 14.3 years of available FD data, upper flux limits have been set on up-going cosmic ray - like particles with corresponding shower energies $\lg E_{sh} \,/\, \mathrm{eV} \in [16.5, 18.5)$ and zenith angles $\theta \in [110^\circ, 180^\circ]$, interacting at heights of maximum 9 km above the detector level. Besides giving the first stringent upper flux limits on such anomalous events, the current study also provides the exposure results in a double differential form, in terms of shower energy, E_{sh}, and height of first interaction, H_1. This approach of presenting the results is extremely important for the academic community and represents a pillar towards testing different physical scenarios regarding the origin of such events. An example application on up-going τ-induced air showers has been investigated, and the corresponding exposure and upper flux limits have been obtained, using the double differential exposure results. This study represents a personal contribution and is discussed in detail in chapter 6.

5.1 Signal simulations

One of the main steps towards any dedicated search is represented by the signal simulations. As mentioned in the previous chapter, the simulation procedure comprises two parts, the initiating of the air showers and their development within the atmosphere, and the simulation of the

[1] Not having access to the ANITA collaboration exposure data, one can only try to estimate their exposure via dedicated studies. However, the real numbers may differ from the estimated ones.

detector response. The first exposure results obtained from the preliminary simulations stage have been presented in section 4.4. However, in order to have significant results that are able to give some insight in the context of the anomalous events, massive simulation sets are needed. One of the main constraining parameters in this regard is the computing time. Therefore, even if CORSIKA [79] represents one of the most reliable extensive air shower simulation codes, it has been decided that CONEX [54] is a more suitable option for the current study [2]. CONEX is a simulation code describing the EAS development in the atmosphere, by combining the MC method, used in CORSIKA, with the numerical calculation of the cascade equations. The most energetic part of the shower is obtained via MC simulations, while the low energy sub-cascades are treated numerically. This approach is offering a tremendous decrease in the computation time, allowing for a significant increase of the necessary simulations on a shorter time scale. The limitations in the CONEX simulation code are related to the lateral distribution of the particles: since the numerical calculations are performed only along the shower axis, only the longitudinal profile of the shower is recorded. As the FD is the only detection instrument used within the current study, these constraints do not influence the final results, as the shower development in the atmosphere represents the main quantity of interest. Moreover, the compatibility of the results between the two simulation codes has been cross checked. An exemplary plot showing the agreement of the results is shown in Appendix D.1. Once the simulation code has been decided on, the simulation parameters have been chosen in order to properly cover the characteristics of the anomalous events.

5.1.1 Simulation parameters

As it has been mentioned in the previous chapter, it was soon decided to proceed with the simulation of only one primary particle type. Given the unknown nature of the primary particle in the anomalous events context, the most suitable presentation of the exposure results is in terms of shower energy, rather than the primary energy. Since the shower to shower fluctuations are mainly related to the first interaction, which is fixed within the simulation procedure, the triggering efficiency of showers initiated by protons, nuclei or electrons having the same first interaction point, zenith and azimuth angle, will be the same on average for a fixed value of the energy deposit in the atmosphere, given the shower universality [87]. In the case of unstable or more exotic particles, the propagation process and decay branches have to be considered and further accounted for. See chapter 6 for a dedicated study towards up-going τ-induced air showers using the double differential exposure results.

Up-going proton induced air showers have been simulated using CONEX and further on the detector response has been simulated using the internal Offline framework. The investigated data ranges from 01.01.2004 up to 31.12.2018, and the obtained results are accounting for all five telescope buildings existent within the observatory. The shower parameters are set within CONEX, while the core randomization, first interaction point and detector configuration have been set within Offline, where the real MC parameters, regarding the FD configuration, are also used. The main simulation parameters are listed in Table 5.1. 250.000 events have been

[2] The above presented simulations using CORSIKA for the up-going induced air showers remain the pioneering step. All the corrections implemented and explained in Chapter 4 are extremely useful as they allow for future studies of up-going induced air showers with fixed or variable heights of first interaction

simulated for each energy bin, resulting in a total number of $2 \cdot 10^6$ events per simulation set. A total number of $1.6 \cdot 10^7$ up-going induced air showers with zenith angles of $\theta \in [110°, 180°]$, primary energies $\lg E \in \mathrm{eV}[16.5, 18.5]$ and heights of first interaction $H_1 \leq 9\,\mathrm{km}$ above the core have been generated as a desired simulated signal.

CONEX Parameters	Values	Reasoning
Version	Conex 7.3 (r7454)	Modified for up-going events
Model	Sibyll, URQmD	Fast
ECuts	Standard	Don't affect dE/dX
Primaries	Proton	dE/dX ∼ universal vs E_{Cal}
H_{core}	1.4 km	Altitude of the surface detector
Energy Range	$[10^{16.5}\,\mathrm{eV}, 10^{18.5}\,\mathrm{eV}]$	Covers the energy range of ANITA events
Energy Sampling	flat 0.25 lg(E/eV) steps	Easy to re-weight to any given spectra
Zenith Range	110° to 180°	ANITA events are steeply up-going
Azimuth Range	0° to 360°	covers the whole azimuth range
Offline Parameters		
Version	trunk (r33623+)	Includes rand dist., ADST variables
Core Randomization	100 × 100 km^2 center on SD825	100×100 (from SD825) includes 20 km behind Eyes
Zenith Randomization	Flat in $\cos^2\theta$	Exposure calculated via core tile area 5.1.2
First Interaction	**Flat distance from core**	Easy for further decay models study
Height Range	Up to 9 km over H_{core}	No significant FD sensitivity for larger heights
RealMC Parameters		
FD sites	LL, LM, LA, CO, HE	All FDs are used in the study
Date Range	01.01.04 to 31.12.18	Date range of FDUptime/DBs

Table 5.1: Main parameters used in the signal simulations

The choice of CONEX version is motivated by an additional update implemented in the code towards up-going induced air showers[3]. The energy and zenith angles have been chosen in order to cover all possible ranges of the anomalous events. The minimum investigated zenith angle is $\theta_{min} = 110°$. Lower zenith ranges have not been investigated, mainly because the ANITA events are steeply up-going ($\theta_1 \approx 117.4°$ and $\theta_1 \approx 125°$). The second reason for choosing this minimum value is mainly related to the simulation procedure. For more horizontal angles the curved atmosphere option has to be considered, resulting in a slightly different signal simulation procedure. The more inclined zenith angles are however out of the scope of the current search. The altitude of the shower core position has been set to $H_{core} = 1.4\,\mathrm{km}$ a.s.l, corresponding to the altitude of the observatory. From here on all of the heights are given with respect to H_{core} rather than the sea level (i.e. H = 1 km corresponds to H = 2.4 km a.s.l.). The position of the shower core is randomly chosen within the Offline framework from an area of $100 \times 100\,\mathrm{km}^2$ centered on the surface detector station SD825. This station is placed in the middle of the array. 50 km away from this station is covering 20 km behind each of the telescope sites, ensuring the observation of any event landing behind the eyes. Simulations were performed for different heights of first interaction, up to a maximum height $H_1 = 9\,\mathrm{km}$ above the core level. The main

[3]The calculation of a random zenith angle within a given range in previous versions was only implemented for down-going showers: $\theta \leq 90°$. Since the calculation is based on the cosine of the angle and for up-going showers $\theta > 90° \rightarrow \cos\theta < 0$, an additional condition has been added for the case of up-going showers. As a result the zenith is correctly sampled in the up-going case

procedure regarding the events generation is described in more details below.

5.1.2 Events generation geometry

As mentioned above, the shower core is randomly generated in an area of $100 \times 100\,\mathrm{km}^2$ centered on SD825. By generating an isotropic flux, $dN/d\Omega$ is constant, which results in a flat distribution of the events with respect to the cosine of the zenith angle: $dN \propto \sin\theta d\theta \rightarrow dN \propto \cos\theta$. Since the shower core is constrained to the flat surface, in order to have an isotropic flux of the generated events on this surface, a correction for the projection at ground is needed. As a result, the showers need to be generated with a flat distribution in $\cos^2\theta$.

$$dN \propto \cos\theta \sin\theta d\theta \rightarrow dN \propto \cos^2\theta \tag{5.1}$$

The last parameter to be set regarding the events generation geometry is represented by the height of first interaction of the up-going showers. As this is an unknown parameter within the anomalous events context, studying the sensitivity and exposure for different values of H_1 is necessary in order to provide a complete study of this kind of events. Therefore, the events have been simulated at various values of the height of first interaction. Since the height of first interaction is strongly connected to the zenith angle and the distance of first interaction, a flat randomization of the distance of first interaction has been chosen for the events generation. This is the distance between the shower core position and the first interaction point, as it has been sketched in Fig. 5.1.

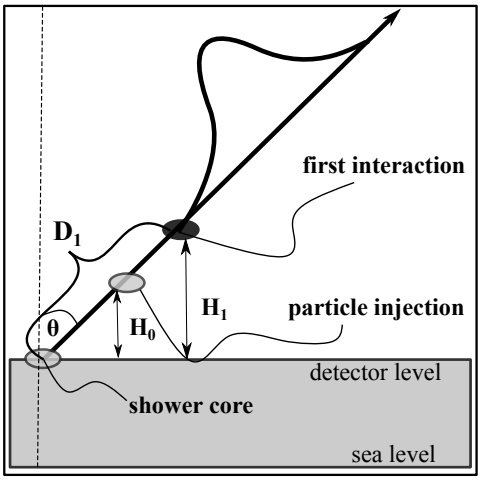

Figure 5.1: Illustrative view of the shower geometry. Events are simulated flat in distance to the first interaction, D_1 and flat in $\cos^2\theta$

Since for heights $H_1 \geq 9\,\mathrm{km}$ the FD sensitivity is negligible, this has been set as the maximum investigated value of the first interaction height. In order to avoid simulating showers with higher H_1, the flat distance generation procedure is divided into two steps. First the height of the first interaction is generated using a flat distribution with $H_1 \in [0, 9]\,\mathrm{km}$. Then the corresponding distance along the shower axis is calculated.

$$D_1 = \frac{H_1}{\cos\theta} \tag{5.2}$$

Using the equalities in Eq. 5.1 and 5.2, it is observed that the event generation with a flat $\cos^2\theta$ zenith sampling and a flat distribution of the first interaction distance, up to a maximum value of $D_1^{max} = H_1^{max}/\cos\theta_{min}$, will be equivalent to the simulation of events flat in height with a $\cos\theta$ zenith sampling, since $D_1\cos\theta\sin\theta d\theta = H_1\sin\theta d\theta = H_1\cos\theta$. In order to insure the correctness of this statement a cross check exercise has been performed and is described in appendix D.2. As explained in the appendix, in order to maximize the simulation efficiency, the events are generated with a flat first interaction height H_1 distribution and a $\cos\theta$ zenith sampling.

The main advantage of simulating the events flat in distance to the first interaction D_1 is having a data set flatly populated with air showers at all heights and distances from the core. This is extremely important as it offers the possibility of searching for more exotic particles which could initiate the showers, as it is desired given the tension between the anomalous events and the SM. Such a study can be done for any BSM particle by considering its propagation and decay products. As an example application, the obtained exposure results, presented Fig. 5.5, have been further used in order to get the exposure results in the context of up-going τ-induced air showers in chapter 6. Moreover, both the point of first interaction as well as the injection point are written in the ADSTs, resulting in the possibility of re-weighting the events to any primary scenario. An exercise showing the possibility of re-weighting the event distribution from being flat in distance to first interaction D_1, to being flat in distance to the injection point D_0, has been performed and is detailed in Appendix D.3.

5.1.3 Geometry implementation in the simulation framework - Offline

Since the current research of steeply up-going air showers with the FD is unique and represents a pioneer within the collaboration, several new utilities had to be implemented within the internal simulation framework, Offline. Some of these have already been mentioned in sections 4.3.2 and 4.3.4. Further specific modifications were applied in order to properly simulate the desired geometry detailed in the previous section. As mentioned above, the main shower parameters (zenith and azimuth angle, primary energy, and the ground level H_{core}) are set within CONEX. However, as the current study aims at investigating the exposure results for different first interaction heights H_1, this had to be implemented within the Offline framework. The goal was achieved by shifting the resulted longitudinal profiles from CONEX, which are calculated for a fixed injection height at ground, corresponding to the altitude of the observatory $H_{core} \approx 1.4\,\text{km}$ a.s.l. For any such shower, CONEX is used to calculate and provide the height and depth of the first interaction: H_1^{CONEX}, X_1^{CONEX}. In order to shift the profiles along the shower axis, a random value of the distance of first interaction, D_1 is chosen: $D_1 \in [0, D_1^{max}]$ where $D_1^{max} = H_1^{max}/\cos\theta$. The maximum value of the height of first interaction is set, as discussed above, to $H_1^{max} = 9\,\text{km}$. The option of setting the value of the first interaction distance within a given range did not exist in Offline and was implemented as part of this thesis. All of the updates have been submitted to the collaboration repository and are currently part of the collaboration software. A schematic representation of the profile shifting is shown in Fig. 5.2.

Once the desired value of D_1 is chosen, the shower profile as resulted from CONEX is used. The shifting is done by making the profile start at the new first interaction depth, X_1,

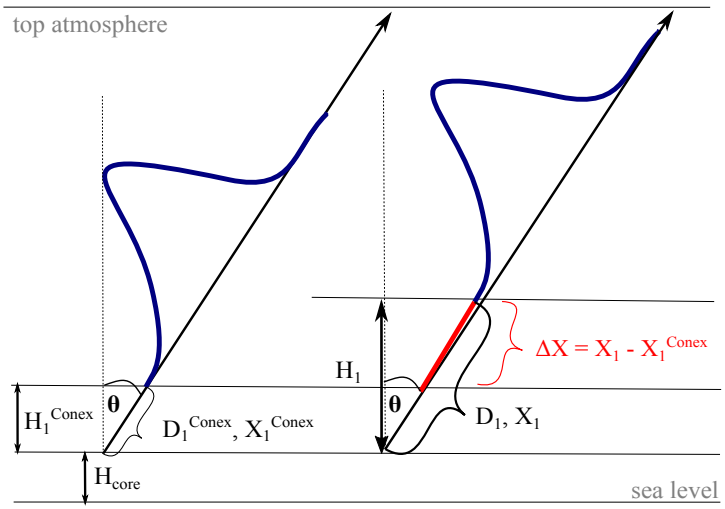

Figure 5.2: Illustrative view of the shower geometry. Events are simulated flat in distance to the first interaction, D_1 and flat in $\cos^2\theta$

which is the slant depth corresponding to D_1. In order to do so, the shifting region marked with red in Fig. 5.2 and defined by $\Delta X = X_1 - X_1^{Conex}$ is filled with zeros in terms of energy deposited by the shower. As a result, the longitudinal profile will start at the desired distance D_1 and will be followed up to the top of the atmosphere.

Once this procedure has been implemented in the Offline framework, the signal simulations with the desired parameters and geometries described above have been possible. Additionally, within the current study, there was a need of accessing several parameters via the output ADST file. As some of the parameters of interest were not accessible within the ADST, with a special interest on the first interaction, respectively, injection heights and depths, H_1, H_0, X_1, X_0, retrieving them and providing an easy access within the output root file was also achieved within the same stage. Having the information regarding the desired quantities, a study towards reweighting the simulated events to a corresponding distribution flat in distance to the particle injection point D_0, rather than the existent flat distribution in distance to first interaction D_1, has been performed. Such a study is useful for testing different exotic model hypothesis and it is presented in details in Appendix D.3.

Besides the signal simulations, a good knowledge of the background is required for a proper exposure estimation in the context of the up-going induced air showers search. This has been studied within the working group, and is described shortly in the next section.

5.2 Background studies

For a good estimation of the detector sensitivity to a specific type of events, the existing background has to be well understood and accounted for. Two main sources can be identified in the context of the up-going search using the FD of the Pierre Auger Observatory. The first one is represented by *natural* factors, coming from the existence of down-going showers with specific geometries which can be missreconstructed within the FD, as explained in subsection 5.2.1. The second background component arises from artificial events related to atmospheric monitoring, which is performed using different lasers within the observatory and is described in

subsection 5.2.2. After dedicated background simulations and laser cleaning methods have been performed, a common reconstruction procedure has been chosen and applied to both the background and signal simulations for a proper candidate selection strategy.

5.2.1 Background simulations

Once the main background sources have been identified, a detailed simulation procedure of such signatures had to be implemented in order to study the detector response to such events. Eventually, specific cuts have to be applied for an optimum differentiation between signal and background. Since this study doesn't represent a personal contribution within the common effort, only the main procedure of the background simulations is described below for consistency.

Within the up-going induced air showers search, the main background source consists of down-going events with specific geometries. Since only the FD-data is used within the signal investigations, as mentioned in the previous sections, no SD data is used for this analysis. As a result, the core position of such events is not known or constrained by the SD information. An example of such an event with the given geometry is shown in Fig. 5.3. A down-going air shower landing behind the telescope site will be missreconstructed as an up-going one.

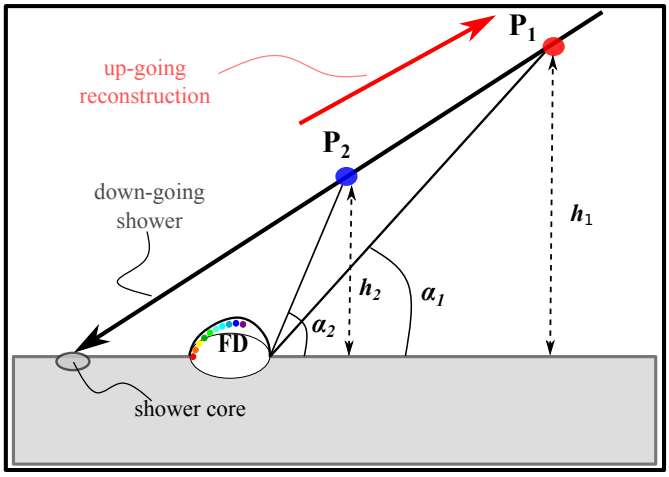

Figure 5.3: Schematic view of a down-going shower being missreconstructed as an up-going event by the FD. Since the shower is landing behind the telescope, for two points P_1 and P_2 on the shower axis, $h_1 > h_2$ and $\alpha_1 < \alpha_2$, resulting in an up-going signature: the signal coming from P_2 is recorded before the one coming from P_1

Since the impact point of the shower is located behind the telescope, by choosing two random points on the shower axis, P_1 and P_2, the following relations between their heights and angles hold: $h_1 > h_2$ and $\alpha_1 < \alpha_2$. As a result, in the telescope CS, the signal emitted from the position of P_2 will reach the camera before the signal coming from P_1. Consequently, the reconstructed event will have an up-going signature within the Eye coordinate system.

Moreover, besides the example mentioned above, there are several other geometries which can result in either a missreconstruction of the event direction or could be reconstructed simultaneously as both up and down-going. Most of the respective showers are either very horizontal or have their core located at extremely large distances away from the FD telescope. Additionally, an extensive air shower doesn't need to reach the ground in order to be detected by the FD. As a result, the background simulations were performed by generating the events' core

position within a sphere around the observatory. A radius of $R_{sphere} = 90\,\text{km}$ has been chosen after several dedicated studies have been performed [88, 89]. A sketch of the generation sphere together with additional information and the energy dependent parametrization are given in Appendix E.

In order to properly describe the background, down-going events have been simulated with zenith angles $\theta \in [0°, 90°]$ and primary energies of $\lg E\,/\,\text{eV} \in [17, 20]$, having their core position randomly sampled within a sphere around the FD. The primary initiating particles studied within the background context are protons, Helium, Nitrogen and Iron [89]. The high and low energy hadronic interaction models are the same as used for the signal simulations. The background simulations are extremely important in the generic study, as they represent one of the main parameters used for defining the event selection criteria for discriminating between false positives and real up-going signals.

5.2.2 Laser cleaning

Besides the above described background events, consisting of down-going showers with specific geometries and missreconstructed with an upward direction, another dominant background component in the up-going searches context is represented by laser shots. As described in Section 3.3, a continuous monitoring of the atmosphere is needed for a proper interpretation of the FD data. This is achieved by using dedicated laser shots, fired from different positions within the Observatory during the data acquisition. As these laser shots are in the upward direction, numerous up-going laser events are present in the data, representing a background source for the current study. In order to identify and reject those events that were not properly vetoed during data taking, a burn data sample constituting of 10% of the total amount of data has been used. A number of $\approx$ 300.000 events from this sample have been identified as up-going [4]. Based on the atmospheric conditions, event time windows (the shooting frequency of the lasers is well-known), as well as on the known location of the lasers, many of these events can be identified and further on rejected. These cuts are applied gradually, resulting in a rejection of more than 50% of the up-going showers present in the burn sample. More information about this procedure can be found in [90]. This procedure has a very generic character and it is not constrained to the current study, focusing on the lasers rejection only.

In order to reject as much as possible from the remaining sample of $\approx$ 60.000 up-going like events in the burn data sample, additional quality cuts have to be implemented. This is only possible via a combined quality selection of background and signal simulations, as it is constrained by the study of interest.

5.3 Events selection procedure

Having the signal and background simulation techniques set, a common procedure regarding the selection of possible event candidates has been implemented. In order to do so, a common simulation technique regarding the event reconstruction has been agreed on. Four different FD reconstruction methods have been used in this regard. Further on, additional selection cuts

[4] The first selection step is only concerning the zenith angle: $\theta > 90°$

have been applied to the burn data sample, based on the reconstruction techniques. The final candidate selection is then performed and the exposure is calculated accordingly.

5.3.1 FD geometry reconstruction strategy

Both the signal events described in section 5.1 and the background events described in section 5.2.1 are first simulated using their individual MC parameters, as well as information regarding the main FD features, including electronics, calibration, triggering, etc. The resulting data is further saved into a root file and used as an input for the different reconstruction techniques enumerated below:

1. **MC reconstruction**: simulates the FD response using the fixed MC axis and geometry

2. **Monocular reconstruction**: this is the standard FD reconstruction procedure described in section 3.4

3. **PCGF - up reconstruction**: the Profile Constrained Geometry Fit (PCGF) is based on the scan in the χ_0 variable. χ_0 represents the angle between the shower axis and the detector plane and is sketched in Fig. 3.9. By definition, the values of this angle determine the shower direction. For the upward mode, $180° < \chi_0 < 360°$. Once the shower detector plane and shower axis are found, as explained in section 3.4, the longitudinal profile in terms of energy deposit and its Gaisser-Hillas fit, together with the pixels timing geometries are evaluated. Compared to the monocular reconstruction, the PCGF reconstruction approach is requiring that the resulting energy deposit for a specific geometry (R_p and T_0 calculated using Eq. 3.2) is compatible with its GH function fit. For a fixed value of χ_0 the corresponding GH profile is calculated and further compared to the measured light flux inside the telescope. As a result, the likelihood for a fixed χ_0 geometry is evaluated and the most probable geometry is found. More details about the PCGF reconstruction method can be found in [91].

4. **PCGF - down reconstruction**: the PCGF - down technique works in the same way as the PCGF - up method, with the requirement that it is only restricted to down-going showers: $0° < \chi_0 < 180°$.

The profile constrained geometry fit (PCGF) reconstruction method is very important for the selection of event candidates.

5.3.2 Candidate events

All signal and background simulated events, as well as the FD data surviving the laser cleaning, are reconstructed using both the PCGF-up and PCGF-down methods. As a result, each shower is reconstructed with both down-going and up-going corresponding geometries and the favored one is evaluated. As mentioned above, the PCGF reconstruction results into a corresponding likelihood for a given χ_0. Events having a higher up-going likelihood, $L_{up} > L_{down}$, are more likely to be traveling upwards, making the discrimination between up and down-going extensive air showers possible. Therefore, a universal variable in terms of the two resulting likelihoods,

L_{down} and L_{up}, can be defined and is further used for a proper discrimination between background and signal events. This is equivalent with having a null-hypothesis in which events are considered to be down-going: $L_0 = L_{down}$ with the alternative hypothesis where the events are up-going: $L_{up,down} = \max(L_{up,down})$. A log-likelihood method is used by defining the l variable: $l \in [0, 1]$ so that a value of $l = 0$ corresponds to a down-going air shower, with an increasing probability of the event to be up-going as l approaches the maximum value of 1.

$$l = \frac{\arctan\left(-2\lg(L_{down}/L_{up,down})/50\right)}{\pi/2} \tag{5.3}$$

with $L_{up,down} = \max(L_{up,down})$ represents the corresponding maximum likelihood of the studied event. When the down-going geometry is favored, $L_{up,down} = \max(L_{up,down}) = L_{down}$ and $l = 0$. The higher the value of L_{up}, the more an upward-going geometry is preferred, with $L_{up,down} = \max(L_{up,down}) = L_{up}$ and the discriminating l-variable defined in Eq. 5.3 approaching the value of 1.

Besides the zenith $\theta \in [110°, 180°]$ and energy $\lg E_{min} / \text{eV} = 16.5$ intervals of interest in the current study, additional selection cuts based on the PCGF reconstruction method are applied to the burn data sample in order to clean as much as possible of the remaining events after the laser cleaning. A list containing all the cuts applied to the burn data can be found at [89]. It is important to mention that no profile-based cut has been applied, allowing for the general procedure to be used for any kind of exotic particles induced air showers searches.

The described procedure is then applied to all of the events of interest, including signal, background and cleaned data, as resulted from the 10% burn data sample, and the resulting events distribution with respect to the discriminating l-variable, as plotted in Fig. 5.4, is obtained. As can be seen, the background simulations (red symbols) are in good agreement with the remaining data in the burn data sample (black symbols). Moreover, the distribution of the signal events (green symbols) has a clear different signature from the background distributions, with an almost flat behavior with respect to l.

As mentioned above, events with higher l-variable values are more likely to be up-going. In order to select the genuine up-going events a cut-value on l has to be set. This has been done by fitting the background events distribution (red symbols in Fig. 5.4) with and exponential function and calculating the corresponding integral upper limit for a $CL = 95\%$, obtained if no candidates are observed after unblinding, for any given value of l. The chosen cut value corresponds to the minimum upper integral limit obtained and has the value of $l = 0.55$. A more detailed description of this procedure as well as representative plots can be found in [92].

Once the cut value of $l = 0.55$ has been defined, a clear discrimination between candidate and background events can be performed. Using this value, the expected number of background events can be calculated[5]:

$$n_{bkg} = 0.45 \pm 0.18 \tag{5.4}$$

As a result, the unblinding of the entire data set has been performed and the final results have been calculated.

[5]The number of background events can be obtained from the background fit function at a value of $l = 0.55$

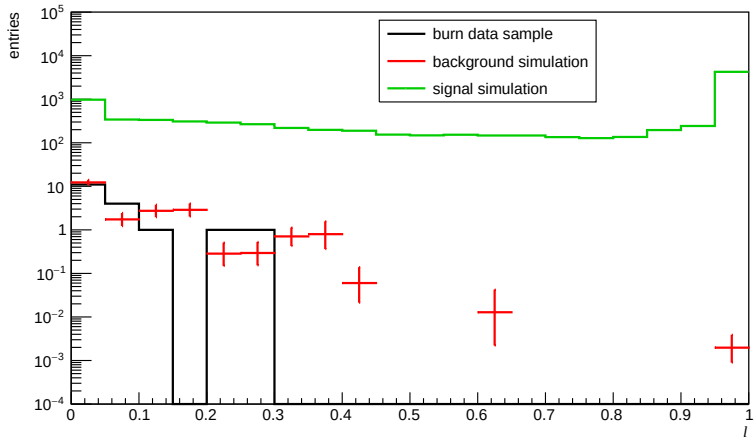

Figure 5.4: Distribution of signal (green symbols), background (red symbols) and cleaned burn data sample (black symbols) events in terms of the l discriminating variable. The background simulations are following the cosmic rays energy spectrum [93]. Since the burn data sample represents only 10% of the total events, the background has been waited accordingly for a better comparison. The signal events are not weighted to the 10% sample and therefore represent the total number corresponding to a 100% data time. Figure taken from [92].

5.4 Results

Having the signal and background simulations set and the burn data sample properly cleaned, and having set the final selection criteria ($l > 0.55$), the unblinding of the entire ≈ 14.3 years data set (01.09.2004 - 31.12.2018) has been performed. One event candidate $n_{cand} = 1$ has been found as the result of the unblinding, passing all the selection criteria discussed above. This number is compatible with the expected background $n_{bkg} \approx 0.5$ in Eq. 5.4 [6]. As a result, after calculating the corresponding exposure resulted from the signal simulations passing the selection criteria, upper limits have been set on the flux of up-going cosmic ray - like particles with shower energies $\lg E\,/\,\mathrm{eV} \in [16.5, 18.5]$ and zenith angles $\theta \in [110°, 180°]$, having their first interaction at heights up to 9 km.

5.4.1 Exposure

Once the final cuts are applied, the exposure calculation regarding the signal simulated events passing the $l > 0.55$ cut has been performed. As mentioned above, it has been decided to provide the FD exposure to up-going induced air showers in terms of shower energy, given the unknown nature of the primary particle initiating the anomalous ANITA events. Furthermore, since the resulting exposure depends on the shower's first interaction point, a double differential approach is chosen. Consequently, the exposure results are presented in a two dimensional form, in terms of shower energy, E_{sh}, and height of first interaction H_1. Similarly to the procedure described in section 4.4, the energy dependent exposure is defined as:

$$\mathcal{E}(E_{sh}) = \mathcal{A}(E_{sh}) \cdot \Delta T \tag{5.5}$$

[6] The candidate event has all the features expected for background EAS events

where $\mathcal{A}(E_{sh})$ is the fluorescence detector aperture at a specific shower energy E_{sh} and ΔT represent the FD operating time: $\Delta T \approx 14.3\,\mathrm{yr}$. In order to ensure a proper result regarding the FD up-time, a time dependent detector simulation [94], accounting for the FD configuration at a given time has been used. The FD aperture is further defined as:

$$\mathcal{A}(E_{sh}) = \int_{\Omega} S_{eff}(E_{sh}, \theta)\, \cos\theta\, d\Omega \tag{5.6}$$

where Ω is the solid angle, θ is the zenith angle and $S_{eff}(E_{sh}, \theta)$ is the effective FD area for the given shower energy and zenith angle:

$$S_{eff}(E_{sh}, \theta) = \int_{S_{gen}} \eta(E_{sh}, \theta) \tag{5.7}$$

S_{gen} represents the generation area. It is the $100\,\mathrm{km} \times 100\,\mathrm{km}$ area at ground where the simulated shower cores have been randomly thrown as described in section 5.1. $\eta(E_{sh}, \theta)$ represents the detection efficiency in terms of events passing the selection criteria, $n_{selected}(E_{sh}, \theta)$ and is defined as:

$$\eta(E_{sh}, \theta) = \frac{n_{selected}(E_{sh}, \theta)}{n_{generated}(E_{sh}, \theta)} \tag{5.8}$$

As a result, the FD aperture becomes:

$$\begin{aligned} \mathcal{A}(E_{sh}) &= \int_{S_{gen}} dS \cdot \int_{\theta} \eta(E_{sh}, \theta) \cos\theta \sin\theta\, d\theta \cdot \int_{\phi} d\phi \\ &= S_{gen} \cdot \int_{\theta} \eta(E_{sh}, \theta) \cos\theta\, d\theta \cdot \int_{\phi} d\phi \end{aligned} \tag{5.9}$$

Taking into account the uniform event generation in terms of azimuth, $\phi \in [0°, 360°]$ and introducing the aperture in Eq. 5.9, the FD exposure becomes:

$$\begin{aligned} \mathcal{E}(E_{sh}) &= 2\pi \cdot S_{gen} \cdot \Delta T \cdot \int_{\theta} \eta(E_{sh}, \theta \cos\theta\, d\theta \\ &\approx 2\pi \cdot S_{gen} \cdot \Delta T \cdot \sum_{i} \eta(E_{sh}, \cos\theta_i) \cdot \cos\theta_i \cdot \Delta \cos\theta_i \end{aligned} \tag{5.10}$$

where $\theta \in [110°, 180°]$ and i iterates over the whole zenith range. In order to get the corresponding differential exposure in terms of height of first interaction, the value of the first interaction height H_1 is fixed. The exposure becomes:

$$\frac{d\mathcal{E}}{dH_1}(E_{sh}, H_1) = 2\pi \cdot S_{gen} \cdot \Delta T \cdot \sum_{i} \eta(E_{sh}, \cos\theta_i, H_1) \cdot \frac{1}{\Delta H_1} \cdot \cos\theta_i \cdot \Delta \cos\theta_i \tag{5.11}$$

where $\Delta H_1 = 0.5\,\mathrm{km}$ represents the preferred height bin width.

The resulting exposure of the FD of the Pierre Auger Observatory to steeply up-going cosmic ray-like induced air showers with zenith angles $\theta \in [110°, 180°]$ are presented in Fig. 5.5.

The division of the zenith range into different sub-ranges provides a further input and additional information regarding the applicability of the presented results for different primary particles scenarios. The exposure results for three zenith sub-ranges $\theta \in [110°, 124.2°], \theta \in$

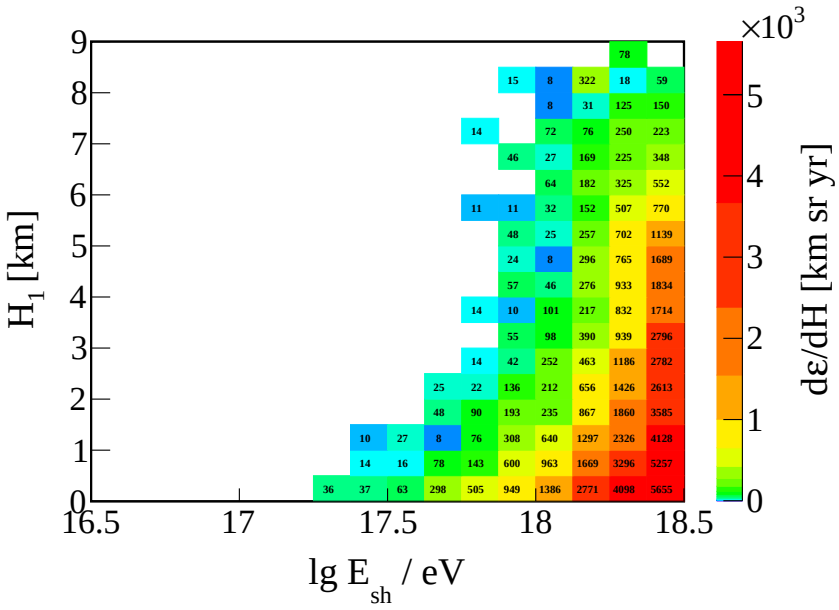

Figure 5.5: Double differential exposure of the FD to up-going cosmic ray - like induced air showers, with primary energies $\lg E\,/\,\mathrm{eV} \in [16.5, 18.5]$ and zenith ranges $\theta \in [110°, 180°]$, in terms of shower energy E_{sh} (x-axis) and height of first interaction H_1 (y-axis). The color code on the z-axis shows the exposure as defined in Eq. 5.11, for each $\Delta H_1 = 0.5\,\mathrm{km}$, with the corresponding values shown in the figure. The presented results have been shown and discussed in [92].

$(124.2°, 141.3°]$ and $\theta \in (141.3°, 180°]$ [7] are plotted in Fig. 5.6. As expected, the dominating channel corresponds to the most inclined zenith interval, which is the decisive one for showers with low calorimetric energies: $\lg E_{sh}\,/\,\mathrm{eV} < 17.6$, as well as for showers interacting high in the atmosphere.

5.4.2 Upper flux limits

As mentioned above, after unblinding the whole data set, one event has been observed, $n_{obs} = 1$, which is consistent with the expected background of $n_{bkg} \approx 0.5$. As a result, integral upper flux limits have been set on steeply up-going cosmic ray - like air showers. The approach used in [92] is using the Rolke limit [95] for the expected number of events, $N^{95\%}$, under the assumption of 1 background event for a confidence level $CL = 95\%$. The integral limit for shower energies $E_{sh} > 10^{17.5}\,\mathrm{eV}$, corresponding to a $CL = 95\%$ is defined as:

$$F^{95\%}(E_{sh} > 10^{17.5}\mathrm{eV}) = \frac{N^{95\%}}{< \mathcal{E} >} \tag{5.12}$$

where $< \mathcal{E} >$ represents the average weighted exposure corresponding to shower energies $E_{sh} > 10^{17.5}\,\mathrm{eV}$ and is calculated as:

$$< \mathcal{E} >= \frac{\int_{E_{sh}>10^{17.5}} E_{sh}^{-\gamma}\mathcal{E}(E_{sh})dE_{sh}}{\int_{E_{sh}>10^{17.5}} E_{sh}^{-\gamma}dE_{sh}} \tag{5.13}$$

Using the exposure defined in Eq. 5.10, the upper integral flux limits on up-going

[7] The zenith ranges have been chosen according to a $\cos\theta$ sampling, by dividing the whole range in 3 equal zenith bins in terms of $\cos\theta$. This ensures an equal distribution of the generated events for each $\cos\theta$ and H_1.

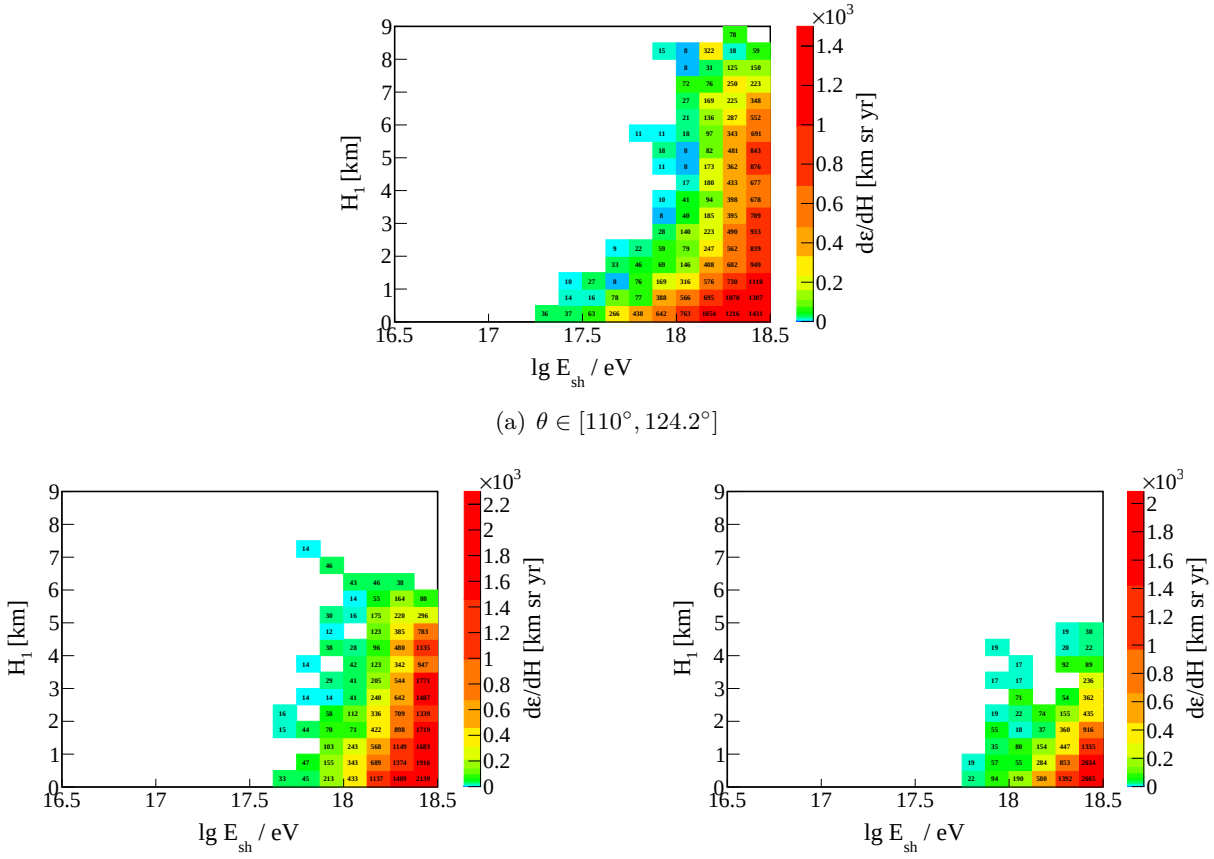

(a) $\theta \in [110°, 124.2°]$

(b) $\theta \in (124.2°, 141.3°]$

(c) $\theta \in (141.3°, 180°]$

Figure 5.6: FD double differential exposure in terms of height of first interaction H_1 and shower energy E_{sh} to up-going cosmic ray - like induced air showers with primary energies $\lg E\,/\,\mathrm{eV} \in [16.5, 18.5]$ and first interaction heights $H_1 \leq 9\,\mathrm{km}$ for three different sub-zenith ranges. The numbers in the figure represent the FD exposure per each $\Delta H_1 = 0.5\,\mathrm{km}$, as defined in Eq. 5.11.

cosmic ray - like induced air showers, with primary energies $\lg E\,/\,\mathrm{eV} \in [16.5, 18.5]$ and zenith angles $\theta \in [110°, 180°]$, interacting at heights up to 9 km above the detector level, have been set using the FD of the Pierre Auger Observatory. The limits are calculated and provided for two different energy spectra, $\gamma = 1$ and $\gamma = 2$. The obtained integral upper flux limits, as published in [92], are [8]:

$$\begin{aligned} F^{95\%}_{\gamma=1}(E_{sh} > 10^{17.5}\mathrm{eV}) &= 3.6 \cdot 10^{-20}\,\mathrm{cm}^{-2}\,\mathrm{sr}^{-1}\,\mathrm{yr}^{-1} \\ F^{95\%}_{\gamma=2}(E_{sh} > 10^{17.5}\mathrm{eV}) &= 8.5 \cdot 10^{-20}\,\mathrm{cm}^{-2}\,\mathrm{sr}^{-1}\,\mathrm{yr}^{-1} \end{aligned} \tag{5.14}$$

By providing the exposure results in a double differential form, as plotted in Fig. 5.5 and Fig. 5.6, any physical scenario can be tested and upper limits on the corresponding particle fluxes can be set. A specific application of these general results towards the calculation of exposure and upper flux limits regarding up-going τ-induced air showers has been studied, representing one of the main personal contributions, and is presented in detail in chapter 6. Furthermore, using the upper bounds on τ-induced air showers, a BSM scenario of up-going particles propagating through Earth and interacting with matter within the last few km distance, resulting in the creation of τ-leptons, has been studied and is discussed in chapter 7. The two applications

[8] More information about the calculation of the integral upper flux limits can be found in [92]. Since this doesn't represent a personal contribution within the up-going search only the final results are presented in the thesis.

presented within the next chapters serve as a proof of concept and emphasize the importance of the generic search for up-going induced air showers with the FD of the Pierre Auger Observatory, as well as its wide applicability within the scientific community.

6

Steeply up-going τ-induced air showers

Up-going showers with the high elevation angles and corresponding energies of the anomalous events observed by the ANITA collaboration [15], shortly described in section 4.2.1, can be potentially explained by particles with very low cross sections which are penetrating the Earth and interacting very close to the surface. As the τ-leptons have a range that can reach up to 50 km inside rock at ultra-high energies, the charged current (CC) interaction of τ-neutrinos, $\nu_\tau + N \rightarrow \tau + ...$, producing τ-leptons has been initially considered as a main candidate. However, as already mentioned within the previous chapters, this potential scenario has been disregarded due to the large attenuation length of neutrinos at the corresponding zenith angles and energies. The required neutrino fluxes that would produce such events exceed the flux constraints published by Auger and IceCube [96, 13, 16]. Given the tension of these events with the Standard Model (SM) of particle physics, various Beyond Standard Model (BSM) scenarios have been proposed in the literature as an alternative interpretation. Many of these, such as stau decays [19], heavy dark matter [17], sterile neutrinos mixing [18], etc. result in the production of τ-leptons. Therefore, the generic search for up-going cosmic ray-like showers using the FD of the Pierre Auger Observatory and detailed in chapter 5, is recast within this chapter in terms of τ-leptons induced air showers.

In order to ensure the wide applicability of the presented results, τ-leptons are investigated independently of their production mechanism. Consequently, the τ-leptons are directly generated both inside Earth and in the atmosphere, with an intensity proportional to the media density, ensuring thus the different interaction rates of any hypothetical particles in different media. The generated τs are propagated, taking into account their energy losses inside the Earth, until their decay point. All τ-decay branches are considered and the resulting daughter particles are further investigated in terms of their contribution to the shower energy E_{sh}. The resulting distributions of τ-decay induced air showers are evaluated in a two dimensional form, in terms of shower energy and height of first interaction H_1, similarly to the double differential exposure plots shown in Fig. 5.5 and Fig. 5.6. The exposure of the FD of the Pierre Auger Observatory to up-going τ-induced air showers is obtained by folding the double differential exposure results, obtained from the generic search in chapter 5, with the 2D distribution of τ-decay induced air showers. As a result, the effective exposure of the Observatory to steeply up-going air showers produced by τ-leptons generated both inside and above[1] Earth by an unspecified mechanism is obtained, as it has been briefly presented in [97]. This can be further used in order to provide corresponding upper bounds on the τ-lepton fluxes. The final results are provided in terms of the primary lepton energies, as this is the main quantity of interest in a subsequent study of BSM particles resulting in the creation of τ-leptons (see chapter 7).

[1] τ-leptons generated in the atmosphere do not have a significant contribution to the total exposure results, given the much lower atmospheric density when compared to the Earth's density: $\rho_{atm} \leq 10^{-3}\text{g/cm}^3$

6.1 Simulation of τ-leptons

The proper simulation of τ-leptons represents the first and most important step towards studying the FD response to up-going τ-induced air showers and further on setting upper bounds on the corresponding fluxes. The simulation code developed for this study used NuTauSim [20] directly as a base. The original version of the code treats the production of τ-leptons that result from CC interactions of tau neutrinos, ν_τ, inside the Earth. Since in the current approach the origin of the τs is disregarded, one of the main implemented changes is regarding the direct generation of τ-leptons, ensuring thus an agnostic simulation with regard to their production mechanisms. Moreover, since in the current study the τ-leptons are injected both below and above the Earth's crust, the code has been enhanced by allowing the particle generation directly in the atmosphere in addition to the Earth generation. As a result, the leptons are directly injected both below and above Earth and are further followed up to their decay point. The τ-decays are being modelled using TAUOLA [21], where all of the decay branches are considered. The energy losses in the atmosphere are neglected, as they are minimal given the low atmospheric density. The τ-propagation and tracking, together with their energy losses have not been modified, but the reporting of the decay secondaries has been enhanced. Only the secondaries contributing to the calorimetric energy deposit are considered, as daughter particles like muons and neutrinos will not contribute to the shower energy. The secondaries of interest are reported from TAUOLA [21], together with their species and energy contribution to a specific τ-decay. The energies in TAUOLA are calculated in the τ-leptons rest-frame, as described in section 4.3.5. Consequently, the energies of the secondaries are also provided in the rest frame of the τ. As a result, the ratio E_i/m_τ, corresponding to the energy fraction carried away by the daughter particles, is saved in the input file, and is further used in order to calculate the corresponding energy of the secondary i for a known τ decay energy E_{decay}.

$$E_i(E_{decay}) = E_{decay} \cdot \frac{E_i}{m_\tau} \tag{6.1}$$

Once the τ-leptons decay, their decay energy E_{decay}, together with the resulting secondaries, in terms of species and energies, as well as the corresponding value of the τ-decay distance, are stored in an output file and can be further accessed. This simulation procedure is contained within the newly modified version of the NuTauSim [20] code, OnlyTauSim, which represents the implemented framework used for the current analysis.

6.1.1 OnlyTauSim: τ simulation software

τ-leptons are injected both inside and above Earth and their behavior is further followed. Since the resulted simulations will be folded with the up-going generic search results in terms of exposure, the same parameters are desired, specifically the shower energy and height of first interaction. As explained within section 5.1.3 and emphasized in Appendix D.2, there are two different ways of generating events in terms of their geometry: either flat in height with a $\cos\theta$ zenith sampling or flat in distance with a $\cos^2\theta$ sampling and with a maximum distance, D_{max}, cut. Given the decaying nature of the τ-leptons, it has been decided to proceed with the second option, of injecting the leptons flat in distance. The value of the maximum injection distance

above the detector level is then defined by Eq. D.1 and shown here again for consistency:

$$D_{max} = \frac{H_{max}}{\cos\theta_{min}} = \frac{9\,\mathrm{km}}{\cos 110^\circ} \approx 26.3\,\mathrm{km} \tag{6.2}$$

In order to find the minimum value of the injection distance, which will correspond to the maximum distance of τ injection inside the Earth, the primary energy range has to be defined. Since the shower energy is defined by $E_{sh} \in [10^{16.5}, 10^{18.5}\,\mathrm{eV}]$, the initial energy of the τ-leptons has to be correspondingly higher considering the energy losses inside Earth. Moreover, the energy carried away by the neutrinos resulted from any τ-decay, as well as the muons resulted from the muonic decay channel, which do not contribute to the shower energy, has to be considered. As a result τ-leptons with primary energies $\lg E_0\,/\,\mathrm{eV} \in [16.5, 20]$ have been investigated. The lower limit coincides to the minimum shower energy, while the upper energy is chosen according to the maximum observed energies.

Having the desired primary energy range, the maximum injection distance inside Earth can be determined. Since for the current study the τ-leptons need to exit the Earth without decay, the maximum injection distance inside Earth represents the distance below which no event is able to exit into the atmosphere with energies above $10^{16.5}\,\mathrm{eV}$. In order to find this value, dedicated simulations of $\approx 10^6$ τ events injected inside the Earth with primary energies $\lg E_0\,/\,\mathrm{eV} \in [16.5, 20]$ and injection distances up to 100 km, $D_{Earth} \in [0, 100\,\mathrm{km}]$ have been performed. The results are plotted in Fig. 6.1, where all the τ-leptons injected inside Earth (blue symbols), as well as τs surviving the Earth propagation (red symbols) are shown. It can be seen that τs injected at distances greater than $D_{Earth} \approx 40\,\mathrm{km}$ are either decaying or loosing energy during the propagation, and they are therefore not exiting into the atmosphere. Consequently, the maximum injection distance inside Earth has been chosen: $D_{max,Earth} = 50\,\mathrm{km}$ [2]. The value of the maximum distance also has the consequence of having an almost constant Earth density: $\rho_{\mathrm{Earth}} \approx 2.6\mathrm{g/cm}^3$ for any $D \leq D_{max,Earth} = 50\,\mathrm{km}$.

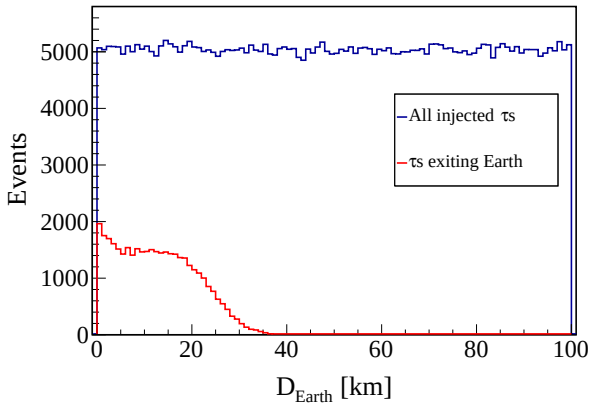

Figure 6.1: τ-leptons surviving Earth propagation (red symbols) as resulted from a simulation of $\approx 10^6$ τs injected up to 100 km inside the Earth (blue symbols) with primary energies $\lg E_0\,/\,\mathrm{eV} \in [16.5, 20]$, with respect to their injection distance inside Earth, D_{Earth}

As a result, τ-leptons with primary energies $E_0 \in [10^{16.5}, 10^{20}]\,\mathrm{eV}$ are generated, follow-

[2] The choice of a 50 km maximum distance, rather than 40 km as suggested from Fig. 6.1, is ensuring the coverage of any additional events missing due to limited statistics

ing a spectrum $dN/dE \propto E^{\gamma}$ with $\gamma = -1, -2$. Due to energy losses and decays, the location of the leptons injection is of key importance. The injection distance, D_{inj}, is defined as the distance between the injection point and the Earth's surface along the τ-lepton propagation axis (negative when the injection is inside Earth and positive when in the atmosphere). A number of $10^7 \tau$ events are injected flat in distance, both below and above Earth, with $D_{inj} \in [-50, 26.3]$ km. τ-energy losses in the atmosphere are minimal, given the low atmospheric density, and are therefore neglected in the current study. Given the constant Earth density for the distances of interest, this also has the consequence of removing the zenith dependence in the τ-simulation stage. As a result, the simulations are performed for a fixed zenith angle [3] and further on extended to the entire zenith range of interest. The zenith angle is further taken into account and has an important role in the calculation of the first interaction height H_1, as detailed in section 6.1.2.

The flat distribution in D_{inj} is further re-weighted using the media density, in order to account for different interaction rates of any hypothetical particles which could create the investigated τ-leptons in different density media. The weights are calculated accordingly:

$$w(H_{\text{inj}}) = \begin{cases} 1 & : H_{\text{inj}} \leq 0 \\ \frac{\rho_{\text{atm}}(H_{\text{inj}})}{\rho_{\text{Earth}}} & : H_{\text{inj}} > 0 \end{cases}, \tag{6.3}$$

where $\rho_{\text{atm}(H_{\text{inj}})}$ represents the average atmospheric density profile as a function of the height above the Observatory: $H_{\text{inj}} = D_{\text{inj}} \cos\theta$ and $\rho_{Earth} \approx 2.6\,\text{g/cm}^3$ is the constant Earth density.

The main τ-generation method is sketched in Fig. 6.2. Depending on their injection point, the τ-leptons are treated slightly different. As already mentioned, the main difference is regarding the energy losses, which are neglected once the leptons reach the atmosphere.

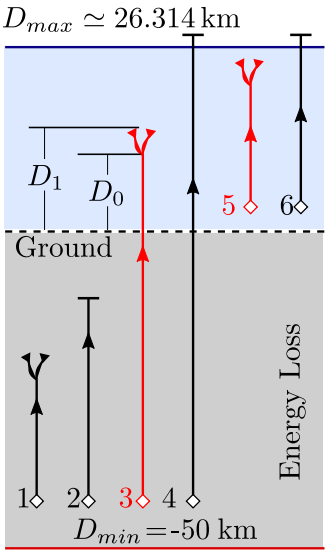

Figure 6.2: Schematic view of τ simulations. τ decays which might trigger the FD are illustrates with red color.

[3] Since the τ-simulations are performed flat in distance, the zenith angle is not used at all in the simulation stage, everything being evaluated in terms of propagation distance.

τ-leptons inside Earth

All τs injected inside Earth (cases 1 - 4 in Fig. 6.2) are subject to energy losses. The generic equation for the τ lepton energy loss rate when propagating through any material is:

$$\left\langle \frac{dE_\tau}{dX} \right\rangle = -a(E_\tau) - b(E_\tau) \cdot E_\tau \tag{6.4}$$

where $a(E_\tau)$ represents the energy loss due to ionization processes, which can be considered constant for the investigated lepton energies, $a \approx 2 \times 10^6\,\mathrm{eV/\,cm^2/g}$. The second parameter, $b(E_\tau)$, includes the energy loss contributions from bremsstrahlung, pair production and photonuclear interactions. At the energies of interest ($E_\tau > 10^{16.5}\,\mathrm{eV}$), photonuclear interactions represent the largest contribution to the energy losses, being at the same time the main source of uncertainties, given the limited knowledge in the parton distribution functions at those energies. There are several models describing this process and the corresponding parton functions. Within the current study, we adopt the energy loss model of the ALLM [98] parametrization for the potonuclear processes, as detailed in [20].

For a given primary energy and injection distance, the τ-leptons are propagated in small steps inside the Earth, from the injection point up to the surface. The step length is calculated based on the local density, the corresponding τ-lepton energy and the fraction of energy lost in each step, $f = 10^{-3}$, according to [20]:

$$dL = \frac{E_\tau}{\left\langle \frac{dE_\tau}{dX} \right\rangle \cdot \rho_{Earth}} \cdot f \tag{6.5}$$

At each propagation step the decay probability is calculated:

$$P_{decay}(E_\tau) = 1 - \exp\left(- dL \cdot \frac{m_\tau}{E_\tau \cdot c \cdot t_\tau} \right) \tag{6.6}$$

where dL represents the propagation step defined in Eq. 6.5, $m_\tau \approx 1.777\,\mathrm{GeV/c^2}$ is the τ-mass, t_τ is the mean τ-lifetime, corresponding to a mean decay length of $d_\tau \approx 86.93 \cdot 10^{-4}\,\mathrm{cm}$.

The propagation distance is further advanced by the step dL and the τ-lepton energy losses within this step are accounted for, according to Eq. 6.4. The propagation process is repeated until one of the following outcomes appears:

1. The τ-lepton decays inside Earth (case 1 in Fig. 6.2): the resulting event will not contribute to the τ-decay distribution within the FD - FoV, as it doesn't survive Earth propagation;

2. The τ-lepton reaches the minimum energy $E_{threshold} = 10^{16.5}\,\mathrm{eV}$ (case 2 in Fig. 6.2): due to energy losses inside Earth, depending on their primary energy and injection distances, the leptons are loosing a significant amount of energy; since in the generic study described in chapter 5 the minimum investigated energy corresponds to $E_{sh} = 10^{16.5}\,\mathrm{eV}$, leptons with energies below this limit are disregarded

3. The τ-lepton reaches the Earth's surface without decay and energies above $E_{threshold}$ (cases 3 and 4 in Fig. 6.2): events surviving Earth propagation are further tracked in the atmosphere, as detailed below.

τ-leptons in the atmosphere

The treatment of the τ events in the atmosphere is following a similar approach as in the case of the Earth propagation, with the main difference of energy losses being neglected, due to the low atmospheric density. The propagation is also performed gradually, in small steps. In order to keep a similar tracking step length, the value of dL is defined as:

$$dL \propto \frac{1}{\rho_{atm}(D_{atm})} \tag{6.7}$$

where in the first iteration, $D_{atm} = D_{inj}$ for events directly injected in the atmosphere, and $D_{atm} = 0$ for events surviving Earth propagation and further entering the atmosphere. The definition of the atmospheric density has been chosen according to [99], for a reference zenith angle $\theta = 180°$.

As described above, at each propagation step the decay probability is evaluated, according to Eq. 6.6, with dL defined in Eq. 6.7. As no energy losses are considered, the propagation distance is then further incremented and the procedure is re-iterated until one of the two following scenarios takes place:

1. The τ-lepton decays in the atmosphere, at a distance $D_0 < D_{max}$ (cases 3 and 5 in Fig. 6.2): the decay distance of the τs in the atmosphere is defined as the distance from the surface of the Earth to the point of decay and coincides with the injection distance D_0 of a τ-induced air shower;

   These represent the main candidate events which could contribute to the FD exposure to up-going τ-induced air showers, since they are decaying within the potential field-of-view (FoV) of the FD

2. The τ-leptons escape the atmospheric region of interest, defined by D_{max} from Eq. 6.2, without decay (cases 4 and 6 in Fig. 6.2): events not decaying within the FD-FoV are not further followed as they will not contribute to the exposure results.

The injection distance, D_{inj}, the decay distance, D_{decay}, together with the primary energy, E_0, as well as decay energy, E_{decay}, and decay products are saved for all 6 cases enumerated above and sketched in Fig. 6.2, with events being flagged accordingly. They can easily be accessed for further analysis and investigations. As a first cross check, the distribution in terms of primary τ-energy and decay distance has been investigated separately for events injected inside the Earth and for those directly injected in the atmosphere, considering a flat energy injection spectrum, $\gamma = -1$. The presented results are obtained before applying the re-weighting procedure related to the different media, defined in Eq. 6.3, and therefore correspond to a flat injection distance. The decay distance is calculated with respect to the Earth crust, having positive values for events decaying in the atmosphere and negative ones for τ-leptons decaying inside Earth. A total number of 10^7 τ-events have been simulated, for a fixed zenith value, with primary energies $\lg E_0 \,/\, \mathrm{eV} \in [16.5, 20]$ and injection distances $D_{inj} \in [-50, D_{max})$, with $D_{max} \approx 26.3\,\mathrm{km}$ according to Eq. 6.2.

Only $\approx 8\%$ of the τ-leptons are found to survive Earth propagation and decay in the atmospheric region of interest. As can be seen in Fig. 6.3(a), most of the events decaying deep

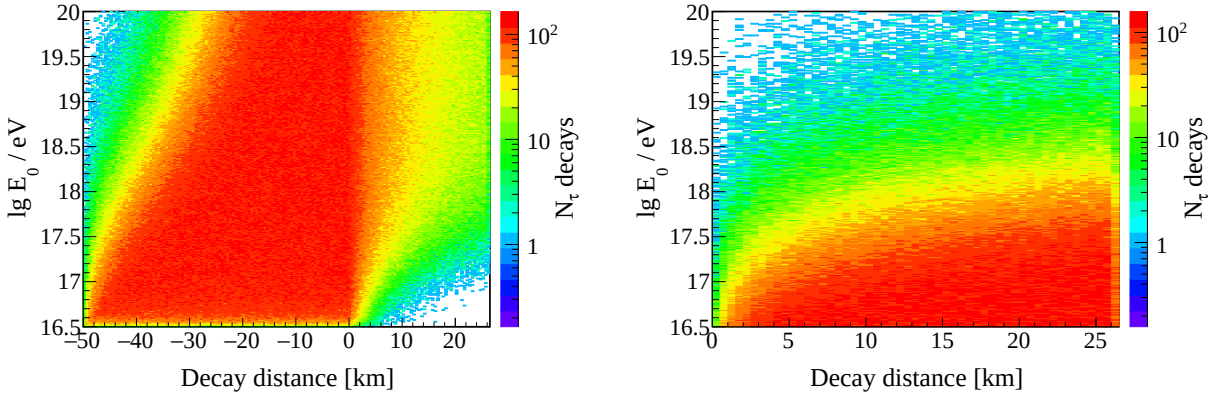

(a) τ-leptons generated inside Earth, with injection distances $D_{inj} \in [-50, 0)$ km

(b) τ-leptons generated above Earth, with injection distances $D_{inj} \in [0, 26.312)$ km

Figure 6.3: Distribution of τ-leptons decays as a function of their primary energies ($y-$axis) and decay distance with respect to Earth's crust ($x-$axis); negative values of the distance indicate decays below the Earth's crust

inside Earth, at the lowest values of the decay distance, corresponding to small propagation distances, are the lower energy ones, where the decay probability is much higher. The higher the τ leptons' primary energy is, the more they can survive the propagation process, shifting the events distribution towards higher decay distances. Events that survive Earth propagation and decay within the atmosphere, $D_{decay} \geq 0$ km, thereby contributing to the FD exposure, are dominated by high initial energies of the τ-leptons. The low energy τs mostly decay at relatively small distances above the Earth's surface and are mainly represented by events injected at small distances below the crust. Due to energy losses inside Earth, the corresponding decay energies in the atmosphere are much lower, increasing thus the decay probability. The decay distribution resulting from τs directly injected in the atmosphere is shown in Fig. 6.3(b). Since the energy losses are neglected, the decay probability and injection distance represent the only influencing factors. As a result, most of the decays in the atmosphere are represented by low energy τ-leptons. For higher primary energies the decay distance increases, yielding events with maximum investigated energies decaying mostly at high distances in the atmosphere. Many of those events will exit the atmospheric region of interest without decay.

Since the τ-leptons decaying in the FD-FoV ($D_{max} \approx 26.3$ km) represent the candidates contributing to the FD exposure to up-going τ-induced air showers, studying their behavior is of particular interest. In Fig. 6.4 the distribution of all τ-leptons decaying in the atmosphere up to D_{max}, as resulted from both injection media, is plotted. This represents the starting point of the up-going τ induced air showers study. Moreover, as the τs injected inside Earth are prone to energy losses, their decay energy represents the energy available to the shower in the atmosphere. Therefore, in Fig. 6.4(b) the distribution of decaying τs is also represented in terms of their decay energy E_{decay}. Leptons that survived Earth propagation represent the majority of decays at small distances above Earth's surface, while the atmosphere injected τs are mainly contributing to higher distances and low energies region. Most of the high primary energy τs decaying within the FD-FoV are events injected inside the crust, which due to energy losses reached the atmosphere with significant lower energies, increasing thus their decay probability. The majority

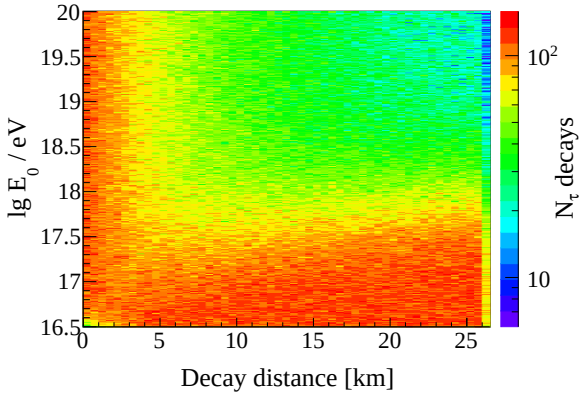

(a) τ-leptons decaying above Earth, in the atmospheric region determined by the FD-FoV in terms of their primary energy

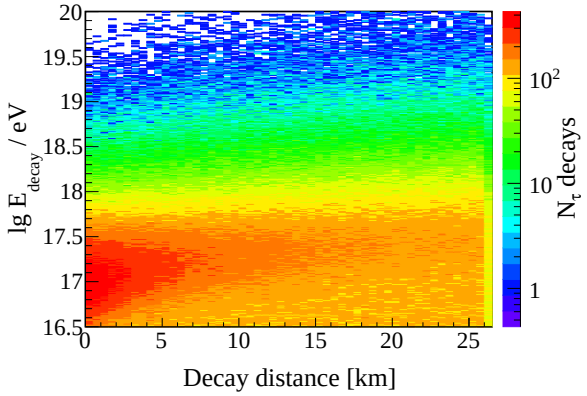

(b) τ-leptons decaying above Earth, in the atmospheric region determined by the FD-FoV in terms of their decay energy

Figure 6.4: Distribution of τ-events decaying in the FD-FoV, with respect to their decay distance ($x-$axis) and primary energy (Fig. 6.4(a)) respectively their decay energy (Fig.6.4(b)). The presented distributions are obtained before applying the different media density re-weighting defined in Eq. 6.3.

of events in Fig. 6.4(b) at distances $D_0 \in [0.5]$ km and decay energies $\lg E_{decay} \,/\, \text{eV} \in [16.5, 17.5]$ is dominated by such τ-leptons injected inside Earth with high primary energies. Depending on the injection distance, different primary energy ranges contribute to this region: high energy events injected deep inside the crust survive Earth propagation and exit Earth with significantly reduced energies, which determines their decay at very small distances. Events injected directly in the atmosphere contribute mainly to high values of the decay distance. However, in the presented plots the different media density and the corresponding events re-weighting in Eq. 6.3 is not accounted for. Since the atmospheric density has much lower values $\rho_{atm} \approx 10^{-3}\rho_{Earth}$, the distribution of events decaying in the FD-FoV will be governed by τ-leptons injected inside Earth and surviving their propagation up to the surface.

As the FD exposure to up-going cosmic ray - like induced air showers, presented in chapter 5, is studied in terms of shower energy E_{sh} and height of first interaction H_1, a similar approach has to be used within the τ-leptons case. The τ decays presented in Fig. 6.4 have to be evaluated in terms of the same parameters. The event distribution in terms of decay energy E_{decay} (Fig. 6.4(b)) represents the starting point towards calculating both E_{sh} and H_1.

6.1.2 Modeling τ-lepton decay induced air showers

As previously discussed, the τ-decays are simulated using TAUOLA [21], accounting for all τ-decay branches. Not all daughter particles resulting from a τ-lepton decay contribute to the calorimetric energy deposited in the atmosphere. Secondaries such as neutrinos and muons will cross the atmospheric region of interest without any interaction. Therefore, one of the features of the OnlyTauSim code is the reporting of all the secondaries with their corresponding energies and further on focusing on those which meaningfully contribute to the shower energy E_{sh}. Consequently, the energy resulting from τ-decays and available to the resulting atmospheric air

shower initiated within the FD-FoV (cases 3 and 5 in Fig. 6.2) is calculated by

$$E_{sh} = \sum_i E_i \left(E_{decay}\right) \ , \tag{6.8}$$

where i iterates over the secondaries with a relevant energy contribution: $\pi^{\pm}, \pi^0, K^{\pm}, K^0, e^{\pm}$. $E_i(E_{decay})$ represents the energy of each daughter particle calculated using the τ-decay energy E_{decay}, according to Eq. 6.1. If the resulting energy is comprised in $E_{sh} \in [10^{16.5}, 10^{18.5}\,\mathrm{eV}]$ corresponding to the shower energy interval studied within the up-going cosmic ray-like induced air showers search, detailed in chapter 5, then that event falls within the range of exposures reported in [92] and is shown in Fig. 5.5. As a result, the specific event can be further used in order to adapt the generic up-going search results to the up-going τ-induced air showers scenario.

However, as the FD exposure in Fig. 5.5 is given both in terms of shower energy E_{sh} and height of the first interaction H_1, the point of first interaction of up-going τ-induced air showers is also required.

First interaction point of τ-induced air showers

In order to calculate the distance to first interaction, D_1, of the τ-induced air showers decaying in the FD-FoV as represented by cases 3 and 5 in Fig. 6.2, the decay distance D_0, as provided by OnlyTauSim code is used. As it represents the point of shower injection, the value of D_0 has to be extended by an additional depth X_1, corresponding to the combined first interaction depth of the daughter particles. X_1 is calculated on an event by event basis, by using the average mean free path of the daughter particles, weighted by their energy:

$$X_1 = \sum_i X_1^i \cdot \frac{E_i(E_{decay})}{E_{sh}} \tag{6.9}$$

where i again iterates over the secondaries $\pi^{\pm}, \pi^0, K^{\pm}, K^0, e^{\pm}$ and the sum is regarding all secondaries i present in the specific τ-decay. The values of X_1^i represent the mean first interaction depth for each particle type.

Depending on the secondary species, the average first interaction depth $< X_1^i >$ has different values. Charged pions $\pi^{\pm}$ and Kaons $K^{\pm}, K^0$ have the same average $< X_1^i >$ for the high energies of interest.

$$< X_1^{\pi^{\pm}} >=< X_1^{K^{\pm}} >=< X_1^{K^0} > \tag{6.10}$$

Moreover, the value of the first interaction depth from Eq. 6.10 is energy dependent, given the cross section dependence on the energy. The corresponding values have been calculated using CONEX [54] simulations with high energy hadronic interactions modeled by Sibyll [56]. Using the results provided by CONEX for pion energies of interest $\lg E \in [16.5, 18.5]$, an interpolation in terms of energy has been performed. As a result, the energy dependent value of the average first interaction length of charged pions and Kaons is defined as:

$$< X_1^j(\lg E_j) >= a + b \cdot \lg E_j + c \cdot (\lg E_j)^2 + d \cdot (\lg E_j)^3 \tag{6.11}$$

where j iterates over $\pi^{\pm}, K^{\pm}$ and K^0. The resulting polynomial coefficients in Eq. 6.11 obtained

as a result of the fitting procedure are: $a = 655.3 \pm 6.75, b = -80.03 \pm 1.13, c = 3.58 \pm 0.06, d = -0.05 \pm 0.001$. Both, the CONEX data (black bullets) and the interpolation function (red line) are plotted in Fig. 6.5. The average value $< X_1 >$ is decreasing with the increase of the particles energy, ranging between $\approx (59 - 47)\,\mathrm{g/cm^2}$ for charged pions and Kaons with energies $\lg E\,/\,\mathrm{eV} \in [16.5, 18.5]$.

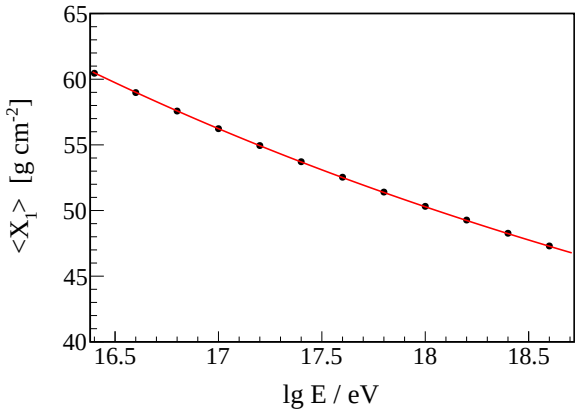

Figure 6.5: Average first interaction depth of charged pions, as provided by CONEX, with respect to the particles energy (black bullets) fitted with the interpolation function defined in Eq. 6.11 (red line)

The average first interaction depth of electrons is equal to the radiation length in air (N_2), and is energy - independent. According to [100], the corresponding value is:

$$< X_1^{e^-} >= 36.66\,\mathrm{g/cm^2} \tag{6.12}$$

The π^0 secondaries are assumed to immediately decay into 2 photons, therefore the average interaction depth for the neutral pions is considered to be equal to that of the photon:

$$< X_1^{\pi^0} >= \frac{9}{7} \cdot < X_1^{e^-} > \approx 47.14\,\mathrm{g/cm^2} \tag{6.13}$$

As the values defined in Eq. 6.11, 6.12 and 6.13 represent the average result, for each of the secondaries of interest the corresponding X_1^i is extracted from an exponential probability distribution $f(x)$ defined below, in order to insure the correctness of the results.

$$f(x) = \frac{1}{< X_1^i >} \cdot \exp\left(- \frac{x}{< X_1^i >} \right) \tag{6.14}$$

To smoothen the results, this procedure is carried out 100 times for each τ-decay and each result is further given a weight of 1/100. Once the value of X_1^i has been extracted from the exponential distribution, the value of the first interaction depth, corresponding to a given τ-decay is calculated according to Eq. 6.9.

The resulting distribution of X_1 is then folded with the atmospheric density profile in order to translate the results from depth of first interaction towards first interaction height H_1. To do so, both the decay distance in the atmosphere D_0, as provided by OnlyTauSim, as well as the zenith angles θ are needed. The procedure is detailed below and sketched in Fig. 6.6.

- *Zenith dependence: from X_1 to H_1*

As stated above, due to both the constant density inside Earth at the investigated injection distances, and the neglected energy losses in the atmosphere, as well as the flat injection of the leptons in distance, the zenith angle does not affect the τ-simulations up to their decay points. However, it has a crucial role in the calculation of H_1. Therefore, all τ-events (cases 1 - 6 in Fig. 6.2) are further studied within the investigated zenith angle range $\theta \in [110°, 180°]$, by re-throwing the simulation set with a flat $\cos^2\theta$ sampling in 30 different zenith bins[4]. For each resulting zenith angle the height of first interaction is calculated, starting from the decay distance D_0 and translating it to the corresponding decay height H_0:

$$H_0 = D_0 \cos\theta \tag{6.15}$$

The atmospheric density profile is further used in order to translate between height and vertical atmospheric depth. Consequently, the average first interaction depth X_1 from Eq. 6.9 needs to be translated in terms of vertical travelled depth for each zenith bin.

$$X_1^{vert} = X_1 \cos\theta \tag{6.16}$$

Since the atmospheric profile needs the vertical depth with respect to the top of the atmosphere, and X_1^{vert} represents the travelled depth, as sketched in Fig. 6.6, the decay height H_0 from Eq. 6.15 needs to be translated in terms of atmospheric depth in order to obtain the corresponding first interaction vertical depth. In order to do so, the atmospheric density profile, $f_{Atm}(H)$ is needed.

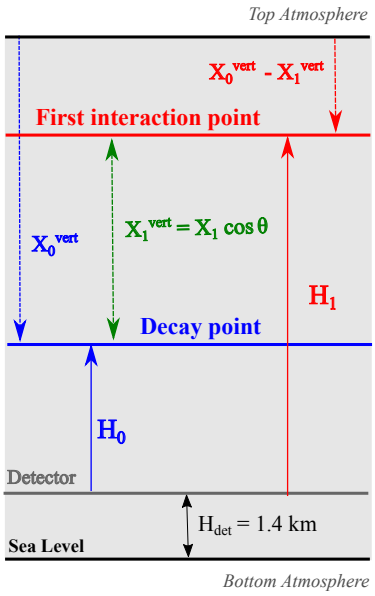

Figure 6.6: Schematic view illustrating the calculation of first interaction height H_1 for τs decaying in the atmosphere at a height H_0 with secondaries having an average first interaction depth X_1

- *Atmospheric profile: from X_1 to H_1*

The atmospheric profile is used for the conversion between height above the sea level and atmospheric vertical depth. The adopted parametrization within this study uses the same parameters provided within the internal Offline simulation software [69] and is detailed in Appendix F. Since the heights considered in the atmospheric modeling are calculated with respect to the sea level and the decay height from Eq. 6.15 is by default calculated relative to the detector level, an additional term of $H_{det} = 1.4\,\text{km}$ a.s.l. has to be considered within the transformation. Consequently, the corresponding vertical depth of a τ-lepton decaying at a height H_0 above the core level is obtained:

$$X_0^{vert} = f_{Atm}(H_0 + H_{det}) \tag{6.17}$$

[4]The flat sampling in $\cos^2\theta$ and the flat injection distance up to D_{max} ensures the same event geometry as in the general up-going search (See section 5.1.3 and Appendix D.2 for more details).

Since the depth in the atmospheric modelling $f_{Atm}(H)$ is calculated with respect to the top of the atmosphere, in order to use this model $f_{Atm}(X_{vert})$ and to obtain the corresponding first interaction height H_1 of τ-decays, the vertical atmospheric depth of the first interaction with respect to the top of the atmosphere is needed. This can be easily obtained by subtracting the vertical travelled depth of the first interaction, X_1^{vert} from the vertical atmospheric depth corresponding to the decay point X_0^{vert}. Consequently, the height of the first interaction, above the detector level, H_1, of an up-going τ-induced air shower is obtained:

$$H_1 = f_{Atm}(X_0^{vert} - X_1^{vert}) - H_{det} \tag{6.18}$$

The first interaction distance D_1 can be further calculated for each zenith angle $\theta \in [110°, 180°]$.

$$D_1 = \frac{H_1}{\cos\theta} \tag{6.19}$$

As the τ events are simulated flat in injection distance D_0 with a $\cos^2\theta$ sampling, in order to follow the event geometries adopted for the generic case and detailed in section 5.1.3, the maximum first interaction height investigated in the generic study, $H_1^{max} = 9\,\text{km}$ is taken into account. Therefore, only τ-events with first interaction heights $H_1 \leq H_{max}$ are further considered, as limited by the FD-FoV to up-going air showers.

As a result, up-going τ-leptons with zenith angles $\theta \in [110°, 180°]$, decaying in the FD-FoV (cases 3 and 5 in Fig. 6.2), with shower energies (Eq. 6.8) $E_{sh} \in [10^{16.15}, 10^{18.5}\,\text{eV}]$ and heights of first interaction (Eq. 6.18) $H_1 \leq H_{max} = 9\,\text{km}$, represent the main candidates contributing to the FD exposure to τ-induced air showers.

A number of 30 different zenith bins have been chosen with a $\cos^2\theta$ sampling for the study of up-going τ-induced air showers with $\theta \in [110°, 180°]$. As expected, most of the interacting events correspond to the most inclined zenith bin ($< \theta >= 111.28°$), given the H_1^{max} cut: $D_1 \cdot \cos\theta \leq H_1^{max}$.

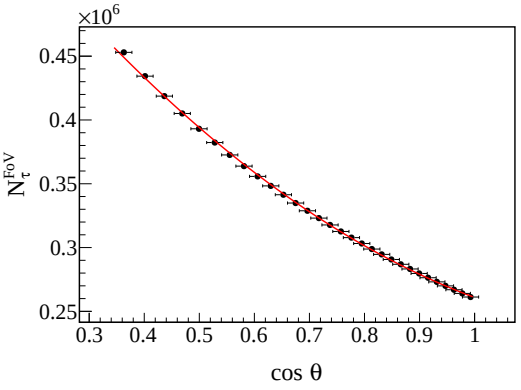

Figure 6.7: Total number of τ-leptons decaying in the FD-FoV

The maximum number of events decreases with increasing zenith angle, with a polynomial behavior in terms of $\cos\theta$. This can be seen in Fig. 6.7, where the total number of τs decaying in the FD-FoV, with a maximum first interaction height $H_1^{max} = 9\,\text{km}$ and shower energies $\lg E_{sh}\,/\,\text{eV} \in [16.5, 18.5]$, is plotted for different zenith angles. The red line corresponds to the fit-

ting function: $N_\tau^{FoV}(\theta) = a{\cdot}\cos^2\theta + b{\cdot}\cos\theta + c$ with $a = 2.12{\cdot}10^5 \pm 2.4{\cdot}10^4$, $b = -5.84{\cdot}10^5 \pm 3.57{\cdot}10^4$ and $c = 6.33 \cdot 10^5 \pm 1.28 \cdot 10^4$.

The distribution of τ-decay induced air showers within the FD-FoV is plotted in Fig. 6.8 in a double differential form in terms of height of first interaction H_1 and shower energy E_{sh}. Six different zenith angles are shown for comparison, with the average value of the zenith angle $< \theta >$ corresponding to the specific zenith bin. Besides the varying number of interacting events

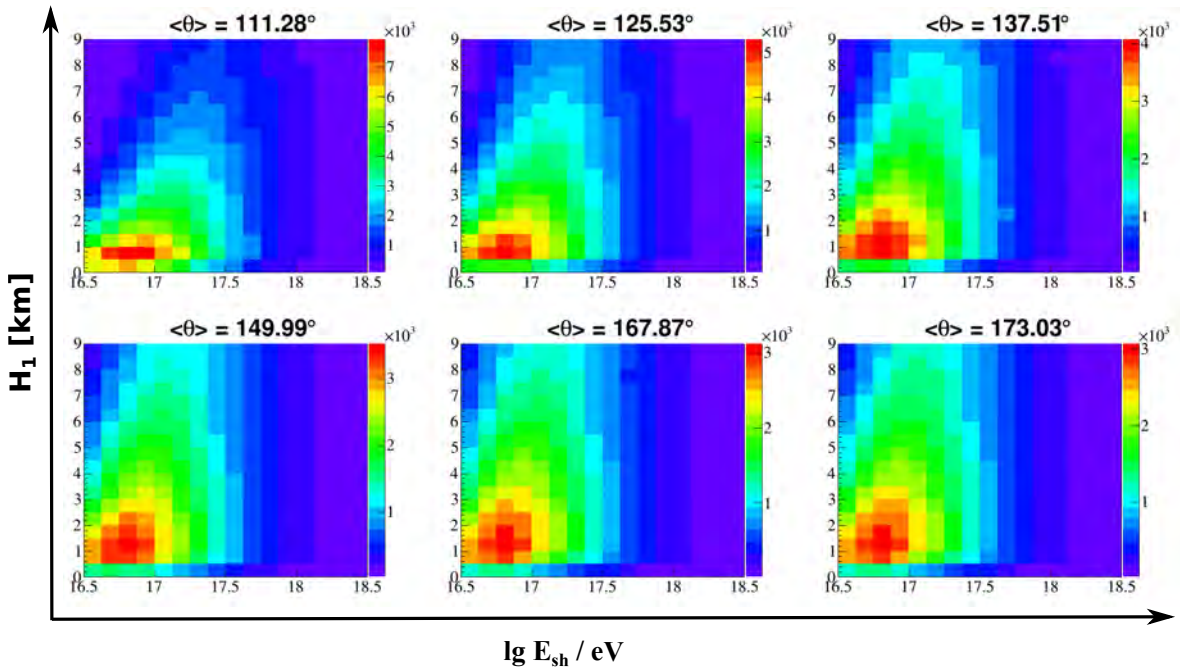

Figure 6.8: Distribution of τ-decay induced air showers in the FD-FoV, in a double differential form, with respect to the height of first interaction H_1 and shower energy E_{sh} for different average zenith angles

at different zenith angles, another interesting feature is observed concerning the heights of first interaction H_1. The majority of events are interacting at low values of H_1 for the most inclined zenith angles, forming a bump at $H_1 \leq 1.5\,\text{km}$ and low shower energies for $< \theta >= 111.28°$. For more vertical zenith angles, most of the τ-events interact higher in the atmosphere, moving the event distribution towards higher values of H_1. This is physically understood and shows the correctness of the obtained results: events decaying at a known distance D_0 will have a correspondingly higher value of the decay height H_0 with the increase of the zenith angle, according to Eq. 6.15. This results in a lower value of the vertical atmospheric depth X_0^{vert}, as sketched in Fig. 6.6. Moreover, as inclined showers are crossing a larger amount of atmosphere than the more vertical events, they would interact at correspondingly smaller vertical depths. Consequently, the first interaction depth defined in Eq. 6.16 will have significantly lower values for the most inclined zenith angles. As a result, it is expected that the more vertical τ-induced air showers interact higher in the atmosphere than the most inclined ones, which can be observed in the obtained results. The event distribution in terms of shower energy is not dependent on the zenith angle, as the calculation of the shower deposited energy in the atmosphere is only dependent on the τ-primary energy and its decay products. As explained within this chapter, the τ-simulations are performed in a one dimensional way up to their decay in the

atmosphere. Consequently, the event distribution in terms of shower energy is influenced only by the corresponding decay energy of the τ-leptons within the FD - FoV, and follows the distribution plotted in Fig. 6.4, in terms of E_{decay} and decay distance. As the shower energy E_{sh} defined in Eq. 6.8 is always smaller than the decay energy, due to secondary daughters that do not deposit their energy in the atmosphere, the majority of events are interacting up to $\lg E_{sh} \,/\, \mathrm{eV} \leq 17.125$, while the bump in Fig. 6.4 is up to $\lg E_{decay} \,/\, \mathrm{eV} \leq 17.5$.

6.2 FD exposure to up-going τ-induced air showers

In order to get the corresponding exposure of the fluorescence detector to steeply up-going τ-induced air showers, the double differential exposure to cosmic ray - like induced air showers, as obtained from the generic study and plotted in Fig. 5.5 is used. As mentioned in the previous section, a similar double differential representation is needed for the τ-leptons decaying in the FD-FoV and represented with red arrows (cases 3 and 5) in Fig. 6.2. Such a distribution has already been plotted in Fig. 6.8, for different zenith angles. Considering the entire studied zenith range, $\theta \in [110°, 180°]$, the double differential distribution of all τ-decay induced air showers with a maximum first interaction height $H_1^{max} = 9\,\mathrm{km}$ and shower energies in the range of interest, $\lg E_{sh} \,/\, \mathrm{eV} \in [16.5, 18.5]$, is obtained and plotted in Fig. 6.9 for a $\gamma = -1$ primary energy spectrum. As expected from Fig. 6.8, most of τ-leptons decaying in the FD-FoV are interacting at low heights of first interaction H_1 and low shower energies. As the shower energy increases, the majority of τs will interact at higher values of H_1, given the correspondingly higher primary energy and reduced decay probability.

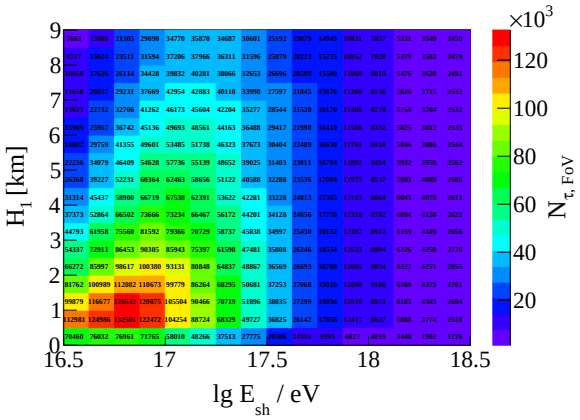

Figure 6.9: The distribution of τ-decay induced air showers within the FD-FoV, for a $\gamma = -1$ energy spectrum.

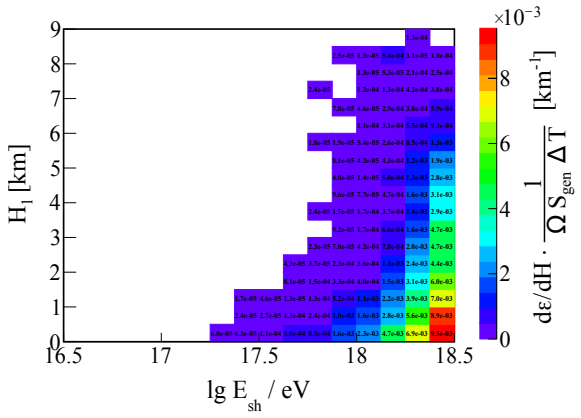

Figure 6.10: The distribution of detector sensitivity, as obtained from the FD exposure to up-going cosmic ray like induced air showers

In order to get the corresponding distribution of τ-lepton induced air showers which would trigger the FD and would be selected as candidates within the FD analysis, the double differential exposure from the generic study (Fig. 5.5), is used. The number of τ-leptons recorded by the FD can be obtained as:

$$N_{trigg,\tau}(E_{sh}, H_1) = N_{\tau,FoV}(E_{sh}, H_1) \cdot \frac{\mathcal{E}(E_{sh}, H_1)}{\Omega\, S_{gen}\, \Delta T} \tag{6.20}$$

where, according to the general study described in chapter 5, $S_{gen} = 10^4\,\mathrm{km}^2$, $\Delta T \approx 14.3\,\mathrm{yr}$ and

$\Omega = 2\pi \cdot \int_{110^\circ}^{180^\circ} \sin\theta \mathrm{d}\theta$. The resulted double differential distribution, which will further be referred to as the detector sensitivity, $\frac{\mathcal{E}(E_{sh},H_1)}{\Omega\, S_{gen}\, \Delta T}$, is plotted for consistency in Fig. 6.10.

By combining the two distributions, according to Eq. 6.20, the up-going τ-leptons induced air showers which would trigger the FD, $N_{trigg,\tau}(E_{sh}, H_1)$, and will be further used in the corresponding exposure and upper flux limits analysis, are obtained and presented in a similar form, in terms of shower energy and height of first interaction. The corresponding distribution is plotted in Fig. 6.11. Both $N_{trigg\,\tau}(E_{sh}, H_1)$ and $N_{\tau,FoV}(E_{sh}, H_1)$ distributions are dependent on the primary energy spectrum. As this dependence is cancelled out within the exposure calculations, in order to simplify the notation, the spectral index γ dependency is not used. However, the energy spectrum effect becomes important in the upper flux limits results, presented in section 6.3. Therefore, the equivalency between $N_{trigg\,\tau}(E_{sh}, H_1) \leftrightarrow N_{trigg\,\tau}(E_{sh}, H_1; \gamma)$ is noted here for consistency.

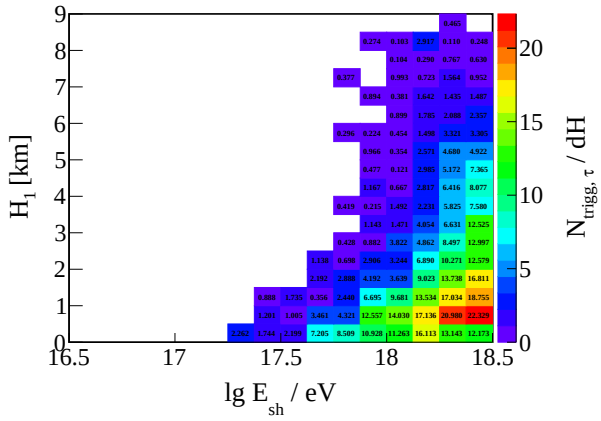

Figure 6.11: The distribution of τ-lepton induced air showers, selected as candidates in the FD analysis, for a $\gamma = -1$ energy spectrum

The FD exposure to τ-induced air showers can be presented in different forms, depending on the investigated case of interest. As outlined in section 6.1.1, all τ-leptons variables are stored and can be further accessed at any time. This leads to the possibility of presenting the exposure results both in terms of τ-leptons energy at injection, i.e. the primary energy, and in terms of τ-decay energy. Since each bin (E_{sh}, H_1) in the double differential distribution of τ-decay induced air showers $N_{\tau\,FoV}(E_{sh}, H_1)$ is populated by several events with different primary and decay energies, each event in each bin needs to be back-tracked, through the OnlyTauSim code, to the corresponding energies. By doing so the distribution $N_{\tau\,FoV}(E|E_{sh}, H_1)$ of τ-events contributing to the given bin (E_{sh}, H_1) is obtained in terms of the energy of interest, E. The corresponding exposure in terms of the energy of interest E, for a given (E_{sh}, H_1) bin, is obtained by folding the generic exposure $\mathcal{E}(E_{sh}, H_1)$ defined in Eq. 5.11 and plotted in Fig. 5.5, with the ratio of the τ-leptons decaying in the FD-FoV and the number of generated events at the given τ-lepton energy E:

$$\mathcal{E}_\tau(E\,|E_{sh}, H_1) = \frac{N_{\tau\,FoV}(E\,|E_{sh}, H_1)}{N_{gen\,\tau}(E)} \cdot \mathcal{E}(E_{sh}, H_1) \tag{6.21}$$

The final exposure is then obtained by integrating $\mathcal{E}_\tau(E\,|E_{sh}, H_1)$ over all shower energies and heights of first interaction considered, which is achieved by summing over all bins in terms of E_{sh} and H_1:

$$\mathcal{E}_\tau(E) = \sum_{E_{sh}} \sum_{H_1} \mathcal{E}_\tau(E\,|E_{sh}, H_1) \tag{6.22}$$

The FD exposure to τ-induced air showers is thus obtained. The exposure results can be presented both in terms of τ-decay energy, and in terms of τ-primary energy, depending on the physical scenario of interest. As a result, the energy E in Eq. 6.21 and 6.22 can be further replaced either with E_{decay} or with the primary energy E_0. Each of the two scenarios is useful for investigating different phenomena and are discussed in further details.

6.2.1 Exposure in terms of τ-decay energy: comparison to CR-like EAS

The exposure in terms of τ-decay energy represents the case of interest for a direct comparison to cosmic ray-like induced air showers and therefore to ANITA estimated exposure. No official estimates regarding the ANITA exposure have been yet published by the collaboration. However, given the cosmic ray - like signature of the anomalous events, it is expected the exposure calculation would be performed accordingly. The τ-decay energy represents the analogous of the cosmic rays primary energy. Therefore, for an exact comparison between cosmic ray-like induced air showers and τ-induced air showers, the number of generated events has to be properly chosen. As a result, for this scenario, not all generated τs are considered. Leptons which decayed or have been killed inside Earth due to energy losses will never exit Earth and therefore will further be disregarded, given the cosmic rays induced air showers nature[5]. Consequently, within this approach, the number of generated τ-leptons, $N_{gen\,\tau}$, will only refer to τs which have a non-zero probability of exiting Earth, represented by cases 3-6 in Fig. 6.2.

The exposure to τ-lepton induced air showers, with a non-zero probability of exiting Earth, is calculated starting from the double differential distributions of τ-leptons in the FD-FoV $N_{\tau\,FoV}(E_{sh}, H_1)$, using the generic search results, $\mathcal{E}(E_{sh}, H_1)$, as explained above. By back-tracking the τ-events to their decay energy, and correspondingly replacing $E \rightarrow E_{decay}$ in Eq. 6.21 and 6.22, the exposure is obtained as a function of the τ-decay energies. This is further compared to the corresponding energies of proton-induced air showers and the results are plotted in Fig. 6.12.

As it has been emphasized within section 5.1.1, presenting the exposure results in terms of the calorimetric energy and height of first interaction, and by forcing the shower's first interaction point, allows for universal results in terms of exposure to cosmic ray - like induced air showers. As a consequence of this universality, only proton showers have been simulated. Therefore, even if the exposure results in terms of shower energy E_{sh} are not dependent on the primary particle, the corresponding results with respect to the primary energy are only provided for protons. The FD exposure to proton induced air showers, contributing to the double differential exposure plotted in Fig. 5.5, is increasing with the primary energy, as it can be seen in Fig. 6.12. This behavior is expected, given the flat generation in heights of first interaction,

[5] As detailed in chapter 5, CR-like induced air showers are generated at different heights above the core level. Therefore, in order to make a one-to-one comparison, only τ-events exiting Earth or generated above it have to be considered.

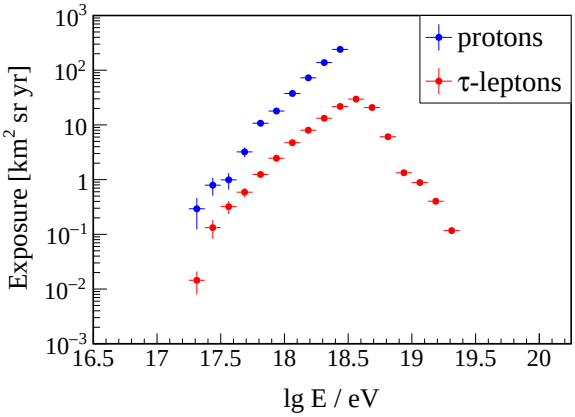

Figure 6.12: FD exposure to up-going protons and τ-induced air showers as a function of the protons primary energy, respectively the τ decay energy. The proton results are obtained up to a maximum energy of $lg\,E\,/\,\mathrm{eV} = 18.5$, corresponding to the maximum simulated energy within the general study.

and the increasing FD sensitivity towards higher energies. As most of the τ-leptons decaying in the FD-FoV and plotted in Fig. 6.9 are leptons surviving Earth propagation, a different behavior is observed in the exposure results in terms of energy. The exposure to τ-induced air showers has a similar behaviour to the proton ones, up to a decay energy of $\lg E_{decay}\,/\,\mathrm{eV} \approx 18.5$, where it reaches its maximum. For higher values of the energy the τ-exposure starts to decrease. This is due to a lower τ-decay probability with higher lepton energies. Moreover, the overall FD exposure to τ-leptons is always lower than the one for proton induced air showers. The majority of τ-leptons are decaying at small heights and low shower energies, as shown in Fig. 6.9, where the FD sensitivity is minimum (Fig. 6.10). By contrast, as the cosmic ray - like induced air showers are generated flat in H_1 and shower energy E_{sh}, the resulting candidates peak corresponds to the maximum detector sensitivity.

Given the strong tensions with the SM physics, different hypothetical scenarios have been proposed in order to explain the nature of the ANITA anomalous events. In order to test any such hypothesis, exposure results and corresponding fluxes need to be provided in terms of primary energies.

6.2.2 Exposure in terms of τ-primary energy: towards BSM scenarios

Since the main goal of the current study is to provide a frame for testing several BSM scenarios which result in the production of τ-leptons, exposure results in terms of the τs primary energies are required. Consequently, all injected τ-leptons (cases 1-6 in Fig. 6.2) are considered and contribute to $N_{gen\,\tau}$. By back-tracking all τ-induced air showers from the double differential distribution plotted in Fig. 6.9 to their energy at injection, E_0, and by replacing $E \rightarrow E_0$ in Eq. 6.21 and 6.22, the exposure can be calculated correspondingly. The FD exposure to τ-leptons generated both below Earth, within a less than 50 km path, and above Earth, with a production rate mirroring the relative interaction rates in matter, is obtained. The exposure to steeply up-going τ-induced air showers is plotted in Fig. 6.13 with respect to the τ-primary energies E_0. The results for the entire studied zenith range, $\theta \in [110°, 180°]$ (green bullets), as well as for three different zenith sub-ranges, corresponding to the ones investigated within the

generic search, are displayed in the figure.

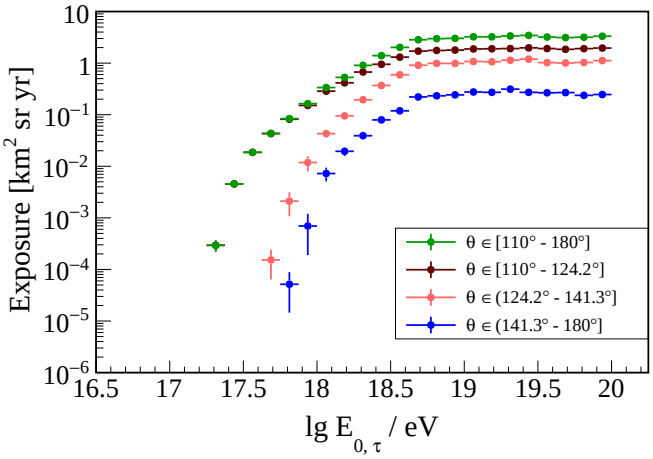

Figure 6.13: FD exposure to up-going τ-induced air showers as a function of primary energy, for different zenith angle ranges

Two different behaviors are observed in Fig. 6.13. The first one is represented by the increase in the exposure with energy, up to $\lg E_0 \,/\, \mathrm{eV} \approx 18.7$. Even if the exposure is increasing with the energy, as expected, its rate growth is decreasing. This has a pure physical origin. The increase in the FD sensitivity and τ-leptons survival rate inside Earth with higher energies, is competing with the decrease of τ-decay probability. Consequently, more τs are escaping the atmosphere without decay. For primary energies $\lg E_0 \,/\, \mathrm{eV} \gtrsim 18.7$ the exposure is quickly flattening. This is an edge effect, determined by the maximum investigated shower energy of $10^{18.5}\,\mathrm{eV}$ in the general study, given the ANITA anomalous events context. As the primary lepton energy increases past this value, the corresponding shower energy E_{sh} starts to exceed this limit. Therefore, even if the FD sensitivity would increase for these higher energy events, they are cut off the analysis. However, this is compensated for by the increasing rate of τ-leptons survival inside Earth. If the energy range in the general study would be extended, the FD exposure to τ-induced air showers would continue to increase for $E_0 > 10^{18.7}\,\mathrm{eV}$, with the rate of exposure increase slowing down. This increase would continue up to some energy, where the increase in the FD exposure and τ survival probability inside Earth would be insufficient to compensate for the longer lifetime of τ-leptons inside the atmosphere. This would lead to an exposure peak, followed by a flattening and then decrease at the highest energies. The increase in the investigated shower energies would in turn translate into better upper flux bounds than those provided below. Extending the general study to higher energies is planned for the near future.

6.3 Upper flux limits on up-going τ-induced air showers

After unblinding the whole data set, from 01.09.2004 - 31.12.2018, 1 event candidate has been found to pass the analysis cuts. This is consistent with the background expectation of $n_{bkg} = 0.45 \pm 0.18$ in the full energy range. As a result, upper flux limits can be set on steeply up-going air showers using the FD of the Pierre Auger Observatory. The upper bounds on cosmic ray

- like induced air showers have been presented and discussed within section 5.4.2 and in [92]. Having the exposure results to up-going τ-induced air showers (Fig. 6.13), corresponding upper flux limits can be calculated. This is done using the Feldman Cousins (FC) approach [101]. The corresponding limit that can be obtained for a 95% CL when 1 event is observed and consistent with the expected background of $n_{bkg} = 0.45 \pm 0.18$, leads to a flux that would result in an expected number of events $N_{FC} = 4.05$.

The differential upper flux bounds on τ-induced air showers, in terms of leptons primary energies, are obtained by back-tracking the candidate events from Fig. 6.11 to their primary energies, as explained in the previous section. As a result, the number of FC candidates required per energy bin, $N_{FC}(E_0)$, so that a total number of N_{FC} is observed in the full energy range is calculated as:

$$N_{FC}(E_0) = \frac{N_{FC}}{N_{bins}} \Bigg/ \frac{N_{trigg\,\tau}(E_0\,\gamma)}{\sum\limits_{N_{bins}} N_{trigg\,\tau}(E_0,\,\gamma)} \tag{6.23}$$

where N_{bins} represents the total number of primary energy bins investigated and $N_{trigg\,\tau}(E_0, \gamma)$ is obtained by back tracking the τ candidates in Fig. 6.20 to their primary energy E_0:

$$N_{trigg\,\tau}(E_0, \gamma) = \sum_{E_{sh}} \sum_{H_1} N_{trigg\,\tau}(E_0 \,|\, E_{sh}, H_1; \gamma) \tag{6.24}$$

The spectrum effects are folded in $N_{FC}(E_0)$, via the different distributions of the τ candidates, $N_{trigg\,\tau}(E_0,\,\gamma)$. The flux limits can be further calculated by using the exposure defined in Eq. 6.22, in order to translate the FC candidates $N_{FC}(E_0)$ into the corresponding flux:

$$\Phi_{\tau}^{95\%} = \frac{N_{FC}(E_0)}{\mathcal{E}_{\tau}(E_0)} \tag{6.25}$$

Following the above described procedure, upper flux limits are set on all injected τ-leptons, represented by cases 1-6 in Fig. 6.2. Consequently, upper bounds on τ-leptons injected both inside Earth, within a less than 50 km path, and above Earth, with an injection rate proportional to the media density, are obtained using the FD of the Pierre Auger Observatory. The results are provided for two different τ-energy spectra: $\gamma = -1$ and $\gamma = -2$, with respect to the leptons primary energy E_0. The limits for τs with zenith angles covering the entire zenith range $\theta \in [110°, 180°]$ have been presented in [97] and are plotted in Fig. 6.14

The upper flux limits for a spectral index $\gamma = -1$ (black bullets in Fig. 6.14) follow the exposure behavior presented in Fig. 6.13. Consequently it is also influenced by the maximum investigated shower energy in the general study, as explained in section 6.2.2. The limits for a $\gamma = -2$ energy spectrum also follow the exposure trend, up to an energy of $\lg E_0 \,/\, \mathrm{eV} \approx 18.7$, after which they start to get weaker. This is expected given the leptons injection spectrum: $dN_{\tau}/dE_{0,\tau} \propto E_{0,\tau}^{-2}$. The corresponding upper flux limits have also been calculated for the three different zenith angle sub-ranges and are plotted in Fig. 6.15. As expected from the general exposure results plotted in Fig. 5.6, and mirrored in the FD exposure to τ-induced air showers shown in Fig. 6.13, the most stringent upper bounds are obtained for the most inclined zenith angles (brown bullets in Fig. 6.15).

The obtained upper flux limits on up-going τs, created within a maximum range of

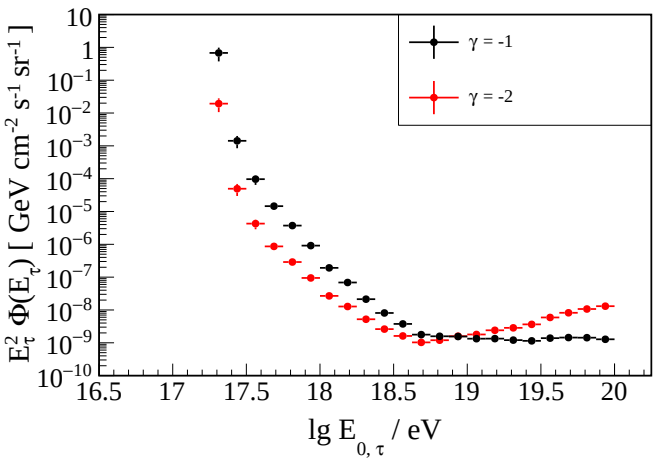

Figure 6.14: $CI = 95\%$ flux upper limits on steeply up-going τ-induced air showers for different primary energy spectra

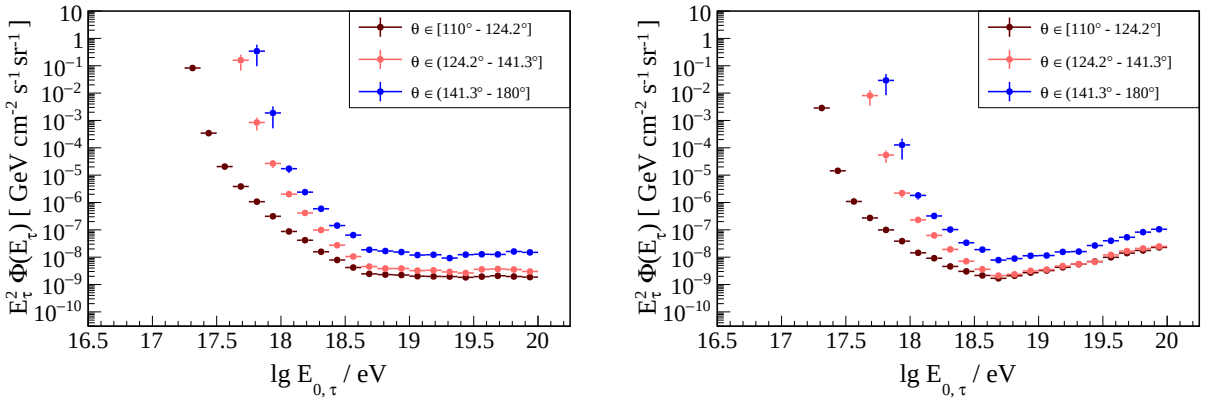

(a) $\Phi_\tau \propto E_0^{-1}$ (b) $\Phi_\tau \propto E_0^{-2}$

Figure 6.15: $CI = 95\,\%$ differential upper flux limits on steeply up-going τ-leptons created at less than 50 km inside Earth vs E_0 energy, for 1 observed event passing the analysis cuts, consistent with $n_{bkg} = 0.5$, for different τ zenith angle ranges and energy spectra.

50 km distance inside Earth and up to 9 km height above it, serve as a proof of concept regarding the wide applicability of the FD exposure results to cosmic ray-like air showers, presented in a double differential form in terms of shower energy and height of the first interaction. Following the approach presented within this chapter, any exotic primary scenario can be tested, as long as the decay length, decay branches and energy loss inside Earth, as well as the average first interaction depth of the resulted secondaries, are known.

Furthermore, the importance of the presented τ study is that it can be easily extrapolated to various BSM scenarios which result in the creation of τ-leptons. As mentioned above, various such hypothesis already exist and are aimed towards explaining the ANITA anomalous events. By folding in the respective cross sections and using the presented upper flux limits, any such model can be constrained. A dedicated study in this regard has been performed as part of this thesis and is described in detail in chapter 7.

7

Beyond Standard Model Particles

As it has already been pointed out, the standard model (SM) physics can not explain the production of τ-leptons with the investigated energies and elevation angles. The required diffuse neutrino fluxes needed for the creation of such showers would exceed the current flux constraints published by both the Pierre Auger [96] and IceCube [16] collaboration. However, several Beyond Standard Model (BSM) scenarios resulting in the production of τ-leptons have been proposed [19], [78], [17]. In all such theoretical predictions the BSM particles need to have a significantly lower cross section than the SM neutrino one, σ_{SM}, in order to survive Earth propagation at the given energies and zenith angles.

A dedicated study of hypothetical BSM particles propagating through Earth and interacting within the last 50 km distance below the surface, resulting in the creation of τ-leptons, has been investigated and is presented in detail within this chapter. Having already studied the behavior of τ-induced air showers and the FD response to such events (see chapter 6), such scenarios can be further tested. By using the above presented upper flux limits to τ-induced air showers, plotted in Fig. 6.14, several BSM models have been investigated for a large range of cross section values. Upper bounds on the hypothetical particles are correspondingly obtained, and the optimum value of the BSM cross section, which results in the strongest upper limits, is found. Two different cases are investigated in detail: an energy-dependent cross section and a fixed cross section scenario. In both of these cases the particles are generated with zenith angles corresponding to the range of interest, $\theta \in [110°, 180°]$. An energy transfer of 50% between the BSM candidates and the τ-leptons is chosen. The value of the energy transfer can be easily changed according to the needs. However, the final results will not be affected significantly, as explained in appendix G.

Based on the dedicated follow-up of the ANITA anomalous events with the FD of the Pierre Auger Observatory, the presented results represent the first constrains of a BSM scenario producing τs with the investigated signatures. Furthermore, the current study shows the importance of the steeply up-going τ-lepton induced air shower results and how any theoretical model resulting in the production of τs can be tested. By using the provided upper flux limits in terms of τ-primary energy and folding in the corresponding cross sections, any such scenario can be correspondingly constrained.

Furthermore, the study has been extended to the Earth Skimming (ES) channel. By using the already published SD exposure results of the Pierre Auger collaboration [7], [8], combined upper limits on various BSM cross sections have been set using the Pierre Auger Observatory. The combined results refer to air showers with zenith angles $\theta \in [110°, 180°]$, as resulted from the FD study, and $\theta \in [90°, 95°]$, corresponding to the ES channel. By doing so, the capacity of the Observatory to constrain a large range of both SM and BSM scenarios resulting in the production of τ-leptons is demonstrated.

7.1 BSM scenario: BSM particles $\rightarrow \tau$-leptons

In order to test any BSM scenario and correspondingly constrain the hypothetical particles, the probability of such a particle to produce the τ-leptons studied within chapter 6 has to be evaluated. The investigated model considers a hypothetical BSM particle with a reduced cross section, which survives Earth propagation and interacts within the last 50 km distance. As a result of its interaction, τ-leptons are created, as sketched in Fig 7.1. The produced τs can in turn exit Earth and induce air showers, which can be detected by the FD of the Pierre Auger Observatory, as detailed within the previous chapter.

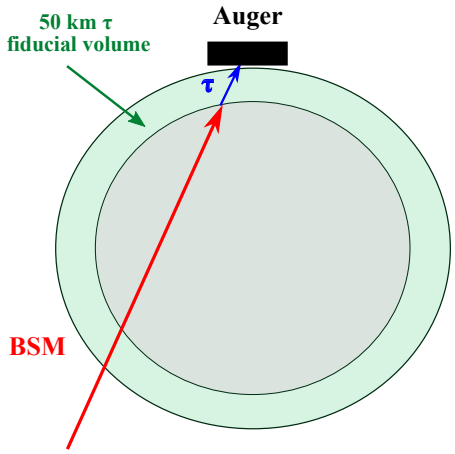

Figure 7.1: Schematic representation of the investigated BSM scenario: the hypothetical BSM-particle (red arrow) crosses the Earth without interacting, due to the reduced cross section, and creates τ-leptons (blue arrow) within the last 50 km distance below the surface. The τs can further initiate EAS and be detected by Auger.

Having the corresponding upper flux limits on steeply up-going τ-lepton induced air showers, $\Phi_\tau(E_{0,\tau})$, the required BSM flux can be further calculated:

$$\Phi_{BSM}(E_{BSM}) = \Phi_\tau(E_{0,\tau}) \cdot \frac{1}{P(BSM \rightarrow \tau)} \tag{7.1}$$

where $\Phi_\tau(E_{0,\tau})$ is plotted in Fig. 6.14 and $P(BSM \rightarrow \tau)$ represents the probability of such particles to create the investigated τs. The BSM particle energy E_{BSM} is related to the energy of τ-leptons via the investigated energy transfer. Since the current study is a hypothetical one, the value of the energy transferred to the τs is not known. Therefore, $E_{BSM} = 2 \cdot E_{0,\tau}$, corresponding to a 50% energy transfer, has been chosen. However, the results have also been investigated for different energy transfer values. The difference in the corresponding flux upper bounds resulted is not relevant, given the several orders of magnitude difference obtained for various BSM cross section values, as shown in Fig. 7.7 and highlighted in Appendix G.

As can be seen in Fig. 7.1, the particles need to survive Earth propagation up to small distances below the crust and further on interact within the last 50 km distance. As a result, two different processes define the probability of τ creation. Therefore, as shown in Eq. 7.2, the BSM probability to produce τ-leptons can be defined as:

$$P(BSM \rightarrow \tau) = P_{survive,\,BSM} \cdot P_{int\,BSM} \tag{7.2}$$

In order for any BSM particle to be able to cross such a significant amount of matter without interacting, the corresponding cross section needs to be lower than the SM neutrino ones. The corresponding survival probability inside Earth, $P_{survive,\,BSM}$, is going to increase with the reduction of the cross section. However, the interaction probability within the last few km distance, $P_{int,\,BSM}$, will decrease with a smaller cross section. Consequently, a competition between the two probabilities in Eq. 7.2 is present. This leads to the conclusion that an optimum value of the BSM cross section, which maximizes the τ-production probability $P(BSM \rightarrow \tau)$, and correspondingly gives the strongest flux upper limit needs to be found.

For a conclusive study, the two probabilities present in Eq. 7.2 are carefully investigated for each zenith angle $\theta \in [110°, 180°]$. The probability $P(BSM \rightarrow \tau)$ is then obtained by integrating over the zenith range of interest, as detailed below.

7.1.1 Survival probability inside Earth

The particles are initially propagated in small steps inside Earth, with their survival probability being evaluated at each step. Since the investigated τ-leptons are created from a maximum distance $D^{max}_{inj,\,\tau} = 50\,\text{km}$ below the surface, the maximum propagation length inside Earth, L_{max}, needs to be evaluated accordingly:

$$L_{max} = 2R_E \cos\theta - D^{max}_{inj,\,\tau} \tag{7.3}$$

where $R_E = 6378\,\text{km}$ is the Earth radius, θ is the investigated zenith angle and $D^{max}_{inj,\,\tau}$ is the maximum τ-injection depth inside Earth, as set for the τ-leptons study within the previous chapter. At each propagation step the surviving probability is evaluated, taking into consideration the various Earth density layers, as defined within the Preliminary Earth Model [102]. The amount of traversed density layers is defined by the maximum propagation length L_{max}, as sketched in Fig. 7.2.

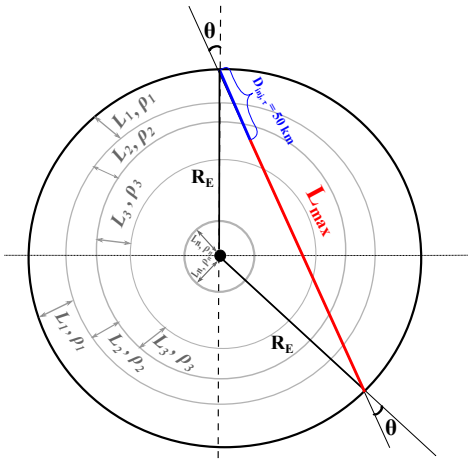

Figure 7.2: Illustrative view of the simulation procedure. The maximum distance the BSM particle can propagate through Earth, L_{max}, (red line) is defined by the zenith angle θ and the maximum τ-lepton injection depth (blue line). Depending on the value of L_{max} a different number of Earth layers L_i, with the corresponding density ρ_i, are traversed.

For an accurate representation, a number of $n = 2 \cdot 6378$ propagation steps have been

chosen, corresponding to a propagation length of $\Delta l = 1\,\text{km}$. The probability for a particle to survive after the propagation step i, up to the distance l_i, is further defined in Eq. 7.4

$$P_{survive,\,i}\,(0, l_i) = \exp\left(- l_i \, \cos\theta \cdot \frac{\rho_i \, N_A \, \sigma}{M} \right) \tag{7.4}$$

where $l_i \cos\theta$ represents the propagation distance. After each propagation step, the step length Δl is added to the propagation distance, such that:

$$l_i = l_{i-1} + \Delta l \tag{7.5}$$

This process is repeated until the propagation length $l_i \cos\theta$ is equal to L_{max}. After each propagation instance, the corresponding value of the Earth density ρ_i at a travelled distance $l_i \cos\theta$ is evaluated, according to the Preliminary Earth Model [102].

The probability of a particle with a zenith angle θ, to survive Earth propagation up to the maximum distance L_{max} is then obtained:

$$P_{survive}(\theta, L_{max}, \sigma) = \exp\left[\frac{-N_A \cdot \sigma \, \cos\theta}{M} \cdot \sum_{i=1}^{n(\theta)} l_i \cdot \rho_i \right] \tag{7.6}$$

where $N_A \approx 6.02214 \cdot 10^{23}\,\text{mol}^{-1}$ is the Avogadro's number, $M \approx 33.4\,\text{g} \cdot \text{mol}^{-1}$ represents the molar mass, calculated considering the Earth's chemical composition from [103]. The sum is calculated up to the total number of propagation steps $n(\theta)$, which satisfies the condition $l_i \cos\theta \leq L_{max}$, as explained above.

The survival probability inside Earth has been calculated for a fixed value of the cross section, $\sigma_{SM} = 0.77 \cdot 10^{-31}\,\text{cm}^2$, for all zenith angles of interest: $\theta \in [110°, 180°]$ and is plotted in Fig. 7.3. This value corresponds to the SM charged current (CC) neutrino cross section at an energy of $E_\nu \approx 10^{20}\,\text{eV}$, according to [99] [1]. As expected from Eq. 7.6, the survival probability

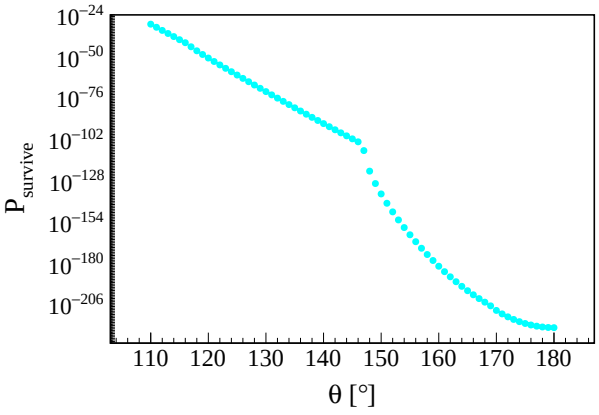

Figure 7.3: Probability of a particle with a fixed cross section $\sigma_{SM} = 0.77 \cdot 10^{-31}\,\text{cm}^2$ to survive Earth propagation up to a distance of 50 km below the surface, as a function of the zenith angle θ

is decreasing with the increasing zenith angle. As more vertical zenith angles will cross a bigger amount of the Earth's matter, they will correspondingly traverse more Earth density layers.

[1] The numerical value of the cross section σ is not of a particular interest in this stage of the study. It can be changed or set to any other value. The main focus here is on the results obtained at the reduction of σ.

Consequently, the behavior of the survival probability with respect to θ is strongly related to the traversed depth inside Earth by the particles under different zenith angles: $X(\theta) = \cos\theta \cdot \sum_{i=1}^{n(\theta)} l_i \cdot \rho_i$. The dependency of the traversed depth $X(\theta)$ on the zenith angles is plotted in Fig. 7.4. For completeness the Earth density with respect to the radius R_E is also plotted. As seen in Fig. 7.2, the most vertical zenith angles $\theta \approx 180°$ will cross all the density layers, resulting in a significantly longer traversed depth.

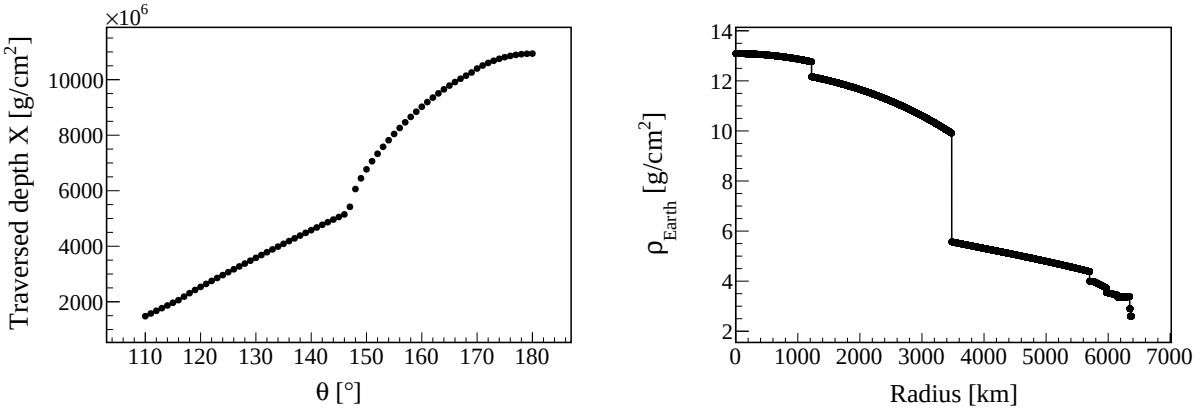

(a) Thickness of Earth encountered by incoming particles with respect to the zenith angle

(b) Earth density profile according to the Preliminary Earth Model [102] with respect to the Earth radius

Figure 7.4: Traversed matter inside Earth for different incidence angles of the incoming particles (Fig. 7.4(a)). The most vertical zenith angles cross a larger amount of Earth matter, passing through all density layers with the corresponding density values (Fig. 7.4(b))

The cross section σ plays a crucial role in the survival probability, according to Eq. 7.6. Therefore, by reducing the interaction cross section σ value, any particle propagating inside Earth will have an increased survival probability. This results in a higher flux at a depth of 50 km below the surface, where the τ-leptons are injected.

7.1.2 Interaction probability within the last 50 km distance below Earth

In order for any hypothetical particle to be able to create the investigated τs, surviving the Earth propagation represents only one of the requirements. Additionally, the particles need to interact within the last 50 km distance below Earth in order to produce the τ-leptons, as sketched in Fig. 7.1. Consequently, the interaction probability within this distance needs to be evaluated. Since the τs are injected flat in distance, as mentioned within the previous chapter, and the Earth density at the corresponding distance is constant, $\rho_{Earth}(D^{max}_{inj,\tau}) \approx 2.6\,\mathrm{g/cm^2}$, the interaction probability will be independent on the zenith angle θ. The cross section value σ, is therefore the main factor which influences the probability of any particle to interact within the last 50 km fiducial volume:

$$P_{int}(D^{max}_{inj,\tau}, \sigma) = 1 - \exp\left[\frac{-D^{max}_{inj,\tau} \cdot \rho_{Earth}(D^{max}_{inj,\tau}) \cdot N_A \cdot \sigma}{M}\right] \tag{7.7}$$

with N_A the Avogadro's number, M the molar mass defined within the previous section and $D^{max}_{inj,\tau} = 50\,\mathrm{km}$ the maximum injection distance inside Earth of the τ-leptons.

The interaction probability has also been evaluated for the same SM cross section of $\sigma_{SM} = 0.77 \cdot 10^{-31}\,\mathrm{cm}^2$ and is plotted in Fig. 7.5, with respect to the zenith angle $\theta \in [110°, 180°]$. The independence of the zenith angle is observed.

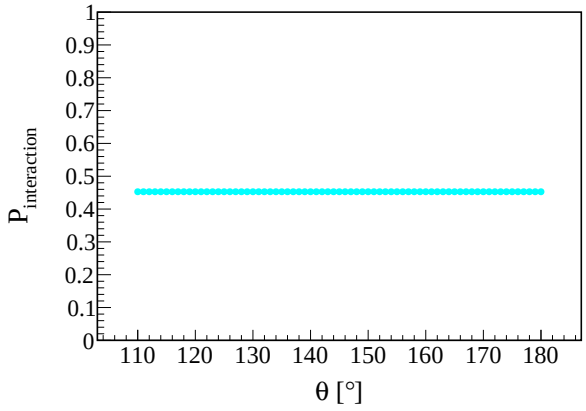

Figure 7.5: Probability of a particle with a fixed cross section $\sigma_{SM} = 0.77 \cdot 10^{-31}\,\mathrm{cm}^2$ to interact within the last 50 km distance below Earth with respect to the zenith angle θ

The reduction of the cross section σ will result in a lower value of the interaction probability, according to Eq. 7.7. As a consequence, the BSM cross section σ_{BSM} can not be infinitely reduced: even if more particles survive Earth propagation, the τ-leptons production would be lower, given the reduced interaction probability value.

7.1.3 Probability of a BSM particle to produce τ-leptons

Since any hypothetical particle that would create the studied τs needs to survive Earth propagation and further interact within the $D^{max}_{inj,\tau}$ distance , the corresponding τ-production probability at a given zenith angle θ is defined as the product of the two likelihoods:

$$P(BSM \rightarrow \tau)(\sigma, \theta) = P_{survive}(\theta, L_{max}, \sigma) \cdot P_{int}(D^{max}_{inj,\tau}, \sigma) \tag{7.8}$$

A competing process between the survival probability inside Earth defined in Eq. 7.6 and the interaction probability within the last km appears, when the cross section value is reduced. This implies that by reducing the SM cross section by several orders of magnitude, the probability $P(BSM \rightarrow \tau)$ is going to increase, reach a maximum value and further on decrease again, when the interaction probability becomes dominant. The cross section value corresponding to the maximum probability $P(BSM \rightarrow \tau)$ will be further referred to as the optimum BSM cross section. At this value of σ_{BSM} the corresponding hypothetical particle fluxes are minimal, resulting in the most stringent upper flux limits.

In order to cross check the competitive process and correspondingly find the optimum cross section value, the probability of the BSM particle to create τ-leptons has to be properly evaluated. Both the Earth survival and the interaction probabilities are calculated for a fixed zenith angle θ, with $\theta \in [110°, 180°]$. The corresponding value of the τ-production probability,

$P(BSM \to \tau)$, is obtained by integrating over the whole zenith range of interest:

$$P(BSM \to \tau)\,(\sigma) = \int_{\theta=110^\circ}^{\theta=180^\circ} P(BSM \to \tau)(\sigma, \theta)\; d\theta \tag{7.9}$$

Different BSM scenarios can then be tested by decreasing the value of the standard model cross section σ_{SM}. The competitive behavior of the τ-production probability $P(BSM \to \tau)$ with the decrease of σ is observed in Fig. 7.6. The lowest value of $P(BSM \to \tau) \approx 3.4 \cdot 10^{-31}$ corresponds to the SM case with $\sigma_{SM} = 0.77 \cdot 10^{-31}\,\mathrm{cm}^2$. By decreasing the cross section,

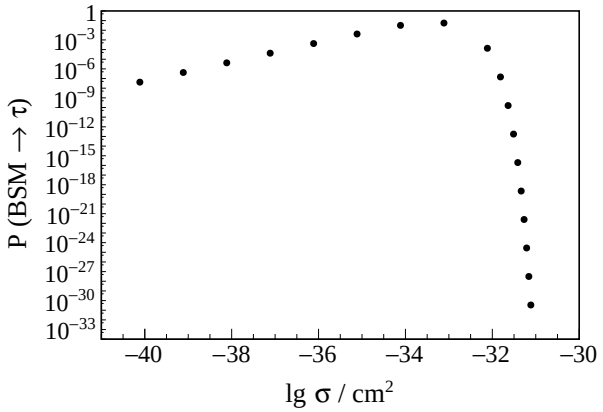

Figure 7.6: Probability of a hypothetical particle with zenith angles $\theta \in [110^\circ, 180^\circ]$ to produce τ-leptons within the last 50 km distance below Earth, with respect to the corresponding cross section. The highest cross section value corresponds to $\sigma_{SM} = 0.77 \cdot 10^{-31}\,\mathrm{cm}^2$

the probability is starting to increase. Having a BSM cross section reduced by one order of magnitude, $\sigma_{BSM} = 10^{-1} \cdot \sigma_{SM} = 0.77 \cdot 10^{-32}\mathrm{cm}^2$ the probability increases by ≈ 26 orders of magnitude. The increase in the probability continues up to an optimum value of $\sigma_{BSM} = 10^{-2} \cdot \sigma_{SM}$, after which point it starts to slowly decrease again. The optimum cross section value marks the region where the required BSM particles flux is minimum, corresponding to the most stringent upper limits. By further decreasing the cross section value, the interaction probability within the last 50 km distance $P_{int}(D^{max}_{inj,\tau}, \sigma)$ starts to dominate, as the survival probability inside Earth $P_{survive}(\sigma)$ is already maximized. This results in lower values of $P(BSM \to \tau)$ and correspondingly weaker upper flux bounds.

7.2 Flux limits on BSM particles producing steeply up-going τ-leptons

Following the above described procedure, the resulting BSM particle fluxes, required to produce the τ-lepton fluxes discussed in Chapter 6.7 and plotted in Fig. 6.14, can be calculated:

$$\Phi_{BSM}(\sigma; E_{BSM}) = \Phi_\tau(E_{0,\tau}) \cdot \frac{1}{P(BSM \to \tau)(\sigma)} \tag{7.10}$$

The conversion between the hypothetical particle's energy E_{BSM} and the τ-leptons energy $E_{0,\tau}$ is obtained by using a fixed value of a 50% energy transfer, resulting in $E_{BSM} =$

$2 \cdot E_{0,\tau}$. Given the unknown BSM process, the choice of this value is somewhat arbitrary and only motivated by several dark matter scenarios [104], [105]. However any other value can be easily implemented and tested for. A first exercise for a 100% energy transfer, $E_{BSM} = E_{0,\tau}$ has been studied and the results are shown in Appendix G. As it can be seen in Fig. G.1, the chosen energy transfer rate is having an insignificant contribution in the resulted upper limits when compared to the cross section effects.

Two different BSM cases are studied within this thesis: a fixed cross section value at any given energy and an energy-dependent cross section. As this is a hypothetical study, both scenarios are pertinent. In any such scenario, the main approach is following the same procedure described in the previous section.

7.2.1 Fixed cross section

A fixed value of the standard model cross section $\sigma_{SM} = 0.77 \cdot 10^{-31}\,\mathrm{cm}^2$ is considered for all of the energies of interest. Given a 50% energy transfer between the BSM particle and the investigated τ-leptons, this leads to $E_{BSM} \in [2 \cdot 10^{16.5}, 2 \cdot 10^{20}\,\mathrm{eV}]$. The probability of such hypothetical particles to create τ-leptons has been plotted in Fig. 7.6, for various BSM cross sections. Using the resulted $P(BSM \to \tau)$ values and introducing them in Eq. 7.10, the corresponding upper flux limits on BSM hypothetical particles with zenith angles $\theta \in [110°, 180°]$, are obtained for a CL=95%. The BSM results, together with the τ-induced air showers (red bullets) are plotted in Fig. 7.7. The fluxes are obtained for an E^{-2} τ-lepton energy spectrum. Following the τ-creation probability behavior, the flux upper limits are significantly improved with the reduction of the SM cross-section, resulting in ≈ 26 orders of magnitude improvement when the cross section is decreased by only one order of magnitude: $\sigma_{BSM} = 0.1 \cdot \sigma_{SM}$. By comparing the resulting SM upper bounds (light blue bullets in Fig. 7.7) with the current upper bounds on diffuse neutrino fluxes published in [8], the incompatibility between such events and the standard model theory becomes evident.

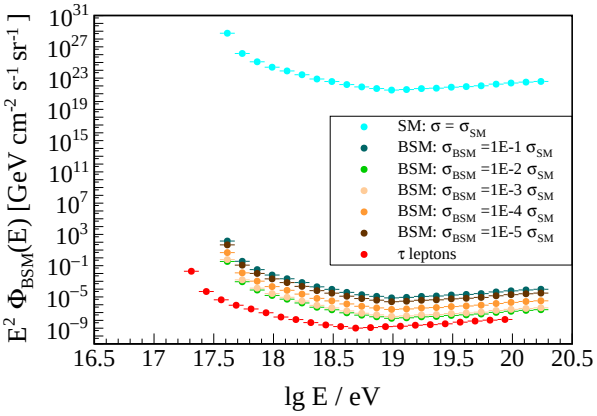

Figure 7.7: Upper flux bounds for a $CL = 95\%$ on steeply up-going ($\theta \in [110°, 180°]$) BSM particles producing τ-leptons. Results are obtained considering a fixed value of the SM cross section, $\sigma_{SM} = 0.77 \cdot 10^{-31}\,\mathrm{cm}^2$, at any given energy. The upper bounds on a flux of τ-leptons produced within the last 50 km below ground (red bullets) are shown for comparison.

By decreasing the cross section with several orders of magnitude, various BSM scenarios

are investigated. The most stringent BSM upper bounds are obtained for the optimum cross section $\sigma_{BSM} = 10^{-2}\sigma_{SM}$. For lower values of the cross section the flux limits are getting weaker, given the competing process between the survival probability inside Earth and the interaction probability within the last few km distance, as discussed above.

Moreover, as an energy transfer between the hypothetical particles and the studied τ-leptons have been considered, the corresponding upper bounds are shifted towards higher energy ranges than in the τs case. However, given the fixed SM cross section value, the BSM upper fluxes are following precisely the τ upper bounds behavior with respect to energy. The only influence of the BSM study in this case is shifting the upper bounds up and down, corresponding to different interaction cross sections studied. This characteristic is vanishing once a cross section energy dependence is considered, in which case the flux upper bounds behavior with respect to energy is influenced by both the τ-leptons fluxes as well as the cross section energy dependence model. Such a scenario has been investigated in detail using the SM cross section for the CC neutrino channel, $\sigma_{CC}(E)$, as explained below.

7.2.2 Energy-dependent cross section

In order to extend the applicability of the current study, a second approach considering a predefined cross section energy dependence is investigated. The chosen cross section energy dependence is the standard model one for the charged current neutrino-nucleon cross section, $\sigma_{SM}(E) = \sigma_{CC}(E)$, as taken from [106] and using the middle parametrization. The cross section behavior for the energy range of interest is plotted in Fig. 7.8 for consistency. The SM values are plotted with light blue, corresponding to the highest cross section values.

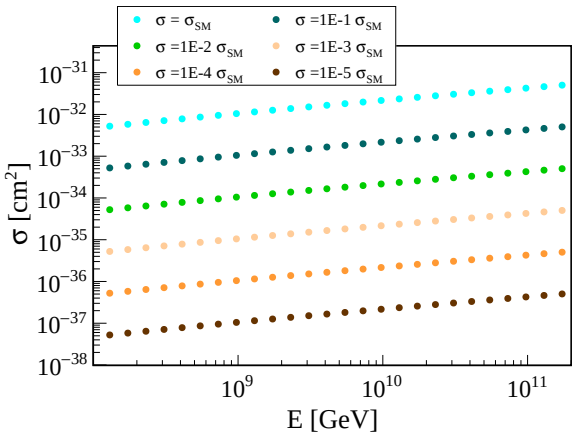

Figure 7.8: Model in which the energy dependence of the CC neutrino-nucleon cross section, $\sigma_{CC}(E)$ from [106] is applied to the BSM particles. BSM values are obtained by gradually decreasing the SM (light blue bullets) cross section values

Various BSM scenarios are investigated by reducing the corresponding cross section values by several orders of magnitude. The energy dependence is kept intact resulting in a BSM cross section defined as:

$$\sigma_{BSM}(E) = 10^{-m} \cdot \sigma_{SM}(E) \tag{7.11}$$

where $m > 0$ represents the reduction factor. Various BSM scenarios have been tested, corresponding to a maximum value of $m = 5$. The obtained results are discussed in detail below.

The Earth survival probability and interaction probability within the last 50 km distance are evaluated as explained above, for the given energy. Thus, Eq. 7.6 and Eq. 7.7 remain unchanged, with the exception that the energy dependence of the cross section is accounted for: $\sigma \to \sigma(E)$. As a result, each of the probabilities are gradually evaluated for each zenith angle θ at a given energy E:

$$P_{survive}(\theta, L_{max}, \sigma, E) = \exp\left[\frac{-N_A \cdot \sigma(E)\ \cos\theta}{M} \cdot \sum_{i=1}^{n(\theta)} l_i \cdot \rho_i\right] \tag{7.12}$$

respectively

$$P_{int}(D^{max}_{inj,\tau}, \sigma, E) = 1 - \exp\left[\frac{-D^{max}_{inj,\tau} \cdot \rho_{Earth}(D^{max}_{inj,\tau}) \cdot N_A \cdot \sigma(E)}{M}\right] \tag{7.13}$$

This in turn results in a corresponding energy dependent probability of hypothetical particles with zenith angles $\theta \in [110°, 180°]$, to create the investigated τ-leptons:

$$P(BSM \to \tau)\,(\sigma, E) = \int_{\theta=110°}^{\theta=180°} P(BSM \to \tau)(\sigma, E, \theta)\ d\theta \tag{7.14}$$

with $P(BSM \to \tau)(\sigma, E, \theta)$, analogous to Eq. 7.8, representing the probability of a hypothetical particle with zenith angle θ and energy E to create the investigated τ-leptons. The obtained values of $P(BSM \to \tau)(\sigma, E, \theta)$ are plotted in Fig. 7.9, using the corresponding cross section values shown in Fig. 7.8.

The probability of the hypothetical particle to create the studied τ-leptons is evaluated considering different BSM scenarios. The SM case, corresponding to the CC neutrino-nucleon cross section values at the energies of interest is plotted in the top left panel of Fig. 7.9. This results in the lowest values of $P(BSM \to \tau)(\theta, E)$, since the particles will interact during their propagation inside Earth and therefore not survive up to the 50 km distance below. As discussed above, the most horizontal zenith angles (light blue) have a significantly higher probability to survive Earth propagation without interacting, given the smaller amount of matter they are traversing. As the cross section is increasing with energy, the probability of any particles to traverse the Earth without interaction, $P_{surive}(\theta, L_{max}, \sigma, E)$, is decreasing, according to Eq. 7.12. As at those cross section values the survival probability inside Earth is very low, it will directly influence the evolution of the particle's probability to produce τ-leptons with respect to energy. When reducing the cross section by one order of magnitude, the probability is significantly increasing. For the most inclined zenith $\theta = 110°$ and highest energy $E_{BSM} = 2 \cdot 10^{20}$ eV, the probability is increasing by ≈ 16 orders of magnitude. However, given the similar probability behavior between the two $\sigma = \sigma_{SM}$ and $\sigma = 0.1 \cdot \sigma_{SM}$ cases (first two top panels in Fig. 7.9), it is clear that the survival probability inside Earth is still the main factor influencing $P(BSM \to \tau)$. This suggests that the cross section should be further decreased in order to obtain a higher τ-creation probability.

Higher τ-production probabilities are further observed for the $\sigma = 10^{-2} \cdot \sigma_{SM}$ scenario (top right panel in Fig. 7.9). Here the probability $P(BSM \to \tau)(\theta, E)$ starts to increase with energy, and therefore with a higher corresponding cross section value, suggesting that the Earth

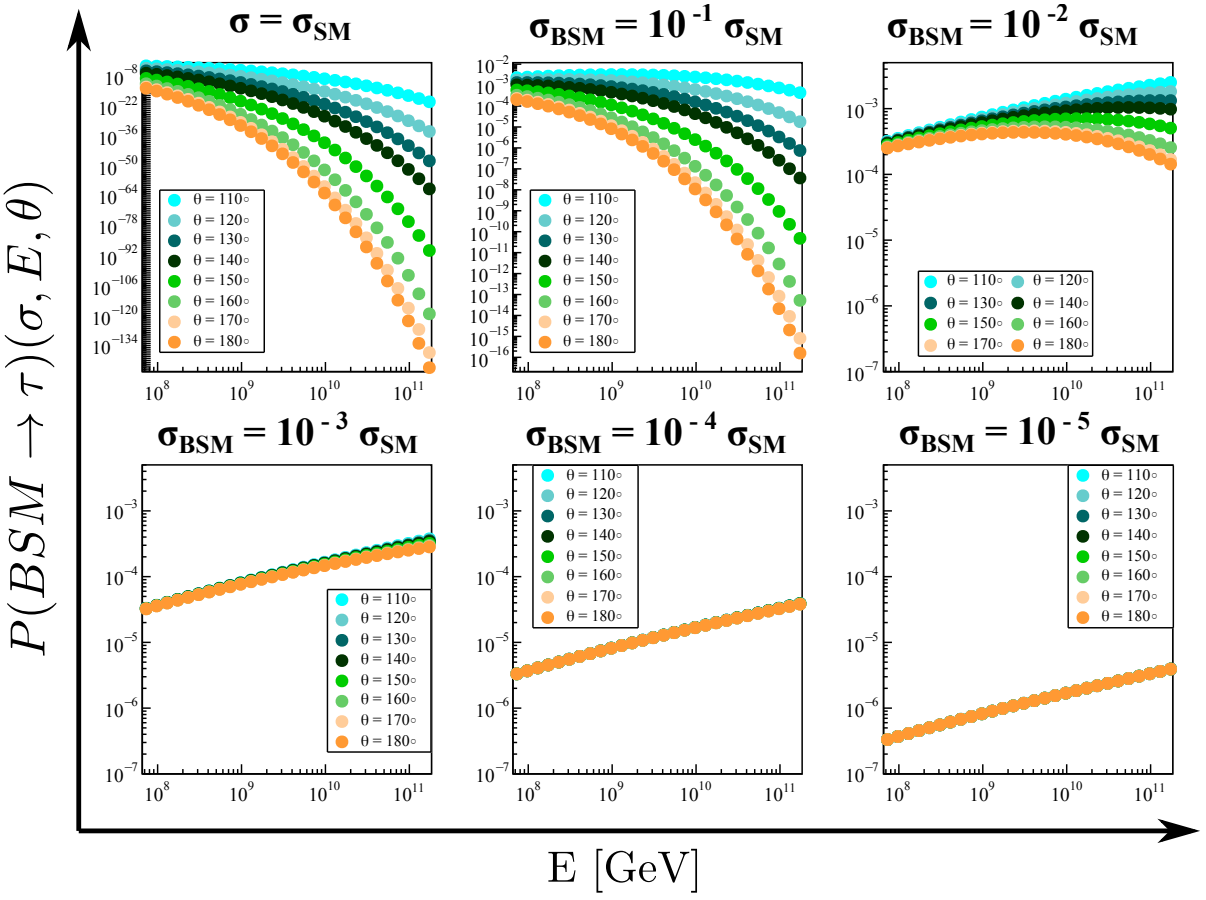

Figure 7.9: τ-production probability at different zenith angles as a function of energy. Various BSM scenarios are plotted in the 6 panels. As the values of $P(BSM \to \tau)(\sigma, E, \theta)$ are much lower for the first two cases, the corresponding y-axis have different ranges compared to the rest of the panels. This is done on purpose in order to observe the zenith dependence

survival probability starts to be maximized, and the interaction within the last few km is becoming dominant. This effect is visible for all zenith angles up to an energy of $E \approx 10^9$ GeV. The most horizontal zenith angles have a constant increase for the entire energy range of interest, while for the most vertical cases $P(BSM \to \tau)$ starts to decrease after a certain energy. This is again due to the different amount of traversed matter: as the most horizontal zenith angles will cross a very small portion of Earth, a reduced cross section by 2 orders of magnitude is able to maximize their survival. As a result, the interaction within the last few km becomes dominant for these events, resulting in an increased probability with respect to energy, according to the cross section energy dependence. In the case of the more vertical events, smaller values of the cross sections are needed in order to maximize their survival through Earth, given the fact that they cross a bigger amount of matter. As a result, at small cross section values (lower energies) they can survive Earth propagation and therefore have an increasing τ-production probability with respect to energy. However, as the cross section is increasing with energy, the survival probability starts to decrease again, according to Eq. 7.12. This results in an increase, followed by a plateau and a further decrease for the most vertical zenith angles, having the maximum τ-production probability value at different energies (cross sections), as it can be seen in the figure.

By further decreasing the cross section values, the zenith angle dependence starts to vanish. This is physically understood, as for sufficiently low cross section values, the survival probability inside Earth is maximized at any incident angle. Consequently, the interaction probability within the last few km distance below Earth, $P_{int}(D^{max}_{inj,\tau})$, becomes dominant. As a result, the τ-production probability is always increasing with respect to energy (bottom panels in Fig. 7.9). Another consequence of maximizing the survival probability inside Earth is the decrease in the resulting probability of hypothetical particles to create τs with lower BSM cross section values. This is pointing to the competitive behavior between $P(BSM \rightarrow \tau)(\sigma)$ and the BSM cross section. As mentioned above, by artificially decreasing the cross section by several orders of magnitude the probability $P(BSM \rightarrow \tau)(\sigma)$ is increased up to a maximum value, corresponding to an optimum σ_{BSM}. After this point it starts to decrease again, as it is mainly influenced by the interaction probability within the last few km distance. This can be already seen in Fig. 7.9, by comparing the top right and bottom three panels values [2].

The competitive behavior can be better studied once the integration over the zenith range of interest, $\theta \in [110°, 180°]$, is performed. As stated in the beginning of this subsection, the cross section energy dependence results in a corresponding energy dependent integrated probability of any particle to produce the investigated τ-leptons. The resulting $P(BSM \rightarrow \tau)(\sigma, E)$, defined in Eq. 7.14, is plotted in Fig. 7.10, for the BSM energies $E_{BSM} \in [2 \cdot 10^{16.5}, 2 \cdot 10^{20}\,\text{eV}]$, corresponding to a 50% energy transfer. As discussed above, the probability $P(BSM \rightarrow \tau)$ decreases with the increasing of energy for the $\sigma = \sigma_{SM}$ and $\sigma = 0.1 \cdot \sigma_{SM}$ cases, given the cross section energy dependence and the corresponding low survival probability inside Earth. By further reducing the cross section values, the integrated probability has an increasing evolution with energy. This is due to the fact that for such low cross sections the survival probability inside Earth is maximized, and therefore the interaction probability within the last few km distance is the main influencing factor. This also has the consequence of significantly lower

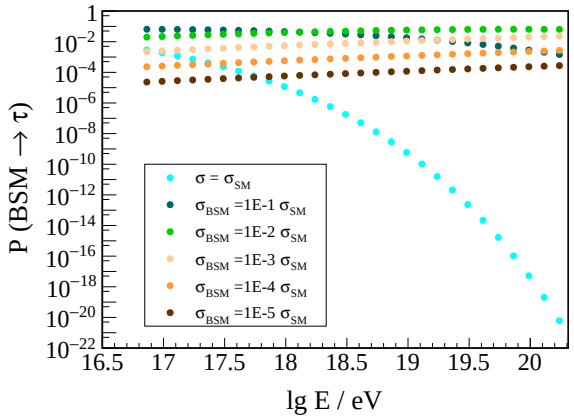

Figure 7.10: Probability of a hypothetical particle, $P(BSM \rightarrow \tau)$, with zenith angles $\theta \in [110°, 180°]$, to produce τ-leptons within the last 50 km distance below Earth, when a 50% energy transfer is considered. The cross section energy dependence is following the SM CC neutrino-nucleon cross section, $\sigma_{CC}(E)$, from [106].

[2] As the probability values for $\sigma = \sigma_{SM}$ and $\sigma = 0.1 \cdot \sigma_{SM}$ are much lower than for the other 4 investigated scenarios, the y-scale is different. This represents a compromise, as the probability evolution for different zenith angles could not be observed otherwise, which is desired for the discussion.

values of $P(BSM \rightarrow \tau)(E)$ with further reduction of the cross section. This can be seen by comparing the probability values for the last three BSM investigated scenarios, corresponding to $\sigma_{BSM} = 10^{-3} \cdot \sigma_{SM}, \sigma_{BSM} = 10^{-4} \cdot \sigma_{SM}$ respectively $\sigma_{BSM} = 10^{-5} \cdot \sigma_{SM}$, plotted in Fig. 7.10, where the decrease of cross section results in lower values of $P(BSM \rightarrow \tau)(E)$ over the entire energy range.

Furthermore, in the case of an energy-dependent cross section, the optimum cross section value corresponding to the maximum τ-production probability is also energy dependent. For energies $E_{BSM} \geq 10^{18}\,\text{eV}$ the probability is maximized for an optimum cross section of $\sigma_{BSM} \approx 10^{-2} \cdot \sigma_{SM}$, while for lower energies the optimum value is found at $\sigma_{BSM} \approx 10^{-1} \cdot \sigma_{SM}$. This is again due to the lower cross sections at those energies, and correspondingly higher survival probabilities inside Earth. Additionally, at the lowest energies $E \leq 10^{17.7}\,\text{eV}$, the decrease of the cross section by more than 3 order of magnitude results in lower values of $P(BSM \rightarrow \tau)(E)$ than those obtained for the SM case. This is explained by the competitive process between the Earth survival and the interaction within the last km with respect to a reduced interaction cross section.

The corresponding upper flux bounds can be further calculated for the different BSM scenarios with an energy dependent cross section model and a 50% energy transfer.

$$\Phi_{BSM}(\sigma(E_{BSM}), E_{BSM}) = \Phi_{\tau}(E_{0,\tau}) \cdot \frac{1}{P(BSM \rightarrow \tau)(\sigma, E_{BSM})} \tag{7.15}$$

The obtained upper flux limits, corresponding to a 95% CL, on steeply up-going ($\theta \in [110°], 180°]$) hypothetical particles producing τ-leptons within the last 50 km distance below Earth and transferring 50% of their energy to the τs are plotted in Fig. 7.11. The resulting upper bounds for the SM case, with only CC neutrino interactions considered, are plotted in light blue. Since the neutral current (NC) neutrino-nucleon cross sections are lower than the CC ones, the resulting probability which would account for both CC and NC neutrino interactions would be lower. As the current study is not dedicated towards neutrino-induced air showers, the regeneration effect is also neglected. An in-depth study regarding the effects of the neutrino regeneration on the τ-leptons exiting Earth can be found in [20].

The BSM scenarios, obtained by reducing the SM cross section by several orders of magnitude, while keeping the same energy dependence, are plotted with dark green - brown bullets in Fig 7.11. Since the minimum energy of the τ-leptons which are required to induce the extensive air showers triggered by the FD (see chapter 6 for more details) is $E_{0,\tau} \approx 10^{17.3}\,\text{eV}$, the minimum energy of any hypothetical particle producing them is $E_{BSM} \approx 2 \cdot 10^{17.3}\,\text{eV}$. This has the result of having an almost energy independent optimum cross section value of $\sigma_{BSM}(E) \approx 10^{-2} \cdot \sigma_{SM}(E)$, since the low energy region is almost entirely disregarded. However, as seen in Fig. 7.11, the first energy bins corresponding to $E_{BSM} \leq 10^{18}\,\text{eV}$ have a different optimum cross section of $\sigma_{BSM}(E) = 0.1 \cdot \sigma_{SM}(E)$, corresponding to the integrated probability values from Fig. 7.10.

Similar to the fixed cross section case described in the previous section, the artificial reduction of the interaction cross section is resulting in much more stringent flux upper bounds on various BSM scenarios. Since the interaction cross section increases with energy, this effect is much more prominent at the highest energies. Consequently, the best improvement in the flux

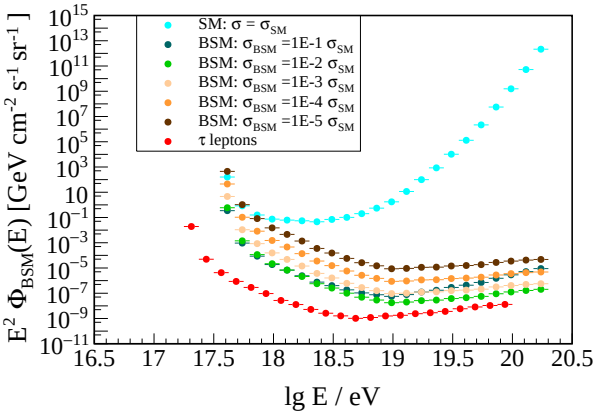

Figure 7.11: Upper flux limits for a $CL = 95\%$ on steepy up-going ($\theta \in [110°, 180°]$) BSM hypothetical particles producing τ-leptons (red bullets) within the last 50 km distance below Earth. The results are obtained using a 50% energy transfer and an energy dependent cross section, using the SM energy dependence model of the CC neutrino-nucleon cross section.

upper bounds, corresponding to the optimum cross section $\sigma_{BSM} \approx 10^{-2} \cdot \sigma_{SM}$, at the highest energy, $\lg E_{BSM} / \text{eV} \approx 20.23$, is on the order of ≈ 19 orders of magnitude. By comparison, the upper bounds at the lowest energies, $\lg E_{BSM} / \text{eV} \approx 17.61$ and an optimum cross section $\sigma_{BSM} = 0.1 \cdot \sigma_{SM}$ are improved by ≈ 2.5 orders of magnitude. Consequently, the cross section energy dependence is also an influencing factor in the upper bounds evolution with respect to energy. As a result, the hypothetical particle fluxes will be influenced both by the τ-leptons upper limits at a given energy, as well as by the corresponding interaction cross section energy-dependence model.

7.2.3 Reduced τ energy losses within several BSM scenarios

The energy loss model, dE_τ/dX, used in the dedicated τ simulations presented in chapter 6 is based on the ALLM [98] parametrization of the photonuclear processes. As discussed within the current chapter, this represents the main source of uncertainties, given the limited data at the corresponding energies. Several other parametrizations exist, resulting in lower values of dE_τ/dX. Consequently, an additional study regarding the energy losses effects on the corresponding flux upper bounds in several BSM scenarios has been investigated. In order to do so, the energy loss is artificially reduced by a given factor n. This results in turn to a corresponding increase of the maximum distance inside Earth from which the τ-leptons can escape with no decay and energies $E_{0,\tau} > 10^{16.5}$ eV, as long as the Earth density can be considered approximately constant.

$$\left(\frac{dE_\tau}{dX}\right)^* = \frac{1}{n} \cdot \left(\frac{dE_\tau}{dX}\right)_{ALLM} \quad \text{and} \quad D^*_{inj,max} = n \cdot D_{inj,max} \tag{7.16}$$

The constant density approximation holds up to maximum distances of $D^*_{inj,\,max} \approx 200$ km. At deeper distances inside Earth the density values start increasing significantly[3]. This

[3]The Earth density is in fact not constant for the 200 km distance: $\rho_{Earth} \in [2.6\,\text{g/cm}^2, 3.38\,\text{g/cm}^2]$. However

in turn results in a maximum decrease of the energy loss model.

It is important to mention that, under the constant density approximation, the artificial reduction of the τ-energy losses and corresponding increase in the maximum injection distance below Earth, is not affecting the τ-leptons study results. The average number of τs escaping Earth and their energy distribution stays the same, within the statistical fluctuation. The only difference is that the leptons are able to escape Earth from deeper distances inside. However, the energy reduction and implicitly the increase in the τ-injection distances is going to influence the hypothetical particles results. As the propagation distance inside Earth is decreased, the survival probability is going to increase, according to Eq. 7.12. Consequently, the overall probability of the hypothetical particles to create τ-leptons within the distance $D^*_{inj,\,max}$ is expected to increase. Thus, the strongest upper flux limits on BSM particles with $\theta \in [110°, 180°]$ are obtained for a minimum investigated value of the τ energy loss, corresponding to a maximum injection distance. The 95% CL integrated upper bounds for various BSM scenarios are plotted in Fig. 7.12, as a function of the investigated energy loss model. The maximum investigated distance coincides to $D^*_{inj,\,max} = 100\,\text{km}$, corresponding to a reduction factor $n = 2$. For a better visualization, the resulted upper bounds corresponding to $\sigma(E) = \sigma_{SM}(E)$ are plotted separately in Fig. 7.12(a). The limits are improved by a factor of ≈ 2 for the minimum investigated energy loss: $dE_\tau/dX = 0.5 \cdot (dE_\tau/dX)_{ALLM}$. However, this improvement is extremely small when compared to the several orders of magnitude gained by reducing the cross section values, as it can be seen in Fig. 7.12(b). Consequently, a reduction of the τ energy losses, under the above mentioned assumptions, does not have a significant effect on the obtained BSM results.

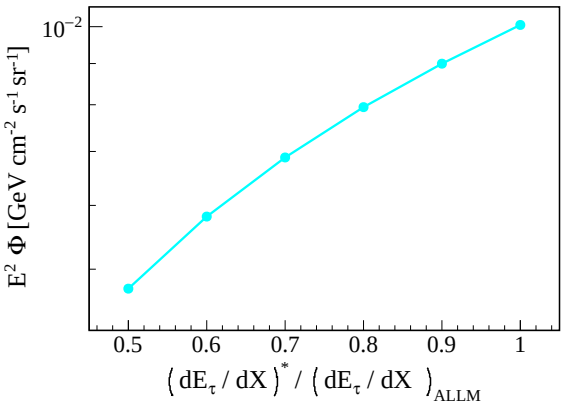

(a) Integrated upper bounds for different τ-energy losses obtained for the SM $\sigma(E) = \sigma_{SM}(E)$ case

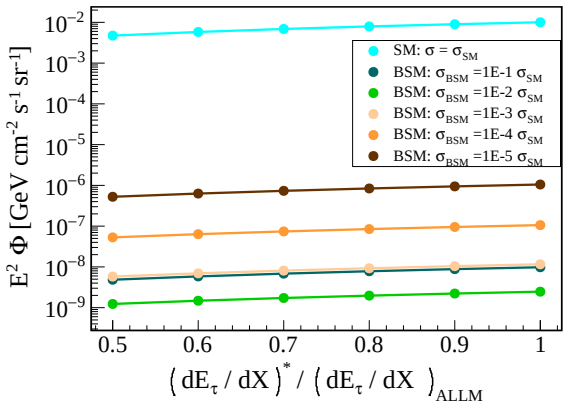

(b) Integrated upper bounds with respect to different τ-energy loses for various BSM scenarios

Figure 7.12: 95% CL integral upper flux limits on hypothetical particles with $\theta \in [110°, 180°]$ which are surviving Earth propagation and produce τ-leptons within the last few km distance below Earth, as a function of various τ-energy loss models

The presented upper flux bounds, studied for both a fixed cross section and an energy-dependent cross section scenario, emphasize the wide applicability of the steeply up-going τ-induced air showers results presented in chapter 6. Following a similar approach, any theoretical model aiming to explain the anomalous ANITA events [14], and resulting in the production of

for the purpose of this exercise an average value of $< \rho_{Earth} >= 3.0\,\text{g/cm}^2$ is considered

τ-leptons can be correspondingly constrained, as long as the cross section energy-dependence is known. Given the non-observation of any candidate event above the expected background, the current research highlights the broad capability of the Pierre Auger Observatory to set stringent upper bounds on various hypothetical models resulting in the production of ultra-high energy, steeply up-going ($\theta \in [110°, 180°]$) τ-leptons. Furthermore, the current results can be extended to the Earth-Skimming (ES) channel ($\theta \in [90°, 95°]$), using the dedicated neutrino searches published by the collaboration [7], [8].

7.3 BSM particles in the Earth-Skimming channel

The Pierre Auger Observatory has a high sensitivity towards the detection of τ-leptons resulting from CC tau-neutrinos, ν_τ, interactions in the Earth's crust. The τs leave the Earth and further decay in the atmosphere, initiating thus Earth-Skimming extensive air showers. In order for the ν_τ to produce such showers, they need to have highly inclined zenith angles. As discussed within the previous sections, the more vertical the events are, the more amount of the Earth matter they traverse. Given the neutrino interaction cross sections values, the Earth-Skimming channel in Auger is defined by zenith angles $\theta \in [90°, 95°]$. Such neutrino-induced air showers, with energies $E_\nu \in [10^{17}, 10^{20}\,\text{eV}]$ can be observed by using the Surface Detector of the Pierre Auger Observatory. Several neutrino searches have been performed by the collaboration [96], [7], [8], [10], [107]. As no candidate event has been found, corresponding upper flux limits have been set on various neutrino sources.

Using the the already published results in terms of upper flux limits and exposure on neutrino induced air showers [7], [8], a similar BSM scenario can be applied to the ES channel. A hypothetical particle with a reduced energy-dependent cross section $\sigma_{BSM}(E)$ defined according to Eq. 7.11, with zenith angles $\theta \in [90°, 95°]$ and energies $E_{BSM} \in [10^{17}, 10^{20}\,\text{eV}]$, is propagated through Earth and its probability to create τ-leptons within the last 50 km distance below the surface is evaluated. In order to translate the neutrino upper bounds published in [8] to corresponding upper limits on BSM particle fluxes, the exit probability of the τ-leptons p_{exit} defined in [8] and [7] has to be re-evaluated correspondingly.

7.3.1 Probability of ES τ-leptons produced by BSM particles to exit the Earth

The probability of an Earth skimming τ-lepton, produced by a ν_τ inside the crust, to emerge in the atmosphere, p_{exit}, is calculated in the dedicated neutrino searches [7], [8]. Both CC and NC interactions, as well as ν_τ regeneration are accounted for. Since the current study is only considering CC interactions, the probability of a τ-lepton to emerge from Earth is correspondingly calculated for this scenario. The BSM probability to produce the leptons within the last 50 km distance $P(BSM \to \tau)(\sigma, E)$ is therefore convoluted with the τ-leptons probability to escape the fiducial volume. Consequently, the probability of an ES τ-lepton with energy $E_{0,\tau}$, produced by a hypothetical particle with energy E_{BSM} within the last few km distance, to escape Earth is defined as:

$$P^*(BSM \to \tau)(\sigma, E_{BSM}, E_{0,\tau}) = P(BSM \to \tau)(\sigma, E_{BSM}) \cdot P_\tau^{escape}(E_{0,\tau}) \tag{7.17}$$

where $P(BSM \rightarrow \tau)(\sigma, E_{BSM})$ is defined according to Eq. 7.14, for $\theta \in [90°, 95°]$. The probability of τ-leptons to escape Earth, $P_{\tau}^{escape}(E_{0,\tau})$, is not influenced by the different cross section values, being only related to the τs propagation[4]. This probability has been calculated for the τ-energies of interest, using the OnlyTauSim code described in section 6.1.1 and is plotted in Fig. 7.13. Given the constant Earth density $\rho_{Earth} \approx 2.6\,\mathrm{g/cm^2}$ at the distances of interest, $D \leq 50\,\mathrm{km}$, inside Earth, and the flat injection in distance, the results are independent on the zenith angles. The τ probability to exit Earth without decay, P_{τ}^{escape}, is increasing with the

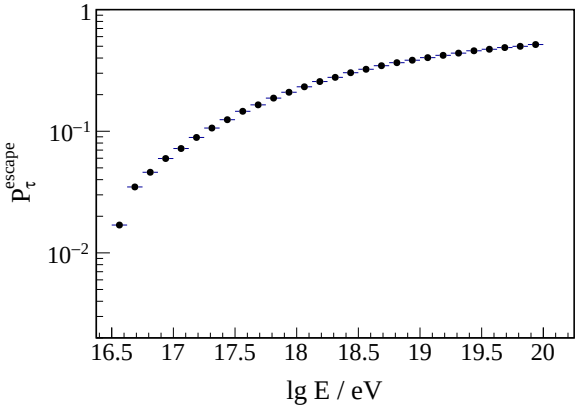

Figure 7.13: Probability of τ-leptons produced within the last 50 km distance below Earth to exit in the atmosphere, as a function of their primary energy. Results are obtained for a flat energy $\gamma = -1$ spectrum in an energy range $E_{0,\tau} \in [10^{16.5}, 10^{20}]\,\mathrm{eV}$ with τs injected flat in distances up to 50 km

leptons energies, given the corresponding decrease in the decay probability at higher energies. The τ-energy losses inside Earth are further contributing to this evolution in terms of energy.

In order to obtain the probability of an ES τ-lepton produced by a hypothetical particle to escape, $P^*(BSM \rightarrow \tau)$, defined in Eq. 7.17, the probability of such particles to produce τs within the last 50 km below Earth, $P(BSM \rightarrow \tau)$, has to be further evaluated. Using the CC neutrino-nucleon cross section energy dependence, $\sigma_{SM}(E) = \sigma_{CC}(E)$ from [106], the BSM scenarios are obtained by gradually decreasing the SM value by several orders of magnitude. The investigated BSM cross section values are the same as in the steeply up-going case, plotted in Fig. 7.8. The probability of a hypothetical particle with a zenith angle θ and energy E to create τ-leptons within the last 50 km distance below Earth, $P(BSM \rightarrow \tau)(\sigma, E, \theta)$ is obtained according to Eq. 7.8. The corresponding values of $P(BSM \rightarrow \tau)(\sigma, E, \theta)$ for the ES channel with $\theta \in [90°, 95°]$ at the energies of interest $E \in [10^{17}, 10^{20}]\,\mathrm{eV}$ are plotted in Fig. 7.14 for various BSM scenarios.

Two main important aspects are immediately observed when comparing the probability of τ-production in the steeply up-going case with $\theta \in [110°, 180°]$, illustrated in Fig. 7.10, with the ES case corresponding to $\theta \in [90°, 95°]$, plotted in Fig. 7.14. For a cross section corresponding to the SM scenarios, (first panel in both figures), the probability $P(BSM \rightarrow \tau)$ is maximized for the Earth skimming channel. This is physically understood, as the very horizontal events are traversing a very small amount of Earth's matter, as discussed within the previous sections. As a consequence, the survival probability inside Earth is already maximized for the most

[4] In the case of the steeply up-going showers this probability is accounted for within the τ simulation procedure, described in section 6.1.1

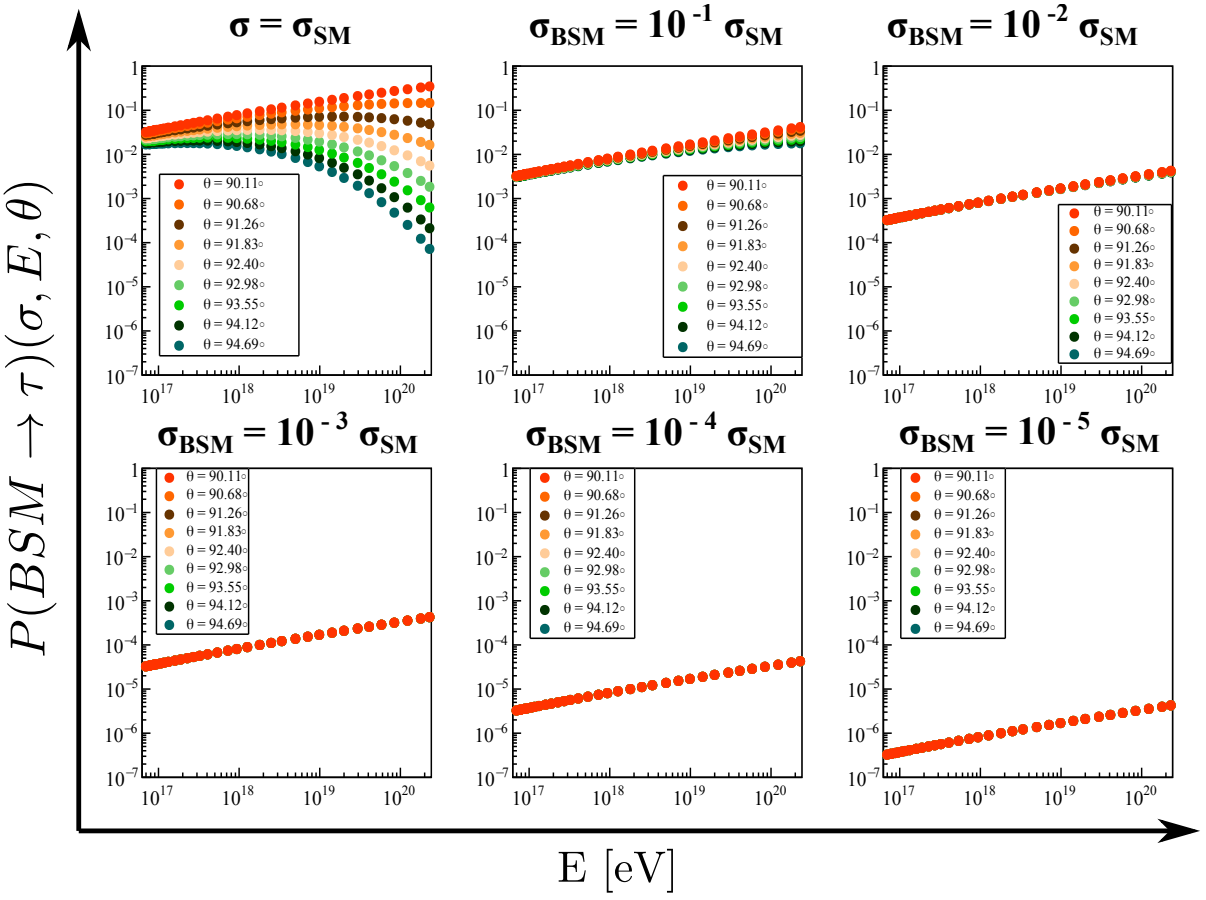

Figure 7.14: Probability of a hypothetical particle with zenith angles $\theta \in [90°, 95°]$ to produce τ-leptons within the last 50 km distance below Earth with respect to its primary energy, for different values of the zenith angle θ. The cross section energy dependence $\sigma_{CC}(E)$ from [106] is used. The probability $P(BSM \to \tau)(\sigma, E, \theta)$ is investigated in several BSM scenarios, plotted in the 6 panels.

horizontal events. As the interaction probability represents the main influencing factor in this case, the τ-creation probability, $P(BSM \to \tau)$, is increasing with the increase of energy, given the corresponding cross section increase with energy. This is seen for the most horizontal zenith angles (red and orange bullets corresponding to $\theta = 90.11°$ respectively $\theta = 90.68°$ in Fig. 7.14) at all energies. For slightly more vertical angles $\theta > 91°$, the probability is increasing up to a certain energy, after which point it starts to decrease again. This behavior can be seen in the steeply up-going case as well, for a $\sigma_{BSM} = 10^{-2} \cdot \sigma_{SM}$ scenario. The reasoning for this behavior is the same in essence: as more vertical zenith angles cross a larger amount of matter, the survival probability inside Earth is correspondingly lower. As the interaction cross section is increasing with energy, the corresponding events have a lower chance of crossing the Earth's matter without interaction. However, as already discussed, (see Eq. 7.14) in order to obtain $P(BSM \to \tau)(\sigma, E)$ in a given zenith range, an integration over the zenith angles of interest is needed. Consequently, the most horizontal events are having the strongest influence in the overall behavior.

The second important difference observed between the steeply up-going and ES channel comes from the study of several BSM scenarios. As discussed above, in the $\theta \in [110°, 180°]$ case, by decreasing the cross section by several orders of magnitude, the probability of a hypothetical

particle to produce τ-leptons within the last few km below Earth can be significantly increased. The opposite situation is seen in the ES case, where the cross section reduction is resulting in lower probabilities. This is again due to the fact that the interaction probability within the last km below Earth is dominant for the Earth skimming events. Moreover, as the last few km distance below Earth is considered, the interaction probability within this distance is independent on the zenith angle, as shown in Fig. 7.5. As a consequence, once the Earth survival is maximized for all zenith angles, the probability of a hypothetical particle to produce τ-leptons $P(BSM \rightarrow \tau)(\sigma, E)$ is the same for any θ. This is observed in the bottom 3 panels, corresponding to $\sigma_{BSM} \leq 10^3 \cdot \sigma_{SM}$, of Fig. 7.9 and Fig. 7.14.

As seen in Eq. 7.17, the τ-production probability $P(BSM \rightarrow \tau)(\sigma, E)$ is only one of the terms needed for estimating the ES τ-fluxes. However, as the probability of τ-leptons to exit Earth $P_\tau^{escape}(E_{0,\tau})$ is not influenced by the different cross section values, it will only lower the final $P^*(BSM \rightarrow \tau)$ value, without changing the obtained results for any BSM cases. This can be seen in Fig. 7.15(a), where the probability of a hypothetical particle to create the τs, $P(BSM \rightarrow \tau)$ is plotted for the the $\sigma = \sigma_{SM}$ case. In the Fig. 7.15(b) the resulting probability of a hypothetical particle to create τ-leptons which would exit the Earth, $P^*(BSM \rightarrow \tau)$, defined in Eq 7.17 is plotted for the zenith angles of interest.

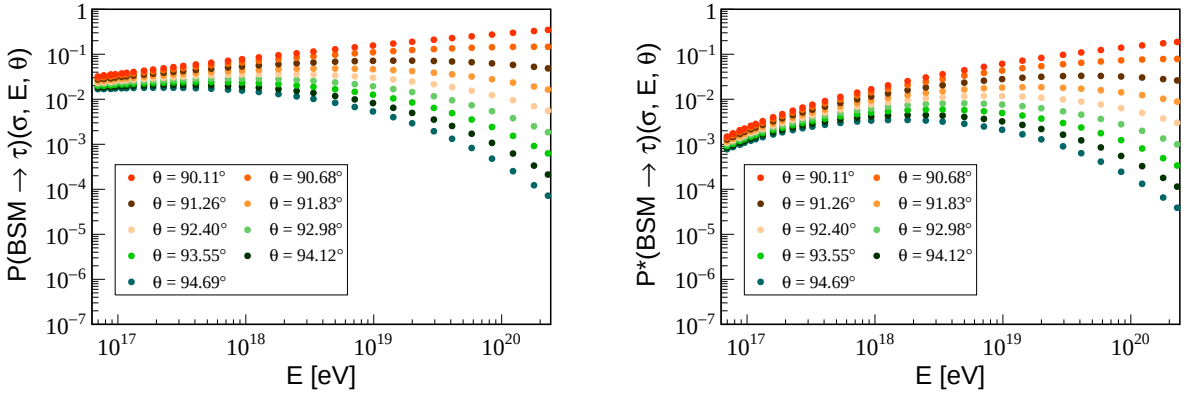

(a) Probability of a hypothetical particle to produce τ-leptons in the last few 50 km distance below Earth

(b) Probability of a hypothetical particle to produce τs, within the last 50 km below Earth, which exit the Earth and can further decay in the atmosphere

Figure 7.15: Influence of the τ escape probability P_τ^{escape} on the expected number of τ-leptons created by a hypothetical particle and entering the atmosphere. Results are presented for a $\sigma = \sigma_{SM}$ scenario

The τ probability to exit Earth without decay, $P_\tau^{escape}(E)$, reduces the final probability $P^*(BSM \rightarrow \tau)$. This effect is especially important at low energies $E \leq 10^{18}$ eV. As the τ energies are increasing, the escape probability is also increasing (see Fig. 7.13) and approaches a maximum value. For a one to one comparison, the results in Fig. 7.15 are obtained considering a total energy transfer between the BSM particle and the τ-leptons: $E_{BSM} = E_\tau$. This is further changed in the context of upper flux bounds, as described in section 7.3.2.

As discussed in the beginning of the subsection, the values of the τ escape probability are independent on the interaction cross section values, having the overall effect of decreasing the total probability $P^*(BSM \rightarrow \tau)$ values. Consequently, as seen in Fig. 7.14, the ES channel is going to be most sensitive to the SM case and gradually loose its sensitivity to any BSM

scenario with a reduced cross section. This effect is further reflected in the corresponding upper flux limits plotted in Fig. 7.17.

7.3.2 Flux upper bounds on BSM particles in the ES channel

Since in the ES case the exit probability plays a crucial role in the exposure calculation [8], this has been re-evaluated accordingly for the different BSM scenarios, as explained in the previous section. According to Eq. 3.2 from [8], the SD exposure to earth-skimming events is defined as:

$$\mathcal{E}_{ES}(E_\nu) = \int_A \int_\theta \int_\phi \int_{E_\tau} \int_{h_{dec}} \int_t |\cos\theta| \sin\theta \, p_{exit} \; p_{dec} \; \varepsilon_{ES} \; \mathrm{d}A \, \mathrm{d}\theta \, \mathrm{d}\phi \, \mathrm{d}E_\tau \, \mathrm{d}h_{dec} \, \mathrm{d}t \tag{7.18}$$

In order to calculate the corresponding exposure to BSM particles producing τ-leptons with zenith angles $\theta \in [90°, 95°]$, the exit probability, p_{exit}, in Eq. 7.18 is replaced by the corresponding $P^*(BSM \rightarrow \tau)$ defined in Eq. 7.17. Additionally, the neutrino energy E_ν is further referred to as the hypothetical particle's energy E_{BSM}. Thus, the exposure becomes:

$$\begin{gathered} \mathcal{E}_{ES}(E_\nu) = \mathcal{E}_{ES}(E_{BSM}) \\ \text{with} \\ p_{exit}(E_\nu, \theta, E_\tau) = P^*(BSM \rightarrow \tau)(\sigma, E_{BSM}, \theta, E_\tau) \end{gathered} \tag{7.19}$$

Having access to the collaboration data, the other terms in Eq. 7.18 are directly accessed during the calculation and remain unchanged. As the exposure results are provided in terms of neutrino energies, additional calculations need to be performed in order to translate it in terms of τ-lepton energies. This is of a particular importance for the further considerations of the energy transfer. Consequently, additional MC simulations have been implemented in this regard.

Energy transfer to τ-leptons

In order to properly calculate the corresponding upper bounds on BSM particles in the ES channel, an energy transfer to τ-leptons has to be considered. Therefore, the exposure results from [7] and [8] has to be provided in terms of τ-leptons energies. As seen in Eq. 7.18 and 7.19, the only factor depending on both E_τ and E_ν comes from the probability of a particle to create a τ-lepton which would in turn exit the Earth, $p_{exit}(E_\nu, \theta, E_\tau)$. Having direct access to the collaboration data used in the dedicated searches, and using the fact that the energy dependence of the exposure is mainly influenced by the most horizontal zenith [9], the disentanglement between E_τ and E_ν in Eq. 7.18 has been achieved. Therefore, by fixing the zenith angle to $\theta_{min} = 90.11°$[5] and calculating the τ exit probability for a total energy transfer $E_\nu = E_\tau$, the detector identification efficiency with respect to the neutrinos primary energy is obtained.

$$Eff(E_\nu) = \frac{\mathcal{E}(E_\nu)}{p_{exit}(E_\nu, \theta_{min}) \sin\theta_{min} \cos\theta_{min}} \tag{7.20}$$

[5] This coincides with the minimum zenith investigated in [7], [8], [9].

where $p_{exit}(E_\nu, \theta_{min}) = P^*(BSM \rightarrow \tau)(\sigma, E_{BSM}, \theta_{min})$ has been calculated for $\sigma = \sigma_{SM}$ and is plotted with red bullets in Fig. 7.15(b). The resulting efficiency for the neutrino energies of interest, as obtained within the dedicated ES studied from [7], [8] is plotted in Fig. 7.16 with black bullets.

Having the neutrino energy dependence, the results can be further translated in terms of the τ-lepton energy. As in the dedicated neutrino searches, the parton distribution results from [108] have been used for the energy transfer calculations, the same data is further used. The corresponding Bjorken-y distributions are directly taken from [108], with y defined as:

$$y = \frac{E_\nu - E_\tau}{E_\nu} \tag{7.21}$$

In order to obtain the τ-energy distribution, a MC simulation has been used. For each neutrino energy E_ν a number of 1000 CC interactions have been simulated and the resulting τ-lepton energy distribution has been obtained according to Eq. 7.21. The resulting identification efficiency in terms of E_τ is plotted with red bullets in Fig. 7.16. This would coincide to the corresponding efficiency for a total energy transfer: $E_\nu = E_\tau$.

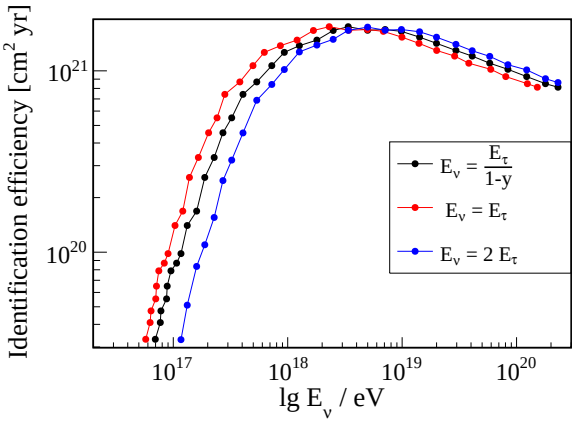

Figure 7.16: Identification efficiency (defined in Eq. 7.20) of the SD of the Pierre Auger Observatory to ν_τ ES induced air showers, as a function of the neutrino energy, when different energy transfer rates to the τ-leptons are considered

As it can be seen in Fig. 7.16, the identification efficiency is increasing up to $E_\nu \approx 10^{18}$ eV, where it reaches a maximum and then starts to decrease again. This is physically understood as a competing effect between the detection efficiency and the τ-decay probability. As the energy increases, the shower detection is improved, while the probability of τ-leptons to decay decreases (see Eq. 6.6). As different energy transfer rates are considered, higher neutrino energies are needed to produce the studied τ-leptons. This results in a shift of the corresponding identification efficiency towards higher energies, as observed in Fig. 7.16.

In order to be consistent with the steeply up-going BSM searches detailed in section 7.2.2, a 50% energy transfer between the BSM particles and the τ-leptons is investigated: $E_{BSM} = 2\,E_\tau$. The corresponding identification efficiency is plotted with blue bullets in Fig. 7.16. The resulting values of the identification efficiency are inserted back in the exposure formula in Eq.7.18. The probability of a hypothetical particles to produce τ-leptons

within the last 50 km distance below Earth, which would in turn decay in the atmosphere, $P^*(BSM \to \tau)(\sigma, E_{BSM} = 2\,E_\tau, \theta, E_\tau)$ is calculated according to Eq. 7.17.

Having the exposure results in terms of the BSM particles energies, corresponding to a 50% energy transfer to τ-leptons, the flux upper limits for a 95% CL for the ES channel can be obtained, according to [7], [8]:

$$\Phi_{ES}(E_{BSM}) = \frac{3.02}{\int\limits_{E_{BSM}} E_{BSM}^{-2}\,\mathcal{E}_{ES}(E_{BSM})\,\mathrm{d}E_{BSM}} \cdot E_{BSM}^{-2} \tag{7.22}$$

where 3.02 is the Feldman-Cousin [101] factor corresponding to non-observation of events when no background is expected, taking into account the systematic uncertainties[6].

Various BSM scenarios are studied, similar to the steeply up-going case described in section 7.2.2, by artificially reducing the SM cross section $\sigma_{SM}(E)$ by several orders of magnitude. The corresponding 95% CL upper flux bounds on hypothetical particles with zenith angles $\theta \in [90°, 95°]$, interacting within the last 50 km distance below Earth and producing τ-leptons which enter the atmosphere, are obtained and plotted in Fig. 7.17.

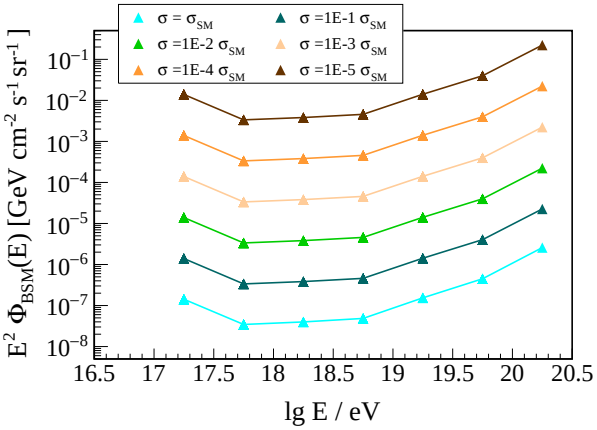

Figure 7.17: Upper flux limits for a 95% CL on ES ($\theta \in [90°, 95°]$) hypothetical particles creating τ-leptons within the last few km distance below Earth for several BSM scenarios

As expected from the probability of τ-production $P(BSM \to \tau)$ in different BSM scenarios, plotted in Fig. 7.14, the most stringent upper bounds are obtained for the SM scenario (light blue symbols in Fig. 7.17). This is again confirming the fact that the Earth Skimming scenario represents a golden detection channel for the standard model neutrino nucleon interaction cross sections. The upper bounds are gradually weakening by one order of magnitude when the BSM cross section is correspondingly decreased by the same factor, as expected from the probability $P(BSM \to \tau)$ of such highly inclined particles to produce τ-leptons within the last few km below Earth. The resulting upper bounds on ES hypothetical particles for $\sigma = \sigma_{SM}$ represent one of the most competitive limits set on neutrino induced air showers at the corresponding energies. As a result, the ES channel is providing an unmatched sensitivity towards SM particles, while the steeply up-going channel is more sensitive towards BSM scenarios. This

[6] In the dedicated searches from [7] and [8] a 90% CL is studied. In order to properly combine the resulted flux U.L for both the steeply up-going and ES channels, the same CL needs to be used. This is why a CL = 95% is used for the ES channel, while the systematic uncertainties are kept intact

is showing the ability of the Pierre Auger Observatory to constrain a large variety of physical models, by combining the obtained results from both the SD and FD.

7.4 Combined upper limits on BSM particles: ES and steeply up-going τ-induced air showers

Using the above presented results for both the ES channel and the steeply up-going τ-induced air showers, various BSM scenarios can be strongly constrained. Consequently, competitive upper flux limits on hypothetical particles with zenith angles $\theta \in [90°, 95°]$ and $\theta \in [110°, 180°]$, traversing the Earth and creating τ-leptons within the last 50 km distance have been obtained. The resulted differential combined upper bounds are plotted in Fig. 7.18, for a 50% energy transfer to the τ-leptons and an energy-dependent interaction cross section $\sigma(E)$ [7]. As discussed within the previous section, the ES channel provides competitive upper bounds for the SM case, where the steeply up-going showers result in very weak U.L. Consequently, the combined upper limits are following the ES ones, as seen in the top left plot from Fig. 7.18. With the reduction of

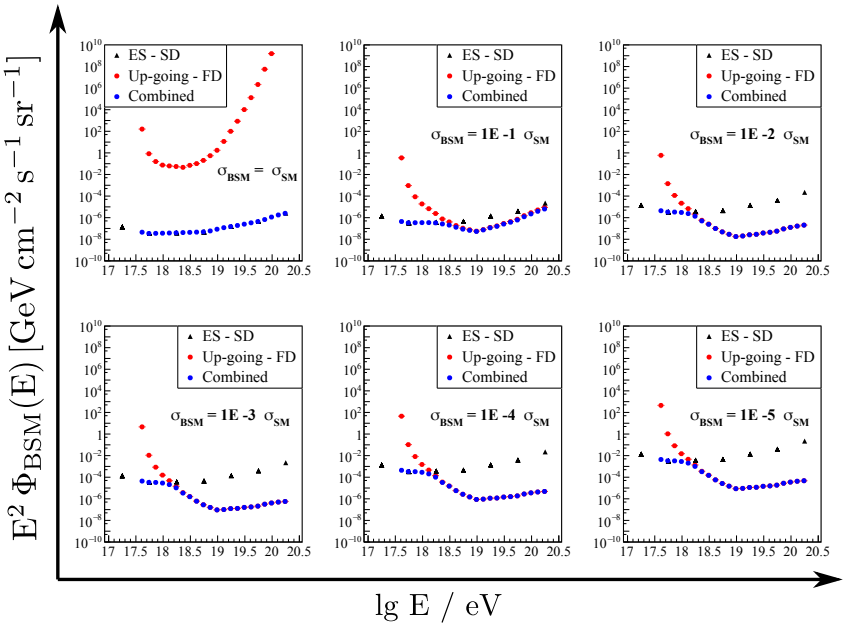

Figure 7.18: 95% CL flux upper limits on hypothetical particles surviving Earth propagation and producing Earth-Skimming (black triangles: $\theta \in [90°, 95°]$) and steeply up-going (red bullets: $\theta \in [110°, 180°]$) τ-leptons within the last 50 km distance. The resulting combined upper limits at are plotted with blue bullets, for different investigated BSM scenarios.

the cross section, several BSM scenarios are tested, where the steeply up-going channel provides stronger upper bounds and becomes the influencing component for the combined results. The limits improvement by several orders of magnitude between $\sigma = \sigma_{SM}$ and $\sigma = 0.1 \cdot \sigma_{SM}$ for this channel can be observed by comparing the first two top plots in the figure. The weaker limits for the steeply up-going case (red bullets in Fig. 7.18) at low energies are due to the very low FD exposure at the corresponding energies, as seen in Fig. 6.13. However, at energies

[7] The energy dependence of the cross section is the CC neutrino-nucleon $\sigma_{CC}(E)$ from [106].

$E_{BSM} > 10^{18}$ eV, where the FD exposure becomes significant, the steeply up-going channel provides the most stringent upper bounds for the investigated BSM scenarios.

In order to properly visualize the Auger upper bounds for different BSM cases, and correspondingly find the optimum cross section value which maximizes the τ-production probability, the integrated combined upper flux limits are provided in Fig. 7.19. Three main features are observed in the evolution of the integrated upper bounds with respect to the cross section. A first minimum is obtained for the SM scenario, where the ES channel is providing an unmatched sensitivity. With the decrease of σ the U.L are initially weakening, up to a value of $\sigma_{BSM} = 0.3 \cdot \sigma_{SM}$, where a maximum is reached. This is due to the fact that the entire zenith range $\theta \in [90°, 180°]$ could not be investigated. As there are no dedicated searches for τ-induced air showers with zenith angles $\theta \in [95°, 110°]$, the detector sensitivity at those elevations is unknown. Therefore the corresponding cross section ranges mark the region where the ES channel is the main dominant component in the combined upper limits. Even if the τ-production probability is increased for the steeply up-going case, the resulted τ-lepton upper flux bounds are not sufficiently improved. By further decreasing the cross section, the upper limits start to strengthen again, as the steeply up-going channel starts to become dominant. A second minimum, corresponding to the optimum BSM cross section $\sigma_{BSM} \approx 10^2 \cdot \sigma_{SM}$ is obtained. The competitive behavior between the survival probability inside Earth and the interaction probability in the last few km causes the increase in the upper bounds at cross sections lower than the optimum value. At those values the survival probability inside Earth is already maximized, and therefore the probability of hypothetical particles to create the τ-leptons is mainly influenced by the interaction probability below the surface, which is decreasing with the decrease of the cross section.

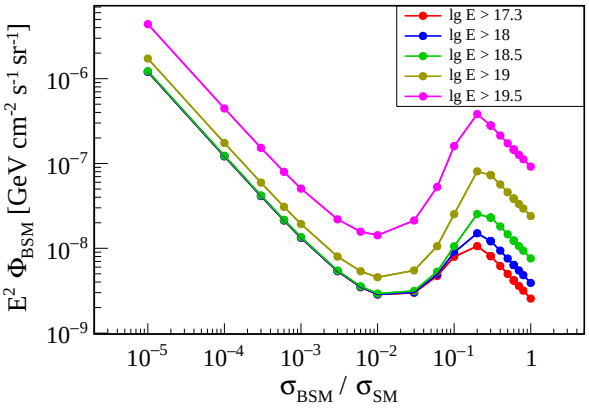

Figure 7.19: 95% CL integral upper flux limits on hypothetical particles with $\theta \in [90°, 95°]$ and $\theta \in [110°, 180°]$, producing τ-leptons within the last 50 km distance below Earth, when a 50% energy transfer is considered, with respect to different interaction cross sections.

The results in Fig. 7.19 are presented for different energy ranges, as well as for the entire energy range of interest: $E_{BSM} > 10^{17.3}$ eV. The best upper bounds are obtained in the SM case, with $E^2 \cdot \Phi = 2.55 \cdot 10^{-9}\,\mathrm{GeV\,cm^{-2}\,s^{-1}\,sr^{-1}}$, followed by the result at the optimum cross section, $\sigma_{BSM} = 10^{-2} \cdot \sigma_{SM}$, of $E^2 \cdot \Phi_{BSM} = 2.85 \cdot 10^{-9}\,\mathrm{GeV\,cm^{-2}\,s^{-1}\,sr^{-1}}$. This emphasizes again the wide capability of the Pierre Auger Observatory to constrain both SM and BSM scenarios resulting in the production of τ-leptons in a 50 km distance below Earth.

8

Conclusions and Future Prospects

In this thesis, the response of the Fluorescence Detector of the Pierre Auger Observatory to steeply up-going showers has been investigated. A generic search for cosmic ray-like air showers, with calorimetric energies $\lg E_{sh} \,/\, \mathrm{eV} \in [16.5, 18.5]$ and steeply up-going zenith angles $\theta \in [110°, 180°]$, motivated by the ANITA observations of two anomalous events with energies of few tenths of an EeV [14, 15, 13] and elevation angles higher than 20° above the horizon, has been performed within the Pierre Auger collaboration. The available FD data from more than 14 years has been analyzed, and no event excess over the expected background has been found. Consequently, upper flux limits have been set on such cosmic ray-like air showers. Moreover, the obtained FD exposure is provided in a double differential form, in terms of shower energy and height of first interaction. This approach of presenting the results is extremely important and useful for theoreticians, as any primary particle scenario can be further adapted and constrained.

An example application of extending the generic exposure results in terms of upper bounds on the fluxes of steeply up-going τ-induced air showers has been implemented and described within this thesis. This was achieved by simulating τ-leptons with zenith angles in the range of $110° - 180°$ and primary energies between $10^{16.5} - 10^{20}\,\mathrm{eV}$. For a maximal flexibility, the leptons are generated independent of their production mechanism. Consequently, τs are directly injected both below and above Earth, with an injection rate proportional to the media density. The τ-leptons are propagated through Earth, where the energy losses are accounted for, and followed in the atmosphere up to a maximum height of 9 km, defined by the FD field of view from the generic search. τ-leptons decaying in the FD-FoV are further used in order to estimate the FD exposure to steeply up-going τ-induced air showers, by using the double differential exposure results in terms of cosmic ray-like air showers. Given the non-observation of any candidate event above the expected background, this is then translated to upper flux limits on up-going τs produced within 50 km distance inside Earth up to 9 km above it. The 95% CL upper flux limits have been calculated for two different primary leptons energy spectra and can be easily re-weighted to any desired energy spectrum. Both the exposure results and the upper bounds on the τ-lepton fluxes have been calculated for the entire zenith range of interest, as well as for three zenith sub-ranges. The highest sensitivity is obtained for the most horizontal zenith scenario, with the strongest upper bound of $E_\tau^2 \cdot \Phi_\tau = 1.68 \cdot 10^{-9}\,\mathrm{GeV\,cm^{-2}\,s^{-1}\,sr^{-1}}$ for a primary energy of $E_\tau \approx 10^{18.7}\,\mathrm{eV}$. As the generic search in terms of cosmic ray-like air showers represents a skeleton of this analysis, the obtained results are strongly influenced by the maximum energy investigated within the general study. This can be clearly observed in the exposure results to τ-induced air showers. Consequently, the obtained upper flux bounds and exposure results correspond to steeply up-going τ air showers initiated by τs decaying in the sensitive volume of the FD of the Pierre Auger Observatory and limited to a maximum shower energy of $10^{18.5}\,\mathrm{eV}$. An improvement in the τ upper bounds could be obtained if the energy

range of the general study would be increased past this value. An energy extension within the signal simulations in the cosmic ray-like air showers study is planned for the near future.

By using the obtained results in terms of upper flux limits on τ-induced air showers, several BSM scenarios which produce τ-leptons can be further tested, by folding in the respective cross sections. Any theoretical model aiming to explain the existence of the steeply up-going events with the observed energies, needs to consider a significantly reduced interaction cross section of the proposed particle, in order to be able to survive Earth propagation. Such a scenario has been presented within this thesis, where hypothetical BSM particles are investigated by propagating them through Earth. Interactions happening within the last 50 km below surface are assumed to produce τ-leptons which can be detected by the FD. Several BSM models have been studied by artificially reducing the standard model neutrino-nucleon CC cross section by several orders of magnitude and further evaluating the probability of the hypothetical particles to produce the investigated τ-leptons. Two main instances are investigated in detail: an energy-depended cross section scenario, as well as a fixed cross section value at any given energy. In both of these cases an energy transfer of 50% between the hypothetical particle and τ-leptons is considered. It has been also shown that the cross section can not be infinitely reduced, given the competing behavior between the survival and the interaction probability within the last few km. Consequently, an optimum value of the BSM cross section of $\sigma_{BSM} = 10^{-2} \cdot \sigma_{SM}$ has been found, which maximizes the hypothetical particle probability to produce the τ-leptons and leads to the most stringent upper flux limits. The obtained results represent the first constrains on a BSM scenario resulting in the production of τ-leptons in the context of steeply up-going ($\theta \in 110^\circ, 180^\circ$) air showers and emphasize the importance of the presented τ study. Following a similar approach, any theoretical scenario can be correspondingly tested and constrained by using the obtained upper flux limits on τ-induced air showers.

Taking advantage of the multiple detection techniques of the Observatory, the BSM study has been extended to the Earth Skimming ($\theta \in [90^\circ, 95^\circ]$) channel. Using the already published results in terms of upper flux bounds on tau-neutrinos obtained with the Surface Detector [7, 8], the SM cross section has been correspondingly reduced in order to obtain the different BSM scenarios of interest. This results in extremely competitive upper flux limits for the SM case, with a gradual weakening of the upper bounds for lower cross sections. This behavior is physically understood, given the very inclined nature of such events. The wide capability of the Pierre Auger Observatory to constrain a large variety of theoretical models, both SM and BSM, resulting in the production of τ-leptons within the last 50 km distance below Earth, has been revealed. The CL = 95% integral combined upper limits on particles producing steeply up-going $\theta \in [110^\circ, 180^\circ]$ and ES $\theta \in [90^\circ, 95^\circ]$ τ-leptons with energies $E > 10^{17}$ eV, have been obtained for a large range of cross sections. The best upper bounds of $E^2 \cdot \Phi = 2.55 \cdot 10^{-9}\,\mathrm{GeV\,cm^{-2}\,s^{-1}\,sr^{-1}}$ are obtained for the SM case, where the interaction cross section is equal to the energy-dependent CC neutrino-nucleon cross section from [106]. However, this limit is closely followed by the BSM case corresponding to an optimum cross section of $\sigma_{BSM}(E) = 10^{-2} \cdot \sigma_{SM}(E)$, which results in an upper limit of $E^2 \cdot \Phi = 2.85 \cdot 10^{-9}\,\mathrm{GeV\,cm^{-2}\,s^{-1}\,sr^{-1}}$.

An immediate improvement regarding the BSM study would be the coverage of the entire up-going zenith ranges. As the zenith range of $\theta \in (95^\circ, 110^\circ)$ has not been studied yet

within the collaboration, sensitivity and exposure information about this channel are missing. This is why in the presented combined upper limits, this interval is skipped. This has an immediate influence on the combined integrated upper limits, and can be clearly seen in Fig. 7.19. As discussed in the respective section, the strongest bounds are obtained for the highest value of the cross section, corresponding to the SM one. By reducing this value the limits are initially getting weaker, resulting in a first peak at $\sigma_{BSM} = 0.3 \cdot \sigma_{SM}$. This feature is due to the fact that the ES channel is loosing sensitivity as the τ-production probability at those zenith angles is decreasing with lower cross sections. Even if for the steeply up-going channel the probability is increasing with the cross section decrease, the increase is not sufficient to overcome the ES channel for any cross section higher than $\sigma_{BSM} = 0.1 \cdot \sigma_{SM}$. If the $\theta \in (95°, 110°)$ zenith range would be considered, the limits would slightly improve within this region ($\sigma \in [0.1 \cdot \sigma_{SM}, \sigma_{SM}]$), as the survival probability inside Earth would start to increase for the corresponding angles. This would result in a smooth transition in the integral upper limits, without the peak at $\sigma_{BSM} = 0.3 \cdot \sigma_{SM}$. As no exposure results are available, it is difficult to predict the exact shape of the combined integrated limits, but if the corresponding sensitivity would be similar to the one in the ES or steeply up-going channel, an almost flat behavior is expected for the corresponding region. The obtained results for $\sigma = \sigma_{SM}$ as well as $\sigma \leq 0.1 \cdot \sigma$ would not change, as the $95° - 110°$ channel would only significantly contribute within the transition region. For lower cross section values the corresponding τ-production probability would rapidly decrease, given the events inclination and the steeply up-going channel would be the dominant component. Signal simulations for this zenith range have already been discussed and corresponding results are expected in the near future.

As there are no published results regarding the exposure of the ANITA experiment, it is difficult to compare the presented results in terms of steeply up-going induced air showers with the FD of the Pierre Auger Observatory to the expectations of the ANITA collaboration. However, by performing the dedicated search and finding no candidate events above the expected background, the Pierre Auger collaboration was able constrain such event signatures by setting stringent upper limits on the fluxes of any primaries with cosmic ray-like signatures. Furthermore, as a result of the personal contribution presented in this thesis, τ-leptons induced air showers have also been investigated within the anomalous events context, resulting in stringent upper bounds on the τ fluxes. This study and the obtained results are of a particular importance for the scientific community, as many theoretical scenarios resulting in the production of τ-leptons and aiming to explain the ANITA observations have already been proposed. BSM scenarios which would produce such τs have also been investigated as part of this thesis, serving as a direct example application of the τ study and representing the first attempt to constrain such events. The wide capability of the Pierre Auger Observatory to test such theoretical models has been presented, by providing integral upper limits on hypothetical particles which would create ES and steeply up-going τ-leptons within the last few km below Earth.

A

CORSIKA input files and configuration

For the very first stage of the simulation sets presented in subsection 4.3.3, *CORSIKA-76900* was used, representing the newest available version at the time. For configuring it, in addition to the QGSJET II-04 and UrQMD1.3.1 models for the high and low energy hadronic interactions, the *flat detector array* has been chosen. Additional options needed for the simulations are: *UPWARD, NUPRIM, THINNING*. With the above configuration, an example input file, used for the simulation library discussed in subsection 4.3.3 is shown. The input file shown in Fig. A.1 simulates a proton induced air shower with a first interaction height $H_1 = 1.4\,\mathrm{km}$ a.s.l. For different values of H_1 the keyword *FIXHEI* can be changed accordingly.

```
DATBAS T
DIRECT '/lustre/caracas/ProtonCorsikaThin1E-4/Height0/THIN1E-4ProtonE17.5_18_theta115-120/data/'
ECTMAP 10000
ECUTS 0.3 0.3 0.003 0.003
ELMFLG T T
ERANGE 316227766.016838 1000000000
ESLOPE -1
EVTNR 349
FIXCHI 875.539
FIXHEI 140000 0
HADFLG 0 0 0 0 0 2
HOST cluster
LONGI T 20 T T
MAGNET 19.4 -14.1
MAXPRT 1
MUADDI T
MUMULT T
NSHOW 1
OBSLEV 4000000
PAROUT T T
PHIP -180 180
PRMPAR 14
RADNKG 20000
RUNNR 349
SEED 347953 0 0
STEPFC 1
THETAP 115 120
THIN 0.0001 31622.7766016838 100
THINH 1 100
USER caracas
SEED 347954 0 0
SEED 347955 0 0
SEED 347956 0 0
SEED 347957 0 0
EXIT
```

Figure A.1: CORSIKA input file for simulating up-going proton air showers with primary energy $E \in [10^{17.5}, 10^{18}]\,\mathrm{eV}$, zenith angle $\theta \in [115°, 120°]$ and first interaction height $H_1 = 1.4\,\mathrm{km}$ a.s.l

B

Gaisser Hillas fit for up-going induced air showers

The fitting procedure uses the longitudinal energy deposit profile provided by CORSIKA in the .long output file. The first step is to calculate the X_{max}, X_0, λ and $(dE/dX)_{max}$ parameters by using the function defined in Eq. 4.3. This is done by using the *TMinuit* package [109]. After defining the fitting function (Eq. 4.3) together with its parameters, the minimization is done by the package using the chisquare method. A starting value has to be given for each parameter before the minimization process can start. For the case of X_{max} and $(dE/dX)_{max}$ the first guess was chosen as the maximum value from the longitudinal profile provided by CORSIKA. In the case of X_0, since it is related to the injection height, the first guess was setting it $X_0 = 10\,\mathrm{g/cm^2}$. For the fourth parameter, $\lambda = 70\,\mathrm{g/cm^2}$ was set as a first value, as explained in [110]. The resulting fit function for a proton induced air shower, with $\theta = 117.5°$, primary energy $\lg E_0\,/\,\mathrm{eV} = 18.23$ and height of first interaction $H_1 = 5.4\,\mathrm{km}$ a.s.l, together with its parameters is shown in Fig. B.1.

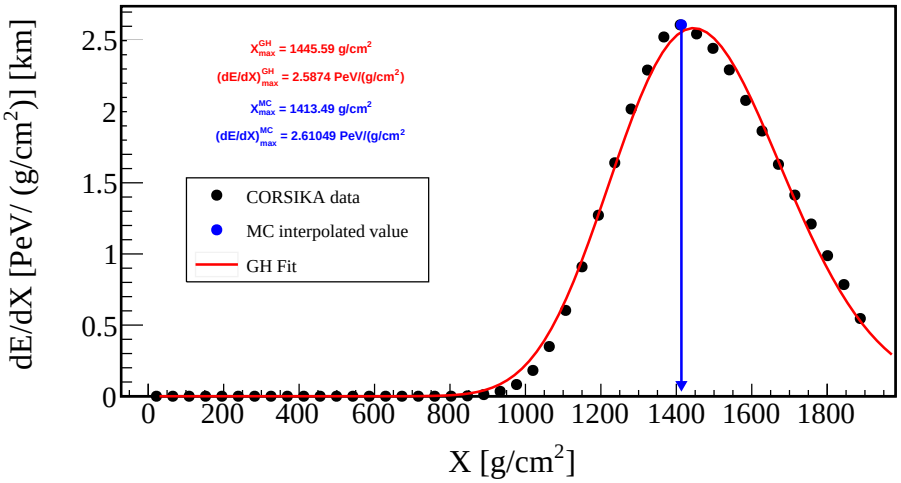

Figure B.1: Energy deposit profile of an up-going ($\theta = 117.5°$) proton induced air shower, with a primary energy of $\lg E_0\,/\,\mathrm{eV} = 18.23$ and a height of first interaction of $H_1 = 5.4\,\mathrm{km}$ a.s.l. The GH function (red line) is correctly describing the data (black bullets), providing a reliable value of X_{max}

The black dots represent the CORSIKA data as resulted from the longitudinal file, the blue point corresponds to the Monte Carlo value of X_{max} and the red curve represents the correct new calculated Gaisser Hillas function for up-going induced air showers, as described in section 4.3.4. The GH fit values of X_{max} and $(dE/dX)_{max}$ are highlighted, together with the MC values. The fit describes the data behavior correctly, resulting in a correct representation of the longitudinal profiles of up-going air showers.

Since the GH fit parameters further used within the Offline framework are X_{max}, X_0, λ and N_{max}, an additional step has to be performed in order to get the corresponding value of

N_{max}. The corresponding GH function has been defined in Eq. 2.10 and is rewritten here for consistency:

$$N(X) = N_{max}\left(\frac{X - X_0}{X_{max} - X_0}\right)^{\frac{X_{max}-X_0}{\lambda}} \exp\left(\frac{X_{max} - X_0}{\lambda}\right) \tag{B.1}$$

In order to calculate the corresponding value of N_{max}, the mean ionisation loss rate, $\alpha_{eff}(X)$ is used, according to [87]:

$$N(X_{max}) = \left(\frac{dE}{dX}\right)_{max} \cdot \frac{1}{\alpha_{eff}(X_{max})} \tag{B.2}$$

where $\alpha_{eff}(X)$ is defined as:

$$\alpha_{eff}(X) = \frac{c_1}{(c_2 + s)^{c_3}} + c_4 + c_5 \cdot s \tag{B.3}$$

In Eq. B.3, the parameters $c_1 - c_5$ depend on the low-energy threshold for electrons and gamma-rays used in the simulations [1]. The corresponding values have been previously defined in [87] for a value of the low-energy threshold of $E_{cut} = 1\,\text{MeV}$ and have been extrapolated within the Offline framework for values up to $E_{cut} = 3\,\text{MeV}$. The remaining parameter in Eq. B.3, s, represents the shower age and is defined as:

$$s = \frac{3}{(1 + 2X_{max}/X)} \tag{B.4}$$

For the desired value of $X = X_{max}$ the shower age $s(X_{max}) = 3/2$. By replacing the corresponding value of s in Eq. B.3 and further on using the resulting value of $\alpha_{eff}(X_{max})$, the N_{max} parameter is correctly calculated. The corresponding value is replaced within Offline for the case of up-going air showers simulated with CORSIKA and using the VERTICAL option for the output of the longitudinal energy deposit profile.

[1] particles below the energy threshold are no further followed within the simulation procedure

C

Calculation of the FD up-time fraction

As mentioned in Chapter 3.2, the FD has an ≈14% duty cycle. As various factors can intervene, like weather conditions and/or technical issues, the duty cycle of each telescope can vary. In order to properly monitor the telescope functioning, the data containing the main parameters is stored within the collaboration database. A root tree with information regarding the ADC variances, the shutter fraction, the telescope up fraction, the eye up fraction, as well as the GPS nanosecond of the given time period, is created monthly.

Since the simulations presented in Chapter 4 represent a very preliminary procedure, no real MC data has been used. Therefore, in order to properly calculate the up time fraction of the telescope, the monitoring database information has been used. The investigated time period was 01.07.2007 - 01.10.2019. The information is stored for each telescope at each eye. The general formula for calculating the up-time fraction of each eye is:

$$t_{up}(Eye) = \frac{\sum_{i=1}^{n_{telescopes}} ShutterFraction8ADC_i \cdot TelescopeUpFraction_i \cdot EyeUpFraction_{Eye} \cdot \Delta T}{n_{telescopes}} \tag{C.1}$$

where ΔT represents the entire period of time, and $n_{telescopes} = 6$ for LL, LA, LM, CO, respectively $n_{telescopes} = 3$ for HEAT. The information regarding the shutter fraction, the telescope up fraction and the eye up fraction is taken directly from the root database file.

Having access to the entire database, the decrease in the FoV of LL eye, corresponding to the dismantling of one of the outer LL telescopes, starting from 14.07.2009, has been accounted for. After this period, part of the pixels in Bay 1 and Bay 6 stopped working, reducing thus its FoV to 162°. Therefore, in the case of LL the data has been divided into two different time periods, resulting in the two different terms used in Eq. 4.13: $t_{up(FoV=180^\circ)}(LL)$ and $t_{up(FoV=162^\circ)}(LL)$.

In the case of HEAT telescope an additional step regarding its tilting position has been taken. Since HEAT can be tilted both in the downward position, which is mainly used for calibration, the data taking is only achieved when the telescope is in the upward position. Information regarding the tilting position can also be accessed from the internal database. There are three kind of information provided: upward tilted, downward tilted and undefined. Within the present study only the upward tilted position was considered. Therefore in case of HEAT an additional loop was needed in order to access the tilting information.

The resulted up-times of the telescopes, for the data period 01.07.2007 - 01.10.2019 are:

1. $t_{up}(CO) = 1.7747\,\mathrm{yr}$
2. $t_{up}(LA) = 1.703\,\mathrm{yr}$

3. $t_{up}(LM) = 1.794\,\mathrm{yr}$
4. $t_{up}(LL) = t_{up(FoV=180^\circ)}(LL) + t_{up(FoV=162^\circ)}(LL) = 0.27 + 1.475 = 1.745\,\mathrm{yr}$
5. $t_{up}(HEAT) = 1.124\,\mathrm{yr}$

These values have been further used for the first exposure calculations presented in Section 4.4.

D

Signal Simulations for the cosmic-ray like up-going EAS

D.1 Transition from CORSIKA to CONEX in the signal simulations

The switch from CORSIKA to CONEX in the extensive air showers simulation has been adopted due to the need of massive simulations towards the study of up-going induced air showers with the FD of the Pierre Auger Observatory. The much reduced computing time required for CONEX represents the main motivation. Furthermore, since the FD observes the longitudinal energy deposit in the atmosphere, using CONEX should not affect the final results in terms of the FD sensitivity and exposure. However, before proceeding with the mass simulations, a cross check has been performed. A number of $5 \cdot 10^4$, and $2 \cdot 10^4$ proton induced air showers have been simulated with CORSIKA and CONEX respectively. The showers have the same parameters, with primary energies $\lg E\,/\,\mathrm{eV} \in [17.5, 18]$, zenith angles $\theta \in [115°, 120°]$ and fixed height of first interaction $H_1 = 1.4\,\mathrm{km}$ a.s.l. Moreover, the same high (QGSJETII-04) respectively low energy (Urqmd) models have been used for describing the hadronic interactions. The obtained results are plotted in Fig. D.1 in terms of FD exposure during 1 year,[1] for one of the telescope buildings (CO). The exposure calculation method is the preliminary one described in section 4.4. In both of the cases the maximum distance between the telescope building and the shower core has been chosen to $R_{FD}^{max} = 25\,\mathrm{km}$. As it can be seen the agreement between the two simulation

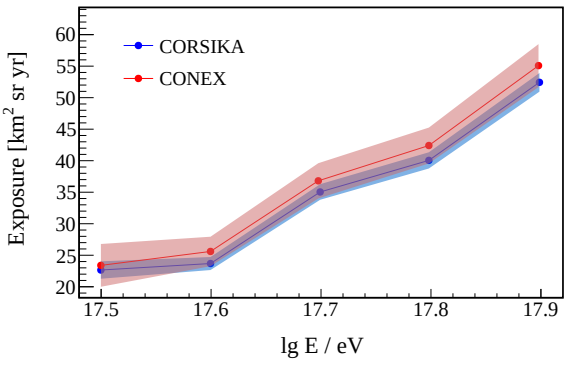

Figure D.1: Preliminary FD exposure results to up-going proton air showers for a zenith range $\theta \in [115°, 120°$ and primary energy $\lg E\,/\,\mathrm{eV} \in [17.5, 18]$, with $H_1 = 1.4\,\mathrm{km}$ a.s.l., resulting from CORSIKA (blue symbols) and CONEX (red symbols) simulation codes.

codes stands, within the uncertainties limits. The CONEX simulations have a larger uncertainty band, as fewer events have been simulated in this case. However, the simulations of more events

[1] the FD operation time is not important within this study, since it will not affect the results behavior

was not necessary given the proximity of the results.

D.2 On the equivalence of flat D_1 with $\cos^2\theta$ sampling and flat H_1 with $\cos\theta$ sampling

As mentioned in section 5.1.2, in order to properly calculate the exposure of a set of isotropic generated events on a flat surface, a zenith sampling in $\cos^2\theta$ is needed. Moreover, it has been decided that a flat generation in the first interaction distance, D_1, is desired, as this can be easily related to any decay models. Since in the current study one is only interested in results up to a maximum height of $H_1^{max} = 9\,\text{km}$, the corresponding maximum distance is related to the minimum investigated zenith angle $\theta_{min} = 110°$ and is defined as:

$$D_1^{max} = \frac{H_1^{max}}{\cos\theta_{min}} \approx 26.3\,\text{km} \tag{D.1}$$

Following the flat generation distance procedure, the distance to first interaction, D_1, will be flatly generated, with $D_1 \in [0, D_1^{max}]$, while the zenith sampling will be done in $\cos^2\theta$ with $\theta \in [110°, 180°]$. However, an additional condition has to be put in order to have all of the events satisfying the criteria of a maximum height of first interaction: $D_1 \cdot \cos\theta \leq H_1^{max}$. By applying this condition a significant fraction of simulated events ($\approx 49\%$) will be lost. This scenario is plotted with grey symbols in Fig. D.2 and represents the desired model within the signal simulation procedure.

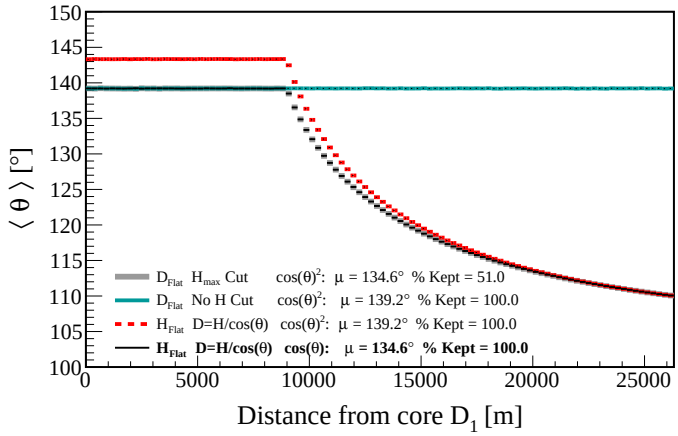

Figure D.2: Possible zenith and distance generation methods resulting from the MC simulations of 10^8 events. The grey line corresponds to the desired simulation procedure: flat in distance and $\cos^2\theta$ zenith sampling with the D_{max} requirement from Eq. D.1 and an $\approx 49\%$ lost events. The black line, corresponding to a flat in height and $\cos\theta$ zenith sampling duplicates the desired results by keeping 100% of the generated events

In order to avoid this significant loss of events, different other scenarios have been investigated, to find an equivalent geometry. A MC simulation code has been developed and used in this scope. A number of 10^8 MC events have been generated for each of the cases of interest. Besides the main scenario described above, three other generation methods have been studied and are plotted in Fig. D.2. The average value of the zenith angle, μ, together with the

percentage of events kept are shown in the legend. A flat generation in distance with a $\cos^2\theta$ sampling and no height cut (blue symbols), a flat generation in height and a $\cos^2\theta$ sampling (red symbols) and a flat generation in height with a $\cos\theta$ sampling of the zenith angle (black symbols) have been investigated. The distance is calculated as $D = H/\cos\theta$, if not directly generated, while the maximum investigated value of the height is $H_{max} = 9\,\text{km}$. The resulting profile histograms [2] in terms of zenith angles vs distance are showing a clear agreement between the gray and black symbols.

As a result, in order to maximize the simulation efficiency, the flat generation in height with a $\cos\theta$ zenith sampling has been adopted. This is translated into having an individual maximum distance, based on the maximum interaction height for each individual zenith angle, as defined in Eq. D.2. Further on, a random distance $D_1 \in [0, D_1^{max}]$ is chosen, as explained in section 5.1.2. Since the zenith angle is fixed, this is equivalent with choosing a random height $H_1 \in [0, H_1^{max}]$.

$$D_1^{max} = \frac{H_1^{max}}{\cos\theta} \tag{D.2}$$

D.3 From flat in distance to first interaction (D_1) to flat in injection distance (D_0)

As mentioned in Section 5.1, the signal simulations are generated flat in distance to first interaction, D_1 with a $\cos^2\theta$ sampling and a maximum value of D_1^{max}, as defined in Eq. D.1. However, in order to investigate specific scenarios a generation flat in the injection distance D_0 is also desired. Having access to all variables of interest, $H_1, H_0, X_1, X_0, \theta$, re-weighting the simulated events towards a flat D_0 distribution is possible. This has been performed as an additional exercise within this thesis.

Starting from the two-dimensional events distribution in terms of D_1 vs $\cos^2\theta$, the equal population of events in each bin is illustrated in Fig. D.3(a). The corresponding event distribution in terms of injection distance, D_0 vs $\cos^2\theta$ is also shown in Fig. D.3(b). As can be seen, the events are flatly distributed in the distance to first interaction, while this is not the case for the injection distance, where less events are present at the maximum D_0 values corresponding to each $\cos^2\theta$ bin. A correct re-weighting should correspondingly result in an equally populated two dimensional distribution in terms of distance to injection point D_0 vs $\cos^2\theta$.

In order to achieve this, the weights have been calculated based on the 2D distributions. To ensure the same range of the two investigated distances, only events with $H_1^{max} = H_0^{max} = 9\,\text{km}$ have been considered. As a first step the 2D distributions have been divided in 15 bins of $\cos^2\theta$. Further on, the ratio between the number of events at a given distance to first interaction and the events at a given injection distance, $\frac{N(D_1)}{N(D_0)}$, has been plotted as a function of the distance values for each individual zenith bin. The resulting ratio behavior versus distance has been fit

[2] The profile histograms show the mean value of the y-variable, together with its error, for each bin on the $x-$axis. This is why even if the zenith angle is simulated with $\theta \in [110°, 180°]$, there are no higher values than 145° in Fig. D.2

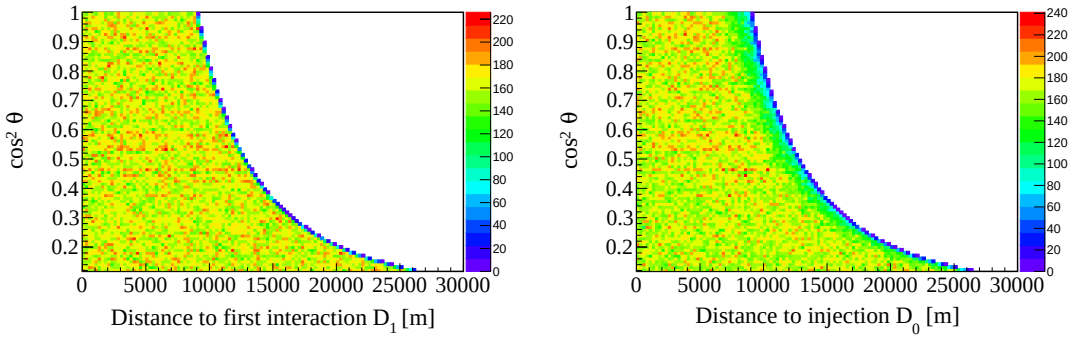

(a) (b)

Figure D.3: Two dimensional distributions of signal simulated events in terms of $\cos^2\theta$ and distance to first ineraction D_1 (Fig. D.3(a) rand distance to injection D_0 (Fig. D.3(b), as resulting from the simulations described in Section 5.1. The number of events is color-coded with the corresponding values represented on the z-axis.

with a distance dependent function, $w(D;\,\theta)$.

$$w(D;\,\theta) = \exp\left[\,P_1(\theta)\,(D - P_0(\theta)\,)\,\right] + P_2(\theta)\cdot D + P_3(\theta) \tag{D.3}$$

An example plot of the fitted data resulted from several zenith bins is shown in Fig. D.4.

The first exponential term in Eq. D.3 describes the exponential increase in the events at some specific value of distance, with the first parameters $P_0(\theta)$ being related to the corresponding maximum distance for the specific zenith bin and $P_1(\theta)$ defining the exponential slope. The last parameter $P_3(\theta)$ describes the shift of the exponential from ≈ 0 asymptotic approach at very small values of the x-variable. The exponential increase comes from the physics behind the simulation procedure: the first interaction distance will always be greater than the injection distance for any event: $D_1 > D_0$, as it can also be seen in Fig. 5.1. As a result, at high distance values, there will always be more events in terms of D_1, having a corresponding smaller D_0 and explaining thus the flat region in Fig. D.4 at lower distance values. The third parameter in Eq. D.3, $P_2(\theta)$ concerns the region corresponding to very small distances. For events having a distance to first interaction very close to the ground (i.e. $D_1 \approx 0$) the respective value of the injection distance D_0 is not calculated, resulting in an under population of events in terms of D_0 at very small distances. In order to account for this, the additional parameter connected to the atmospheric density, is introduced in the fit function.

Once the fit in terms of distance is performed for each zenith bin, the resulting parameters $P_0(\theta), P_1(\theta), P_2(\theta), P_3(\theta)$ are further plotted and parameterized as a function of the zenith angle:

$$\begin{aligned} P_0(\theta) &= \frac{a_2}{\cos^2\theta} + \frac{a_1}{\cos\theta} + a_0 \\ P_1(\theta) &= \frac{b_2}{\cos^2\theta} + \frac{b_1}{\cos\theta} + b_0 \\ P_2(\theta) &= \frac{c_2}{\cos^2\theta} + \frac{c_1}{\cos\theta} + c_0 \\ P_3(\theta) &= d_0\cdot\theta \end{aligned} \tag{D.4}$$

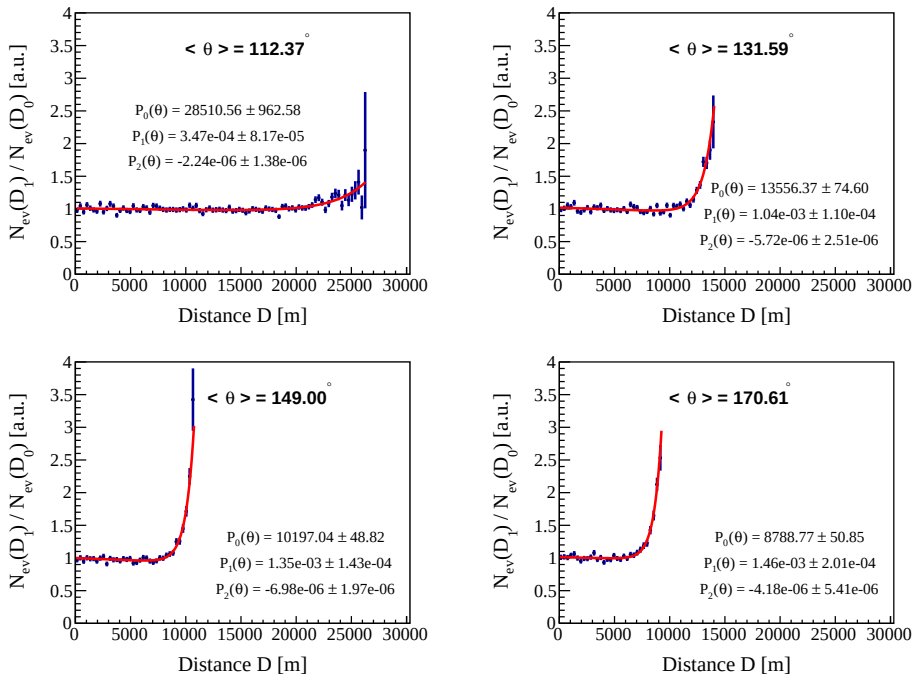

Figure D.4: Weight distributions in terms of the ratio of events present at some given value of the first interaction distance D_1 and events present at the same value of the injection distance D_0. The data obtained from the signal simulations is plotted with blue symbols and fitted with the weight function described in Eq. D.3 (red line). The resulting fit parameters are shown for each of the presented zenith bins.

The behavior of the four parameters in Eq. D.4 as a function of the zenith angle θ is plotted in Fig. D.5 together with the fit function and fit parameters, as obtained from the analysis of $\approx 9 \cdot 10^6$ simulated events within the energy and zenith ranges of interest for the current study.

Having the zenith dependent parameters, the weighting function in Eq. D.3 can be calculated for any value of the injection distance D_0 and zenith angle θ. By applying the resulting weights to the events simulated with a flat distribution in the first interaction distance, the corresponding non-flat distribution in the injection distance, $N(D_0, \theta)$, can be transformed into a flat population of events in terms of injection distance $N(D_0, \theta)^{flat}$, and can be further used for any studies requiring such a hypothesis.

$$N(D_0, \theta)^{flat} = N(D_0, \theta) \cdot w(D_0, \theta) \tag{D.5}$$

Two exemplary plots of the resulting distribution $N(D_0, \theta)^{flat}$ are shown in Fig. D.6. The good agreement between the two profile histograms in Fig. D.6(b), as well as the flat distribution in Fig. D.6(a) prove the efficiency of the implemented re-weighting procedure.

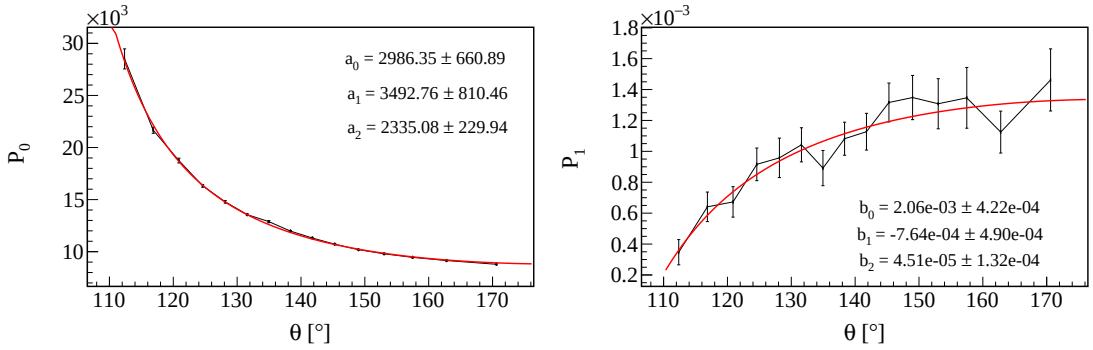

(a) P_0 vs θ

(b) P_1 vs θ

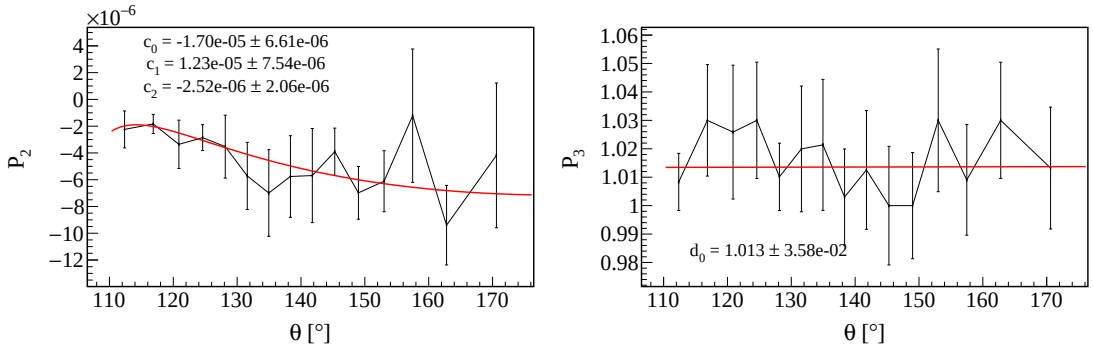

(c) P_2 vs θ

(d) P_3 vs θ

Figure D.5: Distance dependent parameter behavior as a function of the zenith angle θ. Each point on the graph corresponds to the values resulting from the 15 different $\cos^2\theta$ bins, corresponding to 15 individual distance fits according to Eq. D.3

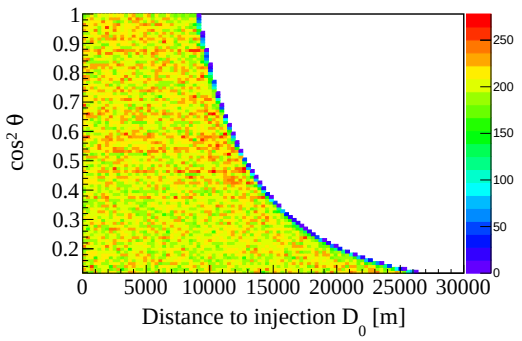

(a) Two dimensional event distribution in terms of $\cos^2\theta$ vs D_0 as resulting from the re-weighting procedure

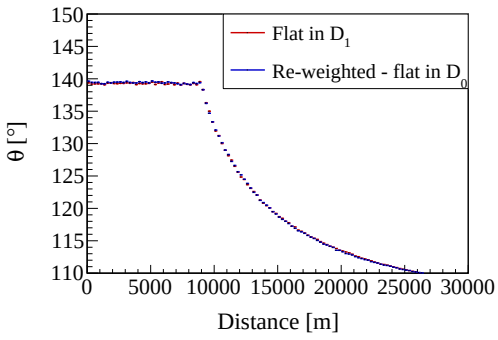

(b) Pofile histogram of the initial distribution flat in D_1 (red symbols) and the re-weighted flat in D_0.

Figure D.6: Flat in injection distance D_0 and $\cos^2\theta$ distribution, resulting from the re-weighting procedure.

E

Background simulations - Generation sphere

As mentioned in Section 5.2.1, the background events are simulated in a sphere centered in the middle of the array and surrounding the FD telescopes. An illustrative view of the generation sphere is shown below, as taken from [88].

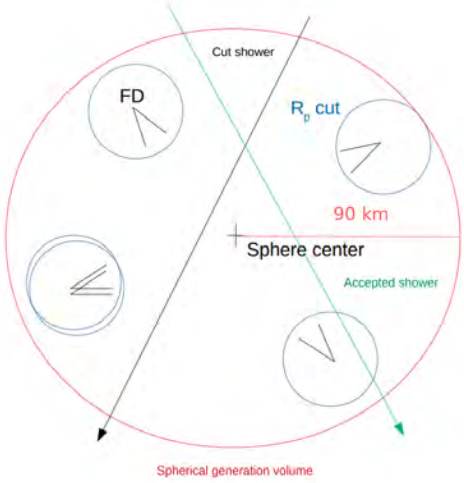

Figure E.1: Spherical generation volume (red) of the background simulated events. Figure from [88].

By choosing a proper value of the sphere radius, R_{sphere}, the simulations cover all the telescope building locations. Each telescope is defined by a maximum distance, R_pcut, which defines the distance between the shower core and the telescope site, at which events are still able to trigger the detector. This variable has been mentioned before within the thesis, in section 4.3.3, where similar studies have been performed in the preliminary signal simulations studies [1]. The value of this distance is energy dependent. The radius of the sphere $R_{sphere} = 90\,\text{km}$, has been chosen as a result of the parametrization of R_pcut as a function of energy, plotted in Fig. E.2. It can be seen from Fig. E.1 that the value of R_{sphere} represents a sum between R_pcut and the distance from the sphere center to the telescope building.

Once the value of R_pcut, and R_{sphere} are set, the generation volume of the background events is fixed. A shower having its core position within the sphere but not intersecting the corresponding R_pcut defined area, represented with blue circles in Fig. E.1, will be disregarded (black arrow in Fig. E.1) as it will not be able to trigger the FD. As a result, only events generated within the sphere and landing in the R_pcut allowed region will be further considered (green arrow in Fig. E.1).

[1] The quantity R_pcut is the equivalent of R_{FD}^{max}

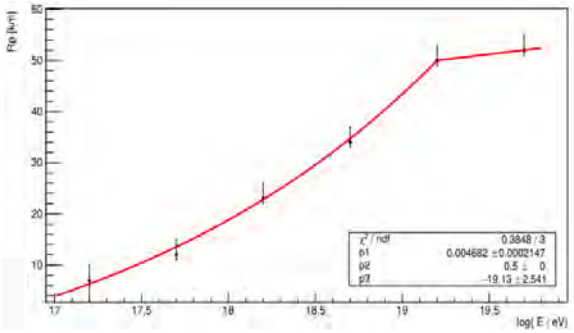

Figure E.2: Parametrization of $R_p cut$. Plot taken from [88].

F

Atmospheric profile parametrization

The atmospheric profile is widely used in cosmic ray studies for translating between the altitude above sea level and the corresponding vertical atmospheric depth. The parametrization used in this thesis is following the U.S. standard atmosphere in [111]. Additional measurements regarding the monthly averages at the detector site, in Malargue, Argentina, are considered by using the same parameters defined within the internal collaboration software, Offline [69]. Input atmospheric parameters in terms of humidity, temperature, pressure and density are provided for altitudes up to 100 km a.s.l.

The vertical atmospheric depth can be calculated, using the corresponding atmospheric pressure values at a given altitude:

$$X_{vert,\,i} = P_i \cdot \frac{k_{SeaLevel}}{P_{SeaLevel}} \tag{F.1}$$

where $k_{SeaLevel} = 1032\,\mathrm{g/cm^2}$ represents the grammage at sea level and $P_{SeaLevel} = 101325\,\mathrm{Pa}$ is the corresponding atmospheric pressure at sea level. The index $i = \overline{0, 100}\,\mathrm{km}$ refers to the different altitudes of interest a.s.l.

As discussed in section 6.1.2, the atmospheric profile $f_{Atm}(H)$ is used in order to translate between vertical depths and corresponding heights a.s.l. The function $f_{Atm}(H)$ describing the relation between the two parameters of interest is obtained by interpolating the input altitude values H_i and the calculated depths $X_{vert\,i}$. The interpolation is performed between the logarithm of the vertical depth, $\log X_{vert\,i}$ and H_i and is plotted in Fig. F.1. Two different interpolation methods are used [1]. It can be seen the two different functions give very similar results up to heights of $H \leq 30\,\mathrm{km}$.

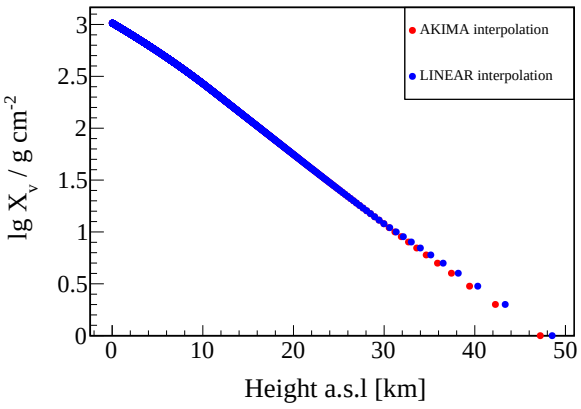

Figure F.1: Two different interpolation methods of the atmospheric profile, $f_{Atm}(H)$.

[1] Both AKIMA and LINEAR interpolation represent interpolation methods already implemented in ROOT [72]. More details about these interpolations can be found at the official website [112].

However, in order to decide on the best interpolation for $f_{Atm}(H)$, the resulting distribution of events in terms of distance to first interaction, defined in Eq. 6.19 is further plotted considering the two different interpolations in Fig. F.2. As it can be seen from this figure, the AKIMA interpolation provides a smoother event distribution. As a result this has been chosen for the atmospheric profile parametrization $f_{Atm}(H)$.

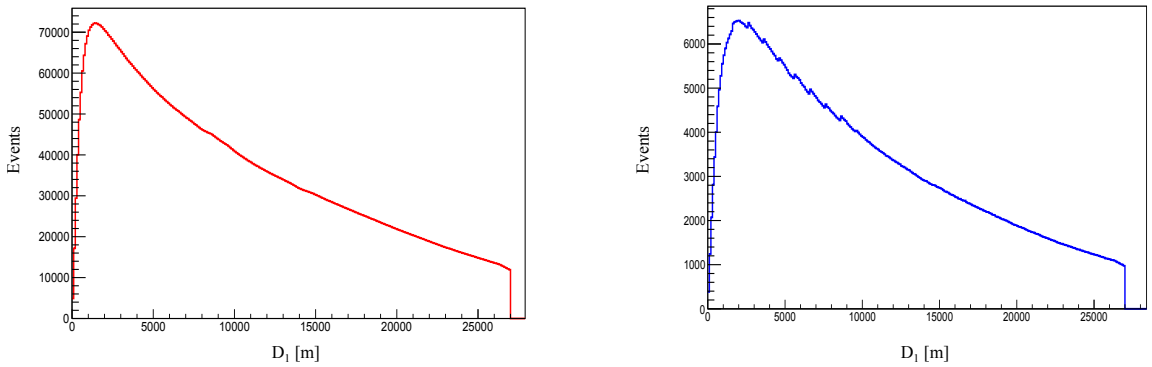

(a) AKIMA interpolation

(b) LINEAR interpolation

Figure F.2: Event distribution with respect to the distance to first interaction, D_1, using two different interpolations of the atmospheric profile $f_{Atm}(H)$

G

Energy transfer impact on BSM upper flux limits

The value of the energy transferred from the BSM hypothetical particles to the studied τ-leptons influences the corresponding upper flux bounds. As pointed out int Chapter 7, an energy transfer of 50% has been chosen for the current results. As the study represents the investigation of a theoretical scenario, any transfer rate can be considered. A comparison between the resulting upper flux limits for two different energy transfer values has been performed. Consequently, the chosen $E_{transfer} = 50\% \rightarrow E_{BSM} = 2 \cdot E_{\tau}$ results are compared to the extreme case of a total energy transfer: $E_{transfer} = 100\% \rightarrow E_{BSM} = E_{\tau}$. The corresponding upper limits for a particle with a fixed cross section of $\sigma_{SM} = 0.77 \cdot 10^{-31}\,\mathrm{cm}^2$ and zenith angles $\theta \in [110°, 180°]$ which would create τ-leptons within the last 50 km distance below Earth are plotted in Fig. G.1(a).

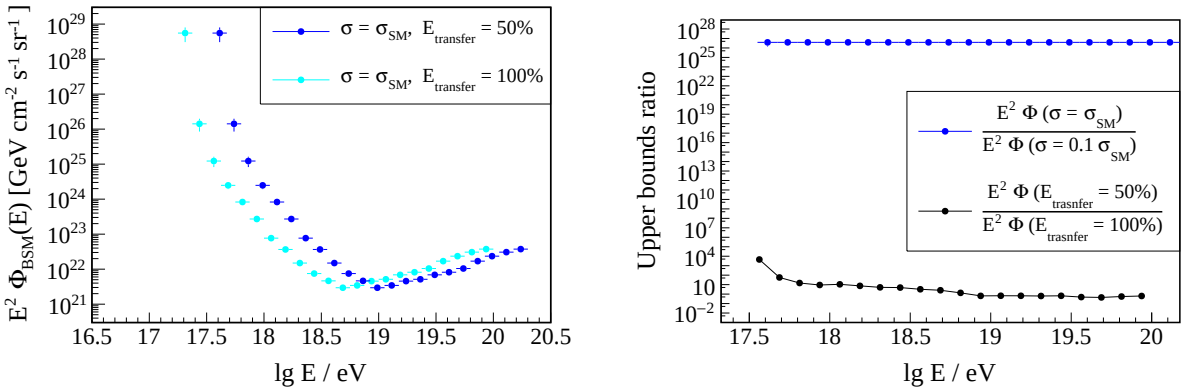

(a) Upper flux limits ($CL = 95\%$) obtained at a fixed $\sigma = \sigma_{SM}$ considering two different energy transfer rates between the BSM particle and the investigated τ-leptons

(b) Upper bounds ratio between different energy transfer rates (black bullets) and different cross section values (blue bullets)

Figure G.1: Impact of the energy transfer rate on the resulted BSM upper flux limits

As expected, different energy transfer values will shift the resulting distribution towards higher energies[1]. The upper bounds will become correspondingly weaker in the case of a 50% energy transfer for $E_{BSM} \leq 10^{18.8}\,\mathrm{eV}$. This is physically understood, given the τ-upper limits evolution with respect to energy (see red bullets in Fig. 6.14). Since the τ bounds are very weak at those energies, this is reflected in the BSM limits as well. Consequently, a fixed energy of the BSM particle is going to be contributing to different energy bins of the τ-distribution, according to the corresponding energy transfer. As a result, in the two cases of interest, a particle of energy $E_{BSM} \approx 10^{17.6}\,\mathrm{eV}$ will either produce a τ-lepton of $E_{0,\tau} = 10^{17.6}\,\mathrm{eV}$ or correspondingly $E_{0,\tau} = 1/2 \cdot 10^{17.6}\,\mathrm{eV}$. As the upper bounds are weaker at lower energies,

[1] A higher energy of any particle is needed in order to produce the τs at the investigated energies for any $E_{transfer} < 100\%$

this results in correspondingly weaker U.L for a 100% energy transfer. The same process is responsible for the stronger upper bounds in the case of 50% energy transfer, at $E_{BSM} > 10^{18.8}$ eV, where the τ fluxes improve significantly. For a better visualization, the ratio between the corresponding upper bounds, $E^2\phi(E_{transfer} = 50\%)/E^2\phi(E_{transfer} = 100\%)$ is plotted with black bullets in Fig. G.1(b). Following the trend in Fig. G.1(a), the biggest impact is visible at low energies, where the resulting upper bounds are different by ≈ 3.5 orders of magnitude. However this ratio is decreasing with the increasing of energy, as visible in the figure.

As the main purpose of the current study is to constrain several BSM scenarios obtained by gradually decreasing the SM cross section, a similar ratio has been plotted with blue bullets in Fig. G.1(b). The SM upper bounds are compared to the obtained limits for a BSM scenario with $\sigma_{BSM} = 0.1 \cdot \sigma_{SM}$. This cross section value doesn't correspond to the optimum one, implying the resulting ratio could be even higher. Nevertheless, as indicated in Fig. G.1(b), by decreasing the cross section by one order of magnitude, the corresponding upper bounds improve by more than 25 orders of magnitude. By comparison, the maximum number of ≈ 3.5 orders of magnitude resulting from the different energy transfer values, for only one energy bin, is almost insignificant. This is proving the affirmation made at the beginning of chapter 7, namely that the considered energy transfer model does not have a significant influence in constraining the studied BSM scenarios.

References

[1] Vanessa Cirkel-Bartelt. 'History of Astroparticle Physics and its Components'. In: *Living Reviews in Relativity* 11 (2008).

[2] A. Aab et al. 'Features of the Energy Spectrum of Cosmic Rays above 2.5×10^{18} eV Using the Pierre Auger Observatory'. In: *Phys. Rev. Lett.* 125 (12 Sept. 2020), p. 121106. DOI: 10.1103/PhysRevLett.125.121106. URL: https://link.aps.org/doi/10.1103/PhysRevLett.125.121106.

[3] Alexander Aab et al. 'Observation of a Large-scale Anisotropy in the Arrival Directions of Cosmic Rays above 8×10^{18} eV'. In: *Science* 357.6537 (2017), pp. 1266–1270. DOI: 10.1126/science.aan4338. arXiv: 1709.07321 [astro-ph.HE].

[4] V. de Souza. 'Measurements of the Depth of Maximum of Air-Shower Profiles at the Pierre Auger Observatory and their Composition Implications'. In: *JPS Conf. Proc.* 9 (2016), p. 010015. DOI: 10.7566/JPSCP.9.010015.

[5] Pedro Abreu et al. 'Interpretation of the Depths of Maximum of Extensive Air Showers Measured by the Pierre Auger Observatory'. In: *JCAP* 02 (2013), p. 026. DOI: 10.1088/1475-7516/2013/02/026. arXiv: 1301.6637 [astro-ph.HE].

[6] Alexander Aab et al. 'Search for photons with energies above 10^{18} eV using the hybrid detector of the Pierre Auger Observatory'. In: *JCAP* 04 (2017). [Erratum: JCAP 09, E02 (2020)], p. 009. DOI: 10.1088/1475-7516/2017/04/009. arXiv: 1612.01517 [astro-ph.HE].

[7] Alexander Aab et al. 'Probing the origin of ultra-high-energy cosmic rays with neutrinos in the EeV energy range using the Pierre Auger Observatory'. In: *JCAP* 10 (2019), p. 022. DOI: 10.1088/1475-7516/2019/10/022. arXiv: 1906.07422 [astro-ph.HE].

[8] J. Abraham et al. 'Limit on the diffuse flux of ultra-high energy tau neutrinos with the surface detector of the Pierre Auger Observatory'. In: *Phys. Rev. D* 79 (2009), p. 102001. DOI: 10.1103/PhysRevD.79.102001. arXiv: 0903.3385 [astro-ph.HE].

[9] Alexander Aab et al. 'Limits on point-like sources of ultra-high-energy neutrinos with the Pierre Auger Observatory'. In: *JCAP* 11 (2019), p. 004. DOI: 10.1088/1475-7516/2019/11/004. arXiv: 1906.07419 [astro-ph.HE].

[10] Alexander Aab et al. 'A Search for Ultra-high-energy Neutrinos from TXS 0506+056 Using the Pierre Auger Observatory'. In: *Astrophys. J.* 902.2 (2020), p. 105. DOI: 10.3847/1538-4357/abb476. arXiv: 2010.10953 [astro-ph.HE].

[11] Stephen Hoover. 'Status of the ANITA experiment'. In: *J. Phys. Conf. Ser.* 81 (2007). Ed. by Lee Thompson, p. 012009. DOI: 10.1088/1742-6596/81/1/012009.

[12] S. Hoover et al. 'Observation of Ultrahigh-Energy Cosmic Rays with the ANITA Balloon-Borne Radio Interferometer'. In: *Phys. Rev. Lett.* 105 (15 Oct. 2010), p. 151101. DOI: 10.1103/PhysRevLett.105.151101. URL: https://link.aps.org/doi/10.1103/PhysRevLett.105.151101.

[13] A. Romero-Wolf et al. 'Comprehensive analysis of anomalous ANITA events disfavors a diffuse tau-neutrino flux origin'. In: *Phys. Rev. D* 99.6 (2019), p. 063011. DOI: 10.1103/PhysRevD.99.063011. arXiv: 1811.07261 [astro-ph.HE].

[14] P. W. Gorham et al. 'Characteristics of Four Upward-Pointing Cosmic-Ray-like Events Observed with ANITA'. In: *Phys. Rev. Lett.* 117 (7 Aug. 2016), p. 071101. DOI: 10.1103/PhysRevLett.117.071101. URL: https://link.aps.org/doi/10.1103/PhysRevLett.117.071101.

[15] P. W. Gorham et al. 'Observation of an Unusual Upward-Going Cosmic-Ray-like Event in the Third Flight of ANITA'. In: *Phys. Rev. Lett.* 121 (16 Oct. 2018), p. 161102. DOI: 10.1103/PhysRevLett.121.161102. URL: https://link.aps.org/doi/10.1103/PhysRevLett.121.161102.

[16] M. G. Aartsen et al. 'A search for IceCube events in the direction of ANITA neutrino candidates'. In: (Jan. 2020). DOI: 10.3847/1538-4357/ab791d. arXiv: 2001.01737 [astro-ph.HE].

[17] Lucien Heurtier et al. 'Explaining the ANITA Anomaly with Inelastic Boosted Dark Matter'. In: *Phys. Rev. D* 100.5 (2019), p. 055004. DOI: 10.1103/PhysRevD.100.055004. arXiv: 1905.13223 [hep-ph].

[18] Guo-yuan Huang. 'Sterile neutrinos as a possible explanation for the upward air shower events at ANITA'. In: *Phys. Rev. D* 98.4 (2018), p. 043019. DOI: 10.1103/PhysRevD.98.043019. arXiv: 1804.05362 [hep-ph].

[19] Amy Connolly, Patrick Allison and Oindree Banerjee. 'On ANITA's sensitivity to long-lived, charged massive particles'. In: *arXiv e-prints* (July 2018). arXiv: 1807.08892 [astro-ph.HE].

[20] Jaime Alvarez-Muñiz et al. 'Comprehensive approach to tau-lepton production by high-energy tau neutrinos propagating through the Earth'. In: *Phys. Rev. D* 97.2 (2018). [Erratum: Phys.Rev.D 99, 069902 (2019)], p. 023021. DOI: 10.1103/PhysRevD.97.023021.

[21] N. Davidson et al. 'Universal interface of TAUOLA: Technical and physics documentation'. In: *Computer Physics Communications* 183.3 (Mar. 2012), pp. 821–843. ISSN: 0010-4655. DOI: 10.1016/j.cpc.2011.12.009. URL: http://dx.doi.org/10.1016/j.cpc.2011.12.009.

[22] Theodor Wulf. 'Observations of the radiation of high-penetration capacity on the Eiffel Tower'. In: *Physikalische Zeitschrift 11* (1910), pp. 811–813.

[23] Jörg R. Hörandel. 'Early Cosmic-Ray Work Published in German'. In: *AIP Conf. Proc.* 1516.1 (2013). Ed. by Jonathan F. Ormes, pp. 52–60. DOI: 10.1063/1.4792540. arXiv: 1212.0706 [physics.hist-ph].

[24] Victor F. Hess. 'Öbservations in low level radiation during seven free balloon flights'. In: *Physikalische Zeitschrift* 13 (1912), pp. 1084–1091.

[25] Jacob Clay. 'Penetrating Radiation'. In: *Proceedings Royal Academy Amsterdam* 30 (1927), pp. 1115–1127.

[26] E. Rutherford and H. Geiger. 'An electrical method of counting the number of α-particles from radio-active substances'. In: *Proc. R. Soc. Lond. A* 81 (1908), pp. 141–161.

[27] Bruno Rossi. 'On the Magnetic Deflection of Cosmic Rays'. In: *Physical Review* 36.3 (Aug. 1930), pp. 606–606. DOI: 10.1103/PhysRev.36.606.

[28] Marcel Schein, William P. Jesse and E. O. Wollan. 'The Nature of the Primary Cosmic Radiation and the Origin of the Mesotron'. In: *Phys. Rev.* 59 (7 Apr. 1941), pp. 615–615. DOI: 10.1103/PhysRev.59.615. URL: https://link.aps.org/doi/10.1103/PhysRev.59.615.

[29] Phyllis Freier et al. 'Evidence for Heavy Nuclei in the Primary Cosmic Radiation'. In: *Phys. Rev.* 74 (2 July 1948), pp. 213–217. DOI: 10.1103/PhysRev.74.213. URL: https://link.aps.org/doi/10.1103/PhysRev.74.213.

[30] H. L. Bradt and B. Peters. 'Investigation of the Primary Cosmic Radiation with Nuclear Photographic Emulsions'. In: *Phys. Rev.* 74 (12 Dec. 1948), pp. 1828–1837. DOI: 10.1103/PhysRev.74.1828. URL: https://link.aps.org/doi/10.1103/PhysRev.74.1828.

[31] Thomas K. Gaisser, Ralph Engel and Elisa Resconi. *Cosmic rays and particle physics*. Cambridge University Press, 2016.

[32] P.A. Zyla et al. (Particle Data Group). 'Review of Particle Physics'. In: *Progress of Theoretical and Experimental Physics* 2020.8 (Aug. 2020). 038C0. DOI: https://doi.org/10.1093/ptep/ptaa104.

[33] T. K. Gaisser and A. M. Hillas. 'Reliability of the Method of Constant Intensity Cuts for Reconstructing the Average Development of Vertical Showers'. In: *International Cosmic Ray Conference*. Vol. 8. International Cosmic Ray Conference. Jan. 1977, p. 353.

[34] Rodney Hillier. *Gamma ray astronomy*. 1984.

[35] T. Antoni et al. 'KASCADE measurements of energy spectra for elemental groups of cosmic rays: Results and open problems'. In: *Astropart. Phys.* 24 (2005), pp. 1–25. DOI: 10.1016/j.astropartphys.2005.04.001. arXiv: astro-ph/0505413.

[36] ENRICO Fermi. 'On the Origin of the Cosmic Radiation'. In: *Phys. Rev.* 75 (8 Apr. 1949), pp. 1169–1174. DOI: 10.1103/PhysRev.75.1169. URL: https://link.aps.org/doi/10.1103/PhysRev.75.1169.

[37] ZHANG Yi-ran and LIU Si-ming. 'The Origin of Cosmic Rays from Supernova Remnants'. In: *Chinese Astronomy and Astrophysics* 44.1 (2020), pp. 1–31. ISSN: 0275-1062. DOI: https://doi.org/10.1016/j.chinastron.2020.04.001. URL: https://www.sciencedirect.com/science/article/pii/S0275106220300011.

[38] Alexander Aab et al. 'Depth of Maximum of Air-Shower Profiles at the Pierre Auger Observatory: Measurements at Energies above $10^{17.8}$ eV'. In: *Phys. Rev. D* 90.12 (2014), p. 122005. DOI: 10.1103/PhysRevD.90.122005. arXiv: 1409.4809 [astro-ph.HE].

[39] A. Aab et al. 'Depth of maximum of air-shower profiles at the Pierre Auger Observatory. II. Composition implications'. In: *Phys. Rev. D* 90.12 (2014), p. 122006. DOI: 10.1103/PhysRevD.90.122006. arXiv: 1409.5083 [astro-ph.HE].

[40] Jose Bellido. 'Depth of maximum of air-shower profiles at the Pierre Auger Observatory: Measurements above $10^{17.2}$ eV and Composition Implications'. In: *PoS* ICRC2017 (2018). Ed. by Darko Veberic, p. 506. DOI: 10.22323/1.301.0506.

[41] L Cazon and. 'Studying the nuclear mass composition of Ultra-High Energy Cosmic Rays with the Pierre Auger Observatory'. In: *Journal of Physics: Conference Series* 375.5 (July 2012), p. 052003. DOI: 10.1088/1742-6596/375/1/052003. URL: https://doi.org/10.1088%2F1742-6596%2F375%2F1%2F052003.

[42] R. U. Abbasi et al. 'Indications of Proton-Dominated Cosmic Ray Composition above 1.6 EeV'. In: *Phys. Rev. Lett.* 104 (2010), p. 161101. DOI: 10.1103/PhysRevLett.104.161101. arXiv: 0910.4184 [astro-ph.HE].

[43] Karl-Heinz Kampert and Peter Tinyakov. 'Cosmic rays from the ankle to the cutoff'. In: *Comptes Rendus Physique* 15 (2014), pp. 318–328. DOI: 10.1016/j.crhy.2014.04.006. arXiv: 1405.0575 [astro-ph.HE].

[44] Zatsepin, G T and Kuz'min, V A. 'UPPER LIMIT OF THE SPECTRUM OF COSMIC RAYS'. In: *JETP Lett. (USSR) (Engl. Transl.)* Vol: 4 (Aug. 1966). URL: https://www.osti.gov/biblio/4515382.

[45] V. A. Kuzmin and G. T. Zatsepin. 'On cosmic-ray interactions with photons'. In: *Canadian Journal of Physics* 46.10 (1968), S617–S619. DOI: 10.1139/p68-309. eprint: https://doi.org/10.1139/p68-309. URL: https://doi.org/10.1139/p68-309.

[46] M. G. Aartsen et al. 'Differential limit on the extremely-high-energy cosmic neutrino flux in the presence of astrophysical background from nine years of IceCube data'. In: *Phys. Rev. D* 98.6 (2018), p. 062003. DOI: 10.1103/PhysRevD.98.062003. arXiv: 1807.01820 [astro-ph.HE].

[47] Pedro Abreu et al. 'A search for ultra-high-energy photons at the Pierre Auger Observatory exploiting air-shower universality'. In: *PoS* ICRC2021 (2021), p. 373. DOI: 10.22323/1.395.0373.

[48] Karl-Heinz Kampert. 'Cosmic Rays from the Knee to the Ankle – Status and Prospects'. In: *Nuclear Physics B - Proceedings Supplements* 165 (Mar. 2007), pp. 294–306. DOI: 10.1016/j.nuclphysbps.2006.11.048.

[49] Pedro Abreu et al. 'Combined fit of the energy spectrum and mass composition across the ankle with the data measured at the Pierre Auger Observatory'. In: *PoS* ICRC2021 (2021), p. 311. DOI: 10.22323/1.395.0311.

[50] Kseniya V. Ptitsyna and Sergei V. Troitsky. 'Physical conditions in potential sources of ultra-high-energy cosmic rays. I. Updated Hillas plot and radiation-loss constraints'. In: *Phys. Usp.* 53 (2010), pp. 691–701. DOI: 10.3367/UFNe.0180.201007c.0723. arXiv: 0808.0367 [astro-ph].

[51] Lorenzo Caccianiga. 'Anisotropies of the Highest Energy Cosmic-ray Events Recorded by the Pierre Auger Observatory in 15 years of Operation'. In: *PoS* ICRC2019 (2021), p. 206. DOI: 10.22323/1.358.0206.

[52] Armando di Matteo et al. 'Full-sky searches for anisotropies in UHECR arrival directions with the Pierre Auger Observatory and the Telescope Array'. In: *Proceedings of 36th International Cosmic Ray Conference — PoS(ICRC2019)* (Aug. 2019). DOI: 10.22323/1.358.0439. URL: http://dx.doi.org/10.22323/1.358.0439.

[53] A. Aab et al. 'Cosmic-Ray Anisotropies in Right Ascension Measured by the Pierre Auger Observatory'. In: *The Astrophysical Journal* 891.2 (Mar. 2020), p. 142. DOI: 10.3847/1538-4357/ab7236. URL: https://doi.org/10.3847/1538-4357/ab7236.

[54] T. Pierog et al. 'First results of fast one-dimensional hybrid simulation of EAS using CONEX'. In: *Nucl. Phys. B Proc. Suppl.* 151 (2006). Ed. by P. K. F. Grieder, B. Pattison and L. K. Resvanis, pp. 159–162. DOI: 10.1016/j.nuclphysbps.2005.07.029. arXiv: astro-ph/0411260.

[55] W. Heitler. *Quantum theory of radiation*. 1954.

[56] Felix Riehn et al. 'The hadronic interaction model SIBYLL 2.3c and Feynman scaling'. In: *PoS* ICRC2017 (2018), p. 301. DOI: 10.22323/1.301.0301. arXiv: 1709.07227 [hep-ph].

[57] 'The Pierre Auger Cosmic Ray Observatory'. In: *Nuclear Instruments and Methods in Physics Research Section A: Accelerators, Spectrometers, Detectors and Associated Equipment* 798 (2015), pp. 172–213. ISSN: 0168-9002. DOI: https://doi.org/10.1016/j.nima.2015.06.058. URL: https://www.sciencedirect.com/science/article/pii/S0168900215008086.

[58] Sijbrand De Jong. 'The Radio detection of inclined showers at the Pierre Auger Observatory'. In: *PoS* ICHEP2020 (2021), p. 829. DOI: 10.22323/1.390.0829. arXiv: 2012.05044 [astro-ph.IM].

[59] Pedro Abreu et al. 'Antennas for the Detection of Radio Emission Pulses from Cosmic-Ray induced Air Showers at the Pierre Auger Observatory'. In: *JINST* 7 (Sept. 2012). DOI: 10.1088/1748-0221/7/10/P10011.

[60] Benjamin Fuchs. 'The Auger Engineering Radio Array'. In: *Nuclear Instruments and Methods in Physics Research Section A: Accelerators, Spectrometers, Detectors and Associated Equipment* 692 (Nov. 2012), pp. 93–97. DOI: 10.1016/j.nima.2012.01.058.

[61] Tim Huege. 'Radio detection of cosmic rays with the Auger Engineering Radio Array'. In: *EPJ Web of Conferences* 210 (Jan. 2019), p. 05011. DOI: 10.1051/epjconf/201921005011.

[62] The Pierre Auger Collaboration. 'The Pierre Auger Cosmic Ray Observatory'. In: *Nuclear Instruments and Methods in Physics Research. Section A, Accelerators, Spectrometers, Detectors and Associated Equipment* 798.C (Oct. 2015). DOI: 10.1016/j.nima.2015.06.058.

[63] Pedro Abreu et al. 'Status and performance of the underground muon detector of the Pierre Auger Observatory'. In: *PoS* ICRC2021 (2021), p. 233. DOI: 10.22323/1.395.0233.

[64] A. Aab et al. 'The Pierre Auger Observatory Upgrade - Preliminary Design Report'. In: (Apr. 2016).

[65] Pierre Auger Collaboration. URL: https://www.flickr.com/photos/134252569@N07/20097628351/in/album-72157656013297308/.

[66] Jiju Abraham et al. 'Trigger and aperture of the surface detector array of the Pierre Auger Observatory'. In: *Nuclear Instruments and Methods in Physics Research Section A: Accelerators, Spectrometers, Detectors and Associated Equipment* 613 (Jan. 2010). DOI: 10.1016/j.nima.2009.11.018.

[67] J. Abraham et al. 'The Fluorescence Detector of the Pierre Auger Observatory'. In: *Nucl. Instrum. Meth. A* 620 (2010), pp. 227–251. DOI: 10.1016/j.nima.2010.04.023. arXiv: 0907.4282 [astro-ph.IM].

[68] Hartmut Gemmeke et al. 'The Auger Fluorescence Detector Electronics'. In: (Aug. 2001).

[69] S. Argiro et al. 'The Offline Software Framework of the Pierre Auger Observatory'. In: *Nucl. Instrum. Meth. A* 580 (2007), pp. 1485–1496. DOI: 10.1016/j.nima.2007.07.010. arXiv: 0707.1652 [astro-ph].

[70] Pedro Abreu et al. 'Identifying Clouds over the Pierre Auger Observatory using Infrared Satellite Data'. In: *Astroparticle Physics* 50-52 (Dec. 2013), pp. 92–101. DOI: 10.1016/j.astropartphys.2013.09.004.

[71] P. M. Younk and B. Fick. *On SDP Reconstruction Accuracy*. GAP-2006-086 Internal Auger GAP-note.

[72] R. Brun and F. Rademakers. 'ROOT: An object oriented data analysis framework'. In: *Nucl. Instrum. Meth. A* 389 (1997). Ed. by M. Werlen and D. Perret-Gallix, pp. 81–86. DOI: 10.1016/S0168-9002(97)00048-X.

[73] D. Fargion et al. 'Tau Air Showers from Earth'. In: *The Astrophysical Journal* 613.2 (Oct. 2004), pp. 1285–1301. DOI: 10.1086/423124. URL: https://doi.org/10.1086/423124.

[74] Jiwoo Nam. 'Overview of the Fourth Flight of the ANITA Experiment'. In: *PoS* ICRC2017 (2017), p. 952. DOI: 10.22323/1.301.0952.

[75] UCL ANITA. URL: https://www.hep.ucl.ac.uk/uhen/anita/.

[76] Debasish Borah et al. 'Connecting ANITA anomalous events to a nonthermal dark matter scenario'. In: *Physical Review D* 101.7 (Apr. 2020). ISSN: 2470-0029. DOI: 10.1103/physrevd.101.075039. URL: http://dx.doi.org/10.1103/PhysRevD.101.075039.

[77] Derek B. Fox et al. *The ANITA Anomalous Events as Signatures of a Beyond Standard Model Particle, and Supporting Observations from IceCube*. 2018. arXiv: 1809.09615 [astro-ph.HE].

[78] Arman Esmaili and Yasaman Farzan. 'Explaining the ANITA events by a $L_e - L_\tau$ gauge model'. In: *JCAP* 12 (2019), p. 017. DOI: 10.1088/1475-7516/2019/12/017. arXiv: 1909.07995 [hep-ph].

[79] D. Heck et al. *CORSIKA: a Monte Carlo code to simulate extensive air showers*. 1998.

[80] K. Kamata and J. Nishimura. 'The Lateral and the Angular Structure Functions of Electron Showers'. In: *Progress of Theoretical Physics Supplement* 6 (Jan. 1958), pp. 93–155. DOI: 10.1143/PTPS.6.93.

[81] K Greisen. 'Cosmic Ray Showers'. In: *Annual Review of Nuclear Science* 10.1 (1960), pp. 63–108. DOI: 10.1146/annurev.ns.10.120160.000431. eprint: https://doi.org/10.1146/annurev.ns.10.120160.000431. URL: https://doi.org/10.1146/annurev.ns.10.120160.000431.

[82] W. Ralph Nelson, H. Hirayama and David W. O. Rogers. 'The Egs4 Code System'. In: (Dec. 1985).

[83] H. Fesefeldt. In: *PITHA 85/02, RWTH Aachen* (1985).

[84] D. Heck and T. Pierog. *Extensive Air Shower Simulation with CORSIKA: A User's Guide(Version 7.7410)from May 1, 2021).* https://web.iap.kit.edu/corsika/usersguide/usersguide.pdf. May 2021.

[85] M Bleicher et al. 'Relativistic hadron-hadron collisions in the ultra-relativistic quantum molecular dynamics model'. In: *Journal of Physics G: Nuclear and Particle Physics* 25.9 (Sept. 1999), pp. 1859–1896. ISSN: 1361-6471. DOI: 10.1088/0954-3899/25/9/308. URL: http://dx.doi.org/10.1088/0954-3899/25/9/308.

[86] S. Ostapchenko. 'QGSJET-II: towards reliable description of very high energy hadronic interactions'. In: *Nuclear Physics B - Proceedings Supplements* 151.1 (Jan. 2006), pp. 143–146. ISSN: 0920-5632. DOI: 10.1016/j.nuclphysbps.2005.07.026. URL: http://dx.doi.org/10.1016/j.nuclphysbps.2005.07.026.

[87] F. Nerling et al. 'Universality of electron distributions in high-energy air showers—Description of Cherenkov light production'. In: *Astroparticle Physics* 24.6 (Jan. 2006), pp. 421–437. ISSN: 0927-6505. DOI: 10.1016/j.astropartphys.2005.09.002. URL: http://dx.doi.org/10.1016/j.astropartphys.2005.09.002.

[88] V. Novotny and J. Blazek. *Integration of PCGF into simulation database.* https://www.auger.unam.mx/AugerWiki/MultiMessenger/MM-PastMeetings. May 2020.

[89] https://www.auger.unam.mx/AugerWiki/FD_Upgoing.

[90] L. Perrone and E. de Vito. *Laser Cleaning and preparation of burn and data sample.* https://www.auger.unam.mx/AugerWiki/MultiMessenger/MM-PastMeetings. July 2020.

[91] Vladimir Novotny. 'Measurement of the spectrum of cosmic rays above $10^{16.5}$ eV with Cherenkov-dominated events at the Pierre Auger Observatory'. In: *PoS* ICRC2019 (2021), p. 374. DOI: 10.22323/1.358.0374.

[92] Massimo Mastrodicasa et al. 'Search for upward-going showers with the Fluorescence Detector of the Pierre Auger Observatory'. In: *PoS* ICRC2021 (2021), p. 1140. DOI: 10.22323/1.395.1140.

[93] A. Aab et al. 'Features of the Energy Spectrum of Cosmic Rays above 2.5×10^{18} eV Using the Pierre Auger Observatory'. In: *Phys. Rev. Lett.* 125 (12 Sept. 2020), p. 121106. DOI: 10.1103/PhysRevLett.125.121106. URL: https://link.aps.org/doi/10.1103/PhysRevLett.125.121106.

[94] P. Abreu et al. 'The exposure of the hybrid detector of the Pierre Auger Observatory'. In: *Astroparticle Physics* 34.6 (2011), pp. 368–381. ISSN: 0927-6505. DOI: https://doi.org/10.1016/j.astropartphys.2010.10.001. URL: https://www.sciencedirect.com/science/article/pii/S0927650510001829.

[95] Wolfgang A. Rolke, Angel M. López and Jan Conrad. 'Limits and confidence intervals in the presence of nuisance parameters'. In: *Nuclear Instruments and Methods in Physics Research Section A: Accelerators, Spectrometers, Detectors and Associated Equipment* 551.2–3 (Oct. 2005), pp. 493–503. ISSN: 0168-9002. DOI: 10.1016/j.nima.2005.05.068. URL: http://dx.doi.org/10.1016/j.nima.2005.05.068.

[96] Alexander Aab et al. 'Improved limit to the diffuse flux of ultrahigh energy neutrinos from the Pierre Auger Observatory'. In: *Phys. Rev. D* 91.9 (2015), p. 092008. DOI: 10.1103/PhysRevD.91.092008. arXiv: 1504.05397 [astro-ph.HE].

[97] Ioana Alexandra Caracas et al. 'A tau scenario application to a search for upward-going showers with the Fluorescence Detector of the Pierre Auger Observatory'. In: *PoS* ICRC2021 (2021), p. 1145. DOI: 10.22323/1.395.1145.

[98] Halina Abramowicz and Aharon Levy. *The ALLM parameterization of $\sigma_{tot}(\gamma * p)$ - an update*. 2004. arXiv: hep-ph/9712415 [hep-ph].

[99] Raj Gandhi et al. 'Ultrahigh-energy neutrino interactions'. In: *Astroparticle Physics* 5.2 (Aug. 1996), pp. 81–110. ISSN: 0927-6505. DOI: 10.1016/0927-6505(96)00008-4. URL: http://dx.doi.org/10.1016/0927-6505(96)00008-4.

[100] https://pdg.lbl.gov/2014/AtomicNuclearProperties/HTML/air_dry_1_atm.html.

[101] Gary J. Feldman and Robert D. Cousins. 'A Unified approach to the classical statistical analysis of small signals'. In: *Phys. Rev. D* 57 (1998), pp. 3873–3889. DOI: 10.1103/PhysRevD.57.3873. arXiv: physics/9711021.

[102] Parameters of the Preliminary Reference Earth Model are given by Adam Dziewonski, "Earth Structure, Global," in The Encyclopedia of Solid Earth Geophysics, edited by David E. James (Van Nostrand Reinhold, New York, 1989), p. 331.

[103] John W. Morgan and Edward Anders. 'Chemical Composition of Earth, Venus, and Mercury'. In: *Proceedings of the National Academy of Science* 77.12 (Dec. 1980), pp. 6973–6977. DOI: 10.1073/pnas.77.12.6973.

[104] E. Ripamonti, Michela Mapelli and A. Ferrara. 'Intergalactic medium heating by dark matter'. In: *Mon. Not. Roy. Astron. Soc.* 374 (2007), pp. 1067–1077. DOI: 10.1111/j.1365-2966.2006.11222.x. arXiv: astro-ph/0606482.

[105] Mary Hall Reno et al. 'Neutrino constraints on long-lived heavy dark sector particle decays in the Earth'. In: *Phys. Rev. D* 105.5 (2022), p. 055013. DOI: 10.1103/PhysRevD.105.055013. arXiv: 2107.01159 [hep-ph].

[106] Amy Connolly, Robert S. Thorne and David Waters. 'Calculation of high energy neutrino-nucleon cross sections and uncertainties using the Martin-Stirling-Thorne-Watt parton distribution functions and implications for future experiments'. In: *Phys. Rev. D* 83 (11 June 2011), p. 113009. DOI: 10.1103/PhysRevD.83.113009. URL: https://link.aps.org/doi/10.1103/PhysRevD.83.113009.

[107] A. Albert et al. 'Search for High-energy Neutrinos from Binary Neutron Star Merger GW170817 with ANTARES, IceCube, and the Pierre Auger Observatory'. In: *Astrophys. J. Lett.* 850.2 (2017), p. L35. DOI: 10.3847/2041-8213/aa9aed. arXiv: 1710.05839 [astro-ph.HE].

[108] H. L. Lai et al. 'Global QCD analysis of parton structure of the nucleon: CTEQ5 parton distributions'. In: *Eur. Phys. J. C* 12 (2000), pp. 375–392. DOI: 10.1007/s100529900196. arXiv: hep-ph/9903282.

[109] F. James. 'MINUIT Function Minimization and Error Analysis: Reference Manual Version 94.1'. In: (1994).

[110] William F. Hanlon. 'THE ENERGY SPECTRUM OF ULTRA HIGH ENERGY COSMIC RAYS MEASURED BY THE HIGH RESOLUTION FLY'S EYE OBSERVATORY IN STEREOSCOPIC MODE'. PhD thesis. The University of Utah, Dec. 2008.

[111] United States Committee on Extension to the Standard Atmosphere. 'U.S. standard atmosphere'. English. In: (1976). U.S. standard atmosphere (1976), xv, 227 p. :

[112] https://web.iap.kit.edu/corsika/usersguide/usersguide.pdf.

Acknowledgments

This thesis and the research presented within wouldn't have been possible without the tremendous help and support of several people.

I would like to start with thanking to Prof. Dr. Karl-Heinz Kampert for giving me the opportunity to be a part of his working group in the Bergische University of Wuppertal. I am grateful for all the support he offered me ever since the very beginning, for all the fruitful discussions and valuable advice! The presented results would have never been possible without his help, patience and guidance! I would also like to thank him for making me realize a professor is not a person to be afraid or ashamed of when having a question, but someone who would always give the best of advice, someone who can guide through the different and unavoidable challenges one would encounter during their research career. I have so many reasons to be thankful to professor Kampert, but I will only limit to the ones enumerated above. Thank you very much for everything!

Secondly, I would like to thank to Prof. Dr. Jaime Alvarez Muñiz, for accepting to be the second reviewer of this thesis. I am grateful for all the very useful discussions we had regarding tau neutrinos studies, regarding the τ-lepton propagation process and the already existent ES studies. He has never hesitated to help me whenever I had any questions, and those were not few times. Thank you!

I would also like to thank to Dr. Eric Mayotte, who was my direct supervisor for more than half of my PhD research. It's difficult to convey in words how much I appreciate his help, the patience he had when I would just not understand the point and he had to draw it on the board and I would still have additional questions. I will always remember the -sometimes very heated - debates we were having, which always ended up with the best results! He was not only my supervisor, but a great friend as well! He has always encouraged me and motivated me to keep on going (or to "just take some time off") when I was feeling down. He also taught me there is always room for improvement and one should never settle for partial "good-enough" results. Thank you, I would have never made it without your help!

I am very thankful to Dr. Julian Rautenberg, for his invaluable advice, friendly and useful discussions and most importantly, amazing coffee!

A big thank you goes to the Astros, for being the most amazing working group I have ever met! I still remember when I have first arrived in Wuppertal, how I was thinking that starting it all over again, in a new place with no one I know, would be extremely complicated and scary. But you had proved me wrong by welcoming me as one of your own since the very first day. Four years have passed since then and we have gathered so many memories together meanwhile. Thank you for the coffee breaks, thank you for the funny beers discussions, thank you for your support and for being the amazing people that you are! Thank you as well for teaching me one of my first German sentences: "Kein Bier vor Vier"!

I wouldn't be here without the amazing support from my parents! I would like to thank them for always being there for me, for always encouraging me into following my dreams and for always repeating the phrase "If you love what you are doing, you will never work a day in your life". They were right!

To my friends from Romania and not only - thank you very much for coping with me during those times when I could barely handle myself! Thank you for helping me stay on the track (I still like to believe I'm almost normal)!

Last but not least, I would like to thank to my Kamil! I am not sure where to start with thanking you. Thank you for bearing me during my lowest moments, for teaching me to take it"one day at a time", for always believing in me even when I stopped doing so! Thank you for always being there and holding my hand through every step, thank you for always making me smile, thank you for being my best friend!

Declaration of Authorship

English

I hereby declare that the thesis submitted is my own unaided work. All direct or indirect sources used are acknowledged as references.

This thesis was not previously presented to another examination board and has not been published.

Deutsch

Hiermit versichere ich, die vorliegende Arbeit selbstständig und unter ausschließlicher Verwendung der angegebenen Literatur und Hilfsmittel erstellt zu haben.

Die Arbeit wurde bisher in gleicher oder ähnlicher Form keiner anderen Prüfungsbehörde vorgelegt und auch nicht veröffentlicht.

Wuppertal, den _____ _____

(Ioana Alexandra Caracas)